LA-8511-PR
Progress Report

inertial fusion program

July 1 - December 31, 1979

University of California
LOS ALAMOS
SCIENTIFIC LABORATORY

The four most recent reports in this series, unclassified, are LA-7328-PR, LA-7587-PR, LA-7755-PR, and LA-8114-PR.

This work was supported by the US Department of Energy, Office of Inertial Fusion.

Edited by Helen M. Sinoradzki
Photocomposition by E. Katherine Valdez
Assisted by Joni L. Powell

LA-8511-PR
Progress Report

UC-21
Issued: October 1981

Inertial Fusion Program

July 1—December 31, 1979

Roger B. Perkins and the
Inertial Fusion Program Staff

Compiled by

Frederick Skoberne

CONTENTS

ACRONYMS

ADC	Analog-to-Digital Converter
ANL	Argonne National Laboratory
ASE	amplified spontaneous emission
AWRE	Atomic Weapons Research Establishment
BNL	Brookhaven National Laboratory
BSS	Beam Simultaneity System
CCD	charge-coupled device
CHS	collimated hole structure
CVD	chemical vapor deposition
DFP	drill, fill, and plug
DFWM	degenerate four-wave mixing
DOE	Department of Energy
EGTF	Electron-Gun Test Facility
EMI	electromagnetic interference
FIF	fast isothermal freezing
FSAR	Laser Fusion Facility Final Safety Analysis Report
GMB	glass microballoon
g_0L	gain-length product
GWTF	Gigawatt Test Facility
HCC	Harshaw Chemical Co.
HEGLF	High-Energy Gas Laser Facility
HIF	Heavy-Ion Fusion
ICF	Inertial Confinement Fusion
IDS	input detection system
I/O	In/Out
LBL	Lawrence Berkeley Laboratory
LIFE	Light Ion Fusion Experiment
LLNL	Lawrence Livermore National Laboratory
LPP	Low Pressure Plasma
LTE	local thermodynamic equilibrium
LTSG	laser-triggered spark gap
MCNP	Monte Carlo code for neutron and photon transport
MCP	microchannel plates
MHD	magnetohydrodynamics
MI	machine interface
MIRAS	microradiographic analysis system
MOPA	master-oscillator, power-amplifier system
MTF	modulation transfer function

NMR	Nuclear Magnetic Resonance
OEL	Optical Evaluation Laboratory
PCDS	phase-conjugate detection system
PDM	Pittsburgh-Des Moines Steel Co.
PFN	pulse-forming network
p-v	peak-to-valley
PVD	physical vapor deposition
RFQ	request for quotation
rfq	radio-frequency quadrupole
RIO	reinjection oscillator
R-T	Rayleigh-Taylor
SCC	subsystem-control computers
SEM	scanning electron micrograph
SPDT	single-point diamond-turn
TEA	transversely excited atmospheric pressure
TPA	triple-pass amplifier
VPP	vapor phase pyrolysis
XRD	x-ray diode

INERTIAL FUSION PROGRAM
July 1—December 31, 1979

by

Roger B. Perkins and the Inertial Fusion Program Staff

Compiled by
Frederick Skoberne

ABSTRACT

Progress in the development of high-energy short-pulse CO_2 laser systems for fusion research is reported. Improvements in the Los Alamos National Laboratory eight-beam Helios system are described. These improvements increased the reliability of the laser and permitted the firing of 290 shots, most of which delivered energies of approximately 8 kJ to the target. Modifications to Gemini are outlined, including the installation of a new target-insertion mechanism. The redirection of the Antares program is discussed in detail, which will achieve a total energy of approximately 40 kJ with two beams. This redirection will bring Antares on-line almost two years earlier than was possible with the full six-beam system, although at a lower energy.

Experiments with isentropically imploded Sirius-B targets are discussed, and x-ray radiation-loss data from gold microballoons are presented, which show that these results are essentially identical with those obtained at glass-laser wavelengths.

Significant progress in characterizing laser fusion targets is reported. New processes for fabricating glass microballoon x-ray diagnostic targets, the application of high-quality metallic coatings, and the deposition of thick plastic coatings are described.

Results in the development of x-ray diagnostics are reported, and research in the Los Alamos heavy-ion fusion program is summarized.

Results of investigations of phase-conjugation research of gaseous saturable absorbers and of the use of alkali-halide crystals in a new class of saturable absorbers are summarized.

New containment-vessel concepts for Inertial Confinement Fusion reactors are discussed, and results of a scoping study of four fusion-fission hybrid concepts are presented.

SUMMARY
(Inertial Fusion Staff)

INTRODUCTION

The Inertial Fusion Program at the Los Alamos National Laboratory is supporting the Department of Energy (DOE) in its quest for a solution to the nations's long-term energy problems, as well as providing support for the nuclear weapons program. The first objective for both of these areas is to demonstrate that the fusion fuel contained in a target pellet can be ignited. To achieve this objective, we are pursuing a broadly based program involving the development of suitable high-power drivers, the design and fabrication of suitable fuel pellets, experimental studies of target phenomenology to provide feedback to the design process, development of suitable diagnostics for such experiments, the pursuit of weapons applications studies, and studies of concepts for the eventual use of inertial fusion for power production.

Three medium-sized CO_2 laser systems are now being used for experiments, while the 40-kJ Antares CO_2 laser is being readied for future tests. This report describes the progress made in unclassified parts of the program.

OPERATING CO_2 LASER SYSTEMS

Helios Laser System

This eight-beam, high-energy, short-pulse CO_2 laser is operating routinely as the principal research facility to investigate laser plasma interaction phenomena. Helios was fired 290 times, with 200 shots in support of main target experiments. The on-target energies with pulse widths of 600 ps provided ~8 TW on target. Important accomplishments include

- development and incorporation of an on-line Beam Simultaneity System (BSS) that allows us to measure and adjust the beam path lengths to within ±1 cm (33 ps);
- development and installation of composite capton/metal electron-beam foil windows, which have greatly improved the reliability of the electron gun;
- improvements in the alignment and optical diagnostic systems, which have led to better characterization of the laser output;
- further development of the Helios control system and software; and
- installation of power-supply oil purifiers of higher capacity to reduce downtime for maintenance.

Significant target experimental results are summarized in another section.

Gemini

The Gemini laser system is devoted mainly to target physics experiments and diagnostics development; 467 shots were fired in support of this program. On-target energies of up to 500 J in 1.0-ns pulses are attained routinely. Important achievements include the following items.

- The internal saturable-absorber gas cell was installed on the north beam to suppress parasitics and to increase the energy delivered to the target.
- A new target-insertion mechanism was installed that replaces the old target wheel and allows changing of targets through an airlock without breaking the vacuum.
- The new oscillator preamplifier front end was completed and is undergoing electrical and optical checkout. Installation is scheduled for early 1980.
- A control system upgrade to improve the reliability and operational aspects of Gemini was begun and will be completed early in 1980.

ANTARES—HIGH ENERGY GAS LASER FACILITY

Redirection of Program and General Progress

The Antares system was designed as a six-beam, 200-TW CO_2 laser with associated target-irradiation facilities. Recent theoretical calculations indicate that on-target energies for breakeven are significantly higher than those thought necessary previously. Uncertainties in theoretical modeling have also pointed up a lack of significant experimental target data. To achieve useful system energies and to provide critical experimental data

in as short a time as possible, the Antares effort has been redirected with DOE concurrence. The goal of this action is to build two power amplifiers as soon as possible with total on-target energies of ~40 kJ. This phase will provide needed target experimental data.

The Antares control system, the target vacuum system, and the target optical system are most heavily affected by the redirection and are being revised to accommodate the new requirements. Joint occupancy of the Antares Laser Hall by the Laboratory and the building contractor, which has been agreed upon to minimize the effect on the program of a significant construction-schedule slippage, has permitted installation of the first power-amplifier control stand and shielded main control room. Installation of the target vacuum system is proceeding under a similar joint-occupancy agreement.

We have received, assembled, and successfully tested many significant components such as the first electron gun, the electron-gun and gas pulsers, the first high-voltage power supply, and the front-end power amplifier. In addition, large-mirror positioners are being fabricated. Prototype parabolic mirrors have been single-point diamond-turned to exceed optical quality requirements. We have almost completed our optical beam-alignment studies and will then select one of the two types under consideration.

Progress in major areas is summarized in the following sections.

Optical System

A single-sector beamline mockup is being tested. An optical-beam ray-tracing code has been applied to the Antares optical train to verify position and tolerance requirements of all optical elements. The optical design of the power amplifier is frozen. Prototypes of alternative alignment schemes (flip-in and see-through) are undergoing tests. The Laser Hall and the Target Building were surveyed, and the first power-amplifier support stand was aligned.

Large Optical Components

Harshaw Chemical Co. (HCC) has improved the yields of the salt windows significantly (from 24 to 50%). The quality of the first full-size parabolic focusing mirror is excellent. The final mirror-positioner prototype was tested and met specifications successfully.

Front End

Performance tests on the driver amplifier showed that the unit purchased from Systems, Science and Software, Inc., met or exceeded all our requirements. Specifically, a gain uniformity of ±7% and a maximum gain-length product (g_0L) of 8.5 were achieved.

Power Amplifier

We installed and aligned the first support stand. The design of the entire pressure vessel is complete. The pumping-chamber sections have been received, and the end domes are being manufactured. The In/Out (I/O) optical sections have been designed and are being fabricated. Prototypes of the anode bushing and dielectric divider were tested successfully.

The electron-beam gun was assembled and vacuum-tested. After lengthy development, the titanium electron-beam window foils were bonded successfully to a stainless steel support grid. The high-voltage coaxial cable was received, and cable termination and assembly hardware is being fabricated.

Energy Storage

The gas pulser, manufactured by Maxwell Laboratories, Inc., passed a 2000-shot performance test. A prototype gun pulser was built and tested at Los Alamos. The first high-voltage power supply, manufactured by Universal Voltronics, met our specifications. A prototype fault-diverter gap is being tested.

Control System

The design of the control system was revised to meet the Antares redirection requirements. The UNIX operating system for the Antares computer network replaced the previous DECNET II system. The shielded main control room was installed. The standard fiber-optic modules are being produced.

Target System

Pittsburgh-Des Moines Steel Co. (PDM), under contract to DOE, completed the design of the target vacuum system. System installation began under a joint-occupancy arrangement with the building contractor. Six 1.9-m-diam beam tubes, connecting the Laser Hall and Target Building, and three beam-turning chambers in the target building were installed. PDM began the design of the target-chamber space frame. Alternative target optical system designs under study will convert the six-beam geometry into the two-beam geometry, while retaining the six-sided target illumination.

Building Construction

There has been a significant schedule slippage in the construction of the Laser Hall and the Target Building. To minimize the impact on Antares, joint occupancy of the Laser Hall by the contractor (Allen M. Campbell Co.) and the Laboratory, and of the Target Building by Campbell and PDM was begun in October 1979.

ADVANCED LASER TECHNOLOGY

The advanced laser technology program aims at improving the performance of current operating systems as well as at satisfying future program requirements by concentrating on (1) phase conjugation, which has a potential for improving the optical performance of future laser systems and for being applied diagnostically; (2) gaseous saturable absorbers, which have provided substantial performance improvements to Helios and can provide similar improvements to Antares; and (3) investigations of a new class of saturable absorbers based on doped alkali-halide crystals. The investigations of phase conjugation and gaseous saturable absorbers have been extremely successful in advancing the understanding of the processes involved.

TARGET EXPERIMENTS AND MILITARY APPLICATIONS

In our CO_2 laser fusion experiments, we try to develop and verify the calculational models used to extrapolate from target designs to the ignition and high-gain regimes. Ultimate laser and target requirements for pellet ignition will be determined in a carefully planned sequence of experiments. Single-shell, DT-gas-filled targets were isentropically imploded in our Sirius-B experiments. Spectroscopic analysis of x-ray line emissions from argon dopants in the fuel provided accurate determination of compressed fuel densities, whereas continuum radiation yielded the electron temperature. These data demonstrated that earlier density measurements, made with other diagnostic techniques, were correct within their experimental uncertainty and that the electrons and ions in the compressed fuel were in thermal equilibrium.

Gold microballoon targets, irradiated at intensities from 10^{14} to 5×10^{16} W/cm^2, have shown x-ray radiation losses of greater than 50% (of absorbed laser light) at 10^{14} W/cm^2 decreasing to 10% at 5×10^{16} W/cm^2. These results are essentially identical with those obtained with 1.06-μm laser light and 1-ns pulselengths. Spectral fits and continuum spectra demonstrated the nearly blackbody nature of the gold emitter.

Lateral transport of absorbed laser energy away from the laser focal spot along the surface of a target proceeded at a velocity of 2×10^8 cm/s if hydrogen was present in the target. This velocity is consistent with lateral energy flow velocities estimated in Nd:glass laser irradiation experiments. Our studies have shown a strong dependence of lateral energy flow on the presence or absence of hydrogen in the target; thus, some control of lateral flow is possible with the addition or exclusion of hydrogen from the target.

Experiments that display the characteristic K_α x rays generated deep within a target by the laser-excited hot electrons have shown that electron energy has a Maxwellian distribution up to an energy level several times that of hot electrons. More sensitive detection schemes are being developed to determine whether a cutoff occurs in the high-energy portion of the electron distribution.

TARGET DESIGN AND FUSION THEORY

Studies continued to increase our understanding of basic plasma processes crucial to target design. We concentrated on the characteristics of the electron spectrum produced by the resonance absorption process and the motion of the absorbing surface, which critically affect the overall hydrodynamic efficiency of the target and have not been adequately treated by our target design code.

Our research in target design has been expanded to include heavy-ion drivers; we prepared a single-shell

design driven by several megajoules of heavy ions. The Rayleigh-Taylor (R-T) instability, which remains an important problem in reactor-scale targets, has been further analyzed both linearly and nonlinearly. The inclusion of compressible-fluid effects in the code has altered the character of the instability, substantially reducing the growth rate in some cases and increasing it in others.

LASER FUSION TARGET FABRICATION

Significant progress has been made in characterizing laser fusion targets. We are developing laser Raman spectroscopy for nondestructive analysis of the contents of glass microballoons (GMBs), as well as for analysis of the gases trapped in the glass itself and of the chemical composition of surface coatings on GMBs.

By microradiography, we can now determine wall-thickness variations of 100 Å caused by nonconcentricity in a 120-μm-diam GMB having a 1-μm-thick wall. Detection is possible (with 99% confidence) of a 0.05-mm-high irregularity (bump) on the surface over a 5.6- by 5.6-μm area. We are completing the development of a computer-interfaced microradiographic analysis system (MIRAS).

A dye-laser hole-drilling technique was developed successfully for fabricating GMB targets with holes drilled with 1- to 5-μm diam. The GMBs are filled with the desired gases, and the holes are then sealed by melting and curing preplaced epoxy plugs while the GMBs are under pressure. Glass plugs are being developed.

We have continued our development of high-quality metallic coatings on selected GMBs. The deposition processes being studied are electroplating, electroless plating, physical vapor deposition (PVD), and chemical vapor deposition (CVD).

Smooth, thick plastic coatings can now be applied to microballoons. The Low Pressure Plasma (LPP) process routinely yields a surface roughness of ~30 nm with concentricities much better than 1% at 20-μm thickness. These results are also obtained when multiple layers are applied to achieve thicker coatings; a change in the polymer has yielded a 40-μm-thick coating in one step, the thickness being limited only by the supply of polymer. The Vapor Phase Pyrolysis (VPP) process can keep the surface roughness to 10 nm and concentricities to 1% at thicknesses up to 60 μm on stalk-mounted GMBs. We have increased the high-Z metal content of codeposited LPP coatings to as much as 56% lead and have extended our work to include bismuth and mercury.

Extremely low-density, small-cell-size plastic foams for use as cushions between pushers in advanced targets are being developed in our laboratories. We have demonstrated the ability to produce foams at a density of 0.10 g/cm^3 with cell sizes of 1 to 2 μm. This is only 50% higher than the specified density, which we should be able to achieve soon. Techniques for fabricating such foams into shells need to be developed.

The design of the cryogenic target-insertion mechanism for Helios is 85% complete.

We are continuing the development of gas-levitation techniques to support GMBs without mechanical contact during PVD coating. This method has great promise for producing coatings of extremely high quality on previously characterized GMB substrates.

DIAGNOSTICS DEVELOPMENT

X-ray diagnostics continue to be of primary importance because they provide much information on temperatures, densities, energy deposition and flow, and hydrodynamic quantities. Significant advances have been made in the development of fast-response x-ray diodes (XRDs) and the analysis of their data, in intensified imaging techniques, and in low-energy high-resolution spectrography.

Ion diagnostics, particularly the Thomson parabola, have been improved significantly to extend their ranges to both lower and higher ion energies. Analysis of such data is close to yielding sufficient understanding of coronal blowoff to provide an answer to the discrepancy between calculated and inferred hydrodynamic compression efficiencies. LASNEX calculations have consistently overestimated blowoff velocities and underestimated hydrodynamic efficiencies in spherical implosion calculations.

The first direct use of fiber optics for the transmittal of signals from an instrument close to the target to a recording apparatus outside the target chamber holds promise for direct readout of data from an exceedingly high-noise background environment.

HEAVY-ION FUSION DRIVER DEVELOPMENT

Heavy ions provide a promising new approach to inertial fusion. Particle accelerators generate intense beams of heavy ions (for example, uranium), which can be used to heat a pellet target. Our role in heavy-ion fusion research includes programs in accelerator development, target design, beam transport theory, and system studies. DOE has designated Los Alamos as the lead laboratory in the technical management of the national heavy-ion program.

SYSTEMS AND APPLICATIONS STUDIES OF INERTIAL FUSION

In Inertial Confinement Fusion (ICF) reactor studies, we have made significant progress in the development of a new containment-vessel concept, in calculation of reactor cavity and first-wall phenomena, and in neutronic analyses. We also report results of a preliminary examination of compatibility of heavy-ion beam drivers with available reactor cavity concepts. And finally, we summarize results of a preliminary scoping analysis of four fusion-fission hybrid concepts, which we conducted as part of our fissile-fuel production studies.

I. OPERATING CO_2 LASER SYSTEMS

(J. P. Carpenter, J. F. Figueira)

Three high-energy, short-pulse CO_2 laser systems are operating routinely at Los Alamos in support of the target experimental program: Helios, which first demonstrated a 10-kJ, 1-ns output in June 1978, is operating at ~10 TW on target in subnanosecond pulses; Gemini, a two-beam system that served as a prototype for Helios, operates at 300 J on target in a nanosecond pulse; and a smaller system, the Gigawatt Test Facility (GWTF), comprising two lasers, operates at outputs on target in the 1-2 GW range with nanosecond pulses.

A fourth system, Antares, is being constructed. This system, described separately in Sec. II, is being built to advance the understanding of ICF physics so that scaling to ignition conditions can be pursued with greater confidence.

HELIOS LASER SYSTEM

Introduction (E. L. Jolly)

The eight-beam, high-energy, short-pulse CO_2 laser system, Helios, is now an operational facility capable of irradiating targets on a routine basis. The system was fired at energies in the range of 6 kJ with pulse lengths of 600 to 800 ps; most of these shots were in direct support of target experiments, and the remaining shots were used for further system development and/or maintenance. Important accomplishments during this reporting period include

- measurement and adjustment of beam path lengths to ±1 cm (±33 ps simultaneity),
- use of composite metal-plastic foil windows for the electron-gun foil,
- development of Helios operating software, and
- installation of a higher capacity oil purifier in the pulse-forming-network (PFN) power supplies.

Significant target results obtained on Helios are discussed separately in the section on target experiments.

The 2:1 ratio of target shots to development shots underscores the transition of Helios to an operating facility. A major factor that increased the time available for target experiments is the increased reliability and operational efficiency during this reporting period. This report lists major improvements; however, there are numerous minor improvements whose cumulative effect upon reliability and efficiency is comparable to that of the major items. We are emphasizing reliable operation. Helios has become the most important instrument for assessing empirically the viability of the CO_2 laser for ICF, and it will remain so for the next few years. Its improving operational reliability and efficiency will be a continuing asset to the program.

Operations (E. L. Jolly)

During the second half of 1979, Helios was fired 290 times, 197 times in support of the target experimental program (a 130% increase over the first half of 1979) and 93 times in system development and/or maintenance tests. As in the first half of 1979, about two out of every five workdays were target shooting days; the remaining three days were used for target diagnostics installation, modification of system hardware and software, and routine maintenance. The system is currently capable of routinely delivering a maximum energy of 6 kJ in a 0.8-ns pulse (FWHM) to a target, at a system shot rate of about one per half-hour.

During the next 6 months, the primary operational objectives are to increase system reliability and the time that the system is available for target experiments.

Front End (R. Carlson, M. Weber, R. Pretzel)

The accuracy of the Helios BSS was improved. We installed a reference beam path with the proper optical attenuation and path length (multiple of a wavelength at 41.7 MHz) to simulate the signal returned by any of the eight beam paths. Using this system, the path length of a beam can be determined to within ±3 mm (10 ps). This accuracy, which is three times the BSS resolution (±3.3 ps), is limited by vibration and turbulence along the 200-m round-trip optical path. The reference beam does not degrade the BSS resolution.

To maintain the simultaneity of the eight beams within a prescribed tolerance, the alignment system must not be allowed to change the path length appreciably by walking or steering the beam. We met this requirement by allowing the automatic alignment system to align the beam-path mirrors from an out-of-tolerance condition to an aligned condition and by measuring the indicated path change caused by alignment. The change in path length from realigning the system was less than ± 3 mm. The system has been used routinely to adjust all beam paths to within the Helios goal of ± 1 cm (33 ps).

As part of the continuing effort to improve the front-end system and the long-term reliability of Helios, we also accomplished the following.

- We fabricated an improved switchout assembly of modular construction including transport optics and a mode-matching telescope.
- We installed improved vacuum pumping stations for the plasma tube and the saturable-absorber gas cell.
- We began designing a computer-based control system that provides stand-alone capability and easier operation.
- We started the construction of a prototype oscillator to demonstrate the feasibility of producing and time-stacking two lines. This prototype should lead to an oscillator with an output composed of four lines in the 10-μm band and two lines in the 9-μm band. Such an oscillator could be used to time-shape the Helios triple-pass amplifier (TPA) output.
- We began the construction from spare parts of an oscillator preamplifier system, which will provide ~1 J of energy in a 1-ns pulse, to be used for calibration, repair, and diagnostic checkout of Helios equipment.

Controls (E. L. Jolly, R. J. Johnson, M. D. Thomason, K. M. Spencer)

The control tasks fall into two categories, programming and control hardware, as summarized below.

Programming. A new Helios operating program, HELIOS II, was designed, coded, and tested. This program is used routinely for storage and review of beam diagnostic and front-end data, and for comprehensive shot summary.

Control Hardware. Complete major accomplishments included the following items.

- Installation and checkout of optical encoders on all target-chamber mirror mounts. The system is in operation.
- Repackaging of the two beam-positioner units in the control room into a single chassis. Optical isolator circuits were installed; the units are completely ground-isolated from the circuits they control. The instruction manual for this equipment was written.
- Construction and bench-scale testing of a microprocessor-based control system to control the Helios oil transport system to be installed after the oil transport system is completed.
- Construction and installation of shutters to block the four beamlines leaving the front-end room. A control panel indicating their position and interfacing to the building safety system was installed.
- Completion and bench-scale testing of a microprocessor-based automatic gas-mixing station to facilitate the mixing of up to 10 different saturable-absorber gases.

Laser Physics (G. Schappert, I. Bigio, D. Gasperson, R. Gibson, R. Haglund, E. Salesky, J. Busse, R. Jones)

Most of our efforts were directed toward characterizing, understanding, and improving the operations of Helios. Our major accomplishments are summarized below.

Energy Extraction Code Development. The standard rate-equation energy-extraction code used at the Laboratory is basically a single-line code, although it can be extended to treat both multiline and two-band operation. Pulse shapes can be controlled by operating with lines of substantially different gain. The two bands also have significantly different gains. In anticipation of having a two-line oscillator available in a few months, a code package to deal with energy extraction and pulse-shape propagation of two distinct lines was developed, which is nearly complete.

Laser Performance Study. In a one-beam experiment, we measured the reproducibility of energy output on a

Helios TPA. Energy measurements were taken with a 40.6-cm (16-in.) calorimeter placed at the output of the TPA. To test the possible loss of energy caused by breakdown at the spacial filter in the TPA sidearm, five shots were taken with the spacial filter in place and the sidearm pumped down to the nominal operating pressure of 2 torr of air; then five shots were taken with the spacial filter removed and the sidearm evacuated. The results, shown as Cases 1 and 2 in Table I-I, indicate no loss of energy at our operating point.

The next experiment involved a change in the timing of the 1-ns oscillator pulse relative to the peak gain of the TPA. If the oscillator pulse passes through the amplifier at a time other than peak gain and if there is jitter in the peak gain caused by spark-gap jitter or other factors, then the energy output will not be reproducible. This is borne out by the shots taken in Cases 1, 3, and 4 (Table I-I). Energy was increased 20% by advancing the oscillator pulse 0.5 μs from the setting that should have been optimal based on earlier small-signal gain measurements. This part of the experiment suggests that further work in TPA gain-timing is necessary.

Line Content and Dispersive Pulse Propagation Studies. A spectrometer was constructed that uses a high-dispersion grating in Litrow configuration. The resulting dispersion in a fairly compact device allows the use of Gen Tec Corp. ED-100 detectors to measure the energy in each line conveniently. These detectors are read by the computer-controlled CAMAC system in Gallery West (our optics diagnostic system) in the same way that the main energy detectors are read. The data are transmitted, along with the other diagnostic data, to the central Helios computer.

We accumulated data from several shots for which both the front-end (TPA input) line content and the TPA output-line content were measured. The ratios appear to track and correlate well. With the relatively low gains at which the system has been operated lately, the saturation effects are visible but relatively mild, as we expected.

We designed and built fast pyroelectric detectors, which would fit in the place of the energy detectors at the focal plane of the line-constant spectrometer in Gallery West. Thus, it is now possible to measure the temporal pulse shape and relative propagation times of the individual lines that compose the total energy output of the amplifier.

Very preliminary measurements suggest that pulse widths of individual lines are shorter (~60%) than the total spectral envelope. This dispersive propagation may cause the "bump on the tail" seen in several envelope pulse shapes.

Dogleg Modification. Design was completed and parts were manufactured for modifying the Helios triple-pass optical system to eliminate the dogleg [that is, the two 10-cm (4-in.) windows, the Mylar transporter, the SF4 pinhole, and the convex mirror] and replace it with a single convex mirror.

Laser Gas Deterioration Studies. Carbon dioxide dissociates into CO and O_2 in electrical discharge lasers. The dissociation rate has never been measured in electron-beam-controlled lasers; a method was therefore

TABLE I-I

ENERGY OUTPUT FROM AMPLIFIER 2B FOR FOUR DIFFERENT SHOOTING CONDITIONS[a]

Case	Shot Conditions	Output Energy (J)
1	Five shots, Pinhole SF4 in place, sidearm at 2 torr	600 ± 45
2	Five shots, Pinhole SF4 out, sidearm evacuated	607 ± 22
3	Three shots, oscillator pulse advanced 0.5 μs	720 ± 31
4	Three shots, oscillator pulse advanced 1.0 μs	495 ± 50

[a]The amplifier was fired at 52 kV/stage PFN and at 55 kV/stage electron beam for all shots. The saturable absorber was set at 11 torr of Mix 907 for all shots.

developed to measure CO concentrations with the existing gas chromatograph. Preliminary results from Gemini and Helios TPAs indicate that the dissociation rate is low enough to be of no concern in present systems. Accurate quantitative results are expected shortly.

Saturable-Absorber Studies. An automated absorber-gas mixing station for Helios was completed, which greatly simplifies the problem of mixing absorber gases reproducibly. Also, the gas chromatograph now being used for routine analyses of the absorber-gas mixtures (rather than the infrared spectrophotometer) is proving to be a simple and flexible instrument.

Considerable effort was devoted to finding a chromatographic technique suitable for analyzing $He:N_2:CO_2$ mixtures; a method was finally found that was simple to set up, reproducible, and accurate (compared to mass spectrographic methods). We can now routinely analyze CO_2 laser-gas mixes to an accuracy of 1% with a setup time of <1.0 h and an analysis time of ~7 min. The technique has already been used in resolving calibration problems with flowmeters in the GWTF.

Our continuing interest in multiline saturation properties of Mix 907 and its constituent absorber gases has motivated the construction of a saturable-absorber test bench for use in the Helios front end. Experiments for this setup include further transmission studies and pulse-shaping measurements.

We installed new half-length beam tubes through the saturable-absorber cells at the entrance to each TPA. This new design represents a tradeoff between the old full-length beam tubes, which contributed to a low parasitics threshold on target, and no beam tubes, which led to a degradation of the output pulse width from poor transmission of the oscillator pulse through the full length of the saturable-absorber cell. Preliminary data show that the output pulse width with the new design is narrower than with no beam tubes, and the parasitics threshold on a bare GMB is higher than with full-length beam tubes.

Gain Uniformity. We measured the spacial uniformity of small-signal gain in a Helios TPA. The g_0L was measured in a three by three array (Fig. I-1) encompassing the 35-cm aperture of TPA 4B. Full arrays were obtained for three different pumping conditions in the amplifier.

Pumping Condition	Operating Condition
(1) Electron beam at 55 kV/stage, PFN at 52 kV/stage	"Present" operating conditions
(2) Electron beam at 60 kV/stage, PFN at 55 kV/stage	First full-power test conditions (FIST I, April 1978)
(3) Electron beam at 50 kV/stage, PFN at 55 kV/stage	Second full-power test conditions (FIST II, June 1978)

The g_0L values are displayed in Fig. I-1. Two nonuniformities are evident.

- An up-down asymmetry exists under all three firing conditions. The two most likely causes for this asymmetry are (1) magnetic-field effects caused by currents in the electron-beam cables that enter from the top of the amplifier, and (2) an imbalance in electron emission from the top and bottom tantalum blades of the electron-beam gun. Further investigation will be required to distinguish between these two causes.

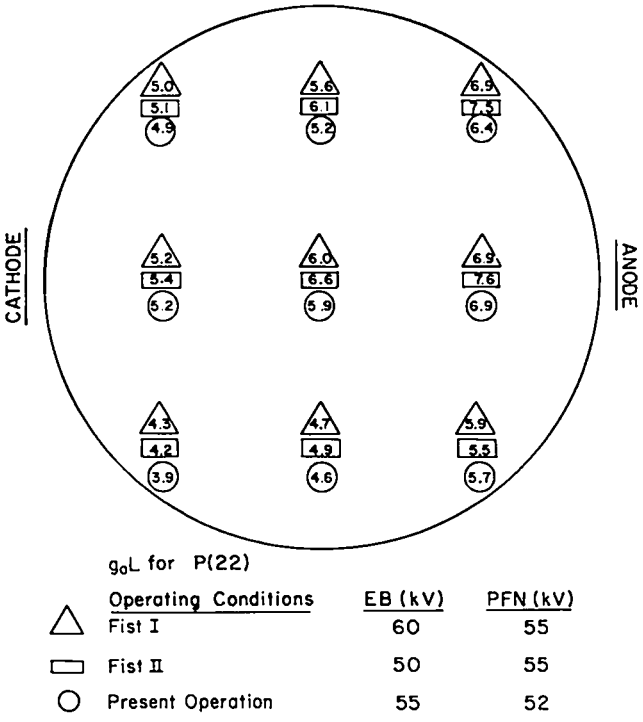

Fig. I-1.
Gain uniformity across the 35-cm aperture of Helios TPA 4B. The numbers represent the single-pass g_0L at P(22) for three different pumping conditions: FIST I, FIST II, and "present" operating conditions.

- An anode-cathode asymmetry exists for all three conditions, but is enhanced for the FIST-II firing conditions. Under these conditions the electron-beam voltage and therefore the range is reduced, and the gain is higher at the anode. Because the target-induced parasitics must be quenched with a saturable-absorber pressure sufficiently high to stand off this gain along the anode, the lower gain regions near the cathode will be less effective in bleaching the absorber. The result is enhanced nonuniformity in energy output and perhaps even a net loss in total energy output. It is recommended, therefore, that the amplifiers be operated at the higher electron-beam voltages, for example, during FIST I to reduce this asymmetry.

Optics (J. Hanlon, I. Liberman, V. K. Viswanathan, P. Bolen)

We concentrated on finishing and improving the alignment system and the optical beam train for Helios. Major accomplishments are listed below.

- Laser operations were improved significantly.
- Beam quality measurements were performed, as summarized in Table I-II. As a result of these measurements, corrective steps were taken to bring Beamlines 2A, 1B, and 3A to the same level of performance as the other beams.
- Twenty-four antireflection-coated salt windows were installed.
- New beam tubes were designed, tested, and installed.

TABLE I-II

HELIOS BEAM QUALITY DATA

Beamline	Diameter (μm)	Strehl Ratio
2B	65	0.60
1A	77	0.58
4B	90	0.54
4A	110	0.46
3B	120	0.43
2A	150	0.28
1B	160	0.28
3A	250	0.23

- We demonstrated that fringe patterns at the Helios target-chamber focal plane could be obtained with a Smartt interferometer.
- By lowering the gain on all data-acquisition units and raising the alignment laser power to compensate, we determined that the major source of noise on detectors in the alignment system was thermally induced. We significantly improved the stability, repeatability, and alignment time of the alignment system.
- The target-chamber encoder systems were installed, and each of the 48 mirror-mount drive motors was checked out.
- Most interferograms of the optical-train components as mounted (from the front end through the salt windows to the target chamber) have been completed.
- The preliminary design was initiated for an optical system to be used for aligning cryogenic targets and vaporizing the fuel.
- Alignment procedures for the Helios optical-system beam train were documented.
- Testing of the Rocketdyne adaptive optics was completed.

By using interferometric techniques for experiments as well as computer codes, we evaluated the Rocketdyne deformable mirror for applicability to our CO_2 laser fusion systems. The evaluation was made at 10.6 μm with a Smartt interferometer that we developed for the purpose. One of the Helios beamlines was duplicated optically for this experiment, and the collimating mirror in the TPA was replaced with the deformable mirror. The evaluation shows that the deformable mirror was able to correct the types of aberrations believed to exist in Helios beams. The inability of the mirror to raise the Strehl ratio above 0.6 was traced to the mirror edge-mounting constraints.

GEMINI LASER SYSTEM (J. P. Carpenter)

Introduction

The following target experiments were performed using the Gemini Laser System during the past 6 months:

(1) an x-ray diagnostics and shadowgraph experiment,

(2) calorimeter calibration,

(3) impulse measurements using pendulum targets,

(4) Mira-II target stability tests,
(5) diffuse-reflector experiments,
(6) free-surface velocity measurements, and
(7) x-ray channel-plate diagnostic development.

Significant results are discussed elsewhere in this report. Of the 467 shots fired in support of these experiments, 92% produced the desired energy with no measurable prelasing or prepulsing.

Laser Performance and Diagnostics (J. J. Hayden, J. McLeod)

The Gemini laser was fired at energies ranging from 5 to 295 J for the calorimeter calibration experiment. The low energies were attained by injecting the oscillator-preamplifier pulse before the final amplifier gain rose very high. The pulser was then quickly diverted to prevent subsequent repumping.

The saturated-absorber gas-cell retrofit was installed on the north beam. This major modification removed the saturable-absorber cell from the target-chamber entrance window and placed it between Passes 2 and 3 inside the TPA. This modified amplifier is being tested.

The airlock single-target insertion mechanism was installed on the Gemini target chamber. This system permits experiments to shoot as many targets as desired before breaking vacuum on the chamber.

Oscillator-Preamplifier System (V. Romero, E. Coffelt)

The smoothing-tube and switched-out oscillator assembly and two preamplifiers were tested electrically for use in the new Gemini front end. The optical quality of the output beam is being analyzed, and the system will be installed in Gemini during the summer of 1980.

In addition to actual target shots, the present Gemini front end fired 5125 shots during the past 6 months for diagnostic trigger tests and system alignment.

Computer and Control System (S. Hackenberry, P. Castine)

All Gemini logging and display programs were modified to permit the addition of another CAMAC crate for the control-system retrofit. The control-system monitoring plans call for the addition of six transient recorders and enough event timers to monitor an additional 24 events.

GIGAWATT TEST FACILITY (J. F. Figueira, S. J. Czuchlewski, A. V. Nowak)

Introduction

The upgrade of the GWTF has been completed; the GWTF comprises two short-pulse CO_2 lasers, the System 1 and the RIO/Lumonics device. Both laser systems are fully functional, routinely supporting a wide variety of laser and plasma physics experiments. The design and performance of both lasers is discussed in more detail below.

Obtaining Unconditional Stability in System 1

For many applications, ranging from laser-plasma interaction studies to phase conjugation using degenerate four-wave mixing (DFWM), it is necessary to arrange a laser-amplifier illuminating system in such a way that the output from the laser system is fed directly back into itself. For a CO_2 amplifier, the optical inversion in the CO_2 molecule is typically maintained for several microseconds, which is long enough for unwanted parasitics modes to develop and to cause a loss of energy stored in the amplifier. To eliminate such problems completely, we designed and built the laser oscillator/amplifier system shown in Fig. I-2.

A conventional transversely excited atmospheric pressure (TEA) oscillator operating at 600 torr is used in conjunction with a low-pressure discharge tube to produce a single longitudinal mode[1] at a frequency controlled by an intercavity grating. The 70-ns output from this system is then sent to a two-stage Pockels-cell system[2] where a 2-ns pulse with a 200-ps (10 to 90%) risetime is selected. The two-stage Pockels cell has an extinction ratio in excess of 10^5 and completely decouples any external feedback from the oscillator to the amplifier.

The selected pulse is sent to a two-pass amplifier operating at 600 torr with a small-signal gain g_0L^* of 4.8 and a 10-cm^2 cross-sectional area. To stabilize the

*The small-signal g_0L is related to the single-pass gain G by $G = e^{g_0L}$.

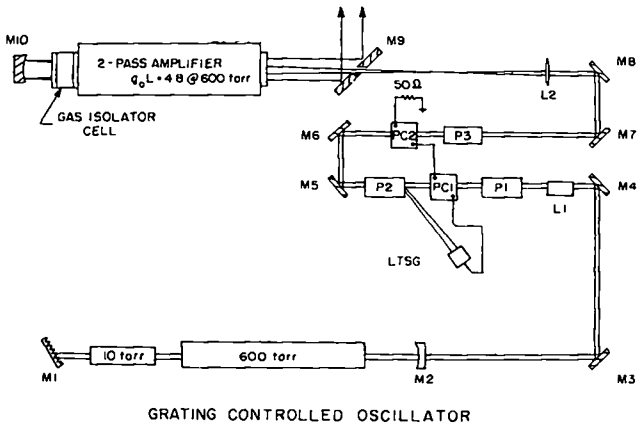

Fig. I-2.
Multipass amplifier system. P1, P2, and P3 are stacked-plate Ge or ZnSe polarizers; PC1 and PC2 are 1-cm-diam CdTe Pockels cells; L1 and L2 are lens systems; M10 and M2 are concave mirrors. (All other mirrors are flat.) A laser-triggered spark gap (LTSG) provides high-voltage switching pulse to the Pockels cells.

amplifier against parasitic oscillations, a 3.95-cm-long gas-isolator cell is placed at the end of the first pass. The beam from the oscillator is focused through a small hole in the flat input mirror (M9 in Fig. I-2) and makes an expanding pass through the amplifier and gas-isolator cell to the 4-m-radius recollimating mirror (M10 in Fig. I-2). The beam then makes a collimated pass along the main axis of the amplifier and is extracted by mirror M9. The first pass through the amplifier is partially saturated and produces a fluence of about 10 mJ/cm^2 at the gas-isolator cell. In the absence of the gas isolator, the two-pass amplifier system is unstable against 1.5% reflections from a CaF_2 disk inserted at the amplifier output.

To stabilize the two-pass system, the isolator cell is filled with Mix 804 (a standard gas isolator).* The measured transmission characteristics of the isolator gas at 10 μm P(20) in a 77.5-cm-long cell** are shown in Fig. I-3.

This figure shows that input intensities ≥1.0 MW/cm^2 are required for efficient operation. Mixtures corresponding to a small-signal absorption-length product of αL = 0, 2.4, and 4.8 at 10.59 μm were introduced into the

*Mix 804 is composed of five gases in the following proportion: SF_6, 1.5%; C_4F_8, 4.04%; Freon 115, 12.2%; Freon 1113, 19.85%; and Freon 12, 62.3%.

**The transmission characteristics of Mix 804 at a higher pressure in a shorter cell are similar, but the saturation threshold is shifted to a slightly higher energy.

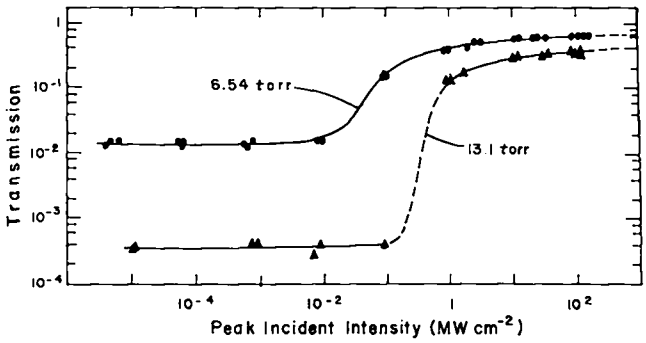

Fig. I-3.
Measured transmission curves for gas-isolator Mix 804, using two values of αL, αL = 4.2 (6.5 torr) and αL = 8.2 (13.1 torr) with 1.2-ns, 10.6-μm pulses.

isolator cell. Figure I-4 shows the measured output energy in a 1.8-ns pulse for these conditions. When the system was fully stabilized (gain equals loss for small signals) at αL = 4.8, the output power decreased by 60% to a value of ~200 MW for an input energy of 1 mJ. As the input flux is reduced, the output power for the fully stabilized case drops dramatically because of the incomplete bleaching of the gas isolator by the first pass of the beam through the system, as predicted in Fig. I-3. Further increases in the input energy in excess of 1 mJ would reduce the 60% loss encountered in the fully stabilized case. The pulse shape was measured with a

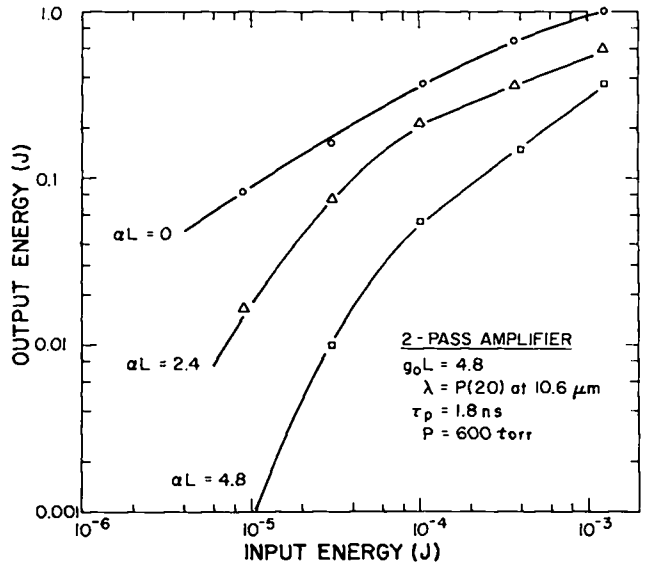

Fig. I-4.
Measured amplifier output for several levels of stabilization. The curve for αL = 4.8 represents the "zero gain" configuration.

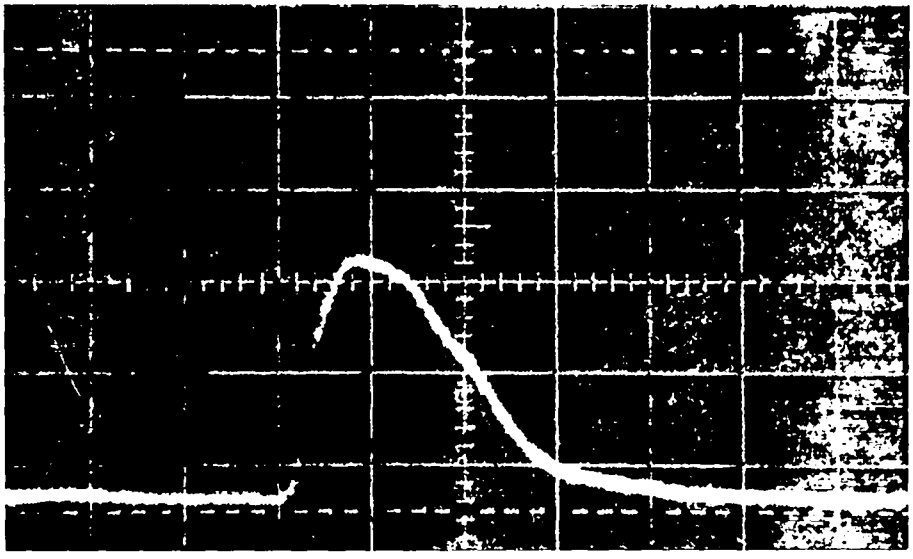

Fig. I-5.
Output pulse shape. Horizontal scale, 1 ns/div; vertical scale uncalibrated.

high-speed pyroelectric detector and a 5-GHz oscilloscope.[3] Figure I-5 shows the output-pulse waveform, which has a 10-90% risetime of 200 ps with a duration of 1.8 ns. No variation in pulse shape was observed for variations in the gas-isolator filling pressure over the αL range from 0 to 4.8.

Enhancing the Performance of the RIO/Lumonics System

The RIO/Lumonics system is the second GWTF laser. It employs a reinjection oscillator (RIO) that drives a multipassed Lumonics-601 amplifier.[4,5] The system is capable of producing 1.1-ns pulses with a 5-J multifrequency output. When configured for plasma physics experiments, it can produce focused powers approaching 10^{14} W/cm^2.

The output energy of this system was increased from 3 to 6 J by carefully adjusting the timing signals to the oscillator and the amplifier so that both units operate at peak gain. The contrast ratio was improved significantly by inserting a saturable-absorber cell containing SF_6 buffered with helium (see Sec. III) between the RIO and the Lumonics amplifer. In this manner, prepulse energy was reduced by a factor of 10^5 to a level of 3 μJ, whereas the main pulse energy decreased only slightly to 4.8 J (Fig. I-6). By varying the SF_6 concentration in the absorber cell, we should be able to vary the prepulse energy systematically, a capability that should be useful for many experiments.

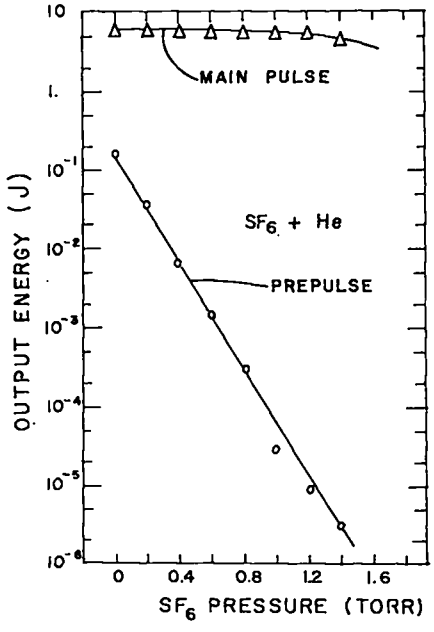

Fig. I-6.
Prepulse and main pulse energy from the RIO/Lumonics laser as a function of the SF_6 partial pressure in the saturable-absorber cell. The cell is 19 cm long, and the SF_6 is buffered with 50 torr of He.

The temporal pulse shape has remained very reproducible. The pulse width is 1.1 ns with a 10-90% risetime of 350 ps. Peak intensity for a 5-J pulse is 4.4 GW.

The diameter of the beam at the focal plane of a well-designed f/2 optical system was measured several times with an ir vidicon. The measured diameter at 1/e of the peak on-axis fluence is 96 ± 10 μm. These measurements are summarized in Table I-III.

We have also been able to generate subnanosecond pulses by adding a third stage to the electro-optical switch. This assembly yields an output pulse with a 710-ps FWHM pulse duration and a 340-ps risetime. Output energy is 1.8 J with a peak intensity of 2.1 GW.

Conclusion

Both laser sytems of the GWTF are fully operational. System 1 is being used to support the CO_2 laser development effort, whereas the RIO/Lumonics system supports both the laser development experiments and, more recently, a variety of plasma physics experiments.

The addition of target irradiation work to the GWTF schedule has required extending conventional solutions to the prepulse attenuation problem into new performance regions.

TABLE I-III

SPECIFICATIONS FOR GWTF RIO/LUMONICS LASER AND f/2 FOCUSING SYSTEM

Output energy, J	5
Prepulse energy, μJ	<10
Pulse width, ns	1.1
Risetime, ps	350
Beam diameter (1/e), μm	96
Peak intensity, W/cm^2	$\geq 5 \times 10^{13}$

REFERENCES

1. A. Gondhalekar, E. Holzhauer, and N. R. Heckenberg, Phys. Lett. **46A**, 229 (1973).

2. E. J. McLellan and J. F. Figueira, "Ultrafast Pockels Cells for the Infrared," Rev. of Sci. Instrum. **50**, 1213 (October 1979).

3. E. J. McLellan and J. S. Lunsford, CLEA abstracts, IEEE J. Quantum Electron. QE-13, 38D (1977).

4. "Inertial Fusion Program January—June 1979," Los Alamos National Laboratory report LA-8114-PR (June 1980).

5. S. J. Czuchlewski, E. J. McLellan, J. F. Figueira, E. Foley, C. E. Knapp, and J. A. Webb, "A High-Power (10 GW) Short-Pulse (≤1 ns) CO_2 TEA Amplifier," Proc. of the Int. Conf. on Lasers—1978, pp. 498-505.

II. ANTARES—HIGH ENERGY GAS LASER FACILITY
(H. Jansen)

The High Energy Gas Laser Facility (HEGLF) will house the high-power, short-pulse, CO_2 laser, Antares, which is being designed to investigate laser fusion phenomena. The Antares project has been redirected, as a result of funding delays, to provide 40 kJ on-target energy approximately 1 yr earlier than the full design (100 kJ) schedule.

INTRODUCTION (H. Jansen)

Antares is a DOE line-item construction project designed to investigate the feasibility of ICF near the breakeven point. As originally planned, it was a six-amplifier, 100-kJ (1-ns) CO_2 laser system. However, recent theoretical calculations indicate that the breakeven energy requirements are much higher than 100 kJ and point out the lack of target data required for realistic modeling. To achieve significant experimental target data in as short a time as possible, the Antares program, with the concurrence of DOE, was redirected. The goal of the redirection is to build two power amplifiers (instead of six) as soon as possible with total on-target energies of 35 to 40 kJ. Based on projected funding, this will be completed at the end of FY 1983, almost 1 yr earlier than the presently scheduled full design (100 kJ) date.

The Antares effort is currently focused on the construction and installation of major components. Although Laser Hall construction is behind schedule, joint occupancy by the Laboratory and the contractor has permitted the installation of the first power-amplifier support stand and the shielded main control room. Joint occupancy of the Target Building by the building contractor and the vacuum system contractor has permitted the installation of major vacuum system components.

Our first electron-beam gun has been assembled and vacuum tested. The electron-gun and gas pulsers have been built and tested. The first high-voltage power supply has been built and meets specifications. The Systems, Science and Software, Inc., front-end driver amplifier has undergone checkout and has passed performance tests.

Fabrication of large optical components is on or ahead of schedule. High-quality prototype parabolic mirrors that exceed our requirements were successfully diamond-point machined. Prototype tests of large-mirror positioners were successful; production quantities of these units are being procured. Two optical alignment systems, the flip-in and see-through, are in the final stages of evaluation; final selection of one is expected early in the next reporting period.

The controls system, the target vacuum system, and the target optical system, which were most heavily affected by the redirection, are under revision to accommodate the required changes.

OPTICAL SYSTEM (A. C. Saxman, Q. Appert, C. Bjork, J. Munroe, W. Reichelt, C. Silvernail, E. Sklar, J. Sollid, T. Swann, W. Sweatt, P. Wolfe)

Introduction

Our main efforts in the development of optical systems for beam alignment and diagnostics focused on

- the completion of the Antares single-sector beamline mockup and evaluation of the beam-alignment techniques,
- the completion of the Antares prototype calorimeter designs and testing of calorimeter components,
- the surveying and layout of a master grid of primary manual-alignment reference points and lines throughout the Laser Hall Target Building, and
- the positioning of Power Amplifier Stands 2 and 5 and of target system Beam Tubes 1 through 3.

All these major tasks were completed on schedule.

Optical System Code

Two new ray-trace computer programs were established for the entire Antares optical beam path. These programs can predict accurately the geometric beam-energy distribution throughout the beam path and also verify the height and angles of incidence for each ray at each optical element. In addition to calculating the energy distribution at each optical element, these programs have been used to verify the ACCOS optical design code for various subsystems. Current use of these

codes has provided information on component position, radius of curvature, and tip-tilt tolerance requirements for the entire Antares optical train.

Beam Diagnostics Design Efforts and Evaluations

The power-amplifier vacuum-input-window cell, and the vacuum-input-window calorimeter and its supporting structure were designed to the layout stage. The calorimeter was drawn in more detail for evaluation.

We also designed the full-power calorimeter assembly and developed a method for supporting it in the diagnostic spool. An individual calorimeter for a single sector was drawn in more detail, again for evaluation.

We completed the design for the input-sector calorimeter and a layout drawing for its position in the power amplifier. A prototype is being fabricated.

We completed the layout of the 50-cm-diam disk calorimeter and support structure for the turning-mirror chamber, including four photon-drag detectors, two fast pyroelectric detectors, and one mercury-doped germanium detector.

A vacuum test fixture (chamber and mounting plate) was designed to evaluate various calorimeter configurations under vacuum. In addition, the design of a test stand for the new Lumonics-103 oscillator was begun. This stand will incorporate continuously variable crossed polarizers for attenuating the beam from the oscillator. The test assembly will be used to align the turning mirror for the input-sector calorimeter prior to installation.

A test and calibration station for use with the Lumonics-103 oscillator is being designed for the input-sector calorimeters. Multilayer dielectric polarizers will be used for this application because these polarizers appear to offer a modest extinction ratio (85:1) with higher damage threshold and larger beam aperture than ZnSe or germanium stacked-slab polarizers.

The effect of surface loading by multiple thermocouples was tested. The effect of detector-system sensitivity on the complexity and fabrication of the total system is being evaluated. To verify our calorimeter design criteria, we determined the minimum detectable 10.6-μm flux that can be measured with type-E thermocouples and thermoelectric modules. Our current designs are five times more sensitive than required.

An initial analog design for a ±0.2% repeatable electrical energy measurement was agreed upon. A pulser, which will deliver the requisite electrical pulses in times that are short compared to thermal response times, has been designed, breadboarded, debugged, and is being built.

Optical System Engineering

Power Amplifier. Various power-amplifier tasks were completed as summarized below.

Specifications. Revision A for purchase of 45-cm-diam salt windows was written; also, revisions were written to HCC's proposed acceptance-testing procedure. Revised blueprints were drawn for mounting the 45-cm-diam salt windows, including changes to the retaining ring and cover plates, and the design of a lithium-fluoride-coated diaphragm. A wedge angle was added to the 45-cm-diam salt window, and the blueprints were brought up to date, as were the beam profile drawings for these windows. Final specifications for the optical design of the power amplifier were completed (Specification No. 89Y-224832) following a design review meeting. The specifications contain all current optical design parameters for the power amplifiers; the entire power-amplifier optical design has been frozen.

Calculations. Effects of moving Power Amplifiers 2, 3, 4, and 5 on the power-amplifier optical design were calculated by ACCOS-V simulation of the power-amplifier optical train. Mounting requirements for the power-amplifier back reflectors were calculated, including new tolerances for the relay mirrors. Calculations for the spacial filter, including the motion of focusing and relay mirrors, and aberration-balancing, were performed. A complete ray trace through the trombone and other input optics was completed.

Target System. A first-order design for the beam-alignment see-through telescope was developed. A low-cost prototype model will be fabricated for laboratory verification of the important design parameters. The design and prototype will be used for guidance in the design and fabrication of an Antares beam-alignment telescope.

Based on the new two-beam target optics design, the power-amplifier/target system beam convergence interface requirements were defined.

The engineering design for a new beam-alignment target fixture is 90% complete, and prototype parts are being fabricated and procured. This fixture will allow a number of beam characterization subsystems to be

pointed accurately at each beam-focusing parabolic mirror sector. Measurements of beam quality, pointing and centering, focusing, encircled energy, and pulse synchronization can be performed in the target position with this fixture.

Beam Alignment

Manual Alignment. A survey of the Antares facility (Laser Hall and Target Building) and of all beam-related penetrations (manholes and portholes) has been completed. The as-built dimensions were generally well within specified tolerances. Permanent benchmarks and reference markers for the identification of beamlines and equipment locations were established. The alignment layout uses the target position as the basic reference point.

Power Amplifier Stands 2 and 5 were bore sighted into their designated final positions. The beam tubes between the Laser Hall and the Target Building were bore sighted and Tubes 1 through 3 were permanently positioned. In addition, the positioning of the beam-turning chambers and the target chamber was also verified. These cooperative tasks between the Laboratory and the target-system contractor, PDM, have been completed successfully.

Automatic Alignment. Major gains were realized on the Antares single-sector mockup in the Optical Evaluation Laboratory (OEL) test bed. In this subsystem, we used Antares full-size prototype apertures, mirrors and mirror positioners, and full-length beam paths. The beam path is completed from the front-end-room alignment station to the focusing parabola. The flip-in-detector and see-through beam-alignment techniques are being evaluated. The flip-in-detector sensors and their signal-conditioning packages were interfaced with their respective mirror positioners. A minicomputer (DEC 11/03), integrated with a Laboratory-designed stepper motor driver, and software were used to perform closed-loop control of the mirror positioners throughout the optical train. The pointing and centering requirements, which were determined analytically, were easily met with the flip-in alignment technique.

Verification testing of the requirements for the see-through alignment system was also completed successfully on the optical test bed. The specifications for the alignment telescope for the see-through alignment technique were generated, and a request for quotation (RFQ) was issued. Initial vendor comments were favorable; final bids are due in mid-February 1980. Currently, we are using a commercial telescope for the see-through tests to validate the analytically determined requirements for illumination sources at the mirror, spacial-filter, and target positions. A television image-centroid autotracker was ordered and will be delivered in late February 1980. This unit will be integrated with the current camera/telescope system, and closed-loop control tests, similar to those completed with the flip-in system, will begin.

The see-through technique has been tentatively selected for the Antares alignment system. Recent verification tests indicate that the signal-to-noise, image resolution, field-of-view, and procedural alignment requirements can be satisfied in a cost-effective manner. No major technical problems are foreseen once a new telescope is procured and tested. The see-through technique also can verify the beam position throughout the optical train, check for obscurations, and perhaps most importantly, provide a means for direct observation of the target.

In preparation for Beamline 5 (the Laser Hall optical test bed), a basic design for the front-end-room alignment station was completed, which can support either the see-through or flip-in alignment technique. Basic common components and hardware have been procured. Additionally, a design for the periscope/carousel assembly was completed, checked, and sent out for fabrication bids.

LARGE OPTICAL COMPONENTS (W. H. Reichelt, D. Blevins, J. L. Munroe, R. Cutler, G. Woodfin)

Salt Windows

HCC has done an outstanding job in the salt-window program. Windows are being fabricated; the first is due at Los Alamos in early 1980. Yield results indicate that the decision to build a new production facility was correct. New furnace designs have resulted in better crystal boules as indicated below.

	Yield (%)	
Area	Projected	Actual
Crystal growth	42	75
Forging	68	78
Polishing	85	94

Twice as many windows as expected have been made (>50 vs 24). The improved growth process is reflected in consistent absorption coefficients (α) of ≤ 0.002 cm^{-1}.

Mirrors

Production of substrates for the Antares system was completed. Copper plating has been a continuing problem and the Laboratory, rather than Union Carbide Corporation's Y-12 Plant, has assumed direct responsibility for this process; Y-12 will only single-point diamond-turn (SPDT) the mirror surfaces. The target system mirrors are not yet in fabrication, because the requirements have not been fully defined.

Mirror production at Y-12 has been delayed because of the substrate plating problems, but there is enough slack time in the schedule to prevent problems. An off-axis paraboloid, representative of the paraboloids that will be used on Antares, was received from Y-12. This paraboloid was cut on the Excello SPDT machine using the fixtures already manufactured for the production run. The only substantive difference is that this paraboloid is solid aluminum, lacking the copper plating. Evaluation of this paraboloid leads to two major conclusions.

- The optical figure on the paraboloid is within one visible fringe peak-to-valley (p-v), which means that the optical performance at the Antares wavelength will be excellent and cause little degradation, and that the parabola can be aligned very closely by mechanical means.
- Surface finish was between 0.02 and 0.05 μm. Production of such mirrors indicates that no additional polishing is required. Indeed, this accomplishment represents a technological breakthrough in the fabrication of aspheric optical components.

Positioners

The mirror is connected to the positioner by three posts, which are, in fact, a kinematic mount. The posts are flexures that permit mirror support without optical distortion, as was demonstrated interferometrically in a test case on the Zygo interferometer at the OEL. Prototype mirror mounts were used to demonstrate the reliability and repeatability of the mirror positioners. The sensitivity of the positioners is 3.85 μrad/step. Starting from a null position, each positioner was stepped 10 000 times and returned. After return, the positioner was within a half step of null. The position is linear within a half step over 1000 steps, which is well within requirements. Source selection and production RFQs have been initiated. Initial tests of the prototype actuators for the focusing mirrors in the target system revealed some roughness in the linear ball bearings and self-locking in the direct-driver ball screw. The redesign lowered overall cost and made procurement easier and faster.

Optical Evaluation Laboratory

The OEL, in cooperation with the Y-12 Plant and HCC, is coordinating optical evaluation activities for the production of Antares components. In addition, a small-mirror vendor qualification program designed and run by the OEL provided reliable sources of metal mirrors for the entire Laser Program. Evaluation requirements, particularly those of the Helios system, were met.

Lithium Fluoride Absorbing Surfaces

Lithium-fluoride surfaces can be used as "optical blacks" to prevent parasitic oscillations in the high-gain CO_2 systems. Early attempts at plasma-spraying surfaces with lithium fluoride were supported at Battelle Institute. The program indicated that large particles (50 to 200 μm) were required for a reliable process. In a Laboratory-supported program, TAPCO, Inc., developed such powders successfully for use in a flame-spraying coating process. Flame-spraying is preferable to plasma-spraying because lower temperatures are used and the process is safer. Production of parts coated with flame-sprayed lithium fluoride was initiated.

FRONT-END SYSTEM (W. T. Leland, E. Foley, D. Gutscher, M. Kircher, C. Knapp, E. Yavornik, G. York)

The driver amplifier was performance tested satisfactorily. The manufacturer demonstrated 500 full-power operations without failure, although the unit did not reach gun-current uniformity specifications. Gain-uniformity tests performed after delivery of the unit to the Laboratory showed that gain uniformity was within ±7% as specified. Nonuniformities in the gun current were confined to a small region where they do not materially affect gain uniformity. We achieved g_0Ls of 8.5 at 1500 torr; this result exceeds the design minimum

of 7.5. The driver gun uses a single-blade cold cathode coupled to its power supply by a peaking gap and 30.5 m (~100 ft) of coaxial cable. The peaking gap increases the voltage rise rate at turn-on and improves ignition uniformity.

A spark cathode was used for tests of gun performance. This variant of a cold cathode provides a preselected array of spark-emission sites. The spark cathode did not require the peaking gap for good ignition, gave a slightly better grid-to-cathode current ratio, but provided poorer current uniformity.

The preamplifier was controlled by prototype computer programs. All communication between the preamplifier and associated equipment is by fiber-optic cables.

POWER-AMPLIFIER SYSTEM (R. Stine, G. Allen, W. Bartlett, J. Bickford, W. Gaskill, W. Miller, G. Ross, R. Scarlett, W. Turner, B. Weinstein, N. Wilson)

Primary achievements were the start of power-amplifier installation in the Laser Hall and assembly of the electron gun.

The support stands for the first two power amplifiers were received and installation is under way (Figs. II-1 and II-2). These stands are 3 m high, 4 m wide, and 12 m long. Assembly was delayed from August to October 1979 because the Laser Hall was not available.

The 3.5-m-diam pumping-chamber shells were fabricated and delivered to the Laboratory. They are ready for installation on the support stands.

The 1.5-m-diam by 7.3-m-long electron-gun vacuum shell (Fig. II-3) was received, together with all cathode components; assembly of the electron gun has begun (Fig. II-4).

Pumping Chamber

Electrical Design and Testing. A double-tapered anode-bushing prototype was fabricated and tested to over 1 MV (Fig. II-5). The double taper and soft polyurethane center drive all the air out of the interface when the bushing is assembled. This prototype is a value-engineered version of the initial solid bushing, which was tested to 900 kV during the first half of 1979. The double-tapered design is out for fabrication bid.

A prototype dielectric divider fabricated at the Laboratory was tested in the prototype power amplifier with satisfactory results. An initial set of production units will be obtained from industry.

The anode drawing package was completed and a RFQ sent out.

Mechanical. All detailed engineering design and drafting for the outside shell were completed. Only the top-assembly drawings remain to be finished.

Fig. II-1.
Equipment installation in Laser Hall.

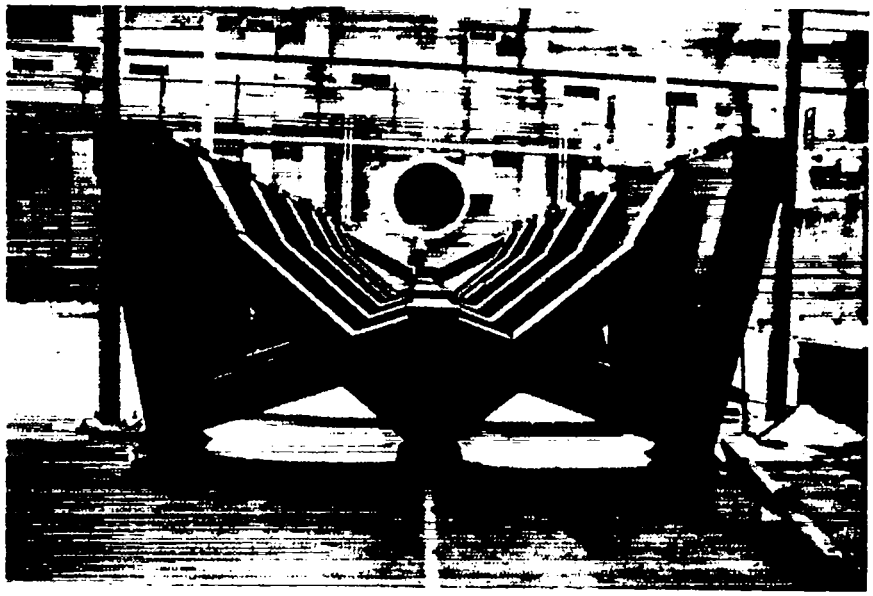

Fig. II-2.
Power-amplifier support stand.

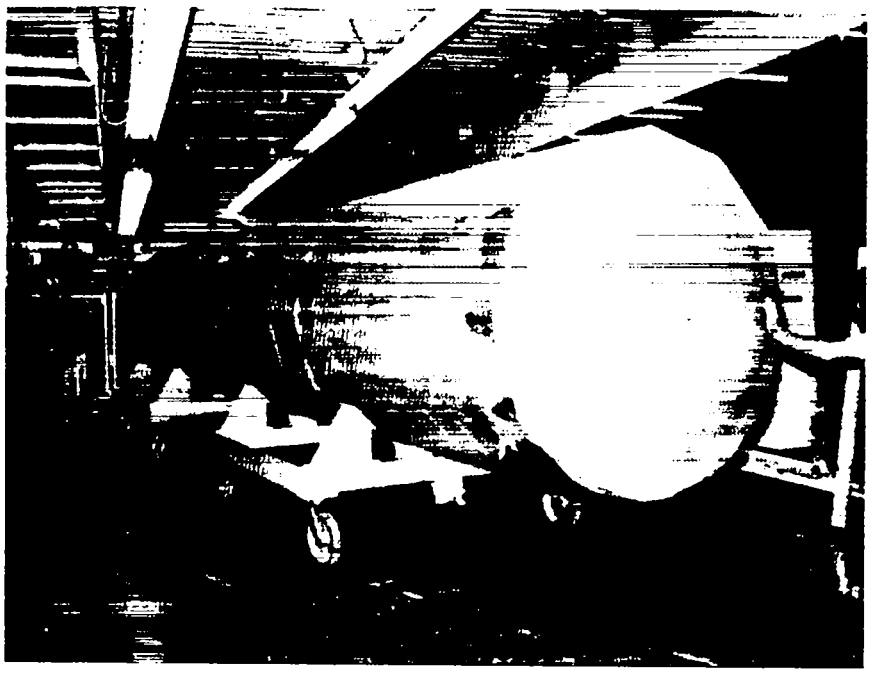

Fig. II-3.
Electron-gun vacuum vessel.

The 8 pumping chambers, 2 spacer spools, and 10 rail support plates for the first 2 power amplifiers were delivered to the Laboratory (Fig. II-6). The electron-gun rails will be delivered early in 1980. Fabrication of the weldment portion of the pressure domes was completed, and the units were sent to the machine shop for final machining.

An order for the I/O optic sections was placed and fabrication has started.

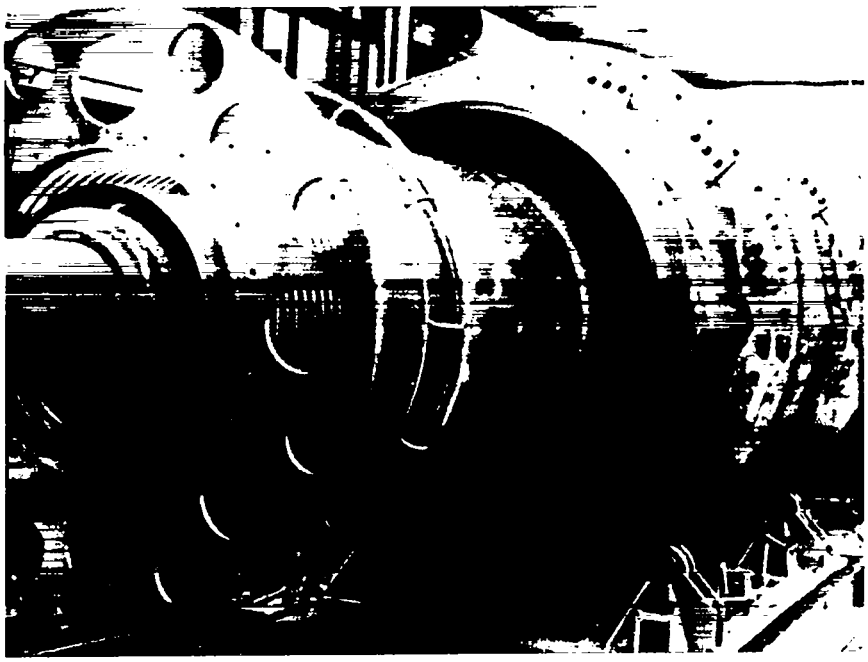

Fig. II-4.
Assembly of electron gun.

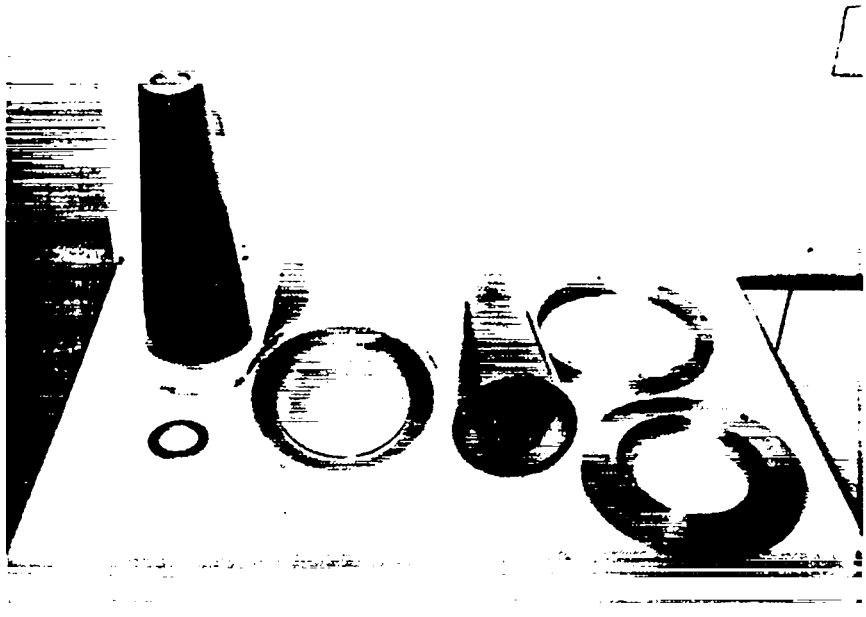

Fig. II-5.
Double-tapered anode bushing.

Fig. II-6.
Pumping chambers arriving at the Laboratory.

Electron Gun

Electrical Design and Testing. The Electron-Gun Test Facility (EGTF) became operational, and assembly of the first electron gun was started.

The electron-gun windows were fabricated successfully by the Laboratory and by an outside vendor. Both succeeded in bonding the titanium foil to the stainless steel back-up grid. Production units were ordered from both sources. Also, a Kapton-aluminum laminate film shows promise for replacing the titanium foil and providing a more reliable window.

Mechanical. The engineering design and drafting for the electron gun were completed, and all parts except the grid have been received. Assembly of the gun has started.

A process for punching the stainless steel material for the grid was developed by an industrial source. Punched material has been sent to the grid vendor for use in the grid assembly.

Gas and Vacuum Subsystem

The prototype electron-gun vacuum system was used during inspection and assembly of the gun in the EGTF. The same type of turbomolecular vacuum pump, mechanical backing pumps, and gate valve will be used in Antares. Based on overall system performance, components were ordered for the first power amplifier.

The main roughing pump for the Laser Hall was received and stored in the warehouse until the Hall is available.

Handling Equipment

The handling equipment for the electron gun was received, including the low-boy fixture to move the shell on air bearings and the cathode carrier fixture to insert the cathode into the shell (Fig. II-7). The low boy permits rotation of the electron gun for window installation and moves the unit on the floor. The cathode-grid assembly is inserted into the shell with the long, cantilevered arm of the cathode carrier fixture. Also, the air compressor required to operate the air bearings was received. All of these units were used during assembly of the gun.

The Laser Hall electron-gun insertion fixture used to load the gun into the power amplifiers was sent out for bid.

Hydraulic man-lift platforms were received and used in the initial operations in the Laser Hall.

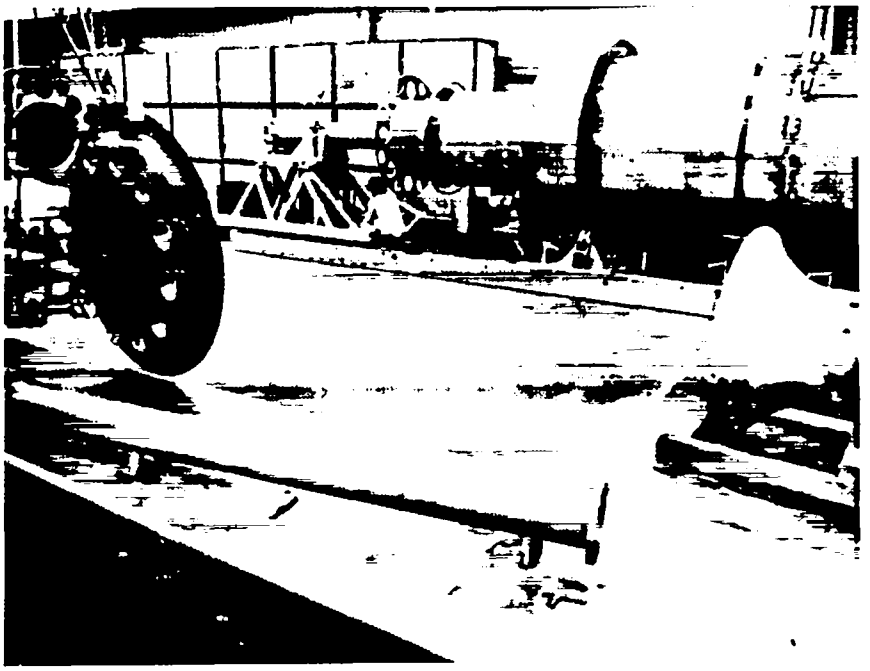

Fig. II-7.
Low-boy and cathode carrier fixtures during assembly of the electron gun.

Design of the anode-bushing assembly fixture was started.

Optical Support Structures

The purchase order for the back reflector, relay, and I/O optical support structures was placed. The aluminum ordered previously for these structures was sent to the vendor and fabrication is under way.

Support Stand

The support stands for the first two power amplifiers were received in August and September 1979. Installation of these stands began in October 1979 when access to the Laser Hall was obtained.

High-Voltage Cable

The first shipment of high-voltage cable from Sweden to connect the power amplifier with the Marx generators was received in New York. The cable-assembly area was prepared for the hardware used to terminate the cables, including cable-straightening fixtures to prepare the ends of the cable for the termination, cable-handling equipment for the 3-m-diam spools, and cable-trimming jigs. EG&G will design and fabricate all the cable-terminating equipment.

ENERGY STORAGE SYSTEM (G. Allen, F. Van Haaften, W. Reichelt, K. Andrews)

Gas Pulser

The Antares prototype gas-pulser performance tests were completed. These tests consisted of 2000 shots at 600 kV into a matched dummy load to simulate normal operation, with a peak load current of 250 kA; of 10 short-circuit shots after 500 and 1500 normal shots to simulate fault conditions, with a peak current of 400 kA; and of 10 shots at 750 kV after 1000 normal shots to establish voltage integrity. These tests clearly established that the following key specifications were met or surpassed.

	Specification	Performance
Jitter, ns	≤20 (1%)	≤10 (1%)
Inductance, H	≤3	≤2.4
Prefire rate, Hz	≤0.01	≤0.01

Although the prototype pulser met the required prefire rate specification of <1%, all future units are expected to have a significantly reduced prefire rate caused by a change in Laboratory-tested spark-gap electrode material and better control of the gap-purging air system.

The prototype gas pulser should be delivered to us by mid-March 1980, which will allow tests of the pulser computer control system to begin during April. Construction of four production pulsers is in progress.

Gun Marx—Antares

A preliminary engineering design of the Antares gun Marx, which used 4-μF, 60-kV capacitors in a compact arrangement, was dropped in favor of the existing configuration used in the TSL-85 Marx (see discussion below). This decision eliminates a sizable drafting/design effort and takes advantage of existing hardware (primarily capacitors) and operating experience. The original TSL-85 Marx drawings are being updated to reflect the as-built changes. The design of service and assembly fixtures, and of a construction and test facility is under way.

Power Supplies

Power supplies for both the gas pulsers and gun Marx for Beamline 2 were installed and successfully completed proof-of-performance tests. The rigorous performance tests required a transformer/rectifier overvoltage of 30%, repeated output short circuits while under full load, and precise constant-current control into a variable load. After initial control problems, the power supplies performed satisfactorily. These power supplies are designed to operate either by hand or under complete computer control. Delivery of these first two supplies is expected by mid-March 1980.

Fault Protection

If the laser gas volume is not ionized when the gas pulser fires because of, for example, gas-pulser prefire, gun-Marx misfire, or improper timing, the gas pulser will have an extremely high load impedance, which will cause the pulser output voltage to attempt to ring up to 2.4 MV, twice its open-circuit voltage. A dielelectric failure would consequently occur in a cable, bushing, dielectric divider, or elsewhere in the system. To channel the pulser energy into a nondestructive path during such a fault, an overvoltage gap has been designed into the system. The design goal of the overvoltage gap is to hold off the normal operating voltage of 600 kV reliably and to break down reliably under overvoltage conditions near 700 kV. Other system components were designed and tested to hold off voltages of 900 to 1000 kV.

Development of a suitable overvoltage gap is in progress, centering around a self-irradiated near-uniform field gap. The typical configuration is shown in Fig. II-8 [an adaptation of a design suggested by C. Martin of Atomic Weapons Research Establishment (AWRE)].

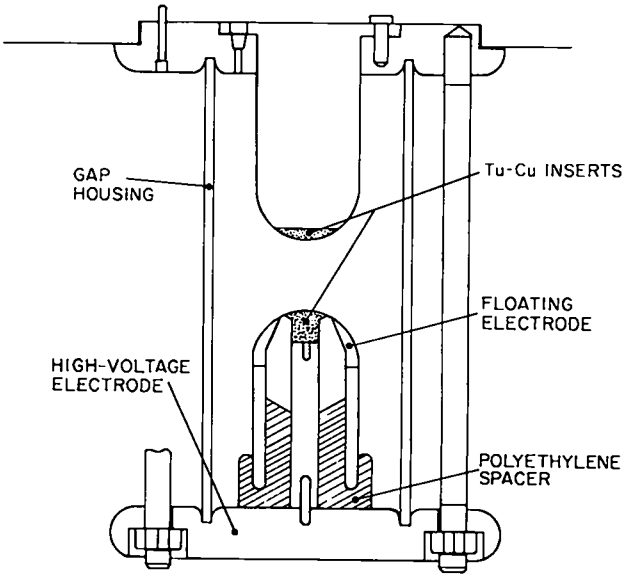

Fig. II-8.
Overvoltage protection gap.

Basically in this gap, interelectrode capacitances cause the floating electrode to arc to the high-voltage electrode, thereby causing irradiation of the main gap. This irradiation is expected to reduce the spread in the main-gap breakdown-voltage characteristics.

Preliminary test results of initial configurations are encouraging. However, the breakdown spread is still too wide to provide reliable overvoltage protection. Our effort to optimize the interelectrode capacitance and the irradiation gap spacing should provide a suitable voltage breakdown spread.

Gun Marx—TSL-85

A Marx generator for the EGTF was designed, constructed, and tested. The generator has an open-circuit voltage of 600 kV and a stored energy of 72 kJ. The design incorporates a dummy load to allow operation in the range of 400 to 600 kV. It also contains the electron-gun grid resistor and a 600-kV switch that converts the Marx configuration from a normal operating mode to a "grid-conditioning" mode in which the grid is shorted to the cathode and a series current-limiting resistor is inserted in the output.

The Marx was fired into an open circuit to test its voltage integrity and into a 10-Ω dummy load to approximate normal operating current requirements. Several short-circuit shots were made to simulate fault conditions. The ringing frequency measured during the short-ciruit shots gave a calculated Marx inductance of 1.3 μH. The open-circuit shots gave a risetime of 100 ns to 600 kV. This dV/dt should provide adequate cold-cathode blade ignition.

In 50 dummy-load shots, the total jitter spread was only 100 ns. Overlaid oscillograms of the erection voltage suggest the possibility of dual erection modes, each with a jitter of ~20 ns. The cause of these apparent dual erection modes will be investigated.

The Marx is expected to be operated into an actual electron-beam gun load beginning mid-February 1980. During these tests, the value of the balancing inductor used to equalize the gun return currents will be established.

TARGET SYSTEM (P. N. Wolfe, J. Allen, C. Cummings, R. Day, W. Dorris, P. Soran, W. Sweatt, B. Thompson, N. Wilson, V. Zeigner)

General Activities

Highlights. The Antares Target Building became available for installation of the target vacuum system by PDM. By December 1979, the six 1.9-m-diam beam tubes connecting the Laser Hall and the Target Building had been installed and three of the six turning-mirror chambers were in place. A contract supplement was issued to PDM for final design and fabrication of the target-chamber space frame. We began evaluating alternative target optical system designs that would permit target experiments to begin when Antares is completed in 1983.

Target Neutron Effects. Although nucleonic calculations were carried out several years ago for the shielding design of the Target Building, we have realized that a more detailed treatment including components in and near the target chamber is now needed to manage both prompt effects on electronics and postshot actuation problems. We are using continuous-energy Monte Carlo techniques consisting of two stages: first, an analysis of components within and including the target chamber; and second, an analysis of the environment outside the target chamber, but within the envelope of the Target Building including the exterior walls, roof, and floor.

The primary concern within the target chamber is the neutron activation of the target chamber itself and of various components including the target-insertion mechanism, mirrors, control motors, wiring, and space frame. Figure II-9 illustrates a portion of the nucleonic model with a plane cut perpendicular to the y-axis, which shows the target-insertion mechanism, some of the mirrors and motors, the space frame, and the target chamber. Using the Laboratory's Monte Carlo code for neutron and photon transport (MCNP) and the target-chamber model, we are calculating the time-dependent transport of neutrons and photons from the source, of photons

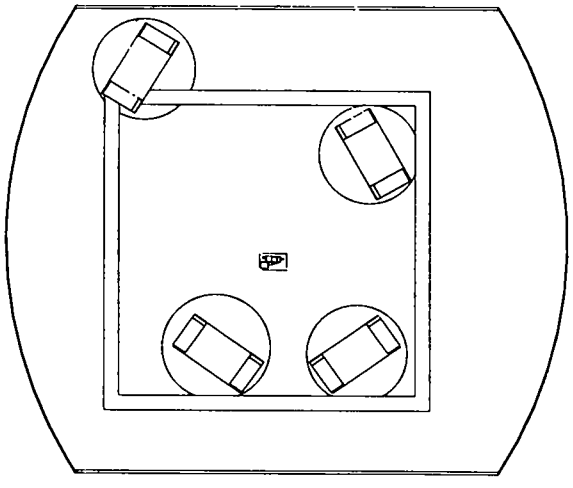

Fig. II-9.
Computer-modeled transverse section of target chamber.

produced by neutron interaction, and of neutrons moderated in the system. We can then study activation resulting from the time- and energy-dependent neutrons.

In addition to neutron activation within the target chamber, neutron and photon leakage out of the target chamber is also of concern. Such leakage can activate equipment in the Target Building and cause radiation damage to electronic gear. Of particular concern is the neutron and photon flux in the electronics room shortly after a target burst. Figure II-10 shows the Target Building model with a cut perpendicular to the z-axis at the source center. Not shown in Fig. II-10, but also present in the model, is the electronics room. Using the Target Building model, we are preparing prompt-neutron and photon mappings and are performing an activation analysis.

Target Vacuum System

PDM Contract. The gauging and electrical designs were reviewed at PDM in July 1979. A final design review was held in Los Alamos in August for DOE. The system configuration developed by PDM appears to meet the principal requirements as defined in the target vacuum system specifications. There is some disagreement about the calculation package provided by PDM to support their pumping system design. However, our calculations show that the several discrepancies tend to cancel each other out, resulting in predicted performance that does meet the specification. Because PDM is

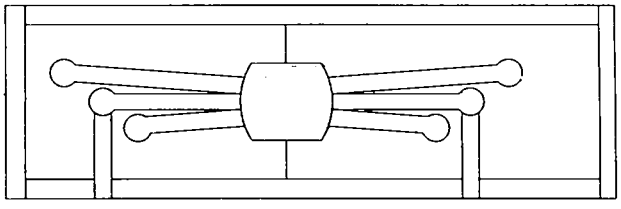

Fig. II-10.
Computer-modeled longitudinal section of Target Building.

building the target vacuum system to meet a performance specification, we are mainly concerned that the calculations provide proper guidance for future integration of equipment to be installed within the target vacuum system.

PDM personnel and equipment arrived on site in August and began leak testing beam-tube sections while the Target Building was not available. Beginning in October 1979, beam-tube culverts between the Laser Hall and the Target Building were prepared and installed; by year-end the six beam tubes had been installed and fitted up, and in-place leak testing had begun. The three turning-mirror chambers at the west end of the Target Building were also installed. Progress in the installation of the target vacuum system is shown in Fig. II-11.

Special isolation valves for the 1.6-m-diam beam tubes and a turbomolecular pump for the target chamber are major items subcontracted by PDM. Performance/acceptance tests of these items were witnessed by Laboratory staff. The valves, manufactured by GNB Corp., were functionally operated and leak tested at the factory, accepted by PDM, and delivered to the Antares site. Test observers were very pleased with the operation of these very large valves. The pump manufacturer, Sargent-Welch, demonstrated it for PDM and Laboratory observers late in November. No specific performance tests were conducted, but the pump had been in operation for almost 200 h and was exhibiting a blank-off inlet pressure of 6×10^{-8} torr. Several features of the turbomolecular pump and its controller will still require attention by PDM before they are integrated into the system.

Component Qualification Program. Outgassing rates in vacuum were measured for materials to be used in the target vacuum system. Tests of connectors and feedthroughs from five manufacturers indicated that metal, ceramic, and glass have acceptable outgassing rates,

Fig. II-11.
Installation in Target Building.

usually less than 1×10^{-6} torr ℓ/s per unit. In contrast, rubbers, phenolics, and other polymerics generally have unacceptably high outgassing rates. The principal gas is water vapor, with varying amounts of higher-molecular-weight materials, some of which can condense on optical components in the vacuum system at room temperature. Measurements were also carried out on lithium fluoride (an optical antireflection coating material), on selected anodizing surface finishes, and on motors and clutches for the target-insertion mechanism. Usable components have been identified in all cases.

Target-Chamber Space Frame

After placing an order for the final design and fabrication of the space frame with PDM, we cross-checked their design with ours in a cooperative effort, as insurance against interference between the space-frame structure and optical beams and mirror supports. As a result of this effort, minor changes in the design were made to relieve crowding at critical points; other refinements increased the resonant frequency of the structure, which had dropped to an unacceptably low 12.5 Hz when the mirror support structures were added.

We further modified the PDM contract to include a 1/5th scale model of the space frame with mirror templates. We will use this model to study space assignments within the space-frame region for optical and target diagnostics and alignment hardware to verify beam-hardware clearances, and to wire harness layouts.

Target Optical System

Image aberration caused by the parabolic focusing mirrors was reduced significantly by tilting the mirrors slightly to orient the parabolic axis parallel to the incoming beam, and then shifting the mirror position slightly to correct for focal-point shift produced by convergence of the incoming beam. Substrate drawings for the focusing mirrors were completed and released for bid.

We began a study to adapt the large optics design for target experiments based on the two-beam system. Two ground rules are being followed: first, impact on the design of the target-chamber space frame should be minimal, because mechanical stability requirements make this a long leadtime item; second, the pseudo-cubic target-illumination symmetry planned for the final six-beam Antares should be preserved. Two approaches were considered. One requires path-length compensation for one-third of the sectors in the turning-mirror

chamber, which needs 32 extra mirrors and positioners for the two-beam system. The other requires that the folding mirrors be relocated in the space frame and that the beam tubes to the target chamber be installed in positions different from those for the six-beam configuration. For schedule, cost, and technical reasons, we chose the second scheme; appropriate design work is proceeding accordingly.

Target-Insertion System

Work was begun on the design of the airlock target-transfer mechanism. Because of the size of the target-chamber vessel, greater misalignment between members mounted to the vessel and members mounted to the space frame must be accommodated in the Antares design than in that of Helios. The design also provides for adjustments to accommodate lack of repeatability in the positions of the target-chamber end dome and space frame, and in space-frame orientation; positional and angular mislocations caused by chamber deflection on pumpdown will be accommodated without adjustments.

A special holder was designed to accommodate optical alignment devices such as a Smartt interferometer system. This holder incorporates a double-gimbal mount, which can be used to orient the primary optical element of the alignment device toward any focusing mirror.

CONTROL SYSTEM (M. Thuot, J. Hong, D. Call, D. Carstensen, D. Gutscher, A. Kozubal, F. McGirt)

Control-System Architecture

The control-system architecture was modified to eliminate some complexity and cost. The modified design fits the reduction from six beams to two. The lowest level of control, the machine interface (MI), remains unchanged: ~29 LSI-11 microprocessors serve as data multiplexers and directly control valves, relays, and data collection devices, for example. Four subsystem-control computers (SCC), PDP 11/60s, control the major subsystems: optics and target, front end, Beamline 2, and Beamline 5. Most of the feedback control resides at this level. These computers also support a man/MI; therefore, each subsystem can be operated separately and concurrently. A DEC 11/70 computer provides overall system control by coordinating the operation of all subsystem computers and providing the operator/MI for the entire system. A block diagram of the revised system is shown in Fig. II-12.

The temporarily installed computers are operating under the UNIX system on a network we designed called TENNET. This change was required when the previous network, DECNET II, failed several parts of its acceptance test.

Front-End, Energy-System, Power-Amplifier, and Optics-Controls Projects

A standard format for subsystem interface-data documentation was established, which lists all the functional I/Os of each subsystem, defines normal and fault operation procedures, and defines every physical I/O control or data channel. An updated list of all the data and control channels for the Antares front-end, power-amplifier, and energy systems is available on the computer. This information forms the basis for our wire-run listing and data dictionary.

The interface-data documents for the front-end and energy systems are nearly finished. The power amplifier lacks definition in the laser-gas and electrical-diagnostic areas. The optics and target data documents have not been started.

Antares Controls Hardware Team

Electromagnetic Interference (EMI) Protection. Installation of the radio frequency interference shielding for the central control room was completed. The shielding

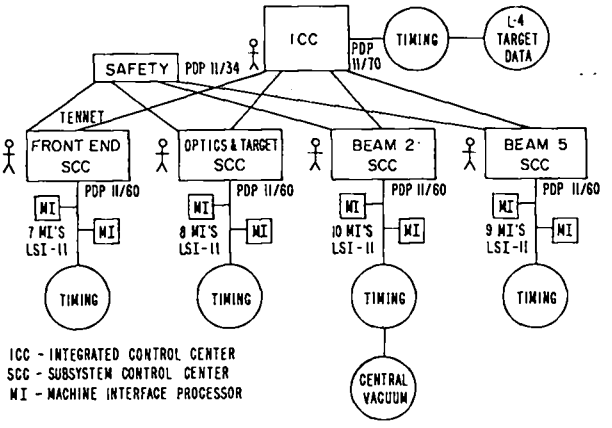

Fig. II-12.
Control-system implementation.

will be tested soon and the interior finishes added. The computers are scheduled to be moved to the control room in March 1980.

About half of the standard fiber-optic modules are being produced. This first beam-related production will generate approximately 80 of each type of module. These units will be installed in the front-end room and the Laser Hall starting in March 1980.

MI Computer Design. A standard set of circuit modules was selected for use in all MIs. We have written test software programs for these modules. An incoming inspection and maintenance test station has been set up and is now operating.

A preliminary design of the analog monitor interface was completed. Several suggested design changes are being implemented.

A prototype of the motor driver was built and sent to OEL for alignment system development

Antares Controls Software Team

Operating System. An interprocessor communications facility was added to the UNIX operating system. This software was installed on one 11/70 and four 11/60 computers and is being tested.

Program transfer from a SCC to a MI was accomplished by a support software package that uses the fiber-optic serial communication lines. With this facility, we will initiate and change application programs for the LSI-11 MIs.

MI Manager. We have implemented and tested part of the MI software that performs laser device-dependent input and output. This software package will control data flow through the MI and provide some low-level feedback control.

SITE AND STRUCTURES (J. Allen)

Construction Package I

As of 31 December 1979, Construction Package I was 96.3% complete. This is a net gain of 31.3% for this reporting period. Complete occupancy is now scheduled for June 1980. Joint occupancy of the Laser Hall began 1 October 1979. The warehouse was occupied in late September. The office building will be ready for occupancy on 17 January 1980. The Laboratory began installation of the controls shielded room in late December. Landscaping, as well as testing and balancing of the air-conditioning systems, will not be finished until June 1980.

All installation is complete except for electrical work, which is affecting the completion of all areas and is delaying the startup of the functional equipment.

A modification was issued to upgrade the air-conditioning filtration for all areas that require stringent cleanliness. Testing and balancing will be performed after this modification.

Construction Package II

This package was 93.8% complete on 31 December 1979. All effort is essentially complete except for electrical work. Beneficial possession of the fire-protection water tank and associated systems was assumed by DOE on 4 December 1979. The Target Building has been jointly occupied by the building contractor and the target vacuum system contractor since mid-October. The scheduled completion date for the Target Building is June 1980.

OTHER—PARTICULATE CONTROL (P. N. Wolfe, J. Allen, W. Bartlett, W. Reichelt, J. Sollid)

Although the design of the buildings that house the Antares facility incorporates reasonable measures for controlling average levels of particulate contamination, the specific local needs of the laser system and the target experiments require additional attention. Two items of concern are contamination of large optical windows and mirrors, which can lower their damage thresholds, and contamination of targets, which can spoil experiments. Earlier in 1979, a rational basis for contamination limits on targets was worked out with the help of A. Gutacker, a consultant from Kodak who has experience with similar problems in the Omega Facility at Rochester, New York. With the start of assembly operations, we have engaged Mr. Gutacker to assist in developing surface contamination limits for Antares optical surfaces. Tentative goals have been set, and practical models of contamination flow are being developed. These steps will enable us to specify economical procedures and minimal facility additions to meet our needs.

III. ADVANCED LASER TECHNOLOGY
(J. F. Figueira)

The advanced laser technology program aims at improving the performance of current operating systems and at satisfying future program requirements by concentrating on: (1) phase conjugation, which can improve the optical performance of future systems and can have diagnostics applications; (2) gaseous saturable absorbers, which can substantially improve performance in both Helios and Antares; and (3) investigation of a new class of saturable absorbers based on doped alkali-halide crystals. The investigations of phase conjugation and gaseous saturable absorbers have been extremely successful in advancing the understanding of the processes involved. Improved saturable absorbers have allowed an increase of on-target energy in Helios.

GENERAL

The results of earlier advanced technology programs have allowed Helios to approach the on-target operating point, primarily by incorporating improvements achieved in our investigation of gaseous saturable absorbers. Because these gaseous saturable absorbers are not completely understood and because identification of new candidates could lead to further improvement in our operating systems, some emphasis has been placed on this program. In addition, we investigated the potential of solid-state absorbers based upon doping and saturable-gas-absorber entrainment, an effort aimed at longer range applications. Continuing phase-conjugation studies offer the promise of self-correcting and self-aligning laser systems with essentially diffraction-limited performance. Phase conjugation has been demonstrated experimentally; further analysis has led to understanding it; and its engineering application to larger laser systems is being studied.

PHASE CONJUGATION

Phase Conjugation and Nonlinear Optics (C. R. Phipps, D. E. Watkins, S. J. Thomas, W. W. Rigrod, R. A. Fisher, B. R. Suydam, B. J. Feldman)

Introduction. Phase conjugation is unique because it provides reflections that reverse not only the propagation vector but also the phase distortion of an aberrated wave. The reconstruction properties of phase conjugation are illustrated in Fig. III-1, which shows the qualitative difference between the twice-aberrated reflection returned by a conventional mirror and that returned by a phase-conjugate reflector.

In a double-pass, static optical configuration such as that already existing in our ICF power amplifiers, fixed wave-front distortions are removed, in principle, and, if the optical wave arises from a point source, the wave would be returned to that point.

The application of phase conjugation in novel laser resonators and in more conventional technologies to shape laser pulses may prove very useful.

We have concentrated on degenerate four-wave mixing (DFWM) as the means for obtaining phase-conjugate reflections for two reasons. First, few suitable materials exist for obtaining such reflections by other means at CO_2 wavelengths. Second, there are relative disadvantages discussed by Lysiak[1] and others with respect to its implementation by stimulated Brillouin scattering or stimulated Raman scattering.

In the 1-yr period since we reported the first observation of phase-conjugate reflections in the 10-μm region,[2] substantial progress has been made both theoretically and experimentally. At Los Alamos, reflectivities as high as 40% have been observed in germanium, 20 times higher than first reported. Equally high reflectivities were seen in the gas SF_6 at Hughes Research Laboratories,[3] in work performed under a DOE-Los Alamos National Laboratory contract. It is encouraging that 10-μm DFWM has now been observed in over 10 different materials, both gaseous and solid state, several with acceptable reflectivities. Inhomogeneous and homogeneous resonant absorbers are represented, as are the nonresonant, Kerr-like media that were the first to be treated theoretically.[4] Our interest in these materials induced us to extend the theory for DFWM in resonant,

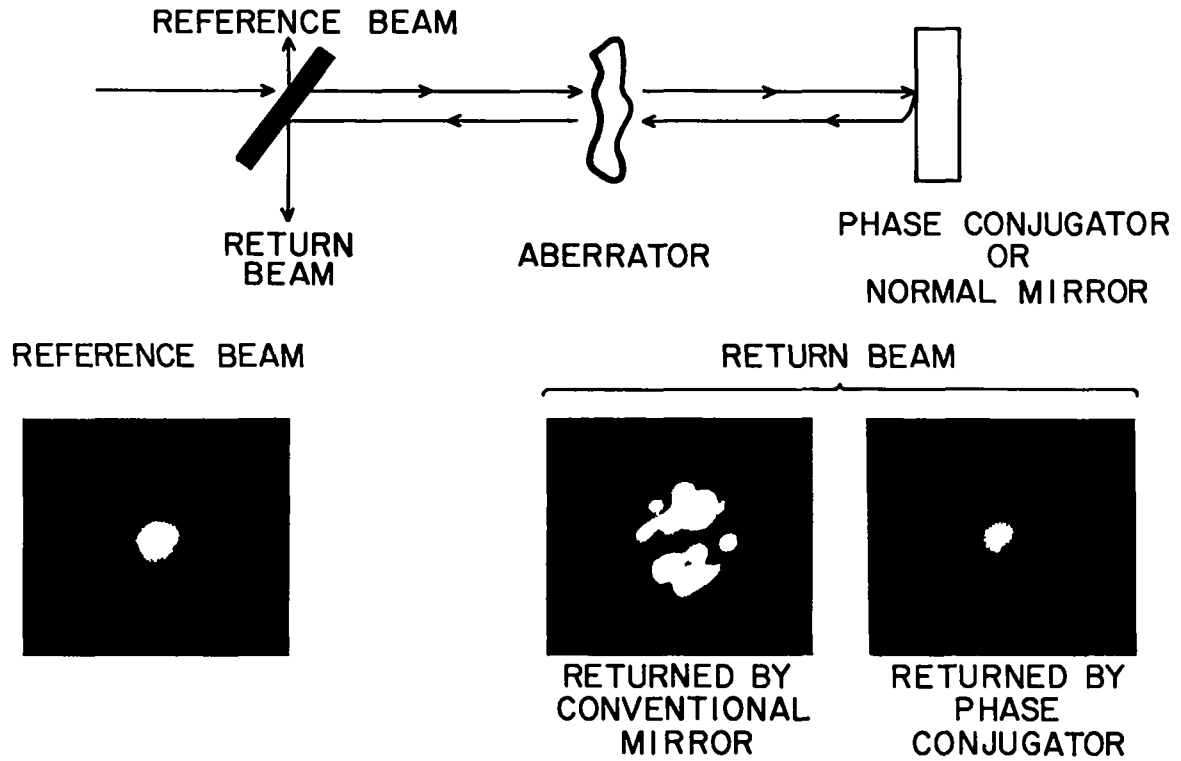

Fig. III-1.
Beam reconstruction using phase conjugation with actual photographs of the return beam provided by a normal and a phase-conjugate mirror.[9]

homogeneous absorbers[5] to include resonant inhomogeneous absorbers such as p-type germanium.[6]

This section also summarizes recent measurements of DFWM reflectivity at CO_2 wavelengths in $KReO_4$-doped KCl, p-type germanium, and intrinsic germanium, materials which represent, respectively, resonant homogeneous, resonant inhomogeneous, and Kerr-like or nonresonant DFWM media. The experimental parameters were chosen to emphasize the areas of agreement between experiment and theory, as well as the areas of obvious disagreement, relating primarily to pump absorption and multiphoton contributions to the reflectivity.

We have also continued the work concerning transient effects for laser pulses that are short compared to their propagation time in the DFWM material.[7,8]

This section concludes with a discussion of outstanding problems that must be solved before DFWM can be applied to ICF-class lasers, including a summary of experimental results at Los Alamos National Laboratory and elsewhere that specifically affect the ICF application at CO_2 wavelengths.

Experimental Arrangement for DFWM Measurements. In our initial work with 10-μm phase conjugation,[9] involving essentially transparent Kerr-like media, it was convenient to test the material within a laser cavity. The advantages to this approach were (1) pump-beam retroalignment was an automatic consequence of oscillation, and (2) no provisions for isolation of the laser from the test setup were required. However, this arrangement lacked the flexibility required for the second generation of measurements reported here. When the pump source is decoupled from the experiment (Fig. III-2), the difficulties associated with isolation and alignment verification are more than offset by the following advantages.

- Pump intensity and beam propagation parameters can be adjusted over a range well beyond that

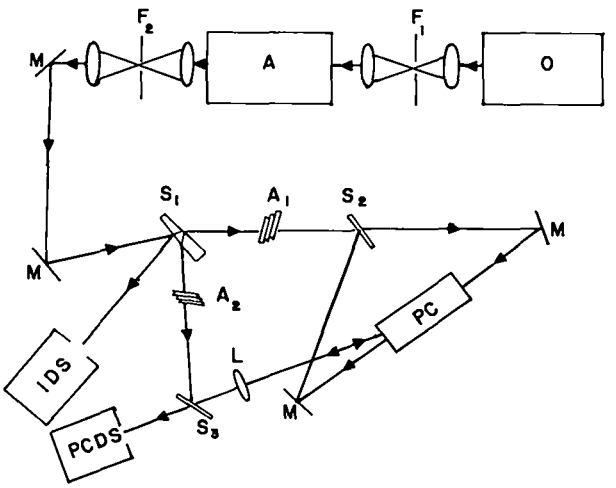

Fig. III-2.
Optical layout of the extracavity arrangement for measuring phase-conjugate reflectivity. Oscillator (O) and two-pass amplifier (A) are isolated from retroreflections by spark-type filters (F_1) and (F_2), which are gas-filled and evacuated, respectively. ZnSe splitter (S_1) provides small beam samples for the input detection system (IDS) and for the probe beam, whereas germanium splitter (S_2) provides equal, counterpropagating pump beams for the phase-conjugation medium (PC). Lens (L) assists in collecting the phase-conjugate reflection and directs it, through splitter (S_3), to the phase-conjugate detection system (PCDS). Calibrated CaF_2 attenuators (A_1) and (A_2) regulate the intensity of the pump and probe beams.

possible within a laser cavity, permitting comprehensive studies of the dependence of DFWM reflectivity on pump intensity, pump misalignment, and polarization, for example.

- Absorbing media, which would quench oscillation in an intracavity experiment, can be tested. Most of the useful parameter space for resonant DFWM materials (for example, p-type germanium) is in this category.
- Even in highly transparent Kerr-type media, it can be shown[10] that substantial phase distortion of a Gaussian-mode pump occurs for intensities sufficient to produce substantial DFWM reflectivity, constituting a fundamental limit to the reflectivities that can be observed in an intracavity experiment.

Two different types of optically initiated, plasma isolators[11] are required for adequate protection of the diffraction-limited oscillator-amplifier system.[12] Spacial filter F_2 (Fig. III-2) has an evacuated focal region to provide a small delay between passage of the forward-going optical pulse and achievement of full reverse isolation; this delay avoids any wave-front distortion of the forward pulse. The mode-locked oscillator is, in turn, protected by a smaller, gas-filled isolator that breaks down only when the amplified reverse transmission of F_2 exceeds safe levels. The combination of isolators renders the laser system stable against a 100% reflection.

The wedged ZnSe splitter S_1 provides a beam sample for the input detection system and the probe beam, which, in the present experiments, is always weak relative to the counterpropagating pump beams generated by the 50% splitter S_2 and controlled by attenuator A_1. The geometry used for the pump beams is reminiscent of Siegman's antiresonant ring:[13] although the 2-ns pulse duration is insufficient to fill the resonator consisting of S_2 and the two mirrors, accurate retroalignment of the pumps in the DFWM test sample is easily verified at the focal-plane iris of F_2. Splitter S_2 transmits the reflected DFWM signal to the phase-conjugate detection system which, in conjunction with the input detection system and the calibrated attenuators A_1 and A_2, permits temporally resolved determination of the pump, probe, and reflected signal intensity. Pump intensities up to 100 MW/cm^2 are possible with this setup at any wavelength in the CO_2 spectrum accessible by the grating-controlled oscillator-amplifier system. Pulse durations of 1.5 to 2.0 ns were used in all measurements reported here to permit higher intensities than in the earlier 50-ns work. In addition, these pulse durations show the effects of finite interaction and coherence lengths for pulses more similar to those that will be present in the actual application of phase-conjugate devices to ICF systems.

Phase Conjugation in Intrinsic and P-Type Germanium. Although differing only in type and density of doped impurities, intrinsic (pure) and p-type (gallium-doped) germanium behave quite differently in the infrared region. Intrinsic germanium is a Kerr-type DFWM material at CO_2 wavelengths; the reflectivity[4] is given by

$$R = \tan^2(KL) \approx (KL)^2 \ , \qquad \text{(III-1)}$$

where the product of the coupling coefficient K and the sample length L is equal to the intensity-dependent phase shift produced by the third-order nonlinear susceptibility of the material ($\sim 2.5 \times 10^{-11}$ esu in germanium).[14]

P-type germanium, on the other hand, is a resonant, inhomogeneously broadened absorber in which the DFWM response[6] is due to scattering off gratings produced by spacially modulated absorption rather than to the modulated refractive index. As might be expected,

the response in this case is usually somewhat less pronounced than for the homogeneously broadened case discussed below, but shares the advantage of being large compared to the Kerr-type response at moderate intensities well below the optical damage threshold. In addition, as shown in Fig. III-3, the theory predicts an order-of-magnitude range of pump intensities within which the reflectivity is nearly intensity-dependent. This circumstance suggests that multiline reflectivity (crucial to the CO_2 ICF application) may be as good as the reflectivity for a single-line spectrum in this material. This expectation is not present for Kerr-type media; Eq. (III-1) or Fig. III-3 suggests that reflectivity for a spectrum consisting of six equal, independent components may be reduced by a factor of 6 relative to that obtained with a single line. However, it is possible that either or both of these predictions may not be valid because of our inadequate current theoretical understanding of the effects of crosstalk between spectral components in DFWM.

Thin samples of intrinsic germanium give DFWM reflections that closely agree with the predictions of Yariv and Pepper's theory[4] for Kerr-type media, except at very high intensities (Fig. III-4). At 100 MW/cm^2, reflectivities as high as 30 to 40% are observed, somewhat in excess of model predictions. The source of this discrepancy has not been identified. However, this result, in a sample only 6 mm thick, is the highest reflectivity yet observed in any material at the P(20), 10-μm wavelength, and is equal to that obtained in SF_6 at P(8).[3] The value for the nonlinear susceptibility in intrinsic germanium, resulting from the fit of theory to experiment in this plot, is exactly equal to the value we found earlier in separate measurements by the technique of polarization ellipse rotation.[14]

However, as shown in Fig. III-5, reflectivity drops rapidly when longer samples are used to enhance the reflection coefficient. No more than 15% reflection could be obtained in a 4-cm-long germanium sample for intensities up to the surface damage threshold. Further, at all intensities used, the observed reflection was two orders of magnitude below theoretical predictions. This result specifically highlights the reduced transient response of phase-conjugate reflectors when the physical length of the laser pulse is made as short as the sample length.[8] This effect is not considered in the time-independent model for Kerr-like media.[4] At the highest intensity used (200 MW/cm^2), additional attenuation of the pumps and the reflected wave because of plasma formation is evident.[15]

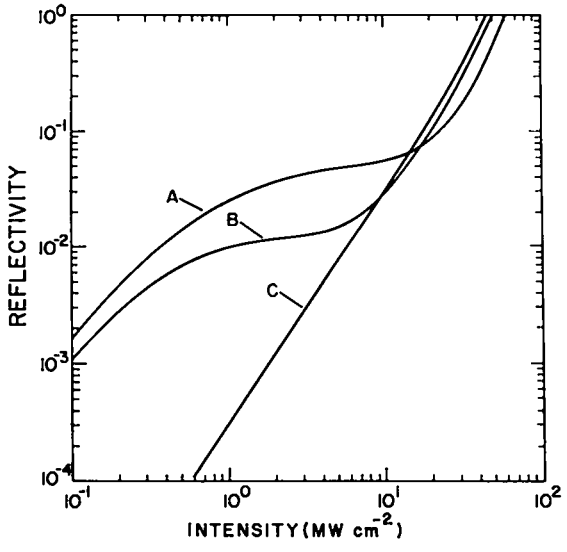

Fig. III-3.
Computed reflectivity vs 10.6-μm intensity for (A) p-type germanium, with small-signal absorption-length product $\alpha_0 L = 4$; (B) p-type germanium, $\alpha_0 L = 1$; and (C) intrinsic germanium, with 1-cm sample length. In the p-type germanium calculations, the Kerr-type contribution has been included. These curves fall below the intrinsic germanium calculation at high intensity because of absorption of the probe and reflected waves.

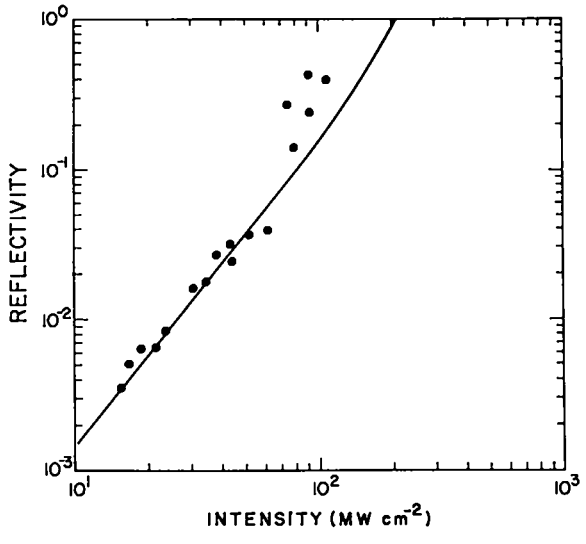

Fig. III-4.
Experimental data for a 1-cm-thick, polycrystalline nearly intrinsic germanium sample are compared to the predictions of Yariv and Pepper's theory[4] using $S_3 = 3 \times 10^{-11}$ esu to obtain the agreement shown. This value agrees with that obtained by different means by Watkins, Phipps, and Thomas.[14]

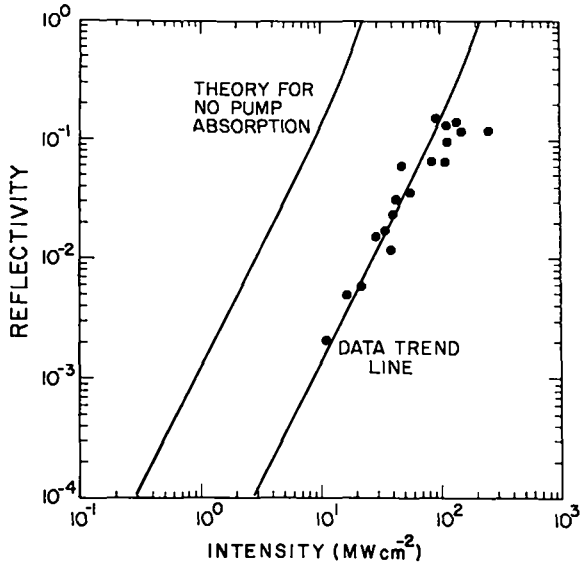

Fig. III-5.
A relatively thick sample (L = 4 cm) shows a two-order-of-magnitude disagreement between Yariv and Pepper's theory[4] (with the same X_3 value used in Fig. III-4) and actual experimental results, illustrating the effects of pump attentuation.

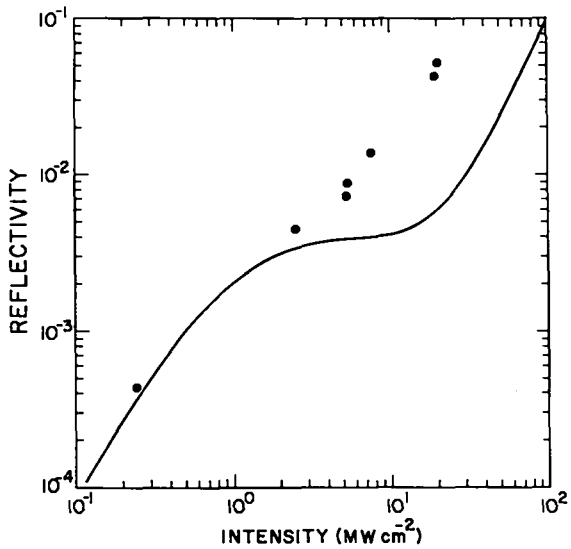

Fig. III-6.
For p-type germanium, with $\alpha_0 L = 0.36$, preliminary data do not agree very well with our model. However, the 5% reflectivity obtained at 20 MW/cm^2 greatly exceeds the reflectivity that we could obtain with intrinsic germanium at the same intensity.

In p-type germanium, preliminary data indicate 5 to 6% reflectivity, but less than ideal agreement with our model, which includes both the resonant inhomogeneous and Kerr-like components of the DFWM reflectivity (Fig. III-6). We are primarily interested in the tenfold improvement in the reflection coefficient obtained at an intensity of only 20 MW/cm^2 with p-type germanium compared to the Fig. III-5 results for samples of similar thickness. This improvement is an important feature, which would allow us to avoid the germanium optical damage threshold by more than an order of magnitude, while maintaining useful reflectivity for systems work.

Phase Conjugation in $KReO_4$-Doped KCl. KCl doped with $KReO_4$ belongs to a family of materials originally developed as solid-state saturable-absorber isolators for high-intensity CO_2 lasers. A discussion of our recent progress in preparing this material, which has highly predictable optical properties, appears below. It behaves in transmission as a classical, two-level, homogeneously broadened system with a P(28), 10-μm absorption resonance peak at room temperature, a linewidth of ~1.5 cm^{-1}, and an anharmonic shift of ~4 cm^{-1} toward the red in the excited-state absorption.[16] Although its spectrum is inappropriate for 10.6-μm isolation application, this absorber offers an excellent opportunity to test the Abrams and Lind theory for resonant homogeneous absorbers,[5] both on- and off-resonance.

We find excellent agreement in samples on-resonance, but, as shown in Fig. III-7, results off-resonance at the P(20), 10-μm line fall both above and below predictions. Just as in the germanium work reported above, the on-resonance discrepancy is mainly due to pump attenuation in the optically thick sample we used. The off-resonance results can probably be explained either by imprecise knowledge of the line shape for a detuning parameter 15 linewidths off line center, or by two-photon contributions to the DFWM signal, which are expected to be present in this absorber. This possibility is being explored.

Transient Phase-Conjugation Studies. Theoretical studies[7] of transient effects in phase conjugation by DFWM have continued. We are interested in the DFWM response when the duration of the pulse to be conjugated is on the order of the pulse transit time in the conjugate material.

We find that the temporal response of a nonlinear resonant or nonresonant phase conjugator subjected to a

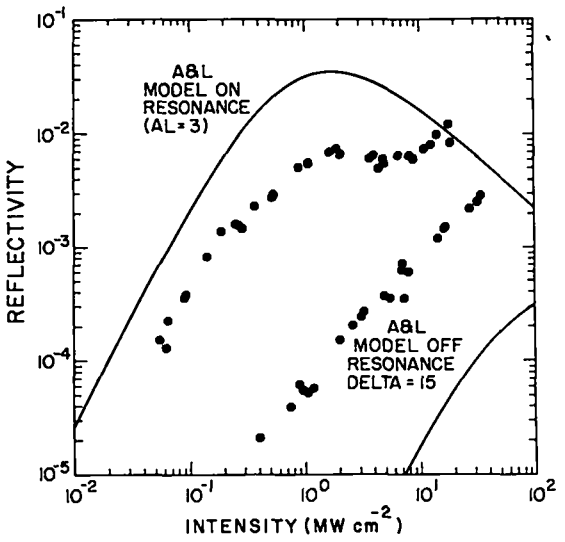

Fig. III-7.
On-resonance data (P-28, 10-μm wavelength) and off-resonance data (P-20, 10-μm) are compared to the Abrams and Lind models[5] for an optically thick sample of $KReO_4$-doped KCl ($\alpha_0 L = 3$). In off-resonance data, substantially more reponse than expected is found, whereas in on-resonance data, the reverse is true. The latter result is due to pump attenuation.

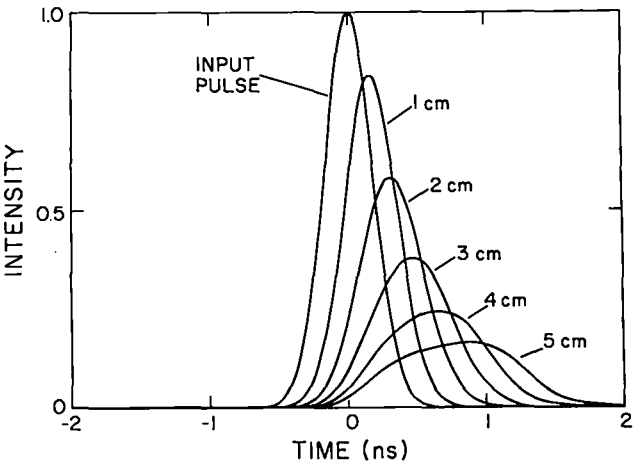

Fig. III-8.
Predicted reflected-pulse shapes for various lengths of germanium (refractive index is 4) when $\kappa L = 45°$ and the input pulse has 0.5-ns duration (FWHM).

quasi-cw nondepleted pump can be obtained from a linear Fourier transform technique, using the steady-state frequency transfer function for the material under study.

In Fig. III-8, we plot the intensity of the reflected phase-conjugate signal from a four-wave mixer for which $|\kappa| L = \pi/4$, corresponding to a reflectivity of unity in the steady state. A Gaussian input pulse with 0.5-ns (FWHM) duration is used. The reflected pulse is reduced in intensity and broadens in time as the interaction length is increased.

Survey of Present Performance of CO_2 DFWM Materials. Table III-I lists the reported performances[3,6,9,17] and the primary advantages and disadvantages of several materials that might be considered for DFWM application in CO_2/ICF lasers. Six materials exhibit reflectivities higher than 5%, and five of these (excluding intrinsic germanium) operate at intensities well below optical damage thresholds.

Despite its high damage threshold, KCl:$KReO_4$ has not demonstrated sufficient off-resonant reflectivity to make it the material of choice for CO_2 lasers. Another material, $Hg_xCd_{1-x}Te$, with $x = 0.8$ has been shown[17] to have the highest nonlinear susceptibility yet reported for a material at CO_2 wavelengths, but this performance depends on internal plasma formation, which also causes transient pump absorption. Therefore, further material development is required in this case. Cadmium telluride (CdTe) and gallium arsenic (GaAs) have shown adequate reflectivity, but they offer no apparent advantages over germanium. Like germanium, they are costly and not always available in the appropriate dimensions. As discussed above, intrinsic germanium has shown the highest single-line reflectivity by far, but it operates at relatively high intensities and would therefore be expected to offer lower efficiency with multiline spectra.

Considering these facts, we would have to conclude that p-type germanium is probably the best overall material for this application now. SF_6 is our second choice because it has coherent propagation effects and relatively low fluences producing good reflectivity, which implies large apertures for significant levels of phase-conjugate energy.

Outstanding Issues for the Application of Phase-Conjugate Reflectors. The practical issues that remain to be resolved before we can use phase-conjugate reflectors in our large laser systems are summarized as follows:

- impact of constraints on available solid angle in practical laser systems,
- effect of pump wave-front distortions arising from static aberrations and intensity dependent distortions in laser and conjugation media,

TABLE III-I

COMPARISON OF 10.6 μm DFWM CANDIDATES

Material	DFWM Type	R (10.6 μm)	I (MW/cm^2)	Reference	Primary Advantages	Primary Disadvantages
$KCl:KReO_4$	R[a]	0.003	35	6	High damage threshold	Inappropriate spectrum
$Hg_{.8}Cd_{.2}Te$	N[b]	0.10	0.2	17	Good reflectivity	Further development required Depends on internal plasma information Low fluence
CdTe	N[b]	0.05	100	6	Good reflectivity	No apparent advantages relative to Ge
GaAs	N[b]	0.15	100			
SF_6	R[a]	0.07	0.3	3	Doubles as isolator	Possible coherent effects Low fluence
Ge(i)	N[b]	0.3-0.4	120	6	Large apertures (40 cm)	Efficiency penalty with multiline spectrum
				9	No further development	Intensities close to those for plasma formation damage
Ge(p)	R[a]	0.05	20	6	Good fluence Large apertures (40 cm) No further development No obvious multiline penalty	Opaque, fragile Pump attenuation

[a]R, Resonant, homogeneous or inhomogeneous.
[b]N, Nonresonant, Kerr medium.

- effect on parasitic stability with targets,
- pump alignment and intensity matching constraints,
- tradeoffs with other technologies, for example, deformable optics and conventional target alignment schemes,
- impact on target fabrication, and
- cost and engineering constraints.

Figure III-9 illustrates the first of these approaches by demonstrating how a limited solid angle in typical system designs can lead to vignetting. A limited solid angle also affects the maximum transverse spatial frequencies that can be reconstructed by phase conjugation. Pump wavefront distortion also requires attention, as does the parasitic stability of the overall design in cases where unsaturated g_0Ls are implied by certain kinds of applications. Better quantitative assessments of the implied constraints on pump beam quality, alignment, and intensity-matching are needed, as are cost comparisons with more conventional means of reaching the same goals. It appears likely that many unique applications for phase-conjugate reflectors will be found.

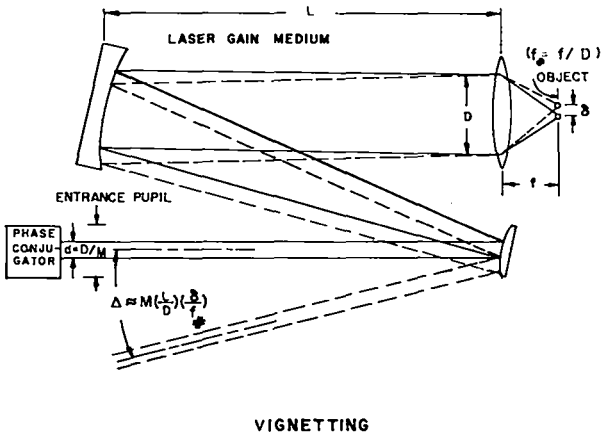

Fig. III-9.
Vignetting, in which a 500-μm motion of a focal-plane object corresponds to 5-cm-motion of the entrance beam pupil in the configuration studied, with a demagnification ratio M = 10.

Short Wavelength Laser Technology (R. A. Fisher, B. J. Feldman)

Saturable-absorber and phase-conjugate reflector studies in the 2500-Å spectral region require an intense, uniform, focusing optical beam with various bandwidths. To this end, we are developing a master-oscillator, power-amplifier system (MOPA) consisting of two 60-cm-long, 1.5- by 3.5-cm-cross-section, Lumonics-620 double-discharge amplifiers. The first amplifier serves as a low-energy, narrow-band oscillator that produces a nearly diffraction-limited beam, whereas the second unit amplifies this beam to high intensities.

Several experimental arrangements have been considered. In the oscillator, we have achieved narrow-band output by operating with an internal grating at high incidence angles (80°). With appropriate apertures, a narrow bandwidth ($\Delta\lambda \lesssim 0.01$ Å) has been achieved with output energies of 5 μJ in a 10-ns pulse.

A single pass of this pulse through the amplifier leads to a narrow-band pulse of 2 mJ superimposed on a 5-mJ, broadband background. This background originates from amplified spontaneous emission (ASE) in the oscillator and can be reduced by spacial filtering between the oscillator and the amplifier. Attempts to use two amplifying passes led to intense ASE, originating in the amplifier, as a result of incomplete saturation with less than twofold amplification of the pulse on the second pass. In this arrangement, the ASE is intense enough to almost completely deplete the gain.

An alternative arrangement consisted of replacing the grating in the oscillator with a highly reflective mirror and placing an etalon in the cavity to obtain the required wavelength selectivity. By using a 25-μm, air-spaced etalon with 90%-reflecting coatings, we achieved a laser output of 5 mJ with a bandwidth of 0.5 Å. Passing this pulse through the amplifier once resulted in a 50-mJ, 10-ns output pulse with less than 20% of the total energy in broadband background.

Studies are in progress to doublepass this pulse by using an additional 250-μm, air-spaced etalon, with 90% reflectivity on both surfaces, in the oscillator. Expected values are 200 μJ in 10 ns with $\Delta\lambda \lesssim 0.05$ Å.

SATURABLE-ABSORBER DEVELOPMENT

Studies of Optical Saturation of Hot CO_2 Absorption (S. J. Czuchlewski, A. V. Nowak)

Introduction. To suppress parasitic oscillations in our high-power CO_2 lasers, we developed[18] broadband gas isolators, which are used successfully in the Gemini and Helios lasers and in the Antares front end. These isolators consist of multicomponent gas mixtures, which employ SF_6 as the optically saturable absorbing component. Because heavy polyatomic molecules (such as SF_6) have high density of states, they undergo multiphoton absorption processes and do not saturate completely. Consequently, some output energy is sacrificed with all saturable absorbers: triatomics may reduce this loss.

Figure III-10 illustrates the measured transmission of pure SF_6 together with that predicted for a simple two-level absorber[19] (solid curve). SF_6 saturates more slowly and less completely than the two-level system. No choice of saturation energy improves the fit of the theoretical curve to the data, demonstrating that SF_6 does not behave as a two-level molecule. Because we thought that simpler molecules (for example, triatomics) might serve as more efficient isolators, we investigated the saturation of hot CO_2, a typical triatomic.

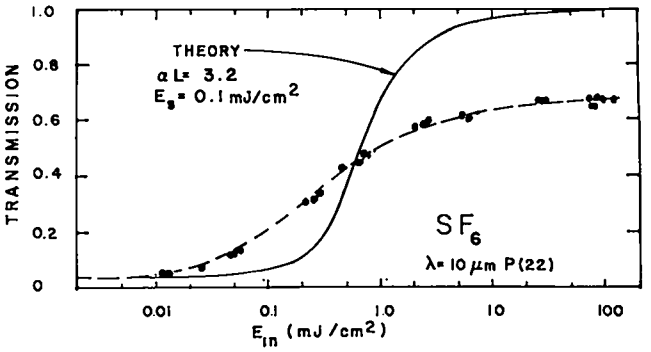

Fig. III-10.
SF_6 transmission for 1-ns pulses. The solid curve illustrates the Frantz-Nodvik theory[19] using the value of αL that yields the observed small-signal transmission. Changing the value of the saturation energy (E_s) merely shifts the theoretical curve horizontally without changing its shape.

Experiment. In this experiment, the transmission of hot CO_2 was measured as a function of input fluence, using single-line, 1.7-ns, 10-μm laser pulses. CO_2 at a pressure of 200 torr was heated to 673 ± 3 K in a ~100-cm-long cell. Data for 10-μm P(20) and P(18) wavelengths are shown in Fig. III-11. The solid curves are the predictions of the two-level Frantz-Nodvik theory.[19] Excellent fits are obtained by using saturation-energy parameters of 7.8 and 6.5 mJ/cm^2 for P(20) and P(18), respectively.

Because the behavior of triatomic CO_2 is fundamentally different from that of polyatomic SF_6, triatomics, as a class, may saturate more effectively than polyatomic molecules. We have identified several triatomic molecules that might make practical isolators and are studying their transmission characteristics. However, the high temperature required for CO_2 absorption makes these triatomics practically infeasible for the intended application.

Our data represent the first saturation measurements of hot CO_2 absorption with 1-ns CO_2 laser pulses and also present interesting information pertaining to CO_2 kinetic processes. The measured saturation energies are in good agreement with the value (6.1 mJ/cm^2) predicted by a simple phenomenological CO_2 model.[20] The observed ratio of the small-signal CO_2 absorption coefficients (1.26) is in excellent agreement with the theoretical value (1.24), which includes the P(20) hot-band contribution. The fact that the P(20) absorption appears slightly harder to saturate than the P(18) may also be a hot-band effect. A detailed comparison of the experimental data

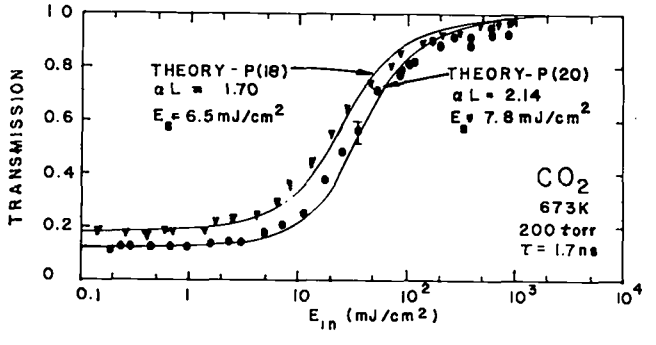

Fig. III-11.
Hot CO_2 transmission for 1.7-ns pulses. The data were obtained for pulses of uniform spacial intensity. The solid curves are the predictions of the Frantz-Nodvik theory.[19]

with the more exact predictions of a fully coherent model[21] for pulse propagation in CO_2 is under way; results will be described in a subsequent report.

Fabrication and Testing of Perrhenate-Doped Alkali-Halide Crystals (J. F. Figueira)

Introduction. Previous collaborative work between Los Alamos and Cornell University identified a new class of nonlinear materials that have multiple potential applications in CO_2 lasers.[7] These materials are created by the selective introduction of impurity ions into normally transparent alkali halides. The ions are optically active in the ir, producing absorptions in the 10-μm region. The first successful demonstration of this concept was made with a KCl host doped with the perrhenate ion, ReO_4^-.[16] This system of ReO_4^-:KCl has little practical value for isolation of multiline CO_2 ICF lasers because of its narrow absorption resonance at room temperature (1.5 cm^{-1}) and the location of its room-temperature resonant frequency (936.5 cm^{-1}). Work is continuing at Cornell University to find more appropriate dopant materials that would alter the bandwidth and resonant frequency to values more appropriate for the isolation application. Other promising applications for this material, including phase conjugation, are being explored separately.

Concurrently with the Cornell University program, a material fabrication study was begun at HCC in 1979 to identify fabrication problems for large-scale crystals of the impurity-doped alkali halides. The program produces large single crystals of KCl and NaCl doped with $KReO_4$. Also, hot-forged crystalline samples will be prepared to test the techniques currently employed for the fabrication of Antares windows.

The following section presents the test results on KCl-based single-crystal material. Attempts to produce measurable concentrations of the ReO_4^- ion in NaCl crystals have proved unsuccessful. The NaCl work continues and will be discussed in a future report.

Single-Crystal Fabrication of KCl:KeO_4^-. The original KCl crystals produced by Cornell University were grown by the Czochralski method and showed large residual strains. Also, control of the ReO_4^- concentration in the final crystal was not demonstrated. Control of

residual strain and ReO_4^- concentration has been improved substantially by the HCC materials development program. The first phase of this work, reported in Ref. 7, included studies of dopant ion concentrations, density gradients of ion deposition, strain fields, and the effect of the impurity on the damage level of the host material.

Using the Bridgeman-Stockbarger[22] technique of crystal growth, HCC produced a series of samples for testing and evaluation by Los Alamos. The samples were tested for strain by examining them with a white-light polarimeter. A comparison of Czochralski and Stockbarger material (Fig. III-12) showed that the Stockbarger technique completely removes the strain pattern present in the Czochralski-grown crystals and allows the fabrication of 5-cm-diam by 15-cm-long samples of strain-free material.

To determine the ability to control the dopant concentration in the finished crystal selectively, we prepared a series of samples in which the starting $KReO_4$ concentration was varied between 10^2 and 10^5 ppm by weight and the resulting ReO_4^- ion concentration was measured by conventional neutron-activation analysis. This technique (which actually measured the rhenium concentration in the sample) can be used to assess the ReO_4^- ion concentration, assuming that all the rhenium present is in the ReO_4^- ion.

Figure III-13 shows the results of these measurements where the starting concentration has been increased to 10% $KReO_4$ by weight. Samples were taken from the "heel" end of the boule to standardize the testing procedure because a longitudinal gradient in the ReO_4^- concentration was observed. Controllable dopant concentrations can be achieved, with maximum ReO_4^- concentrations approaching 10^{17} cm^{-3}.

It is characteristic of the Stockbarger technique that ReO_4^- impurities not trapped by the KCl lattice tend to rise to the top of the boule, causing a higher concentration of the ReO_4^- ion at the upper (or last-grown) part of the boule. In a 17-cm-long boule, we determined the magnitude of this impurity concentration gradient. Figure III-14 shows the result of this measurement for a sample in which the starting impurity concentration was 10^4 ppm. Dopant concentrations differing by factors of 6 are seen in this sample. HCC is evaluating the impact of

Fig. III-12.
Visual comparison of strain-fields of the Cornell University and HCC crystal samples, obtained with a white light polarimeter.

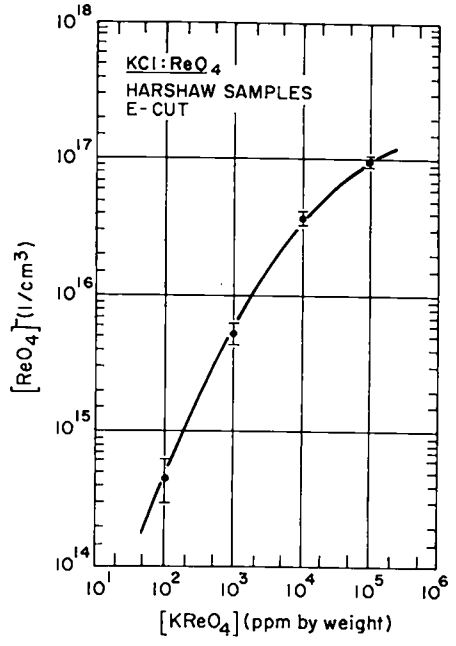

Fig. III-13.
Density of ReO_4^- ions in HCC samples, by neutron activation analysis, vs the starting concentration in the melt prior to crystal growth.

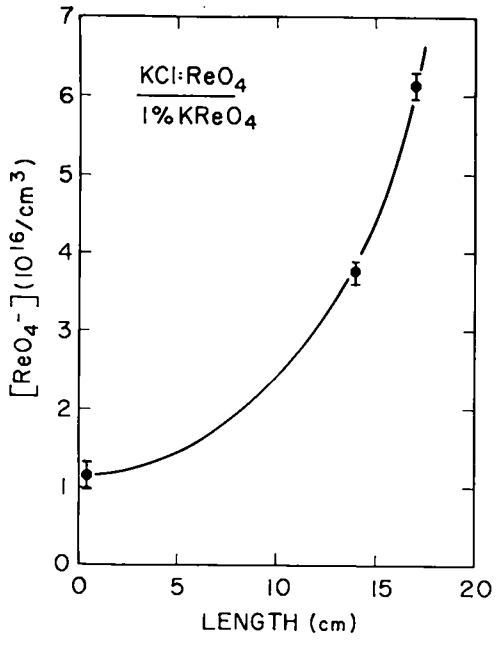

Fig. III-14.
Density of ReO_4^- ions vs length in a single HCC sample in which the starting concentration was 1%.

this nonuniform concentration on the construction of hot-forged polycrystalline samples.

Optical Properties. The optical absorption coefficients of each sample were measured separately on a Fast Fourier Transform Spectrometer with a resolution of less than 0.2 cm^{-1}. Figure III-15 shows a typical absorption spectrum.* From these measurements and those previously described, a value for the optical cross section at 936.45 cm^{-1} of $(0.46 \pm 0.02) \times 10^{-16}$ cm^2 was calculated. The positions of the absorption resonance and the bandwidth were independent of dopant concentration throughout the range studied.

Optical Damage Thresholds. A series of damage measurements were performed on the doped material in the GWTF.[23] As a control, undoped NaCl and KCl were tested under identical conditions. All measurements were made with 1.7-ns (FWHM) pulses at the P(20), 10-μm wavelength. Table III-II presents the results.

The damage threshold of pure KCl is 50% that of pure NaCl. The addition of the $KReO_4$ impurity to KCl causes a 24% reduction in the damage threshold for the host material. Thus, the choice of the host material

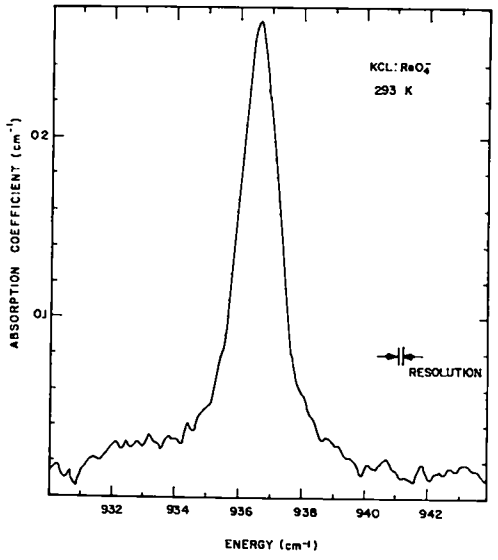

Fig. III-15.
Absorption spectrum of $KReO_4$-doped KCl material at 293 K, obtained by a Fast Fourier Transform instrument.

*Transmission is given by $T = e^{-\alpha L}$.

TABLE III-II

DAMAGE THRESHOLDS—SINGLE CRYSTAL HCC MATERIAL

Material	Dopant	Observed Damage Threshold: Absolute (J/cm^2)	Observed Damage Threshold: Relative (%)
NaCl	None	7.2 ± 0.1	100
KCl	None	3.7 ± 0.6	51
KCl	ReO_4^-	2.8 ± 0.5	38

appears to be the dominant factor in determining optical damage resistance in this class of materials.

Conclusion. The work to date on impurity-doped alkali-halide saturable absorbers has demonstrated that the concept shows promise as a solid-state replacement for the currently employed gas-phase saturable absorbers. We still need to develop a system based on NaCl that has the necessary spectroscopic properties for CO_2 ICF lasers. Having resolved most of the material fabrication problems, we will now emphasize obtaining a better understanding of the spectroscopic properties of these materials. This work will continue at Cornell University under the direction of Dr. A. J. Sievers.

Pulse Transmission Through SF_6 (A. V. Nowak)

Introduction. We have initiated a study of long- and short-pulse transmission of 10-μm CO_2 laser radiation through SF_6 and SF_6 buffered by helium. The purpose of this work was to determine whether the saturation behavior of SF_6 depended on laser fluence or power. Figure III-16 presents the results.

Experiment. The incident beam had a Gaussian profile of 7-mm diam (0.40 cm^2) at the 1/e intensity level for both the long and short pulses. The short pulse had a FWHM of 1.7 ns, with a risetime about three times faster than the fall time. The long pulse had a FWHM of 80 ± 5 ns, with a risetime about twice as fast as the fall time.

The SF_6 was contained in an aluminum cell, sealed off at the ends by NaCl windows at the Brewster angle. The center-to-center window distance was 19 ± 0.5 cm. The cell was filled and emptied in place from a diffusion-pump-controlled filling station.

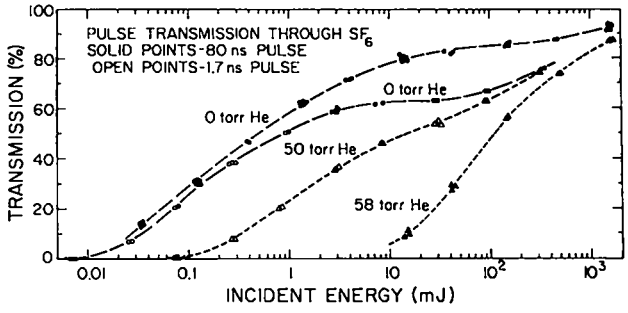

Fig. III-16.
Energy transmission in SF_6 vs input energy, with and without helium buffering. The SF_6 pressure was 1 torr; the cell length, 19 cm; and the beam area, 0.4 cm^2 (at 1/e of peak on-axis fluence). Measurements were performed at the 10-μm P(20) wavelength.

The incident energy was monitored by splitting off a portion of the incident beam with a NaCl wedge. A Laser Precision Corp. pyroelectric ratiometer was used to measure the energy of the incident and transmitted beams and to take their ratio automatically.

The entire experiment was carried out inside a screen room to shield the instruments from the electrical interference generated by the laser system. Transmission could be measured with a precision of ±1/2%.

Discussion. Referring to Fig. III-16, we note that, at incident energies below 1 mJ/cm^2, the saturation of pure SF_6 at 1.0 torr is very similar for both long and short pulses. This suggests that in this low-energy domain, the saturation behavior is fluence dependent.

For fluences above 1 mJ/cm^2, we note a significant decrease in the transmission of the short pulse relative to the long pulse. The only obvious explanation for this observation is bandwidth effects. From our studies of hot CO_2, we have determined that the 1.7-ns pulse has a bandwidth of ~1 GHz, whereas the long pulse has a much narrower bandwidth. Therefore, the short pulse interacts with many more SF_6 molecules than the long pulse. We can explain the lower transmission of the short pulse at higher energy by postulating that this pulse is pumping a greater fraction of SF_6 molecules than the long pulse and that, therefore, the threshold for saturation is higher.

The addition of 50 torr of He to the SF_6 reverses the result: much more of the long pulse is absorbed than of

the short pulse. This is understandable if one considers that many more SF_6-helium collisions occur during the long pulse than during the short pulse. The net effect is a repopulation of absorbing states that is greater during the long pulse than during the short pulse.

Modeling the transmission curves of Fig. III-16 may be difficult. Our recent experimental work shows severe spacial reshaping of a 10-μm Gaussian laser beam passing through SF_6, depending in a complicated way on length of the cell, pulse energy, SF_6 pressure, and wavelength of the pumping line.

ROTATIONAL RELAXATION AND SHORT-PULSE PROPAGATION IN CO_2 LASER AMPLIFIERS (J. C. Goldstein)

We have calculated the rate constants for rotational relaxation in CO_2 caused by collisions with helium and argon.[24] The rate constants, referred to below as the Preston-Pack calculations, have been used successfully[24] to model experimental observations of CO_2 rotational relaxation in gas mixtures of helium, N_2, and CO_2. The J-dependence* of these rates differs significantly from that of the reservoir model, the only rotational relaxation model used in all previous theoretical CO_2 pulse-propagation studies at Los Alamos. The reservoir model postulates that the rate of collisional transfer from a state J to another state J′ (both states being in the same rotational manifold of a particular vibrational level) is characterized by a constant that is independent of J; that is, the coupling is the same for all initial states J and depends only on the final state J′. The Preston-Pack calculation[24] reveals that states J′ near J are much more strongly collisionally coupled to J than are states J′ that differ from J by many units of angular momentum. In the reservoir model, the total rate of collisional transfer from a state J to all other states J′ is very nearly independent of J and is approximately equal to $1/T_R$, where T_R is the rotational relaxation time.

There has been a suggestion[24] that calculations would show that energy could be extracted from a CO_2 laser amplifier 20% faster in the Preston-Pack model than in the reservoir model by using a multiline pulse consisting of frequencies of the P14, P20, P26, and P32 lines of the 10.6-μm band, instead of the P18, P20, P22, and P24 lines. This effect, if real, would have important consequences for the efficiency and power output of large CO_2 fusion drivers.

It was necessary to construct[25,26] an entirely new pulse propagation code to investigate this suggestion and other consequences of the Preston-Pack model fully. The code includes a density matrix description of the interaction of the material medium with the propagating pulse. It does not explicitly include the magnetic degeneracy of the rotational levels: the magnetic levels are in effect summed over in the calculation, an approximation that is valid if no collisional (or other) mechanism exists that distinguishes individual Zeeman levels. This approximation has been justified by previous studies[27] with a code that specifically included individual Zeeman states. The new code can, of course, also be used with reservoir model rotational coupling.

To delineate differences between the two rotational models, we chose a test problem that represents reasonably typical operating conditions for Laboratory fusion lasers, the amplification of a four-frequency nanosecond pulse through three separate stages of gain.* Each stage had a 10-μm P20 small-signal gain coefficient of 0.025 cm^{-1} and a length of 200 cm. The cross-sectional areas (3.0, 308.45, and 807.92 cm^2) were chosen to approximate actual beam paths in the Helios machine, and the intial pulse energy was 50 mJ (divided equally among the four frequencies). Two sets of frequency content were used: (1) P18, P20, P22, P24 and (2) P14, P20, P26, P32. The first set gave the largest output when the reservoir model was used to do the calculation, whereas the second set, as predicted in Ref. 24, allowed a 20% faster rate of energy extraction from the amplifier medium when the Preston-Pack model was used. Other material parameters were fixed by assuming Helios operating parameters, which include a 3:1/4:1::He:N_2:CO_2 gas mix at a total initial pressure of 1800 torr.

The new code[26] worked accurately in comparison with an older code: maximum differences were about 2 to 3% in individual line quantities (peak intensities and energies) and total pulse values were ~1% or less, an agreement that is quite reasonable because the older code used a totally different numerical method and slightly different initialization and material parameter values.

The Preston-Pack rates for the Helios conditions chosen for the test problem were provided by R. T. Pack.

*J represents the rotational quantum number.

*The test problem did *not* try to simulate the actual multipass geometry of Helios; that is, three separate amplifier stages were considered, each with an initial P20 gain coefficient of 0.025 cm^{-1}.

TABLE III-III

COMPARISON OF PULSE PARAMETERS CALCULATED BY USING THE PRESTON-PACK AND RESERVOIR MODELS

Case	I_{max} (GW/cm^2)	T_I (ns)	E (J)	T_E (ns)	f
(1) P18, 20, 22, 24					
Res	0.9539	0.448	885.5	1.16	0.374
Preston-Pack	9.9218	0.45	869.3	1.18	0.357
(2) P14, 20, 26, 32					
Res	0.7692	0.488	791.3	1.25	0.365
Preston-Pack	0.7811	0.48	793.5	1.23	0.371
P20 only					
Res	0.5161	0.50	692.0	1.57	0.312

The results are reported in Table III-III, where the various pulse quantities are the maximum intensity I_{max} in GW/cm^2; the time ΔT_I (in nanoseconds) required for the intensity to increase from 10% of its maximum value to 90% of its maximum value; the total energy E in joules; the time ΔT_E (in nanoseconds) required for the energy to increase from 10% of the total to 90% of the total; and f, the fraction of the total energy delivered at the time I_{max} is reached. All tabulated values refer to parameters of the final ouput pulse after three amplification stages. For comparison, similar figures are given for a single-line pulse in the reservoir model.

E is larger for Case (1) than for Case (2), as it should be for the reservoir model; however, the same is true for the Preston-Pack model. In general, one can see from Table III-III that the differences between results obtained for the two models of rotational relaxation are very small. We expected large differences for these test problems, which, we believe, have parameter values that are reasonably characteristic of conditions in our operational and planned lasers.

Several factors helped us understand these results. First, the energy extraction result in Ref. 24 was obtained by the following procedure: the population equations were solved in time assuming the existence of a large and constant amplitude intensity on each of four lines. The corresponding rates were set large enough to saturate the inversions on each of the four lines rapidly and to hold them at their saturated values while, by rotational relaxation, the entire population of the upper vibrational state was slowly drained. The constant amplitude intensities were equal on all four lines. The time needed to drain one-half of the entire upper-state population (to reduce the total vibrational inversion to zero) was calculated; this calculation was repeated for different line combinations in both the reservoir and the Preston-Pack models.

No propagation effects were taken into consideration in these calculations. (That was the point in constructing the new code.) In addition, the intensities chosen for the four lines were very high: the electromagnetic rates would correspond (at the Helios pressure of 1800 torr) to an intensity of 10.8 I_{sat} or to $\sim 6.15 \times 10^9$ W/cm^2 [$\sigma(I_{sat}/\hbar\omega) = 1/T_R$, where σ is the stimulated emission cross section]. In the realistic test problem, typical individual line intensities were ~ 0.15 to 0.30×10^9 W/cm^2. However, for Case (2), the P32 gain is substantially smaller than the P20 gain, and, in fact, the peak intensity on that line reaches only $\sim 0.008 \times 10^9$ W/cm^2 by the end of the third stage (a total energy of 8 J compared to 100 to 300 J on each of the other lines). The difference of ~ 100 J between the output pulse energies for Cases (1) and (2) lies primarily in the very small output on line P32. Because of propagation effects, it is unfair to compare the rate of energy extraction on lines P18 to 24 in the reservoir model with the corresponding rate on P14, 20, 26, and 32 in the Preston-Pack model using the same intensities on *all lines* equaling ~ 11 I_{sat}. In other words, although the comparison made in Ref. 24 is correct, the conditions assumed for the comparison appear unrealistic or unachievable for typical Laboratory machines.

Another quantity we examined to understand the results better was the actual rotational relaxation rates $1/T_R$ that came out of the Preston-Pack model. These rates are plotted in Fig. III-17 as a function of the upper-level rotational quantum number J. Note, first, that the rates are not constant and that, in fact, the largest rate occurs for $J = 31$ (the rotational partition function peaks at $J = 17$). The latter point recalls that the P32 line was selected[24] as beneficial for faster energy extraction, whereas the fact that the rates are not constant raises a question of consistency in the code. We always assumed that the rotational relaxation rate is exactly one half of $1/T_2$, a figure obtained from the Abrams[28] formula for line-broadening on the P20 line. The experimental evidence[29] indicates that this assumption is almost exactly correct. If one assumes the general validity of that relation, then clearly the code should use different line-broadening rates if the rotational relaxation varies from line to line. This has not yet been done. Another observation should be mentioned in connection with Fig. III-17: the absolute magnitude of $1/T_R$ for the P20 line ($J = 19$) differs considerably (by $\sim 20\%$) from the value we

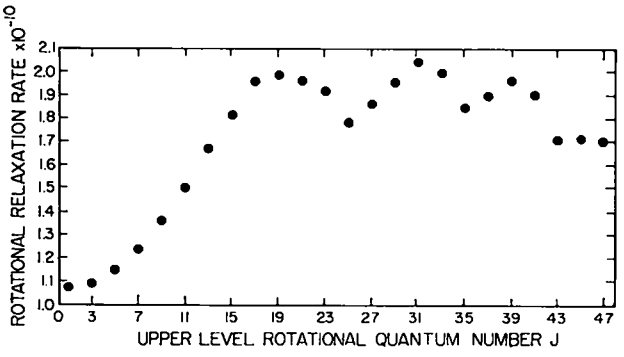

Fig. III-17.
Rotational relaxation rate vs J from the Preston-Pack model for 1800 torr of a 3:1/4:1::He:N_2:CO_2 mix at 340 K.

obtained (and used in the reservoir model calculations) from both the Abrams line-broadening data for the P20 line and from the assumed $1/2T_2$ relation. Initially this observation was most surprising because the Preston-Pack calculation[24] was renormalized to agree precisely with rotational relaxation measurements made on cw lasers. The renormalization was necessary because the unmodified calculations gave results that were too high by about a factor of 2 (Ref. 24). This source of discrepancy can easily be eliminated (but has not been in the results reported); for the pulsed lasers at Los Alamos, the number density of the pumped medium corresponds to that of the initial (presumably room-temperature) gas fill, whereas the temperature(s) do not. Over the several microseconds of pumping, there is no time for sound waves to propagate so that the material may reach the density characteristic of thermal equilibrium at the temperature induced by the pumping. Indeed, the usual determination of T_R by line-broadening takes such conditions into account. Therefore, the magnitude of the P20 $1/T_R$ should agree in both the Preston-Pack and the reservoir models, but the specific value will depend on whether a cw or a pulsed laser is under consideration.

Finally, one may ask a yet more detailed question: how do the individual pumping (decay) rates into (out of) a particular state J vary as a function of the other state's rotational number J'? We refer to specific rates, which, therefore, involve the population density of the collision partner. Consequently, these rates depend on the saturation level of the populations during the short pulse. However, some meaningful comparison can be made by computing these rates before the arrival of the pulse, that is, when the rotational populations are characterized by a Boltzmann distribution. These rates are shown in Fig. III-18.

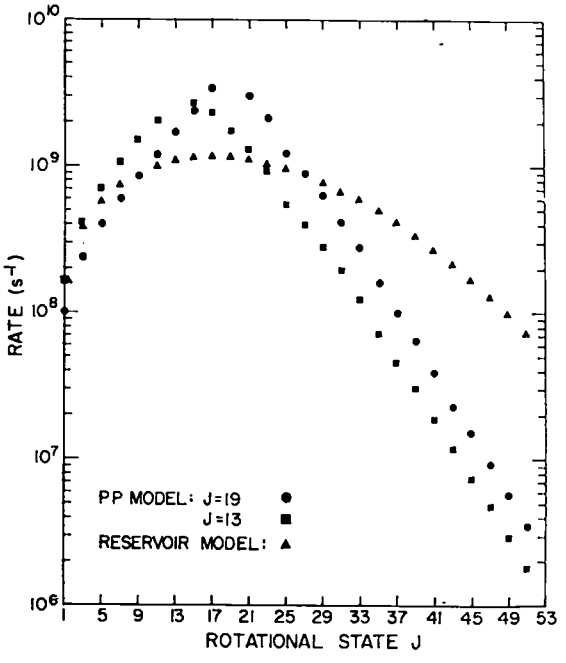

Fig. III-18.
Comparison of in and out rates of Preston-Pack model and reservoir model for J = 13 and J = 19 for equilibrium populations in a 3:1/4:1::He:N_2:CO_2 mix at 1800 torr and 340 K.

Three sets of points are shown: the small dots are the rates into (or out of, as they are equal by detailed balance) J = 19 from other states J'; the solid squares are the rates into J = 13; the triangles are the corresponding rates for the reservoir model, which are the same for *all* J (that is, the loss rate from J = 19 to J' = 31 is the same as the loss rate from J = 13 to J' = 31; again, by detailed balance, the loss rates are equal to the pumping rates in thermal equilibrium). One sees that the two Preston-Pack data sets peak somewhat above the reservoir data maximum (caused in large measure by the problem discussed earlier) but have somewhat narrower extents in J'. Although these rates are strictly correct only in thermal equilibrium, they do suggest another qualitative difference between the two models. In the calculations, the higher Preston-Pack rates around J' = 19 apparently compensated for the sharper falloff in J' to give nearly identical results for the output pulse energies.

In summary, a new pulse propagation code[25,26] has been constructed to study the effects of a new model[24] of rotational relaxation in CO_2 on propagation phenomena. The results of a test problem with realistic light and material parameters do not reveal the predicted[24] difference from results obtained with the reservoir model.

This is understandable because unrealistic light parameters were used in making the prediction[24] and because the total Preston-Pack rates themselves show an anomalous dependence on J that may, in fact, be wrong.* The individual transition rates in the Preston-Pack model are shown to vary somewhat more sharply than those of the reservoir model, but the differences apparently do not cause large differences in calculations of pulse-propagation phenomena.

REFERENCES

1. R. Mays and R. J. Lysiak, Opt. Comm. 31, 89 (1979).

2. "Inertial Fusion Program, January 1—June 30, 1978," F. Skoberne, Comp., Los Alamos Scientific Laboratory report LA-7587-PR (May 1980).

3. R. C. Lind, D. G. Steel, M. B. Klein, R. L. Abrams, C. R. Giuliano, and R. K. Jain, Appl. Phys. Lett. 34, 457 (1979).

4. A. Yariv and D. M. Pepper, Opt. Lett. 1, 16 (1977).

5. R. L. Abrams and R. C. Lind, Opt. Lett. 2, 94 (1978) and 3, 205 (1978).

6. D. E. Watkins and W. W. Rigrod, paper S.4, International Conference on Lasers '79, Orlando, Florida, December 16-21, 1979.

7. Roger B. Perkins and the Inertial Fusion Program Staff, "Inertial Fusion Program, January 1—June 30, 1979," Los Alamos National Laboratory report LA-8114-PR (June 1981).

8. W. W. Rigrod, R. A. Fisher, and B. J. Feldman, "Transient Analysis of Nearly Degenerate Four-Wave Mixing," Opt. Lett. 5, No. 3, 105 (March 1980).

9. E. E. Bergmann, I. J. Bigio, B. J. Feldman, and R. A. Fisher, Opt. Lett. 3, 82 (1978).

10. C. R. Phipps, Jr., S. J. Thomas, and D. E. Watkins, Proceedings of the International Conference on Lasers—'79, Orlando, Florida, December 16-21, 1979 (STS Press, Alexandria, 1980).

11. J. F. Figueira, S. J. Czuchlewski, C. R. Phipps, and S. J. Thomas, Appl. Opt., to be published.

12. C. R. Phipps, Jr., and S. J. Thomas, Opt. Lett. 1, 93 (1977).

13. R. Trutna and A. E. Siegman, IEEE J. Quant. Electron. QE-13, 955 (1977).

14. D. E. Watkins, C. R. Phipps, Jr., and S. J. Thomas, Opt. Lett., to be published.

15. C. R. Phipps, Jr., and S. J. Thomas, paper TuB5, Topical Conference on Inertial Confinement Fusion, San Diego, California, February 1980.

16. R. K. Ahrenkiel, J. F. Figueira, C. R. Phipps, Jr., D. J. Dunlavy, S. J. Thomas, and A. J. Sievers, "A New Saturable Absorber for the CO_2 Laser Using Doped KCl," Appl. Phys. Lett. 33, 705 (1978).

17. R. K. Jain and D. G. Steel, Hughes Research Laboratories, to be published.

18. S. J. Czuchlewski, Opt. Lett. 2, 39 (1978); and R. F. Haglund, in "Proceedings of the LASL Optics Conference," pp. 178-185 (SPIE Vol. 190, 1979).

19. L. Frantz and J. Nodvik, J. Appl. Phys. 34, 2346 (1963).

20. G. T. Schappert, Appl. Phys. Lett. 23, 319 (1973).

21. B. J. Feldman, Opt. Commun. 14, 13 (1975); and H. Volkin, J. Appl. Phys. 50, 1179 (1979).

22. J. H. Schulman and W. D. Compton, *Color Centers in Solids* (MacMillan, 1962).

23. B. E. Newnam, LASL Memorandum AP-2-79:202.

24. R. K. Preston and R. T. Pack, J. Chem. Phys. 69, 2823 (September 15, 1978).

*R. T. Pack, Los Alamos National Laboratory, provided this information.

25. Los Alamos Memorandum L-6(8/79)60; From: J. C. Goldstein; Subject: Comparison of the Calculated Amplification of Nanosecond Pulses in CO_2 using the Pack-Preston Rotational Relaxation Model with Results Obtained using the "Reservoir" Model; Date: August 28, 1979.

26. Los Alamos Memorandum X-1(12/79)33; From: J. C. Goldstein; Subject: Pulse Propagation in CO_2 Using the Pack-Preston Rotational Relaxation Model; Date: December 18, 1979.

27. J. C. Goldstein and F. R. Hopf, "Pulse Propagation in High Pressure CO_2 Laser Amplifiers," Bull. Am. Phys. Soc. 17, 1053 (November 1972).

28. R. L. Abrams, Appl. Phys. Lett. 25, 609 (1974).

29. R. R. Jacobs, K. J. Pettipiece, and S. J. Thomas, Appl. Phys. Lett. 24, 375 (1974).

IV. TARGET EXPERIMENTS AND MILITARY APPLICATIONS
(R. P. Godwin, J. H. McNally)

Through an integrated program of target experiments, theoretical development, and target design, we are establishing a fundamental understanding of laser-target interactions, particularly of relevant plasma physics and hydrodynamics. Experimental and theoretical efforts have addressed the scaling of consistent models to higher laser intensities. We have emphasized the development and demonstration of experimental techniques needed to evaluate conclusively the performance of present and future targets. A modest experimental effort has been directed toward military applications.

LASER FUSION EXPERIMENTS (R. P. Godwin)

Introduction (D. Giovanielli)

Our experiments comprise (1) main-sequence experiments involving all aspects of the laser fusion program and (2) essential as well as support experiments aimed at answering questions specific to a particular target design or to a basic laser-plasma interaction.

The Sirius-B experimental series, a systematic parametric study of fusion-target fuel conditions as a function of plastic coating, has been most successful. In this section, we describe experiments with these targets containing an argon gas fuel dopant that allows us to apply a wide range of atomic spectroscopy to fuel-density measurements. In a limited fuel-density range, the measurements corroborated earlier less direct measurements at densities of a few grams per cubic centimeter.

X-ray spectroscopy of laser-produced plasma yielded data on many important features of laser-plasma interactions that severely test computational models. In this section, we present important new data on the emission of x rays as a function of the intensity of 10.6-μm laser radiation impinging on gold microballoons. The measured weak decrease in emission efficiency and weak increase in effective blackbody temperature with this intensity hint at laser wavelength independence and provide indirect information on the hot-electron spectrum.

Experimental evidence for rapid lateral transport of energy from the laser focus has been accumulating for some time. In this section, we present evidence for rapid transport on the surface of targets and show that target surface contamination can have important effects. Ion spectroscopy is a dramatic example. Other experiments are described in which titanium K_α imaging has been used to examine the spacial distribution of hot electrons.

Spectroscopic Density Measurements on Sirius-B Targets (K. B. Mitchell, A. Hauer)

We have determined the densities of compressed fuel in Sirius-B targets (CH_2-coated GMBs) by analyzing the x-ray line emission from argon gas contained in the target. The GMBs were filled with 4 wt% of argon mixed with DT and were irradiated with 5 kJ of 10-μm laser light from Helios. Fuel densities were determined from the spacial and spectral profiles (Stark effect) of the argon lines and are plotted as a function of plastic thickness in Fig. IV-1. We made spectrographic measurements from spacial profiles of the argon lines for both coated and uncoated targets. Targets coated with 35 μm of plastic were compressed to a density 10 times that of the uncoated (exploding-pusher) targets.

Analysis of Stark-broadened argon lines yielded electron densities of $5 \times 10^{23}/cm^3$ (equivalent DT density, 2 g/cm^3) from these coated targets. We are investigating in more depth the quantitative aspects of Stark-broadening at high density. Typical argon spectra from the compressed cores of uncoated and plastic-coated targets are shown in Fig. IV-2. The helium-like lines dominate in the argon spectrum, which is consistent with the measured electron temperature of 650 eV determined from the free-free recombination continuum. Because the $n = 2$ lines are optically thick in both the helium-like and hydrogen-like series, we considered Stark profiles of the $n = 3$ lines. However, the broadened 1s-3p (Lyman β) line apparently is a blend of lines including the $1s^2$-1s5p line; also, potassium and calcium lines are caused by contaminants in the glass shell of uncoated targets. Therefore, we preferred the $1s^2$-1s3p argon line as a density diagnostic.

Figure IV-3 shows the experimental and theoretical line profiles for the argon ($1s^2$-1s3p) line at two different densities. Electron densities as high as $7 \times 10^{23}/cm^3$ were determined from targets having 35-μm-thick plastic coatings. The theoretical line profiles were calculated by

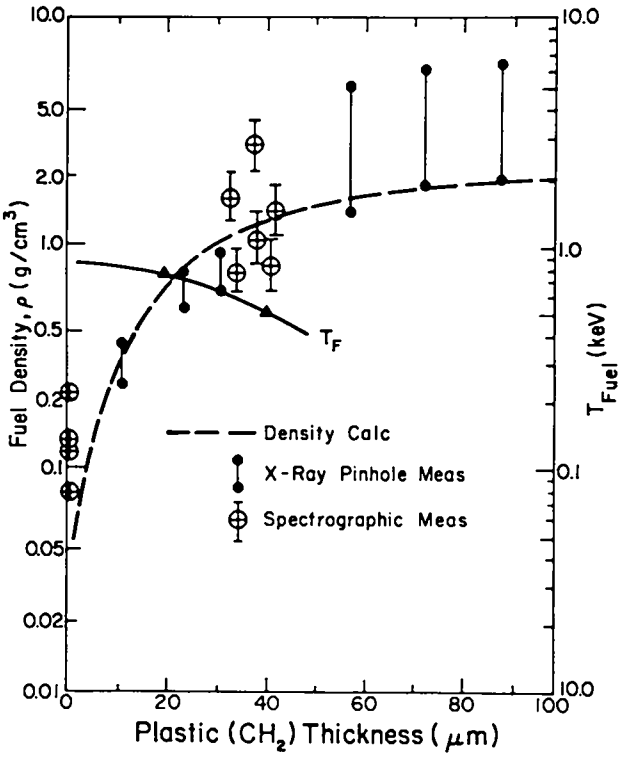

Fig. IV-1.
Densities of compressed fuel in Sirius-B targets as a function of plastic-coating thickness.

the Plasma Radiation Group at the Naval Research Laboratory.

Future work includes extending these measurements to targets with thicker plastic coatings.

Performance Analysis of Sirius-B Targets Containing Argon Seed Gas (A. Hauer)

We compared the results of spectroscopic measurements with numerical hydrodynamic simulations. Table IV-I compares a typical simulation and experiment. Two characteristics of these simulations seemed to be particularly important: (1) fine zoning in the laser absorption region and (2) careful fixing of the hot-electron temperature. The best results are obtained by using the hot-electron temperatures recorded in fast-ion measurements. These results are empirical, obtained from attempts to model many shots. The laser temporal profile used in the calculations accurately duplicates the measurements made with fast pyroelectric detectors and 5-GHz scopes.

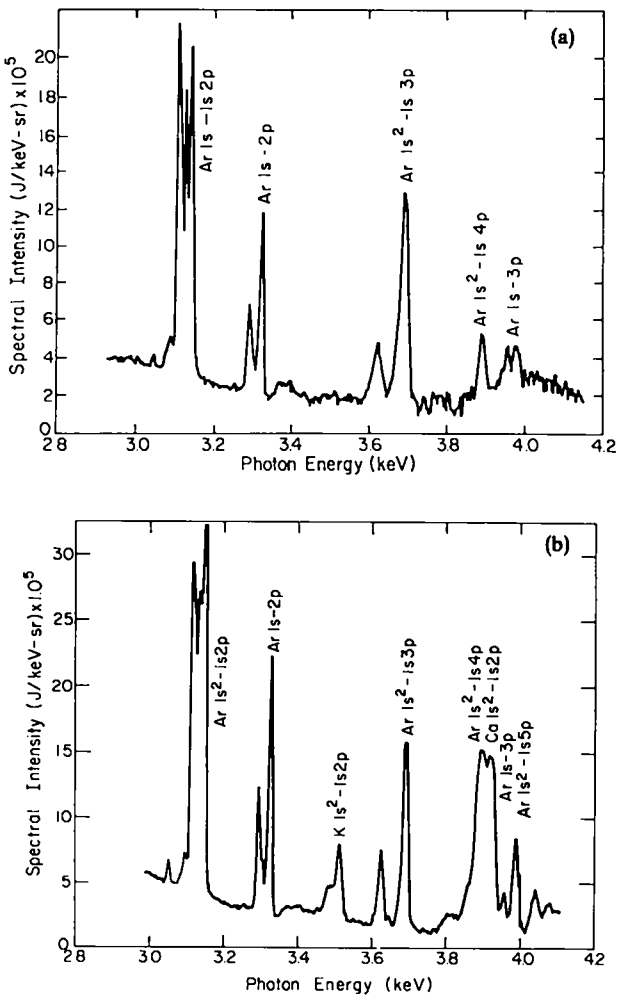

Fig. IV-2.
Typical argon spectra from (a) 230-μm-diam GMB with 30-μm CH_2 coating irradiated with 10.6-μm light at 4900 J, (b) 250-μm-diam uncoated GMB irradiated with 10.6-μm light at 4300 J.

To model the argon radiation accurately, departures from local thermodynamic equilibrium (LTE) must be considered. Non-LTE conditions are modeled with an average ion rate-equation package.[1] We are constructing a collisional radiative code, which will be used as a postprocessor for data from the main hydrodynamic code.

At temperatures on the order of 650 eV and densities of $5 \times 10^{23}/cm^3$, one cannot assume that the plasma is in LTE. The following criterion is used to judge the existence of LTE:[2]

$$n_e > 7 \times 10^8 \frac{Z^7}{(n)^{17/2}} \left(\frac{kTe}{Z^2 E_H}\right)^{1/2} cm^{-3} . \qquad \text{(IV-1)}$$

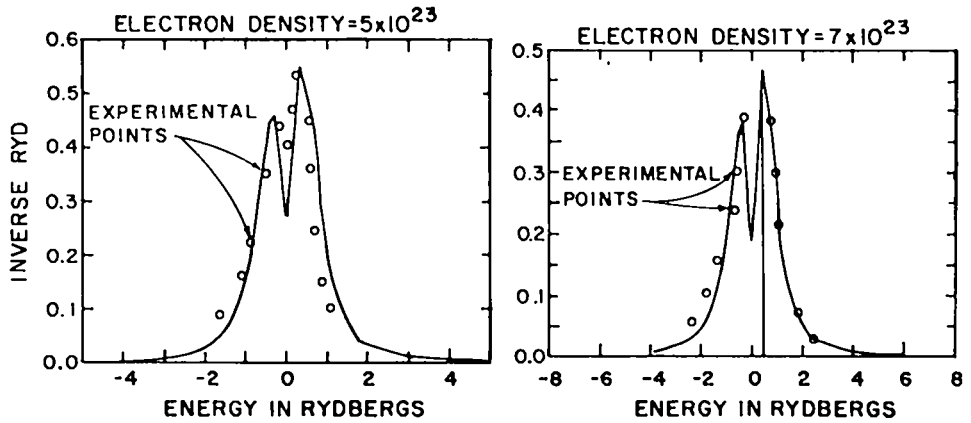

Fig. IV-3.
Experimental and theoretical line profiles for the argon ($1s^2$-$1s3p$) line at two different densities, from Sirius-B targets coated with 35 μm of plastic and irradiated with 4900 J of 10.6-μm laser light.

TABLE IV-I

COMPARISON OF EXPERIMENT AND SIMULATIONS USING SIRIUS-B TARGETS[a,b]

	Total Compressed Density (g/cm^3)	Electron Density	Average Compressed Electron Temp (eV)	Neutron Yield
Simulation	1.5	4.5×10^{23}	680	8×10^7
Experiment	1.7	6.5×10^{23}	620	6×10^7

[a]Target: GMB—230 μm in diam, 30-μm CH_2 coating, 30 atm DT, and 0.4 atm Ar.
[b]Laser: 4.9 kJ, 950 ps FWHM.

This formula states that for n_e greater than the quantity on the right, a level with principal quantum number n is in LTE with all higher levels. In our specific analysis,

for $n = 3$, $n_e > 1.2 \times 10^{23}$;

and

for $n = 2$, $n_e > 4 \times 10^{24}$.

For $n = 3$, the assumption of LTE is good, but for $n = 2$, it is doubtful. However, the very large absorption of the hydrogen-like and helium-like resonance lines may bring the $n = 2$ level much closer to LTE.

Because LTE does not always prevail, a rigorous analysis of optically thick lines (for example, Lyman α, $1s^2$-$1s2p$) requires a non-LTE transport model. We are constructing such a model, but some information can be obtained from a simpler approach. For example, a simple model can be used to fit the optically thick $1s^2$-$1s2p$ line, which introduces only a relatively small error because of non-LTE effects.

Many $1s^2$-$1s2p$ profiles show the characteristic flat-topped structure of very highly absorbed lines. We then normalize the theoretical profiles to this blackbody limit; that is, the profile is

$$P_T(\nu) = B(\nu)\left\{1 - \exp\left[\frac{p(\nu)}{P(o)}\tau_o\right]\right\} ,$$

where P(o) is the theoretical profile value at line center, and τ_o is the optical depth at line center. Figure IV-4 shows the fitting of experimental and theoretical profiles for the argon $1s^2$-$1s2p$ line. In calculating the optical depth at line center (τ_o), we have used the LTE value for ionic population even though it will introduce a small error. This analysis uses the information from optically thick lines to confirm the density measurements from optically thin lines.

Simulations were also performed with the LASNEX non-LTE rate-equation package. This routine treats the argon radiation with the average ion model. A plot given in Fig. IV-5 shows the average occupation of various shells obtained with the non-LTE rate equation and by assuming LTE. The most significant departures from LTE are near peak compression. We will study this behavior in more depth when the collisional radiative postprocessing code is available.

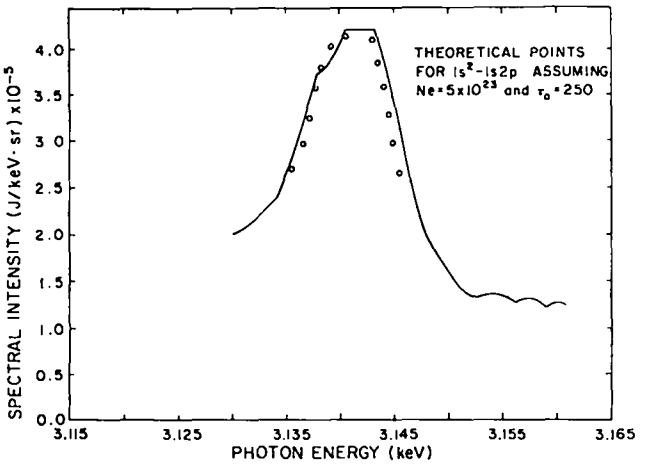

Fig. IV-4.
Experimental and theoretical profile for argon $1s^2$-1s2p line. Optical depth at τ_0 was calculated by using the LTE value for ionic population.

Soft X-Ray Spectroscopy on Gold Microballoon Targets Irradiated with 10-μm Laser Light (K. Mitchell)

We have obtained soft x-ray spectra over the range of 40 to 600 Å (300 eV) from laser-irradiated gold microballoon targets with a 1-m grazing-incidence spectrograph. We used a 25-μm-wide horizontal slit to obtain space-resolved spectra. The spectrograph geometry permitted a twofold spacial magnification of the source on film.

Figure IV-6 shows a spectrum from a laser-irradiated (5254 J) gold microballoon, the first spectrum ever obtained in the region of maximum x-ray emission at laser power levels exceeding 0.1 TW. The spectrum is primarily continuum radiation with some unresolved lines of multielectron spectra superimposed. The line radiation becomes more prominent and the continuum radiation less intense at lower laser power levels. The apparent peak occurs at a photon energy of 210 eV; when corrections are made for radiometric calibrations and carbon absorption in the film, the true peak may occur at slightly higher photon energies.

The diameter of the emitting source (710 μm) was determined from spacial scans of the gold spectrum. The initial diameter of the gold microballoon was 255 μm. In contrast, the diameter of the emitting source from a GMB target was equal to the initial target diameter. If the spacial image is a reflection of the temporal x-ray emission, then x-ray emission can last longer than the laser pulse, and a large fraction of the x-ray emission from a gold target may be recombination radiation.

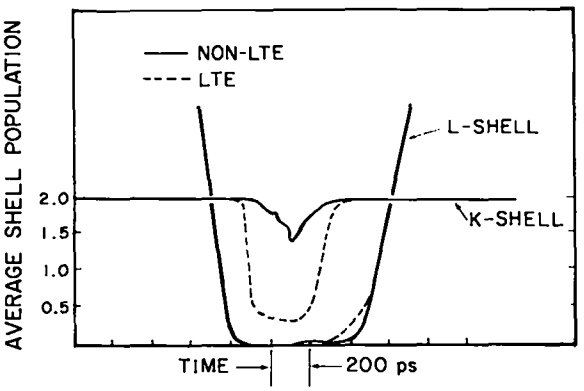

Fig. IV-5.
Average occupation of various electron shells obtained with LASNEX non-LTE rate equation and also assuming LTE.

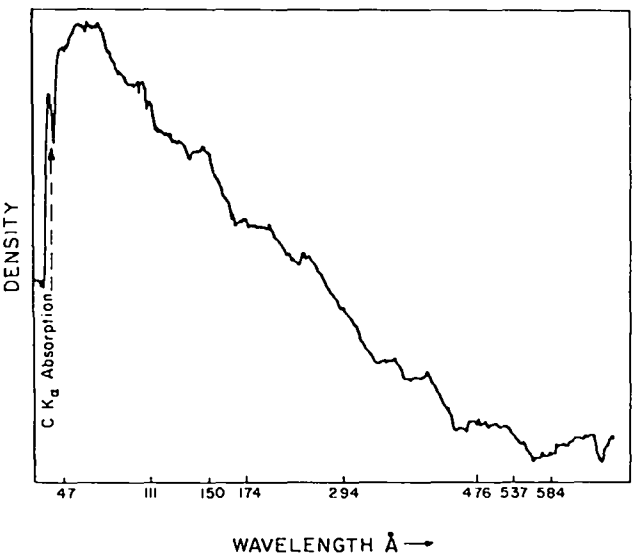

Fig. IV-6.
Spectrum from a gold microballoon 255 μm in diameter, illuminated by 5254 J of 10.6-μm laser light.

X-Ray Emission from Gold Microballoons (P. D. Rockett, W. C. Priedhorsky, D. V. Giovanielli)

The radiation emitted from a hot laser plasma is a key indicator of the atomic processes involved in laser-matter interaction.[3-5] Both the spectral shape of the radiation and the fraction of incident energy appearing as emitted radiation provide clues to the mechanism of optical absorption and the atomic state of the multiply ionized plasma.[2] At sufficiently high laser intensities ($>10^{13}$ W/cm^2), most laser-plasma radiation appears in the

range 10 eV < E < 1 keV, where E is photon energy in the soft x-ray regime. Its spectrum may consist of individual lines, bremsstrahlung, blackbody radiation, or a mix of these. Because the hot-electron temperature T_H probably increases with laser intensity I to the one-third power, the radiated spectrum and energy may well vary with I also, although not necessarily in the same fashion.[5] The level of ionization in the bulk of the material and the particular population of states will be significantly affected by T_H and n_H, the hot-electron density.

We present results of an investigation of the radiation emitted from gold-coated microballoons symmetrically illuminated by Helios operating at 10.6 μm. The laser intensity was varied from 9×10^{13} to 4.5×10^{13} W/cm^2, determined by measuring the fastest ion velocity (a function of laser intensity). Laser spot size was not readily available on all eight beams for each shot, and a measurement of ion velocity accounted for any hot spots within the focused areas. Beams were defocused to provide broad (~200-μm diam) spots of nearly uniform intensity (variation of a factor of 2 or less). The targets were nickel microballoons 1 μm thick and 300 μm in diameter, coated with 8 μm of gold (Fig. IV-7). Spherical symmetry and uniform illumination permitted comparison with radiated yields predicted by hydrodynamic code calculations. These experiments revealed a decreasing fractional radiated yield with increasing laser intensity. The radiation appeared to be blackbody with a slowly increasing color temperature as laser intensity was increased.

The emitted radiation from gold targets was monitored by absolutely calibrated, filtered XRDs. The absolute response of the aluminum photocathode was determined from synchrotron and Henke-tube calibrations covering the range from 20 eV to 10 keV. Filter transmissions were based on tabulated data, on weight, and on x-ray line transmission measurements of filter thickness. Five channels were used, each characterized by a unique spectral response function (Figs. IV-8 through IV-10). Four channels had a slow response time of 3 ns; one channel could resolve a 300-ps risetime when the transmission line response was accounted for. By using the spectral reduction code VARYSP3, we fit time-integrated charge data from each XRD channel to a particular spectral shape. The integral of this spectrum provided a conservative estimate of the total energy radiated.

XRD data were fitted to both a blackbody and a bremsstrahlung spectrum. Reliable results (in the χ^2 sense) were obtained only with the blackbody fits. Temperature was computed as a part of the fitting routine, and total energy radiated was calculated by σT^4.

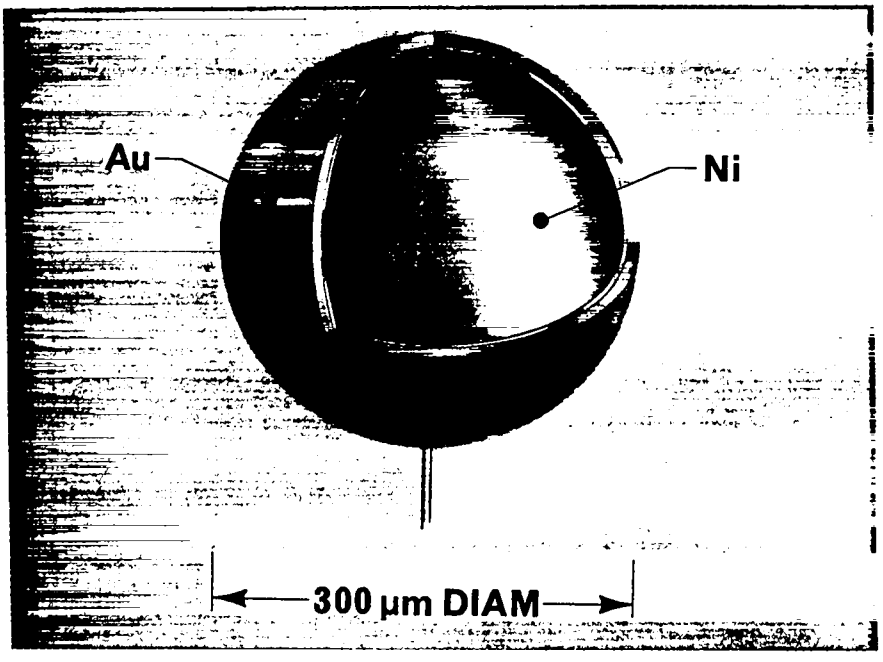

Fig. IV-7.
Nickel microballoon 1 μm thick and 300 μm in diameter, coated with 8 μm of gold.

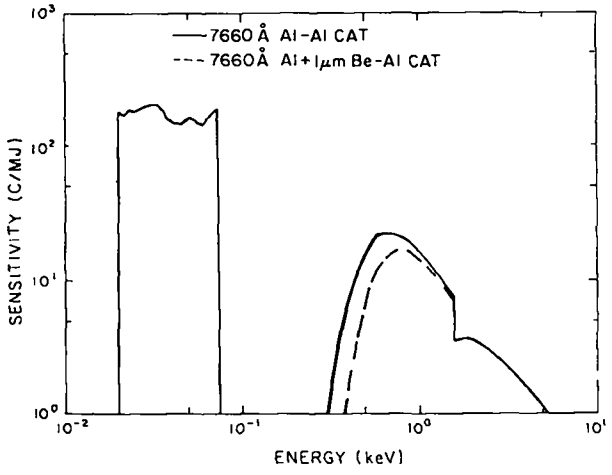

Fig. IV-8.
Spectral response of two filtered XRDs to radiation from gold targets. One filter was 7660-Å aluminum; the other was 7600-Å aluminum plus 1 μm beryllium.

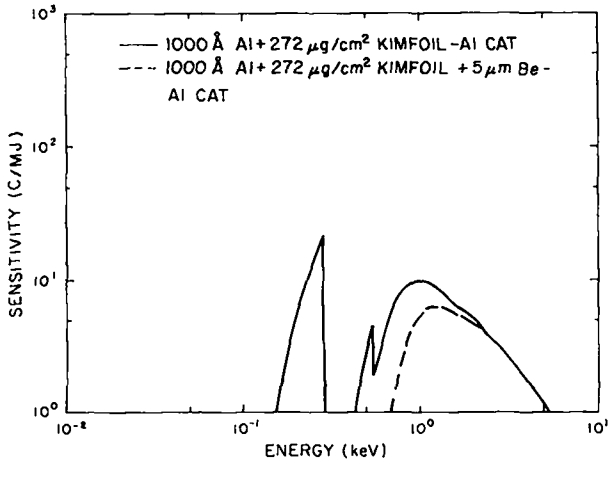

Fig. IV-9.
Spectral response of two filtered XRDs to radiation from gold targets. One filter was 1000-Å aluminum and 272-μg/cm² Kimfoil; the other used the same filter combination plus 5 μm beryllium.

The major error contribution was derived from the breadth of the χ^2 minimum, resulting in errors of ±30% in total radiated energy.

The x-ray pulse at ~280 eV rose from 10 to 90% slightly more slowly (longer by 10%) than the laser pulse; however, the half-width of the x-ray pulse was 20 to 30% wider than that of the laser.

Laser intensity was determined first by estimating spot size and measuring laser energy and then by measuring the fastest ion velocity, calculating a hot-electron temperature T_H, and evaluating the intensity from an empirical model. Intensities derived from both methods coincide below ~8×10^{15} W/cm², but a noticeable divergence appears above this intensity. Beyond 8×10^{15} W/cm², the latter method yields intensities about two times higher at 10^{16} W/cm² and two-three times higher at 10^{17} W/cm². Therefore, plots of functions vs intensity vary in slope by a small amount, depending upon whether one uses geometrical intensity or a fast-ion derived intensity. The plots in this section were made by using the fast-ion intensity, because it is derived from a readily measurable parameter.

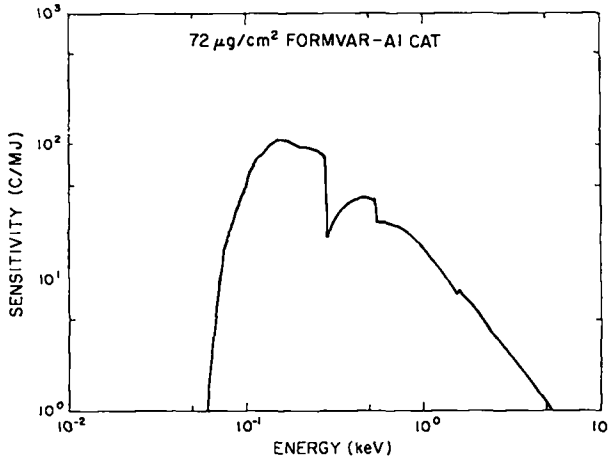

Fig. IV-10.
Spectral response of filtered XRD to radiation from gold target. Filter was 72-μg/cm² Formvar.

Blackbody temperatures were derived from data such as those presented in Fig. IV-11. The complete set of color temperature data is presented in Fig. IV-12 as a function of incident laser intensity. A clearly monotonic scaling varies as $I^{0.13}$. The fraction of incident energy radiated, obtained by integrating the energy under the spectral curve and dividing by the laser energy, is shown in Fig. IV-13 as a function of incident laser intensity. In spite of the ±30% error bars, the circles representing Los Alamos data decline monotonically as $I^{-0.3}$. Published data points from Lawrence Livermore National Laboratory (LLNL),[3,4] taken at an incident wavelength of 1.06 μm on gold disks, are plotted on the same graph. Note that the glass data fall within the error range of the CO_2 data, although glass data are insufficient for a thorough statistical comparison. The scaling of emitted x-ray radiation with laser intensity appears to be wavelength independent, and the absolute fraction of incident laser radiation emitted as x rays differs little between $\lambda = 1.06$ μm and $\lambda = 10.6$ μm.

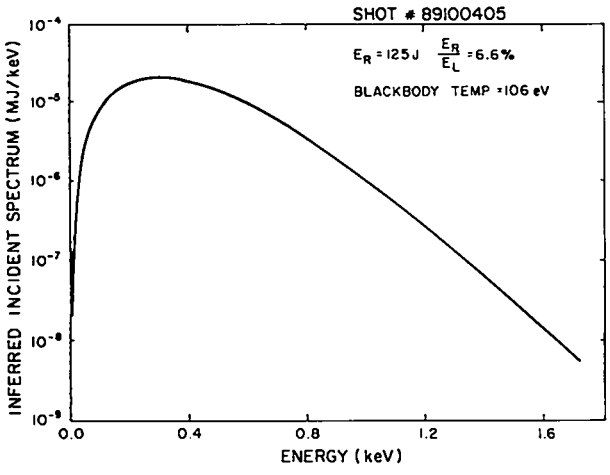

Fig. IV-11.
Best-fit blackbody spectrum deconvolved from broadband XRD self-emission data from an irradiated gold microballoon (E_{Laser} = 1.89 kJ).

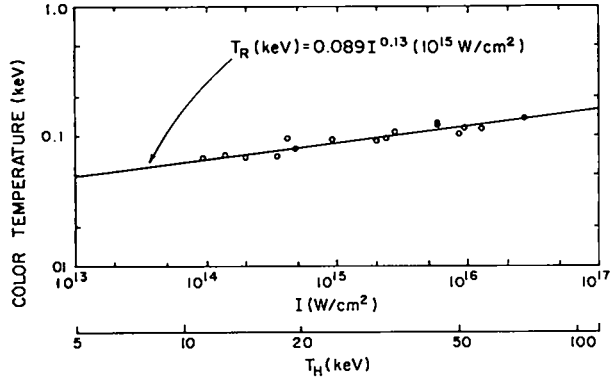

Fig. IV-12.
Color temperature data from XRDs as a function of incident intensity and T_H.

One expects T_H to increase as $I^{1/3}$ as the laser intensity I is increased.[5] This scaling implies a greater electron range and energy deposition at greater target depths. Radiation generated deep within the target cannot escape, so a lower fraction of the incident laser energy is seen as emitted radiation. Thus, a decreased emission fraction is expected in any target.

Lateral Transport of Energy from a Laser-Produced Plasma (W. Ehler, F. Begay, T. H. Tan, P. H. Castine)

One beam of Gemini was focused with an irradiance of 2×10^{15} W/cm^2 in a 1-ns pulse, close to the center of

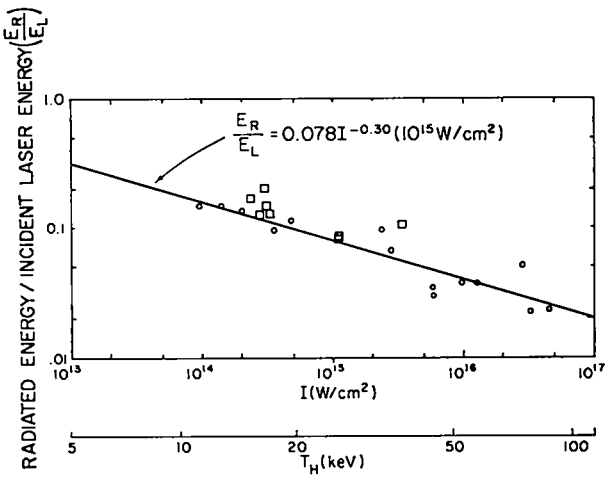

Fig. IV-13.
Fraction of incident laser energy radiated from gold microballoon targets as a function of laser intensity and T_H. Circles correspond to Los Alamos data at 10.6 μm. Squares correspond to published LLNL data at 1.06 μm.

and perpendicular to a 1-cm-long wire target. Wires of different elements and diameters were used. Fast ions from the plasma produced at the front side were measured with a charge collector, a Thomson ion spectrograph,[6] and a photomultiplier-scintillator (crab-eye) ion detector[7] located nearly perpendicular to the laser-irradiated spot. Another crab-eye and a charge collector, installed on the opposite side, measured fast ions emitted from the back surface of the target. Three additional charge collectors were spaced at various angles between the front- and back-viewing detectors.

The targets of pure carbon, titanium, or tantalum wire 250 μm in diameter were maintained at 1773 K before and during laser irradiation to remove surface impurities. Similar targets were then irradiated while at room temperature.[8] Fast protons were observed in the ion spectrograms for the cold targets, and fast ions were recorded on the backside detectors. Cold copper wire targets of various diameters were used to determine the maximum diameter for which fast ions were detected on the backside.

These experiments disclosed the following information regarding lateral energy transport.

- Fast ions are highly bunched in the direction of the target normal.[9] Accordingly, the fast ions observed on the backside of a wire must have been isothermally expanded from a plasma that existed on the back during the laser pulse.

- Hot electrons with energies less than 130, 300, and 600 keV are stopped by 150 μm of carbon, titanium, and tantalum, respectively. Consequently, energy was transported from the focal spot around to the backside of the wire during the laser pulse.[10]
- We assumed that the ions were isothermally expanded and estimated the hot-electron temperature gradient around the wire surface from the speed of the fastest ions observed on the front and the back of the 250-μm-diam target. The frontside hot-electron temperature was 29 keV, and the ratio of the front-to-back hot-electron temperature was 2:1. This ratio gave a value for the gradient of 5×10^5 eV cm^{-1}.
- The transport speed of energy around the surface of the wire was estimated from the distance traveled during the laser pulse (pulse length, 1 ns). The transport speed v obtained was $1.5 \times 10^8 < v < 2.5 \times 10^8$ cm/s^{-1}.
- If the laser plasma contained protons, as all the targets at room temperature did, the energy was transported to the backside of a wire with diameter >1000 μm [transport distance $\simeq 1/2\pi \times$ (wire diameter/laser focal diameter)]. However, for the carbon target at 1773 K, the laser plasma was composed of only carbon ions (average ionization state of 3 to 4), and energy was not transported around a wire 150 μm in diameter. Consequently, an energy-transport mechanism that has a dependence on charge state and/or atomic weight must account for this ratio of 5 or more for the transport speed or distance.
- The five charge collectors, placed around the chamber perpendicular to the length of the 250-μm-diam cold wires, provided an estimate that 7% of the total fast-ion energy is ejected from the backside. The estimate was obtained from the measured fast-ion distribution around the wire compared to that of a flat target and from the front to back ratio of the total fast energy.

Future experiments will include visible-light streak pictures of the energy-transport motion for heated wires of various atomic weights to obtain the relationship of atomic weight and/or ionic charge of the laser plasma to the energy-transport speed.

K_α Measurements in Single-Beam CO_2 Target Experiments (D. B. van Hulsteyn, G. H. McCall, S. Whitchill)

An experiment to measure K_α production from titanium targets was carried out at Gemini. A large-aperture (337-μm) pinhole camera was installed and the image was filtered with 25-μm-thick foil of titanium because a material is relatively transparent to its own K_α radiation. The transmission of the filter is plotted in Fig. IV-14.

The experimental layout (Fig. IV-15) shows the location of the camera relative to the target, the target wheel, and the incident beam. In all cases of interest, the 25-μm-thick foils were 2-mm squares mounted on glass stalks. This relatively large area was used to limit the effect of plasma glow radiating around the edges. The camera was installed at the backside of the target to ensure that we were observing K_α radiation.

For most shots, we used uncoated titanium targets. An image from a 200-J shot is shown in Fig. IV-16. A measurement of the diameter of the central spot indicates that the aperture is being exposed to radiation from a small source. Independent measurements show that the diameter of the K_α radiating region is ~100 μm, less than one-third the diameter of the aperture. As a result, the number of radiating K_α photons N_1 is related to the flux I_1 hitting the film by the expression,

$$N_1 = 4\pi (p + q)^2 I_1 ,$$

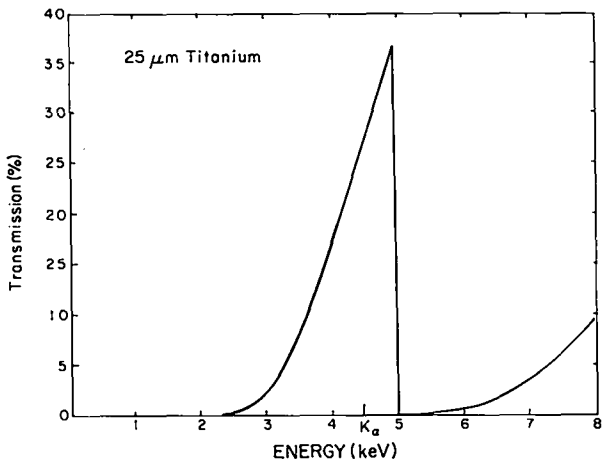

Fig. IV-14.
K_α transmission from a titanium target filtered through a titanium foil and recorded by a large-aperture pinhole camera.

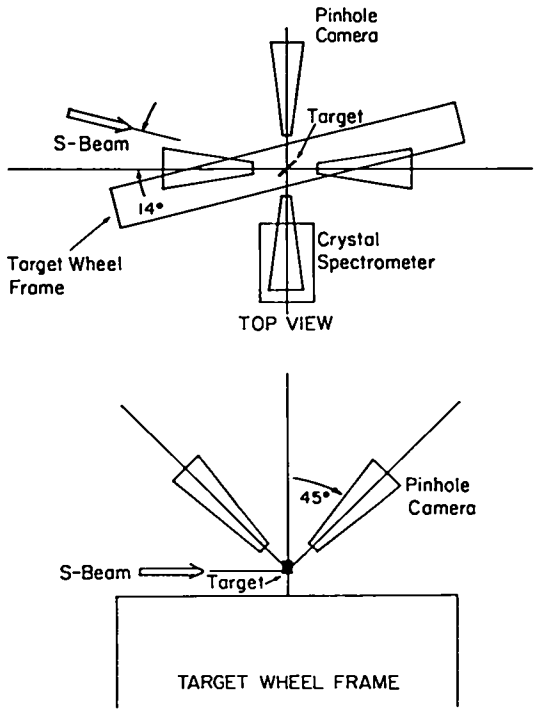

Fig. IV-15.
Experimental layout for measuring K_α production from titanium targets.

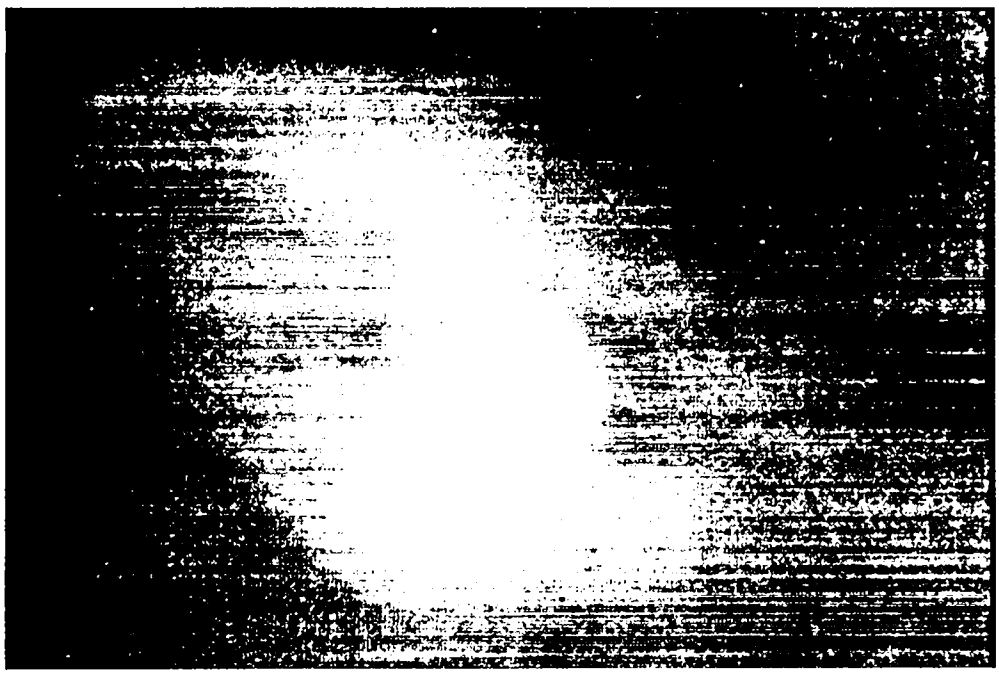

Fig. IV-16.
Image of an uncoated titanium target illuminated with 200 J of 10.6-μm laser light.

where p + q is the target-to-film distance. The value for I_1 is obtained from the x-ray film calibration for titanium K_α lines (4.5 keV) attenuated by the target and the aperture filter. From the central spot in Fig. IV-16, we obtained a yield $N_1 \simeq 5 \times 10^{12}$ photons for 200 J of incident laser energy. This yield agrees with data obtained from a Ge(III) crystal spectrograph.

Figure IV-17 is an image of the front face of a titanium target coated with 30 μm of plastic, taken at the same laser parameters and target orientations. The reduced intensity is due to absorption of the hot electrons by the plastic, which reduces the K_α production. The image from a 50-μm-thick coated target is shown in Fig. IV-18 for comparison; in Fig. IV-18, the intensity in the center is reduced essentially to the background level.

It is significant that a 30-μm plastic coating leads to a tenfold reduction in K_α production. Using a temperature T = 12 keV (obtained from ion measurement), a rudimentary analysis indicates that the hot-electron spectrum may be approximated by a one-dimensional Maxwellian distribution.

Note, finally, the flag-shaped region in Figs. IV-16 through IV-18, which is an image of the 2-mm-square target. This is a true image because the radiating area is much larger than the aperture. The relation between intensity I_2 and number N_2 is given by

$$N_2 \simeq 4\,A \left(\frac{q}{a}\right)^2 I_2 ,$$

where A is the area of the target, a the radius of the aperture, and q the aperture-to-film distance. Again, we find $N_2 \simeq 10^{12}$-10^{13} photons; however, these photons are radiating from a large area so that the image appears much weaker. This radiation is not yet understood. Two possible explanations are wing energy in the laser and hot-electron lateral transport. Future modeling and experiments should resolve this question.

MILITARY APPLICATIONS (J. H. McNally)

Introduction (A. G. Engelhardt, R. H. Robertson, and I. V. Johnson)

Our Nd:glass laser system was used for experiments related to fast streak-camera development, equation-of-state studies, and plasma-opacity determinations.

Our typical firing mode was to use one beam to deliver a pulse of 25 J of laser energy to the target area in 300 ps. We fired 85 shots for opacity experiments and 325 for equation-of-state studies. We used 19 two-beam

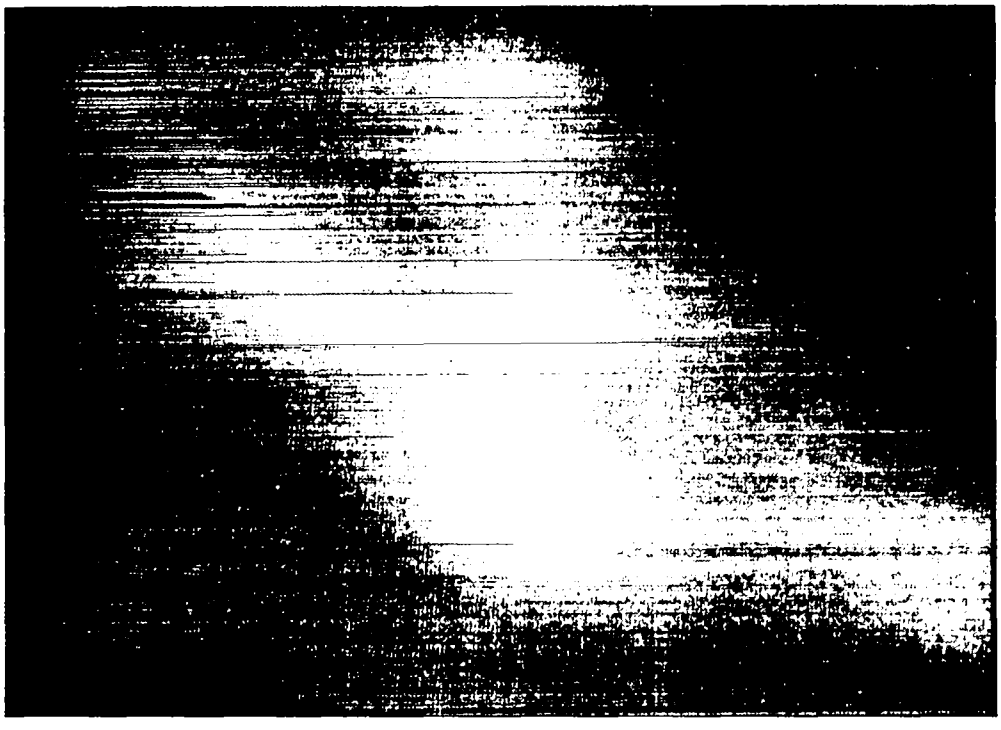

Fig. IV-17.
Image obtained with same target and laser parameters as in Fig. IV-16 but with 30-μm plastic coating on front face of target.

Fig. IV-18.
Same target and laser as in Fig. IV-17 but with 50-μm plastic coating on front face of target.

shots for streak-camera development. The maximum number of shots on any single day was 20, all of which were equation-of-state shots.

For the equation-of-state studies, a portion of the early part of the pulse was split off, amplified, converted into green light, directed onto the streak-camera film through a glass fiber, and used as a fiducial mark for laser operation. This frequency conversion was necessary because of the insensitivity of the film to 1.06-μm light.

Shock Wave and Equation-of-State Studies (L. Veeser, A. Lieber, D. Eckhart, P-3; J. Solem, P-DO)

In earlier studies of shock velocities in impedance-match targets, that is, in foils consisting of adjacent aluminum and gold layers on an aluminum substrate, we had been unable to demonstrate the reliability of our recording techniques. However, during this reporting period, we found that the gold shock velocities were too high to be consistent with the aluminum measurements. We attributed the discrepancy not to an error in the equations of state, but instead to hot electrons penetrating the aluminum substrate and being stopped by the gold layer, heating it, and adding some energy to the gold. To reduce this effect, we prepared targets with a thin gold layer sandwiched between two aluminum layers.

In our initial efforts, we used 1 μm of gold, which reduced the shock velocity discrepancy to about 10%. We then doubled the gold layer and further reduced the discrepancy to 5%.

Our accuracy is limited to 5 to 10% by difficulties in both the shock breakout measurement and the shock generation. We can improve the diagnostics considerably by further characterizing the target foils and by increasing the recording speed of the streak camera. Both possibilities are being investigated. Improving the uniformity of the laser focal spot to generate more uniform shocks is more difficult. We expect to move our project to Gemini soon.

Opacity Studies (N. M. Hoffman, L. W. Miller, J. M. Mack)

Experimental Studies. The last experimental session in our opacity studies program was held in August 1979 to verify the results described earlier. [11] We determined that both the beam quality and the intensity of the glass laser we were using were not adequate for a continuation of the experiment. Therefore, we will redesign this experiment so that it can be continued and extended into the soft x-ray region on Gemini.

Error Analysis. We have begun to assess the accuracy of information that can be reasonably expected from limb-darkening opacity experiments. Accuracy will be limited by both systematic and random errors, which we examined in turn.

The starting point of our study was a set of simulated limb-darkening data generated from a numerical calculation of a laser-heated plasma. The integral equation relating this limb-darkening function to the radiation source function in the plasma was solved by fitting it to a model functional form. We continued our data analysis by solving the source function (assumed to be Planckian) for temperature and concluded by comparing slopes of the optical-depth-vs-temperature function at two or more photon energies to produce information about the ratio of opacity at those photon energies. At each step of the analysis, results inferred from the limb-darkening data (for example, source functions, temperature functions, and finally, opacity ratios) were compared with the values obtained in the original numerical calculation of the plasma. In this way, we judged the magnitude of the systematic errors.

Random error in the opacity ratio was investigated with Monte Carlo simulations to create and analyze large numbers of noisy data sets. In this way, random error in the opacity ratio can be related to random error in the initial data.

Figure IV-19 shows results for three photon energy groups, labeled 7, 8, and 9, which correspond to photon energies of 200, 316, and 501 eV, respectively. The target was an aluminum foil 12.7 μm thick. The simulated data were taken 1.49 ns after the beginning of the 500-J laser pulse. The plot shows opacity ratio vs temperature in the plasma. Solid lines show the calculated opacity ratios used in the code calculation. Dashed lines show the opacity ratios inferred from the simulated data. The deviation of the dashed lines from the solid lines is a measure of systematic error. The error bars show random error arising from an assumed 2% error in relative intensity measurements and 5% error in absolute intensity measurements.

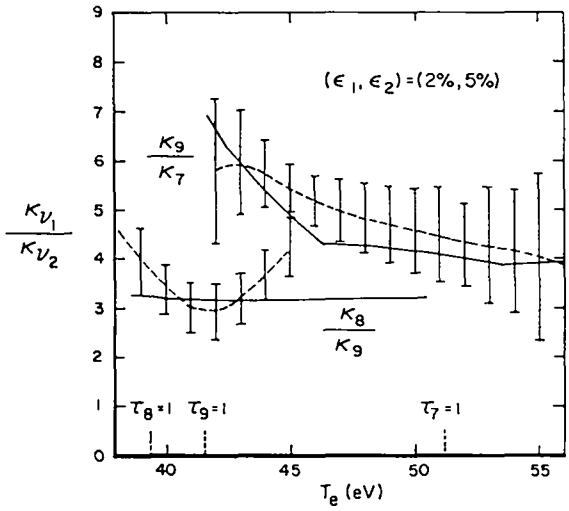

Fig. IV-19.
Opacity ratios vs plasma temperature for photon energies of 200 (K_7), 316 (K_8), and 501 (K_9) eV. Solid lines are ratios used in the code. Dashed lines are ratios inferred from simulated data. Deviation of dashed lines from solid lines is a measure of systematic error.

REFERENCES

1. W. A. Lokke and W. H. Grasberger, Lawrence Livermore National Laboratory report UCRL 52276 (June 6, 1977).

2. H. R. Griem, *Plasma Spectroscopy* (McGraw-Hill, New York, 1964).

3. H. Kornblum and V. Slivinsky, "Laser Program Annual Report-1977," Lawrence Livermore National Laboratory report UCRL 50021-77, C. Bender, Ed., Vol. 1, Sec. 3, 64-68 (July 1978).

4. M. D. Rosen, D. W. Phillion, V. C. Rupert, W. C. Mead, W. L. Kruer, J. J. Thomson, H. N. Kornblum, V. W. Slivinsky, G. J. Caporaso, M. J. Boyle, and K. G. Tirsell, Phys. Fluids 22, 2020 (1979).

5. D. Forslund, J. Kindel, and K. Lee, Phys. Rev. Lett. 39, 284 (1977).

6. F. Young and G. McCall, Bull. Am. Phys. Soc. 22, 1129 (1977).

7. T. H. Tan, A. H. Williams, and G. McCall, "A Thin-Film Detector System for Laser-Fusion Studies," Nucl. Instrum. Methods 131, 425 (1975).

8. A. W. Ehler, F. Begay, T. H. Tan, J. Hayden, and J. McLeod, "Lateral Transport of Energy from a Laser-Produced Plasma," J. Phys. D: Appl. Phys. 13, 65-66 (1980).

9. A. W. Ehler, J. Appl. Phys. 46, 2464 (1975).

10. R. J. Trainor, N. C. Holmes, and R. M. More, Bull. Am. Phys. Soc. 24, 972 (1979).

11. L. W. Miller, H. W. Kruse, P. J. Kruse, D. E. Bartram, N. M. Hoffman, and J. M. Mack, "Design and Operation of a Time-Gated Optical System for Measuring the Angular Distribution of Light Emitted from Laser Targets," Proc. of Los Alamos Conf. on Optics 1979.

V. TARGET DESIGN AND FUSION THEORY
(D. B. Henderson)

Our theoretical support activities are closely coupled to our experimental efforts, with the intent of gaining a fundamental understanding of laser-target interactions, particularly of relevant plasma physics and hydrodynamics. The close coupling of theory and experiment has made it possible to eliminate faulty theories and to design advanced targets for CO_2 laser drivers more reliably. In general, basic studies have shown that the design difficulties associated with long wavelengths are not significantly worse than those at much shorter wavelengths and that breakeven target designs are attainable even in the presence of a hot-electron spectrum. These results have significantly increased our confidence that scientific breakeven can be demonstrated with CO_2 lasers in the megajoule range.

INTRODUCTION

We have continued research in key areas basic to the understanding of inertial fusion target performance and have shown that an inherent randomness exists in the resonance absorption process, which produces a Maxwellian distribution of hot electrons. This distribution is important because it allows us to calculate the preheat on a target with much greater confidence. Calculations performed with our target design code revealed that the motion of the critical surface is an important sign of the overall hydrodynamic performance of a target. We have, therefore, studied the processes introducing overdense bumps in the electron density profile that alter the motion of the critical density and thus change the location and amount of laser light absorption. Much effort went into target design. We have investigated a single-shell design driven by a few megajoules of heavy ions. R-T instability of an imploding target remains a major concern for reactor-scale targets. We have continued the investigation of this instability both analytically, including compressible-fluid effects, and numerically with a PIC hydrodynamic code, which is continuing to be improved and is capable of handling strongly turbulent hydrodynamic flows.

FUSION THEORY (D. Forslund)

Randomness, Maxwellian Distribution, and Resonance Absorption (B. Bezzerides, S.Gitomer, D. Forslund)

Particle simulations of resonant absorption have shown that for a wide range of conditions, the distribution of heated electrons may be identified by a low-density, high-energy Maxwellian with a temperature T_{hot}. We have identified the microscopic processes responsible for the heating and the composition of the time-averaged distribution resulting in the observed Maxwellian. In particular, although one might assume that the heating fields are periodic in time because the driver is strictly periodic, we find that the fields have small-amplitude aperiodic content, which ultimately leads to the observed Maxwellian shape.

Figure V-1 shows a time-averaged distribution resulting from a simulation in which particles move in the field

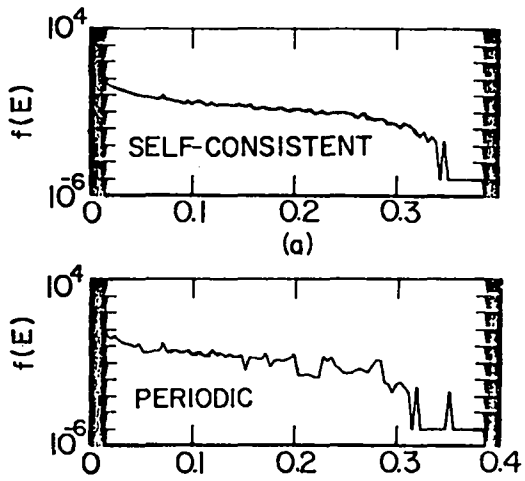

Fig. V-1.
Time-averaged distribution functions f(E) vs E for (a) a self-consistent simulation and (b) a periodic test-particle calculation.

of a self-consistent simulation showing the usual Maxwellian heated tail. The figure also shows a result in which the field

$$P[E(x,t)] = \sum_{n=o}^{N} \frac{E(x,t - 2\pi n/\omega o)}{N+1}$$

is used. This field is a periodic projection of the full field, and the resulting heated distribution exhibits order-of-magnitude deviations from the Maxwellian, although the number of simulation particles remains the same. In general, without the aperiodic content to the field, the *detailed Maxwellian feature is lost* and it is no longer appropriate to define T_{hot}.

Snapshots of phase space show the quasi-periodic nature of the heating. Figure V-2(a) records the velocity vs time for heated particles as they stream in and out of a fixed spacial region localized about the large-amplitude field. As we expected, the acceleration of particles *within a given cycle* is consistent with the model of resonant acceleration in a coherent field. However, from cycle to cycle the heating looks almost random.

Figure V-2(b) plots the average energy per particle within the monitored region as a function of time. The displays of Fig. V-2 illustrate the almost random character of the heating process even for this energy moment. We performed a similar analysis for the case of periodic applied fields (a test-particle calculation). The anticipated result, namely, that each cycle is completely equivalent, is obscured because there were too few simulation particles. To determine how the results for the periodic and aperiodic cases differ, we performed a statistical analysis of the average energy maxima for the cases in which the number N of simulation particles was varied. Figure V-3(a) plots a histogram of average energy maxima for a self-consistent simulation. The standard deviation σ for a number of such aperiodic and periodic runs is plotted in Fig. V-3(b) vs N. The periodic runs show a $1/N^{1/2}$ statistical dependence, a mark or sign of numerical rather than physical effects. However, the self-consistent simulations (aperiodic) show σ independent of N for $N \geq 40\,000$, suggesting that the randomness of the maximum average energy per heated particle is of dynamic origin. The mean average energy per particle ε agrees with that obtained by assuming a Maxwellian tail, $\varepsilon = T_{hot}[1 + 2b \exp(-b^2)/\pi^{1/2}\mathrm{ERFC}(b)]$, where $b = (v_{min}/c)/(2T_{hot})^{1/2}$ and T_{hot} in units of mc^2 is the measured temperature of a self-consistent simulation.

We obtained additional information on cycle-to-cycle randomness by a different test-particle scheme in which

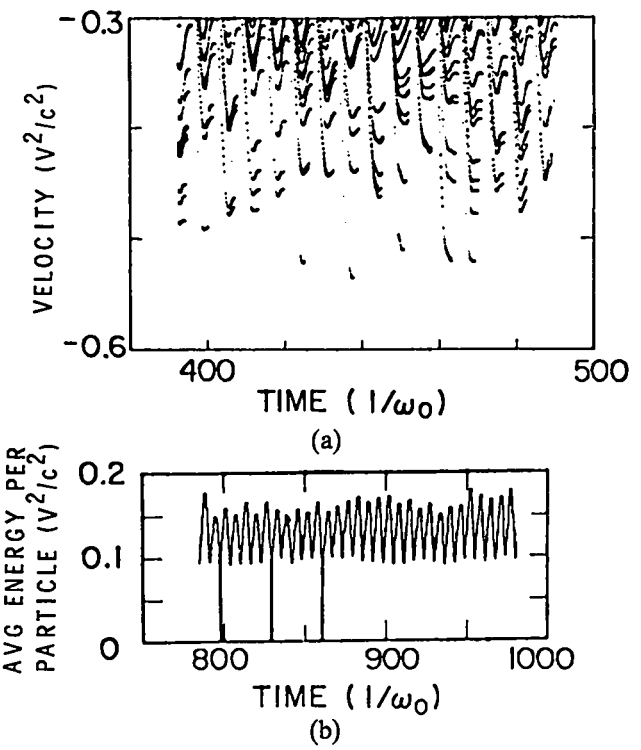

Fig. V-2.
Monitored region of Mach space. (a) Velocity vs time for particles in phase-space region with position $14.25 \leq x\omega_o/c \leq 16.75$ and velocity $-0.6 \leq v/c \leq -0.3$. (b) Average energy per particle in phase-space region above vs time.

particles are injected into the computational box by a spacially uniform beam with a definite beam velocity. After passing through the heating region, particles are collected at a spacial point near enough to the heating region to avoid collection of hot particles originating from a prior laser heating cycle. Thus, we can construct a distribution of hot particles for a given beam velocity created during a given heating cycle.

Figure V-4 shows (a) the distribution of hot particles for 3 different cycles and (b) the time-averaged distribution for 30 cycles of the simulation electric field with a beam velocity set at $v_{beam}/c = 0.08$. The figure shows clearly that the time-averaged distribution (in this case a Maxwellian with a tail temperature equal to the simulation T_{hot}) is obtained by averaging all the single-particle distributions that fluctuate in an almost random fashion. The results for other beam velocities show the same general features. The time-averaged distribution of the simulation is obtained by averaging the result of all the beams, each weighted by the initial Maxwellian. This analysis strongly confirms our speculation that the

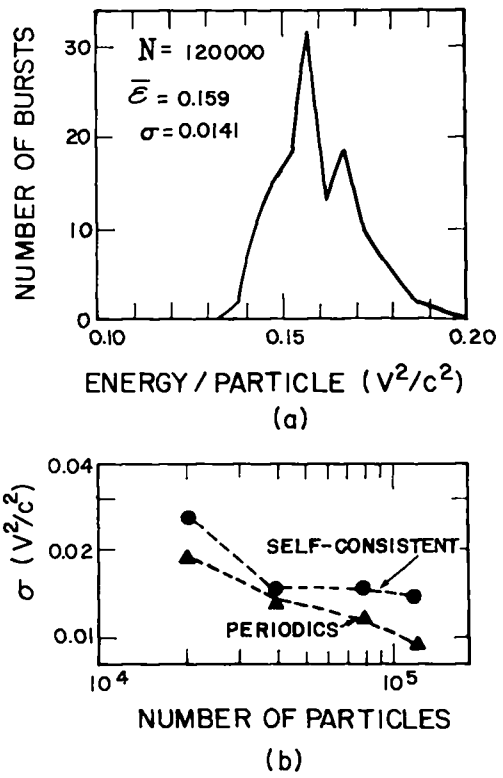

Fig. V-3.
Statistical analysis of monitored region. (a) Pulse height analysis of Fig. V-3(b) data. Number of pulses vs pulse height. (b) Standard deviation of data from (a) vs number of simulation particles for self-consistent simulations and periodic test-particle calculations.

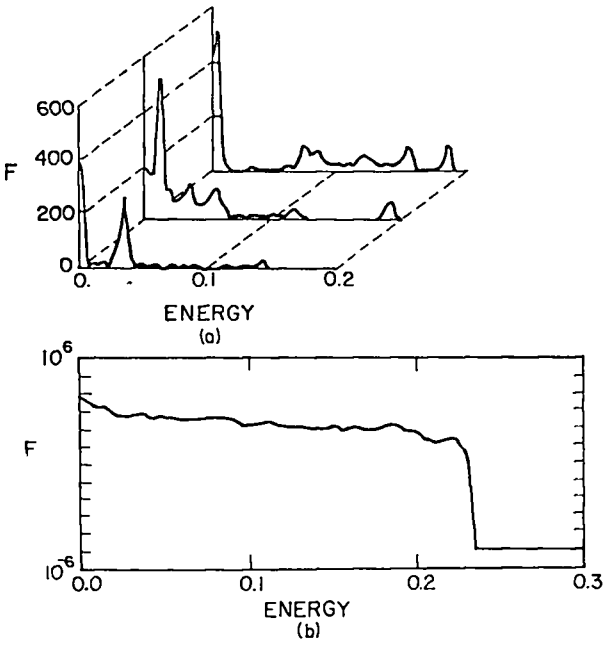

Fig. V-4.
Hot-electron distributions caused by an injected beam with velocity v/c = 0.08. (a) Distributions for 3 different heating cycles and (b) time-averaged distribution for 30 heating cycles.

Maxwellian character of the hot-electron distribution, observed in self-consistent simulations of resonant absorption, is related directly to the random fluctuations in the distribution of hot particles produced cycle to cycle.

The random fluctuations in the hot-electron distribution function from cycle to cycle are caused by aperiodic or free-mode frequency components of the field. To understand how these excitations are self-consistently related to the production of hot electrons, we examine the fully nonlinear equation for the electrostatic field coupled to the capacitor field. The coupling to the particles is by the pressure P(x,t), which is in turn coupled to the heat flux Q(x,t) through

$$\left(\frac{\partial}{\partial t} + v\frac{\partial}{\partial x}\right)\left(\frac{P}{n^3}\right) = -\frac{1}{n^3}\frac{\partial Q}{\partial x}\ , \qquad \text{(V-1)}$$

where v(x,t) and n(x,t) are the local fluid velocity and density and P(x,t), $Q(x,t) = m\int dv[v - v(x,t)]^{2,3} f(x,v,t)$. The field equation was solved numerically; P was obtained from Eq. (V-1) with $\partial Q/\partial x = 0.0$, that is, in the adiabatic limit. As in the case of the simulations, the solutions showed excitations at the driving frequency and several higher harmonics. However, except for some initial transients, there was no free-mode response, the nonlinear convection having damped these modes out. The same result is obtained with a linear form of Q (Landau damping). Thus, the contribution to Q from the pulse-like production of hot electrons leads to a pressure P that ultimately acts as an additional source for the electrostatic field and an aperiodic source.

Laser-Stimulated Overdense Plasma Bumps (C. H. Aldrich, R. D. Jones, K. Lee)

Many recent experimental and theoretical investigations have examined density-profile steepening in laser-plasma interaction. We, specifically, have studied the formation of nonmonotonic supercritical density profiles, or overdense bumps, which can be formed in underdense as well as overdense plasmas. The former case has serious consequences for the transmission of laser light through the pellet corona. If the laser intensity or

wavelength is such that overdense bumps are created out of driven density fluctuations, then absorption and reflection will occur in a region far from the pellet core, resulting in the decoupling of the absorbed laser energy. Therefore, it is very important to understand these enhancements in the density profile. We are presenting here the results from one-dimensional modeling; the stability of the one-dimensional solution will later be studied through two-dimensional simulations.

Figure V-5 is a density profile obtained from interferometry data in an experiment performed at the National Research Council in Canada.[1] The laser is incident from the right. The profile shows a localized region of enhanced density just to the left of the critical density ($\sim 10^{19}$ cm^{-3}). These bumps have also been seen in computer simulations.

Figure V-6 is a hybrid code simulation of an overdense bump. The laser is incident from the right. The electrons are treated as a fluid that obeys an ideal gas equation of state, $p = nT$; the temperature is assumed constant in space and time; and the ions are treated as particles. The density N is given in units of the critical density; the distance R is given in units of inverse vacuum wave number. In this simulation, v_o/v_e, the ratio of the electron quiver speed to thermal speed is 0.71. As Fig. V-6 shows, a localized region of overdense plasma is created in an underdense plasma; in this case, it is caused by density fluctuations driven by Brillouin scattering. Sanmartin and Montanes[2] suggest that these bumps may form spontaneously in a laser-driven plasma in which the temperature is decreasing as a function of time.

The simple model illustrated in Fig. V-7 has provided detailed information about overdense bumps. We assumed that overdense structure is made up of two shocks, ion acoustic compression shock and a rarefaction shock created by laser light normally incident on the plasma. We also assumed that the ions were cold and the electrons were isothermal. The jump conditions for the rarefaction shock are well known.[3] The jump conditions

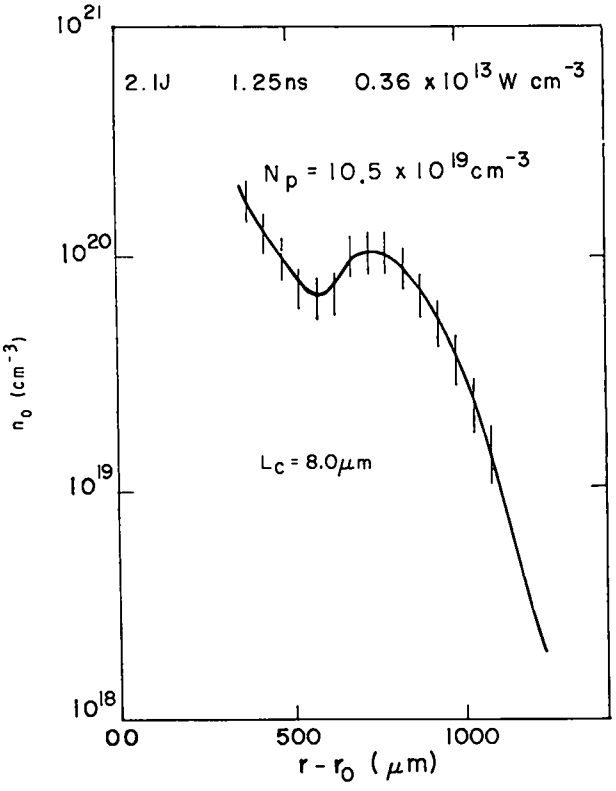

Fig. V-5.
Interferometric observation of an overdense bump. The pulse-length was 1.25 ns. The intensity was 0.36×10^{13} W/cm^2. Total energy was 2.1 J, and the density scale length was 8.0 μm.[1]

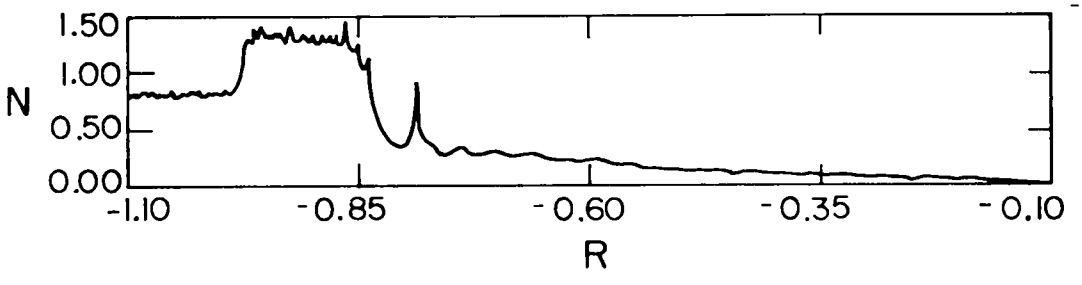

Fig. V-6.
Hybrid code simulation of an overdense bump. The laser is incident from the right. The density N is normalized to the critical density; R is normalized to the vacuum laser wavelength.

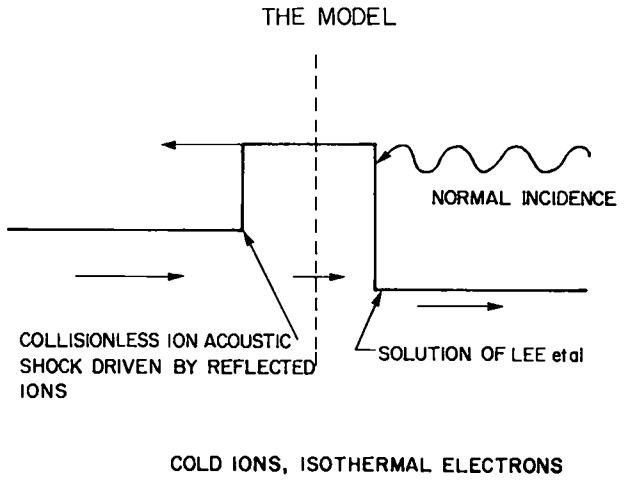

Fig. V-7.
An ion acoustic shock is fitted to the solution of Lee et al.[3]

TABLE V-1

INTERRELATIONSHIP OF PLASMA FLOW PARAMETERS

M_1	M_2	F	$\frac{\zeta_1(1+F)}{\zeta_2}$	log F
1.0	1.0	0	1.0	$-\infty$
1.1	0.9	0.0005	0.819	−3.30
1.2	0.8	0.0041	0.672	−2.39
1.3	0.67	0.022	0.539	−1.66
1.4	0.56	0.052	0.444	−1.28
1.5	0.35	0.194	0.345	−0.712
1.55	0.22	0.369	0.308	−0.433
1.58	0.08	0.701	0.287	−0.154
1.585	0	1.0	0.28	0

for the compression shock, in the compression-shock frame of reference, are

Mass: $\rho_1(1-F)U_1 = \rho_2 U_2$,

Momentum: $\rho_1(1-F)U_1^2 + 2\rho_1 F U_1^2 + (1+F)\rho_1 C_s^2 = \rho_2 U_2^2 + \rho_2 C_s^2$,

Energy: $\frac{1}{2}MU_1^2 + e\phi_1 = \frac{1}{2}MU_2^2 + e\phi_2$,

and

Infinitely Mobile Electrons: $0 = -C_s^2\frac{d\rho}{dx} + \frac{e}{m}\frac{d\rho}{dx}$.

The subscript 1 indicates upstream and the subscript 2 indicates downstream. F is the probability that an ion will be reflected from the shock surface; $\rho_1(1-F)$ is the mass density of transmitted ions; $2\rho_1 F$ is the density of reflected ions; $\rho_1(1+F)$ is the total mass density upstream of the shock; U is the flow velocity; C_s is the isothermal speed of sound; and ϕ is electrostatic potential. With the above jump conditions, any one of the quantities in Table V-I can be found in terms of any other. In the table, M_1 is the upstream Mach number and M_2 is the downstream Mach number.

Given v_o/v_e, $\rho_1(1+F)$ and given the boundary condition that the downstream density of compression shock must equal the upstream density of the rarefaction shock, the overdense shock structure can be determined completely. Figure V-8 is a plot of the Mach number of the rarefaction shock in the rest frame of the ions upstream of the compression shock as a function of the ratio of the upstream density to the critical density. The curve is the theoretical prediction. The boxes are the result of hybrid code simulations. Solutions are possible even when the density upstream of the compression shock is subcritical. Figure V-9 is a plot of the Mach number of the compression shock with respect to the rarefaction shock. For solutions to exist for any length of time, this number must be negative. For very small values of $\rho_1(1+F)/\rho_c$ (that is, very strong shocks), the Mach number becomes positive and the bump annihilates itself. This condition corresponds to the lower boundary of the shaded region of Fig V-10. For a fixed value of v_o/v_e, increasing the upstream density ρ_1 decreases the strength of the shock until F approaches 0. At that point, the solution approaches that of Lee et al.[3] and there is no longer a compressional shock. Then the upper boundary of the shaded region is just the plateau density computed by Lee et al.[3] The parameter regime for the existence of an overdense bump is indicated by the shaded region.

We have studied the conditions for formation of overdense bumps with a one-dimensional hybrid simulation code. The simulation results are in good agreement with theoretical predictions obtained from jump conditions. We will investigate the stability of these solutions to transverse perturbations.

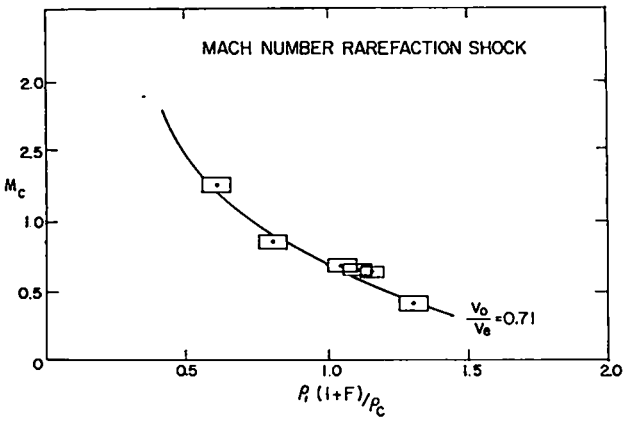

Fig. V-8.
Mach number of rarefaction shock with respect to ions upstream of the compression shock.

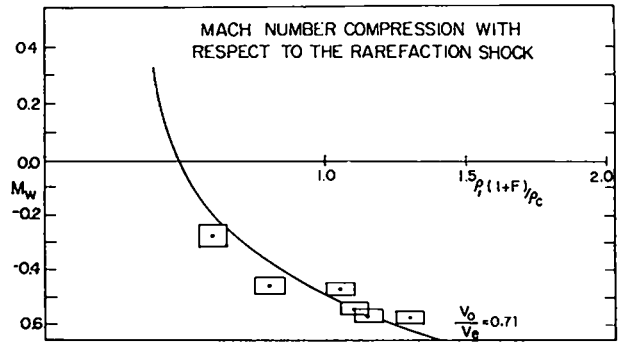

Fig. V-9.
Mach number of compression shock with respect to the rarefaction shock.

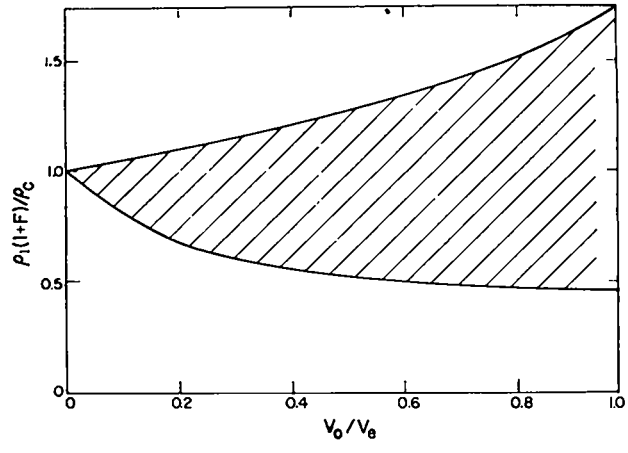

Fig. V-10.
Region in parameter space where overdense bumps can exist.

TARGET DESIGN (E. Lindman)

Target Design for Ion-Beam Fusion (W. P. Gula)

To understand the behavior of ion-beam targets, we have performed calculations for gas-filled gold microballoons. The target was investigated as part of a study to determine the minimum conditions for breakeven. The calculation was a one-dimensional spherically symmetric hydrodynamic computer calculation. The ion beam was a 6.4-GeV xenon beam with a 10-ns pulselength and a constant power of 300 TW (total energy, 3 MJ). The target was a gold microballoon with a 3-mm outer radius, a 0.2-mm-thick gold shell, and a central fuel region with a 50:50 DT mixture (initial density of 2 mg/cm^3). In the calculation, we assumed that all 3 MJ of beam energy were absorbed. The calculated thermonuclear yield was over 42 MJ, a yield ratio of over 14.

Figure V-11, a snapshot of the pellet at 10 ns, just after the ion beam was turned off, shows the density and the ion, electron, and radiation temperatures as a function of radius. At 10 ns the shell has barely started to move inward. The fuel density and the ion and electron temperatures are barely above their initial values. The outer region of the gold shell, which has absorbed the ion beam, has been heated to a maximum temperature of ~250 eV and has started to blow off. The inner region of the gold is still cold, and a portion of it has been compressed to about three times solid density.

A snapshot of the pellet at peak burn (~35 ns after ion-beam turn-on) is shown in Fig. V-12. The situation is quite different from that shown in Fig. V-11. The fuel density is ~100 times that of liquid DT, and its ion temperature is just below 3 keV. The gold is much colder and now shows three regions: a long blowoff region, followed by a highly compressed (~4000 g/cm^3) pusher region, followed by a region expanding into the fuel that has a density of ~300 g/cm^3.

Time plots of various quantities are shown in Fig. V-13 through V-15. Figure V-13 plots the radius of different mass elements vs time. The outer portion of the gold expands outward, whereas the gold-DT interface accelerates inward and shows that the peak fuel compression occurs slightly later than 35 ns. The fuel at the half-radius point does not begin to move inward until 18 ns, 8 ns after the beam is turned off. The inner fuel mass

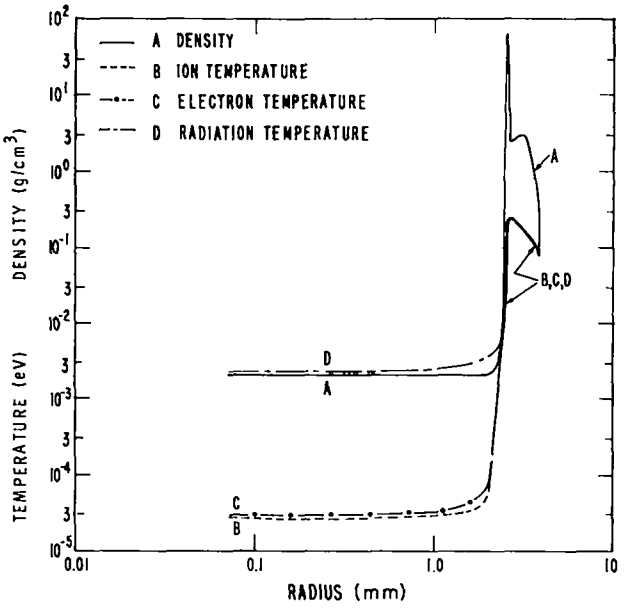

Fig. V-11.
Density and ion, electron, and radiation temperatures as a function of pellet radius 10 ns after the start of the problem, just after the ion beam has been turned off.

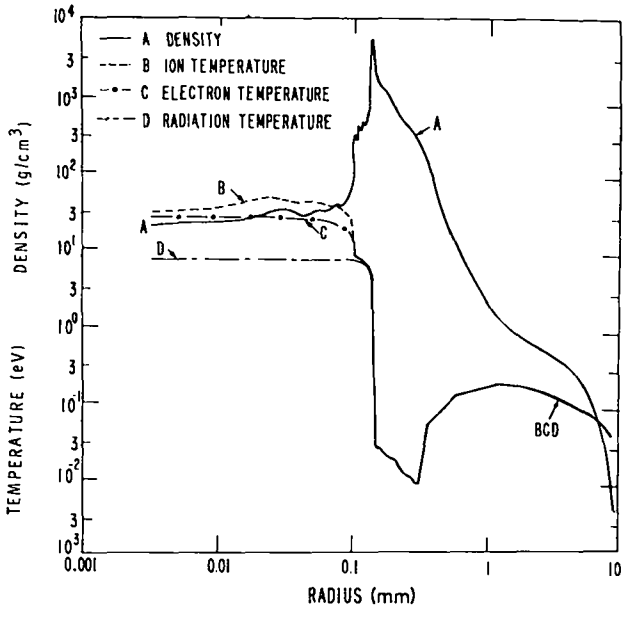

Fig. V-12.
Density and ion, electron, and radiation temperatures as a function of radius ~35 ns after start of the problem, near the time of peak thermonuclear burn.

is hit by a shock wave at 25 ns. The density of different elements and the maximum density anywhere in the pellet, both as a function of time, are shown in Fig. V-14. That the density of the halfway gold zone is monotonically decreasing indicates that it is part of the blow-off region. The sharp density spikes are indications that a shock wave has passed through the region.

Figure V-15 is similar to Fig. V-14, except that it shows the ion temperature as a function of time, rather than the density of different mass elements. The temperature curve of the inner zone shows preheat from thermal conduction and shocks. The strongest shock reaches the center at 25 ns, but the final temperature and the peak burn do not occur until 10 ns later.

This simple target can be improved; however, these calculations definitely show that such targets for ion beams are worth investigating.

Atmospheric Modes in Laser Fusion Targets (A. J. Scannapieco)

Introduction. Laser fusion targets must experience Taylor instabilities at some time during their implosion. This instability can occur anyplace in the target where opposing density and pressure gradients exist, for example, at the ablation layer or at the fuel-pusher interface during deceleration.

However, the classic Taylor instability can be viewed as a particular case of a broader set of normal modes that can exist in the pellet. Investigations of normal modes in planetary atmospheres have been conducted for many years[4,5] and have their direct analog in the study of the laser fusion pellet during implosion.

Studies of atmospheric waves have shown that waves can travel radially and are amplified as they pass from higher to lower density, that waves are refracted and ducted in the atmosphere and, further, that modes can travel perpendicular to a temperature gradient.

In the atmosphere, the density and the pressure gradients are normally unidirectional; however, when the gradients occur in opposite directions, the techniques used in atmospheric studies can still be applied with interesting consequences for laser fusion pellets.

To maintain that the pellet has a pseudo-planetary atmosphere, we assume that at a particular interval in radius, the fluid is accelerating with an effective acceleration g and is moving with a uniform time-varying radial velocity. All calculations will then be valid for the "proper observer," that is, an observer in a noninertial frame moving with the local fluid velocity.

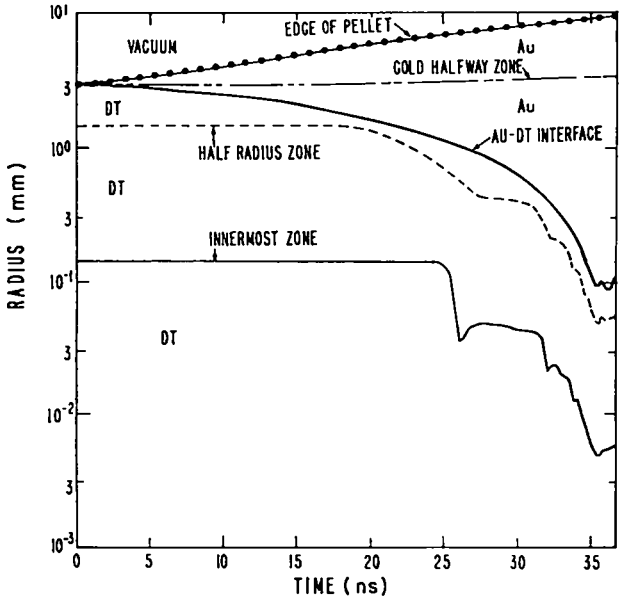

Fig. V-13.
Radial position of selected mass elements as a function of time.

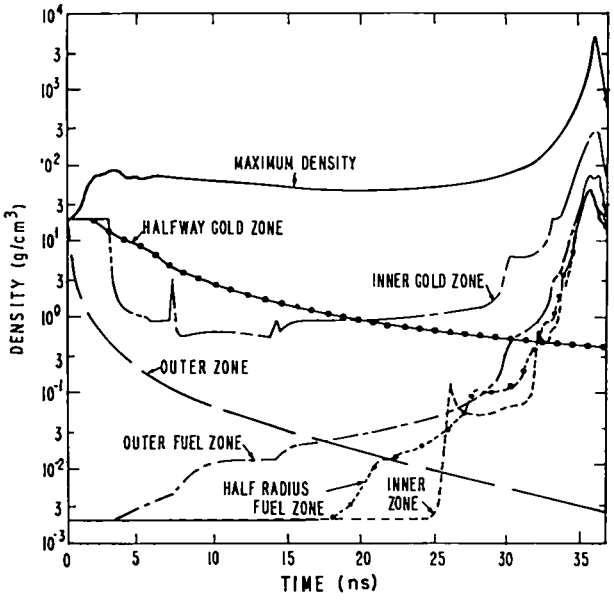

Fig. V-14.
Density of selected mass elements as a function of time. The top curve is the maximum density anywhere in the pellet as a function of time.

Calculations. The following set of fluid moment equations for a fusion pellet illustrate some consequences of our approach:

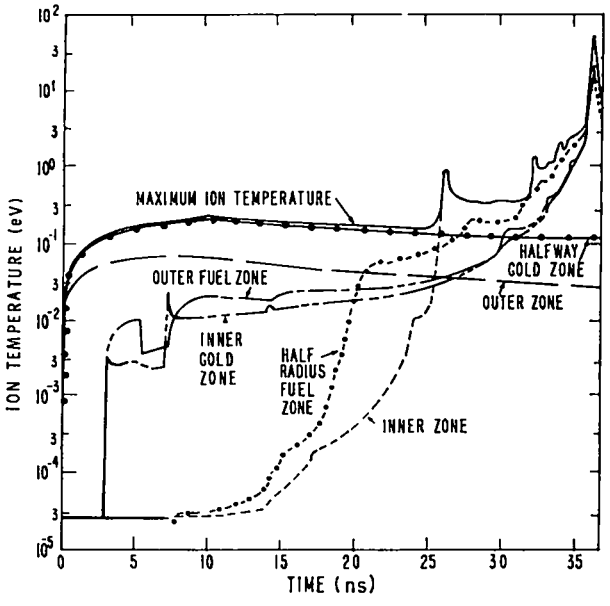

Fig. V-15.
Ion temperature of selected mass elements as a function of time. The top curve is the maximum ion temperature anywhere in the pellet as a function of time.

$$\frac{\partial \rho}{\partial t} + \frac{\partial}{\partial x_i}(\rho V_i) = 0 \ , \tag{V-2}$$

$$\rho\left(\frac{\partial V_i}{\partial t} + V_j \frac{\partial}{\partial x_j} V_i\right) = -\frac{\partial}{\partial x_i} P + g\rho\lambda_i \ , \tag{V-3}$$

and

$$\frac{\partial}{\partial t}(P_\rho{}^{-\gamma}) + V_i \frac{\partial}{\partial x_i}(P_\rho{}^{-\gamma}) = 0 \ . \tag{V-4}$$

In Eqs. (V-2) through (V-4), the quantities are defined as

$\rho \equiv$ fluid density,
$V_i \equiv$ components of fluid velocity,
$P \equiv$ isotropic pressure,
$g \equiv$ effective gravity,
$\lambda_i \equiv$ cosine of angles between the gravity vector and the coordinate axes, and
$\gamma \equiv$ ratio of specific heats (polytropic index).

We chose to study an adiabatic compressible fluid so that the system of Eqs. (V-2) through (V-4) would accommodate acoustic modes.

The pressure is related to temperature by

$$P = \rho\theta \ . \tag{V-5}$$

Further, we assumed that both the wavelength and the interval in radius for which we were performing a stability analysis were small compared to the radius. Under these conditions, the system can be considered rectangular, with the gravity vector g directed in the negative z direction ($\lambda_x = 0$, $\lambda_y = 0$, $\lambda_z = -1$).

The usual expansion of fluid quantities about equilibrium values is made:

$$\rho = \rho_o(z) + \rho_1(x,y,z,t) \ , \tag{V-6}$$

$$V_l = V_{l_o}(z) + V_{l_1}(x,y,z,t) \ , \tag{V-7}$$

and

$$\theta = \theta_o(z) + \theta_1(x,y,z,t) \ . \tag{V-8}$$

The equilibrium quantities indicated by the subscript o vary only in the z-direction and satisfy the relations

$$V_{l_o} = 0 \tag{V-9}$$

and

$$D\theta_o = -\left(\frac{\theta_o D\rho_o}{\rho_o} + g\right) \tag{V-10}$$

where $D \equiv d/dz$.

The perturbed quantities are written as

$$\rho_1 = \rho_1(z) \exp (nt + ik_x x + ik_y y) \ , \tag{V-11}$$

$$V_{l_1} = V_{l_1}(z) \exp (nt + ik_x x + ik_y y) \ , \tag{V-12}$$

and

$$\theta_1 = \theta_1(z) \exp (nt + ik_x x + ik_y y) \ . \tag{V-13}$$

Substituting Eqs. (V-6) through (V-13) into Eqs. (V-2) through (V-4) yields

$$D^2\mu + D\mu \left[-\frac{D\rho_o}{\rho_o} - \frac{(D\rho_o/\rho_o + g/\theta_o)n^2/k^2}{(\gamma\theta_o + n^2/k^2)} \right]$$

$$+ \mu \left\{ -k^2 \frac{(\gamma\theta_o + n^2/k^2)}{\gamma\theta_o} + g\frac{k^2}{n^2}\left(\frac{D\rho_o}{\rho_o} + \frac{g}{\gamma\theta_o}\right) \right.$$

$$\left. + \left[\left(\frac{D\rho_o}{\rho_o}\right)^2 - \frac{D^2\rho_o}{\rho_o} \right] \right.$$

$$\left. - \frac{(D\rho_o/\rho_o + g/\theta_o)(g - D\rho_o/\rho_o n^2/k^2)}{(\gamma\theta_o + n^2/k^2)} \right\} = 0 \ , \tag{V-14}$$

where $k^2 = k_x^2 + k_y^2$ and $\mu \equiv \rho_o V_{z_1}$. (For a detailed derivation of the equations see the Appendix.)

In the special case of an exponentially varying zeroth-order density

$$\rho_o = \rho_o(z = 0) \exp (z/H) \ , \tag{V-15}$$

$$C_s^2 = \frac{\gamma P_o}{\rho_o} = \gamma\theta_o \ , \tag{V-16}$$

where C_s is the local adiabatic sound speed. Therefore, Eq. (V-14) is rewritten

$$D^2\mu + D\mu\left[-\frac{1}{H} - \frac{(1/H + \gamma g/C_s^2)n^2}{(C_s^2k^2 + n^2)} \right]$$

$$+ \mu\left[-k^2 - \frac{n^2}{C_s^2} + g\frac{k^2}{n^2}\left(\frac{1}{H} + \frac{g}{C_s^2}\right) \right.$$

$$\left. - \left(\frac{1}{H} + \frac{\gamma g}{C_s^2}\right)\frac{(gk^2 - n^2/H)}{(C_s^2k^2 + n^2)} \right] = 0 \ . \tag{V-17}$$

Equation (V-17) is a harmonic oscillator equation with inconstant coefficients. If we seek a solution over an interval d so that

$$|H|/d \gg 1 \ , \tag{V-18}$$

we can treat C_s as a constant over that interval.[6] The analysis that follows is a generalization of that found in Ref. 6. Assuming that C_s is constant over the interval

$$0 \le z \le d \ , \tag{V-19}$$

the coefficients of Eq. (V-17) are independent of z, and the general solution of Eq. (V-17) is

$$\mu = A_1 e^{q_1 z} + A_2 e^{q_2 z} \ , \tag{V-20}$$

where A_1 and A_2 are arbitrary constants and q_1 and q_2 are the roots of the equation

$$q^2 + q\left[-\frac{1}{H} - \frac{(1/H + \gamma g/C_s^2)n^2}{(C_s^2k^2 + n^2)}\right] + \left[-k^2 - \frac{n^2}{C_s^2} + g\frac{k^2}{n^2}\left(\frac{1}{H} + \frac{g}{C_s^2}\right) - \left(\frac{1}{H} + \frac{\gamma g}{C_s^2}\right)\frac{(gk^2 - n^2/H)}{(C_s^2k^2 + n^2)}\right] = 0 \ . \qquad \text{(V-21)}$$

If we assume that the fluid is confined between two rigid planes at $z = 0$ and $z = d$, then the perturbed z-momentum density μ is zero at $z = 0$ and $z = d$. The boundary condition that $\mu = 0$ at $z = 0$ requires that

$$\mu = A'(e^{q_1 z} - e^{q_2 z}) \ , \qquad \text{(V-22)}$$

whereas the boundary condition that $\mu = 0$ at $z = d$ requires that

$$q_1 - q_2 = \frac{2\pi i m}{d} \equiv 2ik_z \ . \qquad \text{(V-23)}$$

The solutions to Eq. (V-21) are

$$q_1 = \frac{1}{2}\left(\left[\frac{1}{H} + \frac{(1/H + \gamma g/c_s^2)n^2}{(C_s^2k^2 + n^2)}\right] + \left\{\left[\frac{1}{H} + \frac{(1/H + \gamma g/C_s^2)n^2}{(C_s^2k^2 + n^2)}\right]^2 + 4\left[k^2 + \frac{n^2}{C_s^2} - g\frac{k^2}{n^2}\left(\frac{1}{H} + \frac{g}{C_s^2}\right) + \left(\frac{1}{H} + \frac{\gamma g}{C_s^2}\right)\frac{(gk^2 - n^2/H)}{(C_s^2k^2 + n^2)}\right]\right\}^{1/2}\right) \ , \qquad \text{(V-24)}$$

and

$$q_2 = \frac{1}{2}\left(\left[\frac{1}{H} + \frac{(1/H + \gamma g/C_s^2)n^2}{(C_s^2k^2 + n^2)}\right] - \left\{\left[\frac{1}{H} + \frac{(1/H + \gamma g/C_s^2)n^2}{(C_s^2k^2 + n^2)}\right]^2 + 4\left[k^2 + \frac{n^2}{C_s^2} - g\frac{k^2}{n^2}\left(\frac{1}{H} + \frac{g}{C_s^2}\right) + \left(\frac{1}{H} + \frac{\gamma g}{C_s^2}\right)\frac{(gk^2 - n^2/H)}{(C_s^2k^2 + n^2)}\right]\right\}^{1/2}\right) \ . \qquad \text{(V-25)}$$

Equation (V-22) can be rewritten

$$\mu = A' \exp[1/2(q_1 + q_2)z]\{\exp[1/2(q_1 - q_2)z] - \exp[-1/2(q_1 - q_2)z]\} \ , \qquad \text{(V-26)}$$

or

$$\mu = A \exp[1/2(q_1 + q_2)z]\sin k_z z \ , \qquad \text{(V-27)}$$

where

$$\frac{1}{2}(q_1 + q_2) = \frac{1}{2}\left[\frac{1}{H} + \frac{(1/H + \gamma g/C_s^2)n^2}{(C_s^2k^2 + n^2)}\right] \ . \qquad \text{(V-28)}$$

The dispersion relation for n is obtained by substituting Eqs. (V-24) and (V-25) into Eq. (V-28), which yields

$$n^8 + n^6\left[C_s^2k_z^2 + 3C_s^2k^2 + \frac{\gamma^2g^2}{4C_s^2}\right] + n^4\left[2C_s^4k_z^2k^2 + 3C_s^4k^4 + (\gamma - 1)g^2k^2 - \frac{\gamma g C_s^2k^2}{2H}\right] + n^2\left[C_s^6k^6 + C_s^6k_z^2k^4 + \frac{C_s^6k^4}{4H^2} - \frac{C_s^4gk^4}{H} + (\gamma - 2)C_s^2g^2k^4\right] + \left[-\frac{C_s^6gk^6}{H} - C_s^4g^2k^6\right] = 0 \ . \qquad \text{(V-29)}$$

The perturbed z-momentum density μ is

$$\mu = \mu_o \exp\left\{\frac{1}{2}\left[\frac{1}{H} + \frac{(1/H + \gamma g/C_s^2)n^2}{(C_s^2k^2 + n^2)}\right]z\right\}\sin k_z z \exp(nt + ik_x x + ik_y y) \ , \qquad \text{(V-30)}$$

where n satisfies the dispersion relation Eq. (V-29).

When we substitute Eq. (V-30) into Eqs. (V.A-13) through (V.A-16) of the Appendix, the expressions for all relevant perturbed variables become

$$\rho_1 = -\frac{1}{n(C_s^2k^2+n^2)}\left\{\frac{C_s^2k^2}{H}+gk^2+\frac{n^2}{2}\right.$$

$$\left.\left[\frac{1}{H}+\frac{(1/H+\gamma gC_s^2)n^2}{(C_s^2k^2+n^2)}\right]+n^2k_z\frac{\cos k_zz}{\sin k_zz}\right\}\rho_oV_{z_1}\ , \tag{V-31}$$

$$\theta_1 = \frac{1}{n(C_s^2k^2+n^2)}\left\{\left(\frac{C_s^2k^2}{\gamma}+n^2\right)\left(\frac{C_s^2}{H}+g\right)\right.$$

$$+\frac{(1-\gamma)}{\gamma}n^2\frac{C_s^2}{2}\left[\frac{1}{H}+\frac{(1/H+\gamma g/C_s^2)n^2}{(C_s^2k^2+n^2)}\right]$$

$$\left.+\frac{(1-\gamma)}{\gamma}n^2C_s^2k_z\frac{\cos k_zz}{\sin k_zz}\right\}V_{z_1}\ , \tag{V-32}$$

$$V_{x_1} = -\frac{ik_x}{(C_s^2k^2+n^2)}\left\{\frac{C_s^2}{H}+g\frac{C_s^2}{2}\right.$$

$$\left[\frac{1}{H}+\frac{(1/H+\gamma g/C_s^2)n^2}{(C_s^2k^2+n^2)}\right]$$

$$\left.-C_s^2k_z\frac{\cos k_zz}{\sin k_zz}\right\}V_{z_1}\ , \tag{V-33}$$

$$V_{y_1} = -\frac{ik_y}{(C_s^2k^2+n^2)}\left\{\frac{C_s^2}{H}+g\frac{C_s^2}{2}\right.$$

$$\left[\frac{1}{H}+\frac{(1/H+\gamma g/C_s^2)n^2}{(C_s^2k^2+n^2)}\right]$$

$$\left.-C_s^2k_z\frac{\cos k_zz}{\sin k_zz}\right\}V_{z_1}\ , \tag{V-34}$$

and

$$V_{z_1} = V_{z_1}^o\exp\left\{\frac{1}{2}\left[-\frac{1}{H}+\frac{(1/H+\gamma g/C_s^2)n^2}{(C_s^2k^2+n^2)}\right]z\right\}$$

$$\sin k_zz\quad\exp(nt+ik_xx+ik_yy)\ , \tag{V-35}$$

where n again satisfies the dispersion relation, Eq. (V-29).

The result for an incompressible fluid can be obtained from Eq. (V-29) and Eqs. (V-31) through (V-35) by letting the adiabatic sound speed C_s approach infinity. Under this condition, Eq. (V-30) and Eqs. (V-31) through (V-35) become

$$n^2\left(k^2+k_z^2+\frac{1}{4H^2}\right)-\frac{gk^2}{H}=0\ , \tag{V-36}$$

$$\rho_1 = -\frac{1}{nH}\rho_oV_{z_1}\ , \tag{V-37}$$

$$V_{x_1} = -\frac{ik_x}{k^2}\left(\frac{1}{2H}-k_z\frac{\cos k_zz}{\sin k_zz}\right)V_{z_1}\ , \tag{V-38}$$

$$V_{y_1} = -\frac{ik_y}{k^2}\left(\frac{1}{2H}-k_z\frac{\cos k_zz}{\sin k_zk}\right)V_{z_1}\ , \tag{V-39}$$

and

$$V_{z_1} = V_{z_1}^o\exp\left[\left(\frac{-z}{2H}\right)\sin k_zz\right]$$

$$\exp(nt+ik_xx+ik_yy)\ . \tag{V-40}$$

Equation (V-36) is recognized as the Taylor growth rate for an incompressible fluid with an exponential density profile given by Chandrasekar.[6] Equations (V-37) through (V-40) indicate that the magnitude of the perturbed quantities will increase with decreasing density along the density gradient.

To display the various modes that can exist in the system when the fluid is compressible, we examine Eqs. (V-29) through (V-35). Equation (V-29) is biquartic and admits to eight solutions that occur in complex conjugate pairs. However, Eq. (V-29) admits to only three physically distinct modes, acoustic, gravity, and Lamb.

The nature of these modes changes with the value of H. Distinct regions are separated by the values $H = 0$, $H = -C_s^2/g$, and $H = -C_s^2/\gamma g$. Table V-II indicates how the character of the modes changes as a function of H. ($H = 0$ is excluded in this analysis by the requirement that $H/d \gg 1$.) As can be seen in Table V-II, the only condition for which all the mode types are oscillatory is $H = -C_s^2/\gamma g$.

To determine explicitly whether the Lamb mode is purely oscillatory only when $H = -C_s^2/\gamma g$, we set $\beta(\equiv 1/H)$ equal to

$$\beta = -\frac{\gamma g}{C_s^2}+\varepsilon\quad(\varepsilon\text{ real})\ , \tag{V-41}$$

TABLE V-II

ACOUSTIC, GRAVITY, AND LAMB MODES AT FUNCTIONS OF GRADIENT SCALE LENGTH H.

	Acoustic	Gravity	Lamb
$H > 0$	oscillatory	growing	growing-oscillatory
$H > -C_s^2/\gamma g$	oscillatory	oscillatory	growing-oscillatory
$H = -C_s^2/\gamma g$	oscillatory	oscillatory	oscillatory
$H < -C_s^2/\gamma g$	oscillatory	oscillatory	growing-oscillatory
$H < -C_s^2/g$	oscillatory	growing	growing-oscillatory

where

$$|\varepsilon| \ll \left| \frac{\gamma g}{C_s^2} \right| . \tag{V-42}$$

Next, we write

$$n = \pm iC_s k + \eta , \tag{V-43}$$

where $\pm iC_s k$ is the Lamb mode solution to Eq. (V-29) for $\beta = -\gamma g/C_s^2$ (that is, when $H = -C_s^2/\gamma g$) and set

$$|\eta| \ll |C_s k| . \tag{V-44}$$

If we substitute Eqs. (V-41) and (V-43) into Eq. (V-29) and retain terms to second order in η and to all orders in ε, the dispersion relation becomes

$$\eta^2\left[\frac{4k_z^2}{k^2} + \frac{g^2(\gamma-2)^2}{C_s^4 k^2}\right] \pm \eta i C_s k\left[\varepsilon \frac{g(\gamma-2)}{C_s^2 k^2}\right] - \varepsilon^2 C_s^2 = 0 . \tag{V-45}$$

The solutions of Eq. (V-45) are

$$\eta = \frac{\pm i\varepsilon g(\gamma-2)}{C_s k} \pm \sqrt{16\varepsilon^2 C_s^2 \frac{k_z^2}{k^2} + 3\frac{\varepsilon^2 g^2}{C_s^2 k^2}(\gamma-2)^2}}{2\left[4\frac{k_z^2}{k^2} + \frac{g^2(\gamma-2)^2}{C_s^2 k^2}\right]} . \tag{V-46}$$

It is clear that the solutions for η have both a real and an imaginary part for all $|\varepsilon| > 0$, because the expression under the square root sign is a positive real number. Therefore, the only value of η for which the Lamb mode solution, Eq. (43), is purely oscillatory is $\eta = 0$, which occurs only when $\varepsilon = 0$ or when $\beta = -\gamma g/C_s^2$ (that is, $H = -C_s^2/\gamma g$).

Note that the gravity mode is growing for $H > 0$, the classic Taylor instability, and changes from oscillatory to growing again at $H < -C_s^2/g$, which, however, does not represent a classically stable Taylor condition.

To see analytically that the gravity mode should change from purely oscillatory to purely real at $H = -C_s^2/g$, set $\beta(\equiv 1/H)$ equal to

$$\beta = -g/C_s^2 + \varepsilon \quad (\varepsilon \text{ real}) , \tag{V-47}$$

where $|\varepsilon| \ll |g/C_s^2|$ and substitute Eq. (V-47) into Eq. (V-29). The dispersion relation becomes

$$n^8 + n^6\left[C_s^2 k_z^2 + 3C_s^2 k^2 + \frac{\gamma^2 g^2}{4C_s^2}\right] + n^4\left[2C_s^4 k_z^2 k^2 + 3C_s^4 k^4 + \left(\frac{3\gamma}{2} - 1\right) g^2 k^2 - \frac{\gamma g C_s^2 k^2 \varepsilon}{2}\right] + n^2\left[C_s^6 k^6 + C_s^6 k_z^2 k^4 + \left(\gamma - \frac{3}{4}\right) C_s^2 g^2 k^4 - \frac{3C_s^4 g k^4 \varepsilon}{2} + \frac{C_s^6 k^4 \varepsilon^2}{4}\right] + [-C_s^6 g k^6 \varepsilon] = 0 . \tag{V-48}$$

We seek a mode that changes from $n^2 > 0$ (that is, purely growing) to $n^2 < 0$ (that is, purely oscillatory) as ε goes from positive to negative. For $\varepsilon = 0$, we see that one mode is indeed the trivial mode $n^2 = 0$. To show that this mode is the gravity mode and that it changes character as ε changes sign, we assume that

$$n^2 \ll C_s^2 k^2 , \tag{V-49}$$

and retain terms to second order in n^2 of Eq. (V-48).

The solution to Eq. (V-48), good to second order in n^2, is

$$n^2 = C_s^2 k^2 \left[\frac{gk^2\varepsilon}{k^2 + k_z^2 + \left(\gamma - \frac{3}{4}\right)\frac{g^2}{C_s^4} + \frac{\varepsilon^2}{4} - \frac{3g\varepsilon}{2C_s^2}}\right] . \tag{V-50}$$

Because $|\varepsilon| \ll |g/C_s^2|$, the denominator in the bracket is always positive no matter what the sign of ε. Therefore, because g is positive,

$n^2 > 0$ (growing) for $\varepsilon > 0$,

$n^2 = 0$ for $\varepsilon = 0$,

and

$n^2 < 0$ (oscillatory) for $\varepsilon < 0$.

$H = -C_s^2/g$ represents the value of H at which the last bracket in Eq. (V-48) changes sign back to that for which $H > 0$.

The physical significance of $H = -C_s^2/\gamma g$ is that it represents the only value of H for which the zeroth-order temperature and entropy are constant over the interval d. For any other value of H, there is a zeroth-order temperature and entropy gradient in the z-direction.

This fact reveals why the Lamb mode has a growing component for all H except $H = -C_s^2/\gamma g$ and why the gravity mode changes back to purely growing when $H < -C_s^2/g$. To see that this should be the case, define the vorticity Ω as

$$\underset{\sim}{\Omega} = \underset{\sim}{\nabla} \times \underset{\sim}{V} . \tag{V-51}$$

Next, take the curl of the momentum Eq. (V-3) and use Eqs. (V-2) and (V-51) to give

$$\frac{\partial \Omega}{\partial t} + (\underset{\sim}{V} \cdot \underset{\sim}{\nabla})\underset{\sim}{\Omega} + \underset{\sim}{\Omega}(\underset{\sim}{\nabla} \cdot \underset{\sim}{V}) - (\underset{\sim}{\Omega} \cdot \underset{\sim}{\nabla})\underset{\sim}{V} = \frac{\nabla \rho}{\rho} \times \underset{\sim}{\nabla}\theta \tag{V-52}$$

The important term in Eq. (V-52) is

$$\frac{\underset{\sim}{\nabla}\rho}{\rho} \times \underset{\sim}{\nabla}\theta , \tag{V-53}$$

which is the vorticity source term. If there is no vorticity in the system initially and the gradients in ρ and θ are colinear, there will never be any vorticity in the system. In the zeroth-order system considered here, ρ_o and θ_o are indeed colinear; therefore, $\Omega_o = 0$.

Vorticity can be generated even in the absence of a gravitational field if a sound wave is launched perpendicular to a temperature gradient in the host medium. The varying sound speed along the wave front will produce vorticity because the gradients in temperature and density are no longer colinear. This is the situation for Lamb waves that propagate perpendicular to the gradients in temperature and density. In the linearized perturbed system, the linearized vorticity equation is

$$\frac{\partial \underset{\sim}{\Omega}_1}{\partial t} = \frac{\nabla \rho_1}{\rho_o} \times \underset{\sim}{\nabla}\theta_o + \frac{\rho_o}{\rho_o} \times \underset{\sim}{\nabla}\theta_1 \tag{V-54}$$

In general, the right-hand side of Eq. (V-54) is not zero, which leads to the production of vorticity and to a growth of the modes.

In linear theory, vorticity is driven by the zeroth-order gradients in temperature and density. Although this growth appears rapid in the linear regime, the subsequent nonlinear evolution of the vortex cells will disrupt the zeroth-order gradients that drive the instability and will saturate these instabilities at a low level. This finding is in contradistinction to the classic Taylor instability, which is driven by a constant gravitational potential across an interface. The source of free energy needed for the growth of these modes comes from external sources that maintain the initial temperature gradient. In a fusion pellet, these sources would be hot electron energy deposition and a thermal flux from the critical surface towards the pellet center.

Results and Conclusions

Figures V-16 and V-17 are plots of the growth rate n_R and oscillatory frequency n_I, respectively, as a function of k (the magnitude of the wave vector perpendicular to the density gradient and to the effective gravity) for the growing and purely oscillatory modes. The labels A, L, and G represent the acoustic, Lamb, and gravity modes in the system, respectively. The dispersion relation represented in Figs. V-16 and V-17 was obtained for a fluid with a 10^{-3}-cm scale length H, an average adiabatic sound speed C_S of 5×10^6 cm/s, and a 5/3 polytropic index γ, under the influence of a 10^{16}-cm/s^2 effective gravity g. The wave vector parallel to the density gradient k_Z was chosen to be $2\pi \times 10^4$ cm^{-1} so that Eq. (V-18) was satisfied. The dispersion relation represented in Figs. V-18 and V-19 is equivalent to that represented in Figs. V-16 and V-17, except that the sound speed was changed to $C_s = 5 \times 10^5$ cm/s.

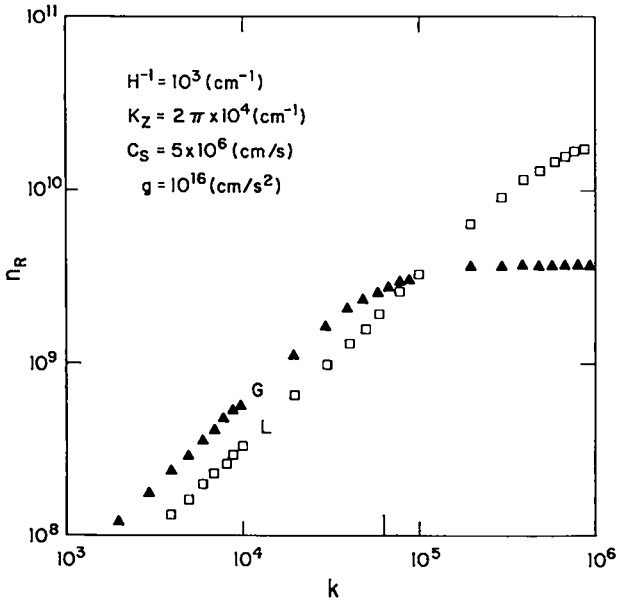

Fig. V-16.
Variation of growth rate n_R with k (the magnitude of that component of the wave vector perpendicular to the density gradient and effective gravity) for the gravity mode (G) and the Lamb mode (L). The average adiabatic sound speed is 5×10^6 (cm/s).

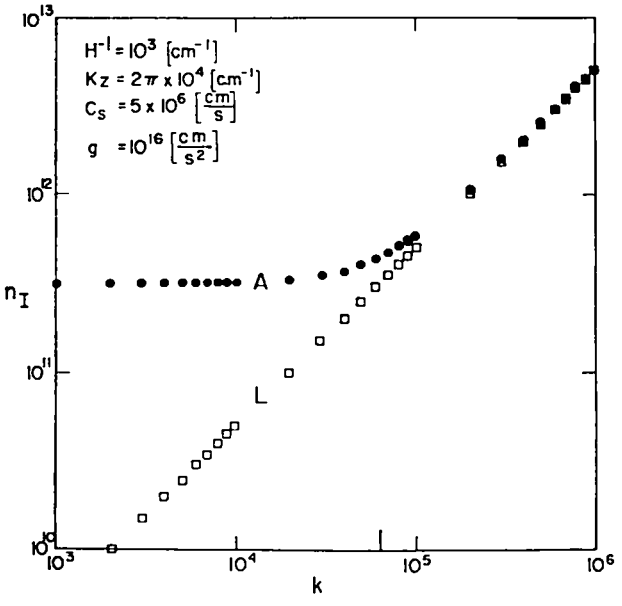

Fig. V-17.
Variation of oscillatory frequency n_I with k for the acoustic mode (A) and the Lamb mode (L). The average adiabatic sound speed is 5×10^6 (cm/s).

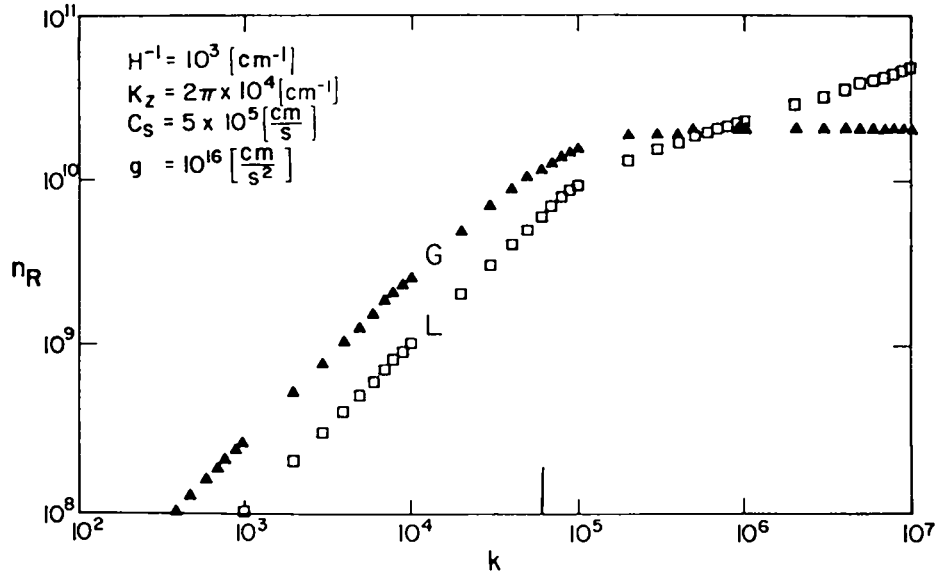

Fig. V-18.
Variation of growth rate n_R with k for the gravity mode (G) and the Lamb mode (L). The average adiabatic sound speed is 10 times smaller than for the case represented in Fig. V-16.

Several conclusions can be drawn from Figs. V-16 through V-19. Of the two modes (G and L) that have a growing component for any combination of k and k_Z, the dominant mode will be the one with the largest growth rate. As k approaches k_Z and becomes larger than k_Z, the dominant mode switches from G (that is, the growing

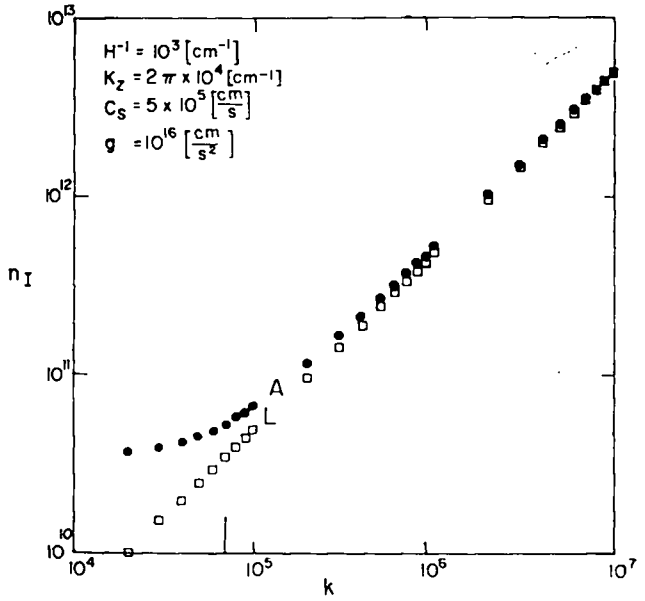

Fig. V-19.
Variation of oscillatory frequency n_i with k for the acoustic mode (A) and the Lamb mode (L). The average adiabatic sound speed is 10 times smaller than for the case represented in Fig. V-17.

Taylor mode) to L (that is, the growing oscillatory mode).

Also, the compressibility of the gas has a destabilizing effect. The bulk modulus of an adiabatic gas is

$$B \equiv \rho \frac{\partial P}{\partial \rho} = C_s^2 \rho \ . \qquad \text{(V-55)}$$

Thus, the lower the sound speed, the more compressible and the more unstable the system (compare Figs. V-16 and V-18).

From Eq. (V-35) it is also apparent that in a laser fusion pellet, the perturbations generated at the fuel-pusher interface during deceleration are amplified in the DT because of the decrease in density from the pusher to the DT.

The question of interface stability in laser targets is made more complicated by the above analysis. At the crucial fuel-pusher interface, not only will perturbations grow during deceleration (that is, by gravity-mode growth), but also during acceleration (that is, by Lamb-mode growth) if a temperature gradient exists across the interface. Once again preheat can affect target performance by producing large temperature gradients at the fuel-pusher interface, making it possible for Lamb modes to grow.

Whether these thermally driven Lamb modes have a deleterious effect on target performance is not clear. An overstable Lamb mode might grow to nonlinear levels at an interface in the pellet while the gravity mode is oscillatory. This growth could smooth the temperature gradient across the interface and produce a turbulent boundary layer there. However, several authors have argued that a turbulent layer would enhance the integrity of pellet shells against breakup,[7,8] which would then enhance target performance rather than degrade it.

The effect of energy dissipation (for example, through thermal conduction and viscosity) on atmospheric modes should be treated at length in future investigations.

REFERENCES

1. R. Fedesojevs, M. D. J. Burgess, G. D. Enright, and M. C. Richardson, Phys. Rev. Lett. **43** (1979).

2. J. R. Sanmartin and J. L. Montanes, "Profile Modification in Laser Plasmas Expanding with Uniform Time Dependent Temperature," to be published.

3. K. Lee, D. W. Forslund, J. M. Kindel, and E. L. Lindman, Phys. Fluids **20**, 51 (1977).

4. C. O. Hines, "Internal Atmospheric Gravity Waves at Ionospheric Heights," Can. J. Phys. **38**, 1441 (1960).

5. S. H. Frances, "Global Propagation of Atmospheric Gravity Waves: A Review," J. Atmos. Terr. Phys. **37**, 1011 (1975).

6. S. Chandrasekar, *Hydrodynamic and Hydromagnetic Stability* (Oxford University Press, London, 1968), pp. 434-435.

7. S. Z. Belenskii and E. S. Fradkin, Theory of Turbulent Intermixing, Fiz. Inst. Akad. Nauk. SSR im. P. N. Lebedeva **29** (1965).

8. Yu. V. Afanas'ev, "Laser Initiation of Thermonuclear Reaction in Inhomogeneous Spherical Targets," Pis'ma Zh. Eksp. Teor. Fiz. **21**, 150 (1975) [JETP Lett. **21**, 68 (1975)].

APPENDIX

Substituting Eqs. (V-5) through (V-13) into Eqs. (V-2) through (V-4) yields

$$n\rho_1 + V_{z_1} D\rho_o + \rho_o(ik_x V_{z_1} + ik_y V_{y_1} + DV_{z_1}) = 0 \ , \tag{V.A-1}$$

$$n\rho_o V_{x_1} + ik_x \theta_o \rho_1 + ik_x \rho_o \theta_1 = 0 \ , \tag{V.A-2}$$

$$n\rho_o V_{y_1} + ik_y \theta_o \rho_1 + ik_y \rho_o \theta_1 = 0 \ , \tag{V.A-3}$$

$$n\rho_o V_{z_1} + \theta_o D\rho_1 + \rho_o D\theta_1 + \rho_1 D\theta_o + \theta_1 D\rho_o + g\rho_1 = 0 \ , \tag{V.A-4}$$

and

$$n\rho_o\theta_1 + (\gamma - 1)\rho_o\theta_o(ik_x V_{z_1} + ik_y V_{y_1} + DV_{z_1}) + \rho_o V_{z_1} D\theta_o = 0 \ , \tag{V.A-5}$$

where

$$D \equiv d/dz \ .$$

Multiply Eq. (V.A-2) by ik_x and Eq. (V.A-3) by ik_y and add

$$P_1 = \theta_o\rho_1 + \rho_o\theta_1 = \frac{n\rho_o}{k^2}(ik_x V_{x_1} + ik_y V_{y_1}) \ , \tag{V.A-6}$$

where $k^2 = k_x^2 + k_y^2$.

Substituting Eq. (V.A-6) into Eqs. (V.A-1) and (V.A-5) reduces the set of equations to

$$\theta_o\rho_1 + \rho_o\theta_1 = -\frac{n}{k^2}(n\rho_1 + V_{z_1} D\rho_o + \rho_o DV_{z_1}) \ , \tag{V.A-7}$$

$$n\rho_o V_{z_1} + D(\theta_o\rho_1 + \rho_o\theta_1) + g\rho_1 = 0 \ , \tag{V.A-8}$$

and

$$n\rho_o\theta_1 + (\gamma - 1)\theta_o \frac{k^2}{n}(\theta_o\rho_1 + \rho_o\theta_1) + (\gamma - 1)\rho_o\theta_o DV_{z_1} + \rho_o V_{z_1} D\theta_o = 0 \ . \tag{V.A-9}$$

Defining $\mu \equiv \rho_o V_{z_1}$ and substituting Eq. (V.A-7) into Eqs. (V.A-8) and (V.A-9) reduce the set of equations to

$$n\mu - \frac{n^2}{k^2} D\rho_1 - \frac{n}{k^2} D^2\mu + g\rho_1 = 0 \tag{V.A-10}$$

and

$$n\rho_1(n^2 + \gamma\theta_o k^2) + n^2 D\mu - \mu\rho_o^{(\gamma-1)} D[\theta_o \rho_o^{-(\gamma-1)}] = 0 \ . \tag{V.A-11}$$

Substituting Eq. (V.A-11) into Eq. (V.A-10) yields, finally, the single equation

$$D^2\mu + D\mu\left[-\frac{D\rho_o}{\rho_o} - \frac{(D\rho_o/\rho_o + g/\theta_o)n^2/k^2}{(\gamma\theta_o + n^2/k^2)}\right] + \mu\left\{-k^2\frac{(\gamma\theta_o + n^2/k^2)}{\gamma\theta_o} + g\frac{k^2}{n^2}\left(\frac{D\rho_o}{\rho_o} + \frac{g}{\gamma\theta_o}\right) + \left[\left(\frac{D\rho_o}{\rho_o}\right)^2 - \frac{D^2\rho_o}{\rho_o}\right] - \frac{(D\rho_o/\rho_o + g/\theta_o)(g - D\rho_o/\rho_o n^2/k^2)}{(\gamma\theta_o + n^2/k^2)}\right\} = 0 \ . \tag{V.A-12}$$

Also, using Eq. (V.A-11), we can write ρ_1 in terms of μ as

$$\rho_1 = \frac{\{-n^2 D\mu + \mu k^2 \rho_o^{(\gamma-1)} D[\theta_o \rho_o^{-(\gamma-1)}]\}}{n(n^2 + \gamma\theta_o k^2)} \ . \tag{V.A-13}$$

Using Eqs. (V.A-7) and (V.A-13), we can write θ_1 in terms of μ as

$$\theta_1 = -\frac{[(\gamma - 1)\theta_o k^2 n^2 D\mu + (n^2 + \theta_o k^2)\mu\rho_o^{(\gamma-1)} D(\theta_o \rho_o^{-(\gamma-1)})]}{n\rho_o(n^2 + \gamma\theta_o k^2)} \ . \tag{V.A-14}$$

Finally, when we substitute Eqs. (V.A-13) and (V.A-14) into Eqs. (V.A-2) and (V.A-3) and write the quantities V_{x_1} and V_{y_1} in terms of μ,

$$V_{x_1} = \frac{ik_x \{\gamma\theta_o D\mu + \mu\rho_o^{(\gamma-1)} D[\theta_o \rho_o^{-(\gamma-1)}]\}}{\rho_o(n^2 + \gamma\theta_o k^2)} , \qquad (V.A\text{-}15)$$

$$V_{y_1} = \frac{ik_y \{\gamma\theta_o D\mu + \mu\rho_o^{(\gamma-1)} D[\theta_o^{-(\gamma-1)}]\}}{\rho_o(n^2 + \gamma\theta_o k^2)} . \qquad (V.A\text{-}16)$$

and

VI. LASER FUSION TARGET FABRICATION
(R. Jay Fries)

Our target fabrication effort, which is supported by extensive theoretical investigations, supplies targets containing thermonuclear fuel for laser-driven compression and heating experiments, as well as providing simpler targets for basic physics experiments. These targets, which range from simple, deuterated, flat plastic films to complex multilayered structures containing cryogenic, solid DT fuel, are optimized for use with high-power CO_2 lasers. After a target has been designed, we develop the technologies to produce the required materials and the methods to measure and characterize them. We then select or fabricate the target core, fill it with the desired thermonuclear fuel and diagnostic gases, and assemble the outer layers over it. Finally, we position the target in a target-insertion mechanism so that it will be at the precise laser focus spot in the target chamber.

INTRODUCTION (N. R. Borch, E. H. Farnum, R. J. Fries)

Our target fabrication effort has two major objectives:

- to supply targets for the experimental program as needed, and
- to develop new techniques and materials for the fabrication of future thermonuclear compression targets.

In addition, we provide micromachining, microassembly, and materials fabrication services to other groups.

Various targets are produced for the first objective: thermonuclear compression targets for main-sequence experiments, partial and modified compression targets for target-essential experiments, a wide variety of targets for supporting-physics experiments, and several types of targets for military applications experiments.

Half our effort is directed toward future target designs. We develop new processes and techniques to produce new or improved materials, and we develop methods of measuring and characterizing these materials and of assembling them into required configurations.

Our initial targets, called Sirius, were simply GMBs filled with DT gas at pressures up to 30 atm. In Sirius these simple shells act as exploding pushers in which the preheated fuel is compressed and heated further. Although these targets do not produce high gains, they do produce thermonuclear reactions and neutrons. Adiabatic or ablation-driven compression is obtained by adding a layer of plastic, ~50 μm thick, which is vaporized by the laser pulse causing the glass shell to implode hydrodynamically. Such a design, called Sirius-B, attained our 20-times-liquid-density milestone. By coating the GMB with molybdenum or another high-Z metal before plastic deposition, we produced a Rigel target that implodes more efficiently than the Sirius-B.

In Polaris, our most advanced target (Fig. VI-1), this high-Z metal coating will be added as a pusher shell for the fuel, a low-density plastic foam will be added to provide a hydrodynamic cushion, and a second pusher layer will be added outside the foam.

In our high-performance targets, such as Polaris, the fuel will be frozen onto the inside surface of the innermost pusher shell as a solid layer of DT ice. Calculations show that this cryogenic modification will improve the yield substantially. We are developing techniques to freeze such layers in place within the Helios target chamber.

For these and other recent targets, and for diagnostic purposes, we are developing high-Z metal shells with diameter and wall-thickness uniformity deviations of not more than 1% and a surface smoothness tolerance of $\ll$1000 Å, as well as low-density, small-cell plastic foams, thick layers of plastic chemically loaded with high-Z metals, metal foams, and smooth metal layers of moderate or low-Z. In addition, we are developing methods to prepare alternative fuels that are solid at room temperature and contain fuel atoms at high density, for example, polyethylene, lithium hydride, or ammonia borane. (In all of these, the hydrogen is replaced by an equimolar mixture of deuterium and tritium.) Even though the nonfuel atoms in these compounds dilute the nuclear fuel and reduce target performance, the solidity of these materials at room temperature may be an advantage, especially in designs that require fuel-containing layers in the outer parts of the target.

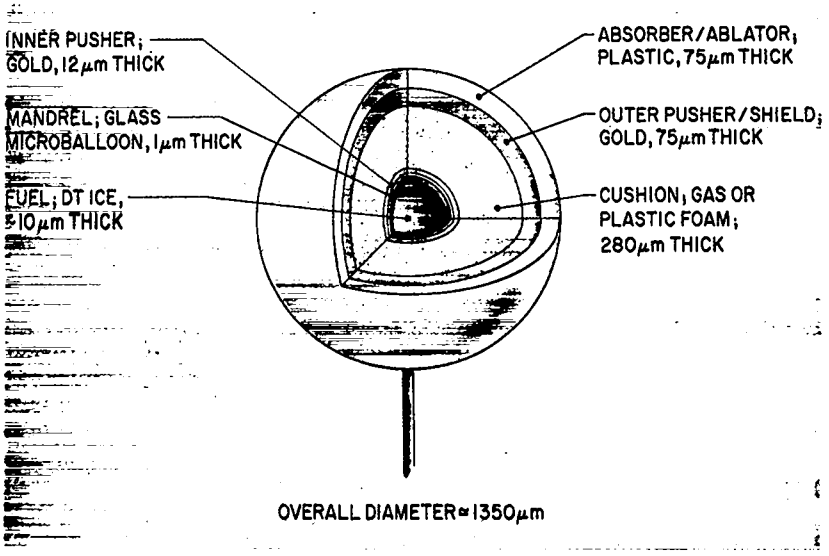

Fig. VI-1.
Polaris Prime, a multilayer, multishell laser fusion target design for Antares and Helios.

Because any target must be characterized completely to understand its performance, we have devoted much of our effort to measuring and documenting all targets we deliver and to developing new, automated high-resolution methods of characterizing target parts. We are developing a surface acoustic-wave resonator/driver to sort batches of target shells for diameter and wall uniformity. We are also automating our x-ray microradiographic method for observing defects and nonuniformities in opaque shells and improving the capabilities of the method. We are developing nondestructive techniques for determining the composition and pressure of the fill gases inside GMBs.

TARGET FABRICATION

General

Because our primary assignment in target fabrication is the assembly, delivery, and postshot analysis of targets for our three operating laser systems, we expend the time necessary to meet delivery requests from these experiments. In addition, we try to maintain a large and very flexible inventory of materials and techniques so that we can respond rapidly to changes in target specifications. As part of target assembly, we also mount and align the targets on the appropriate target-changing mechanism to eliminate any further position adjustment in the target chamber. If we are requested to do so, we photograph and analyze any remnants to supplement target diagnostics.

The process of target fabrication typically includes the following steps. We choose the most suitable GMB for the desired diameter, wall thickness, and gas permeation. (High-quality GMBs are now available from both KMS Fusion Inc. and LLNL.) Suitable GMBs are optically preselected with an interference microscope and then filled with DT or DT:Ne gas mixtures by wall permeation at elevated temperature and pressure. When nondiffusible diagnostic gases are required in the fuel, GMBs are filled by using the drill, fill, and plug (DFP) technique. This technique consists of laser-drilling a small hole (1- to 5-μm diam) into a GMB, covering the hole with a plug of uncured epoxy, and then filling the GMB by pressurizing it in a small pressure vessel containing the gas. To flow and cure the epoxy plug, the filled GMB is heated while still in the vessel. The filled GMBs are cleaned and inspected in three orthogonal planes with an interference microscope. We then apply coatings of metal and/or plastic to these selected GMBs. These coatings are examined in three views by x-ray microradiography (often after each successive layer has been applied) to determine coating smoothness and uniformity. Some targets for laser fusion experiments, such as Polaris, require additional shells of plastic, plastic foam, or various metals. These outer shells are fabricated by coating suitable spherical mandrels with

the desired materials, cutting the coating in half with a laser knife, and then leaching out the mandrel. These shells are assembled around the coated GMB core to complete the target. We then mount the targets for use in one of our laser systems.

Gas Filling and Analysis of Laser Fusion Targets

General. To understand the performance of GMB laser targets, we must be able to measure the gas fill with a high degree of accuracy. To this end we must determine the permeation rates of deuterium and tritium through thin layers (shells) of various coating materials at various temperatures. This information will enable us to select the conditions under which a given target type should be filled. Permeation data at room temperature and below will also be important in selecting the best storage temperature for targets filled with the desired quantity of fuel gas or fuel plus diagnostic gas.

X-Ray Diagnostic Targets (S. Butler). We are continuing our effort to produce GMB targets containing gases not permeable through the wall. We produced DT/argon targets (typically, 30 atm DT and 0.6 atm argon with and without plastic coatings) for laser experiments using the epoxy DFP technique previously described.[1] Our experiments indicate that the mechanism for gas loss from argon and hydrogen-isotope targets is permeation through the epoxy rather than through the bond at the epoxy-glass interface. The gas content for single-component fills is determined nondestructively by interferometry[2] or, in the case of DT, from the β-excited x-ray emission.[3] Some of the data are shown in Fig. VI-2. Exponential fits of such data for GMBs with diameters of 200 to 350 μm and hole diameters of 5 to 15 μm yield the following half-lives: 81 to more than 210 days for argon at 293 K, 10 to 63 days for DT or D_2 at 293 K, and more than 90 days for DT at 220 K. As we expected, qualitative experiments show that the gas-loss rate decreases when smaller holes are plugged. The amount of epoxy applied to the hole is difficult to determine. Figure VI-3 is an electron micrograph of the cross section of an epoxy plug over a 5- to 10-μm-diam hole.

The epoxy seal does not retain more reactive gases containing chlorine or sulfur in the GMBs. The epoxy-to-glass seal was impermeable to air but highly permeable or reactive to H_2S and Cl_2. We demonstrated this by

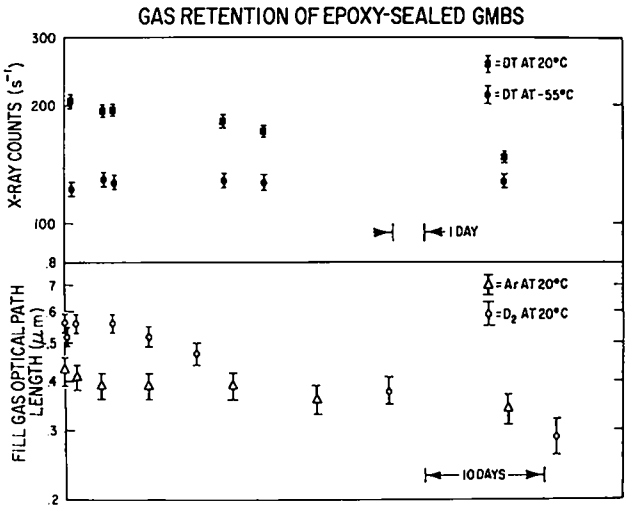

Fig. VI-2.
Retention of DT and argon in GMBs filled by the DFP technique and sealed with epoxy.

filling the GMBs with ~1 atm of the gas and subsequently finding only 0.1 to 0.3 atm when the gas was measured by breaking the seal under glycerin.[4] In addition, CCl_4 and CS_2 apparently interfere with the epoxy-to-glass seal, and the targets, therefore, also leak air.

The problem of containing the more reactive gases may be overcome by plugging the GMB with glass. We are experimenting with low-melting-point solder glasses, which generally have a high lead content, and have held 20 to 24 atm of argon in the target by sealing the GMB with glass at 723 K (450°C).

Filling Tungsten ICF Targets with Gas (W. McCreary, D. Carroll). Our past experience had indicated that filling CVD tungsten shells with D_2 or DT gas by diffusion at elevated temperatures was difficult, and that because of the long periods required at elevated temperature and pressures, an excessive amount of gas was lost by diffusion through the fill vessel.

To circumvent the difficulties inherent in permeation filling, we developed a method for filling a hollow tungsten shell with D_2 through a small hole drilled in the shell wall. The shell, with a brazed plug (silver-copper-palladium) loosely fitted into the hole, is placed in a vessel, pressurized to the desired fill pressure, and heated to melt the plug so it flows and seals the fill hole. The apparatus is shown in Fig. VI-4. The plugged shell is held in a mounting fixture that is placed in a tungsten pressure vessel. The pressure vessel is supported in a molybdenum

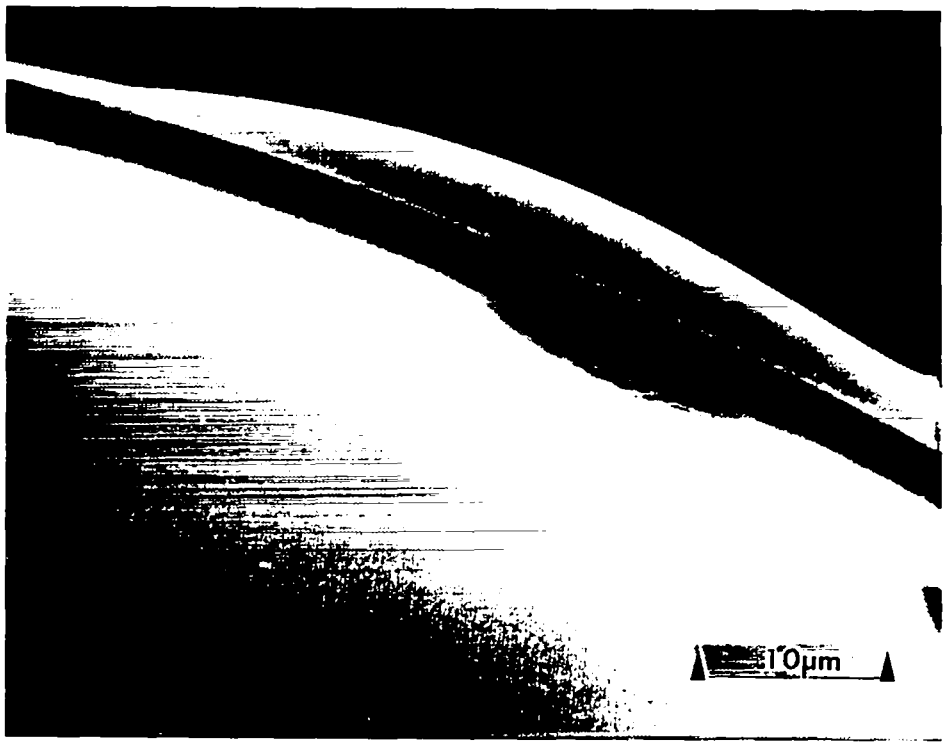

Fig. VI-3.
Photomicrograph of cross section of epoxy-plugged laser-drilled hole in a GMB.

nipple that connects to an Autoclave Engineers, Inc. valve, modified so that the valve stem forms a seal with a seat ground into the pressure cavity. After the apparatus is filled to the desired pressure, the valve is closed and the pressure above the pressure vessel is relieved, leaving only the vessel under pressure. The apparatus is then heated to melt the plug and cooled to plug the fill hole.

Cross sections of the shell in three stages are shown in Fig. VI-5. A plug whose length is about one-half the shell wall thickness essentially fills the hole when melted. In Fig. VI-6, the inner diameter of the shell was 1.15 mm, its wall was ~100-μm thick, and the fill hole diameter was ~64 μm.

The most satisfactory braze material, which consisted of 68 wt% silver, 27 wt% copper, and 5 wt% palladium, is solid at 1080 K and liquid at 1083 K. The apparatus was heated to ~1123 K (thermocouple in contact with the bottom of the pressure cavity) in ~6 min, held for ~10 min, and then free cooled to ambient.

The procedure was adequate to seal ~10 000 psi of D_2 in a tungsten shell, but the shell burst during decompression of the pressure vessel. One shell, which was pressurized to 5 000 psi D_2, contained 4 506 psi when it was crushed in a measuring device.

The above procedure requires very tedious machining, lapping, and assembling. There will always be uncertainty about the shape of the plug; therefore, some perturbations could occur on implosion. However, the procedure appears to be feasible for filling a few shells. In addition, the quantity of DT involved is very small because the volume under pressure at temperature is small (<0.25 cm^3). Also, because the heat cycle is short, loss of DT by diffusion into the pressure vessel wall should be low.

Contamination Control for Laser Fusion Targets (E. H. Farnum, R. Mulford; A. Gutacker, Eastman Kodak Co.)

All high-compression or high-yield laser fusion target designs specify pusher shells with a large aspect ratio (radius vs wall thickness). To minimize the required laser input energy, the aspect ratio is increased until calculated R-T instability growth begins to affect target performance. This instability can be initiated by imperfections in pusher shells and, thus, requires stringent controls on variations in areal density on the surface of the shell. Such variations can be caused by imperfections

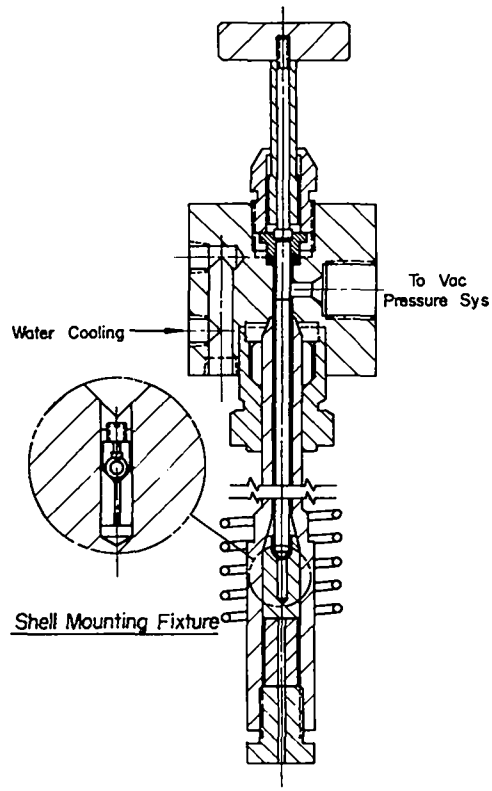

Fig. VI-4.
Apparatus for filling and braze-plugging tungsten ICF targets.

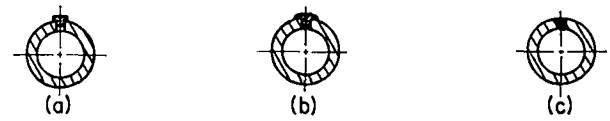

Fig. VI-5.
Tungsten ICF target (a) before brazing, (b) after brazing, and (c) after lapping.

in shell manufacture or by contamination (dirt) that adheres to the shell surface. The more insidious variation is dirt because it can attach itself to the surface in the final stages of assembly after inspection. As a result, we have been trying to find ways of assembling targets in a clean environment and of cleaning single microshells before characterization and assembly. We have made progress in several areas: we developed an aqueous-detergent cleaning process for removing anticipated soils from glass surfaces; we built a uv-ozone cleaner and evaluated its effectiveness in removing various organic soils; we designed a target assembly station that isolates the target from people and other sources of contamination during assembly; and we designed a clean area for our target assembly laboratory.

To develop an effective cleaning process for both target-handling tools and GMBs, we ran a series of tests

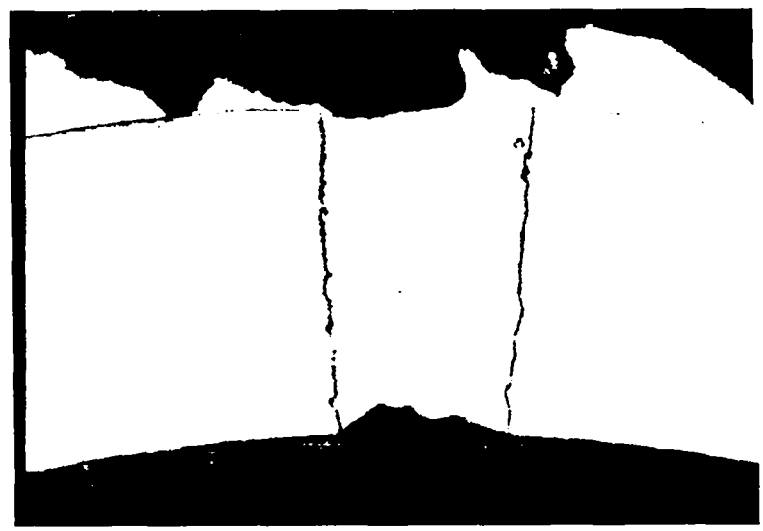

Fig. VI-6.
Photomicrograph of cross section of unlapped braze-plugged tungsten ICF target.

on glass microscope slides purposely contaminated with typical laboratory contaminants such as fingerprints, Apiezon grease, silicone vacuum grease, cigarette smoke, and vacuum pump oil. Some slides were then baked in air overnight at 473 K (200°C). We tested a wide variety of solvents and detergent solutions using ultrasonic cleaning, high-pressure flushing, soaking, and agitated rinsing. A number of detergents used with ultrasonic cleaning proved very effective in removing both normal and tenacious soils from these slides. We developed the cleaning procedure shown in Fig. VI-7. The relative effectiveness of the best detergents tested depends on the pH of the cleaning solution (Fig. VI-8).

The combination of uv light and ozone is effective in removing most organic soils.[5] Irradiation by uv light breaks bonds and frees radicals in the organic contaminants, which then oxidize readily with ozone. Gradually, in the presence of both uv and ozone, organics are reduced to gaseous CO_2 and NO_2. However, in general, the substance must be precleaned with a detergent to obtain atomically clean surfaces because many soils include inorganic materials that are not removed by photosensitized oxidation.

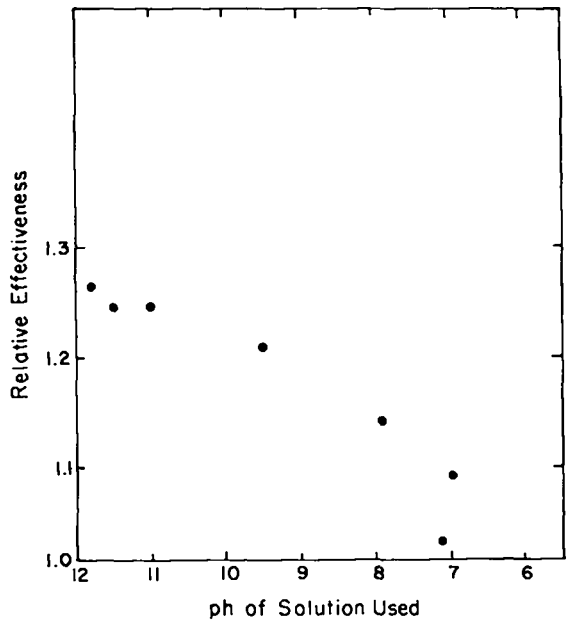

Fig. VI-8.
Relative cleaning effectiveness of many detergents and various cleaning processes as a function of pH of solution used. Substrates were glass microscope slides contaminated with various common laboratory soils.

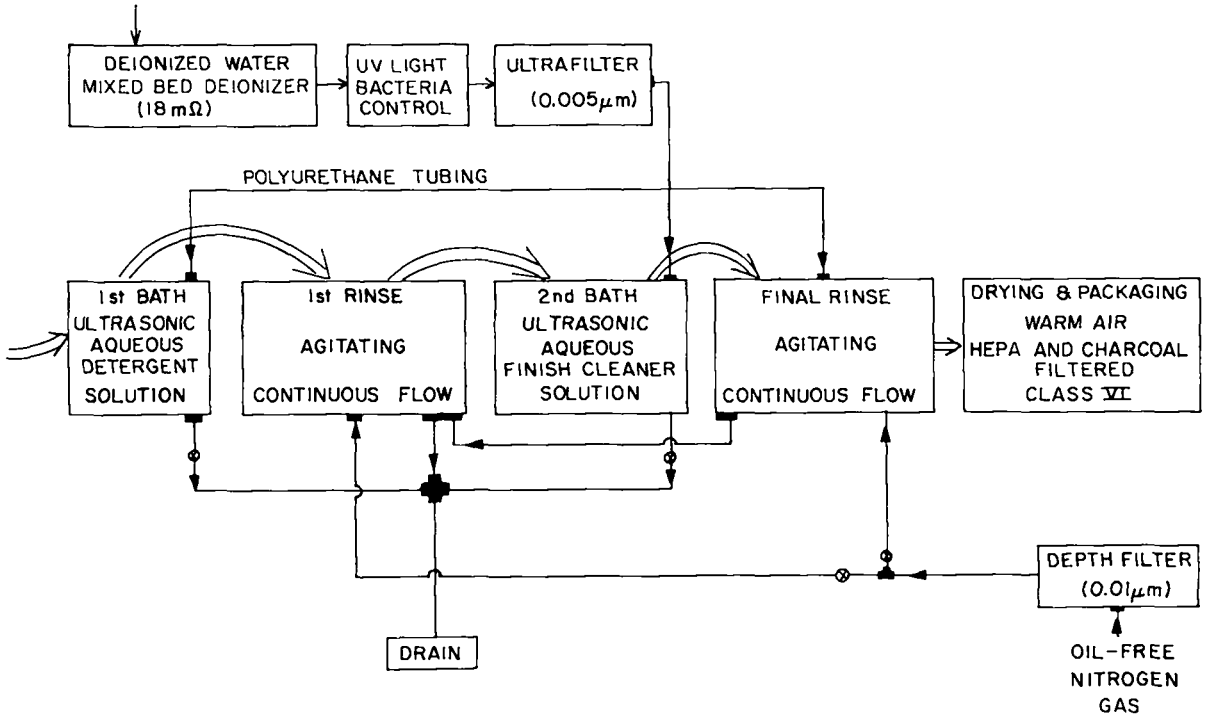

Fig. VI-7.
Cleaning procedure schematic.

We have built a uv-ozone cleaning unit that removes 400 nm/h of cellulose-nitrate film from glass slides. We have been using this unit to clean GMBs and find no visible organic residue on the surface after a 10-min exposure. We are incorporating both detergent and uv-ozone cycles into an automated GMB cleaning system.

Laser Micromachining (J. K. Feuerherd, E. H. Farnum)

We have previously discussed the use of our short-pulse dye laser for micromachining laser fusion targets.[1] In the last 6 months, several dyes, lasing at wavelengths between 450 and 530 nm, have been used to drill holes in GMBs and to cut various materials. Smaller and more uniform holes are obtainable with more efficient dyes lasing specifically at 490 nm. With these dyes, we could drill 1- to 3-μm-diam crack-free holes in thin-walled GMBs with a 70% success rate.

Several improvements in the laser made these results possible. We installed a pinhole in the laser cavity between the maximum reflector and the dispersing prisms to improve mode selection and thus beam profile. Also, to facilitate alignment of the laser cavity and to improve output-beam steering, we improved the lens mounts for the unstable resonator and recollimating lenses. A schematic of the improved laser is shown in Fig. VI-9.

The laser is focused on a sample at a point determined by the position of an X-Y table driven by a PDP 1103 computer/microprocessor combination. To improve our ability to cut and scribe with this laser, we wrote a program for the PDP 1103 computer that drives the X-Y table in circles or other analytic shapes and fires the laser at appropriate predetermined times. Figure VI-10 shows typical patterns obtainable with this program. Figure VI-10 (a) is a photomicrograph of circles cut in a 10-μm-thick silicon sheet, and Fig. VI-10 (b) shows 50-, 100-, 300-, and 500-μm-diam circles cut in a 10-μm-thick platinum sheet.

Target Characterization

Scanning Acoustic Microscope (W. L. Bongianni). In the near future, laser fusion targets of very high geometric perfection will be required. By 1982, laser fusion targets will have thickness and diameter tolerances of better than ±100 Å over spot dimensions of 10-100 μm.

Such targets may also be multishell and/or opaque, which eliminates the use of optical microscopy as a diagnostic technique. X-ray analysis may be used, but quantum noise associated with the measurement now requires examination times approaching 1 min/spot.

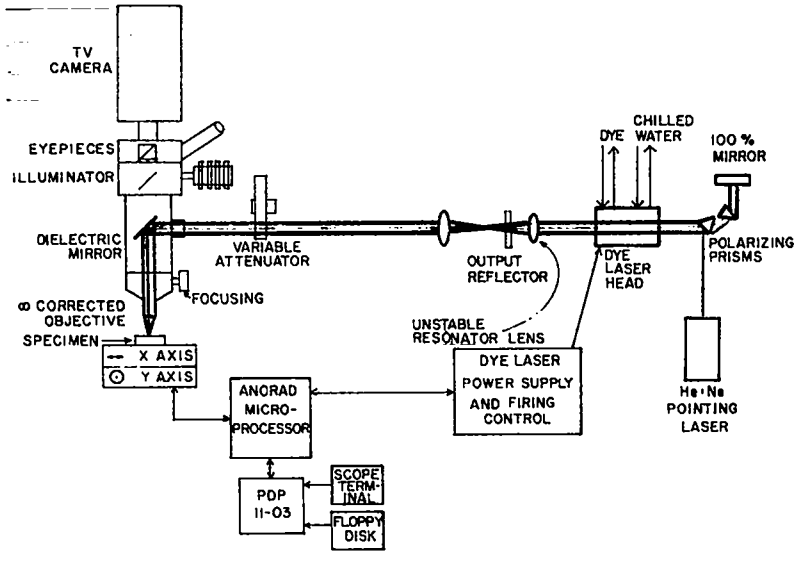

Fig. VI-9.
Pulsed dye laser used in micromachining laser fusion targets.

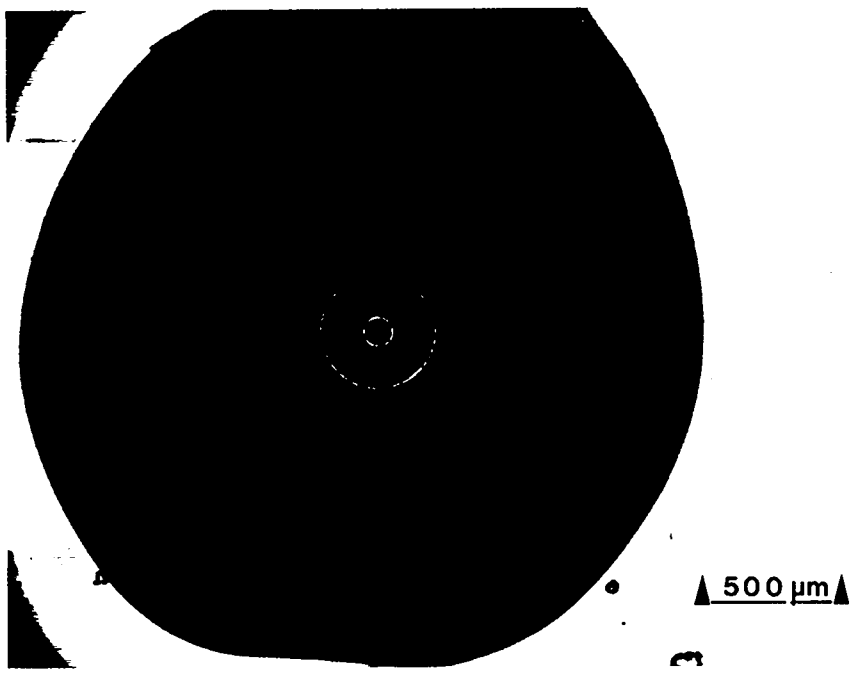

(a)

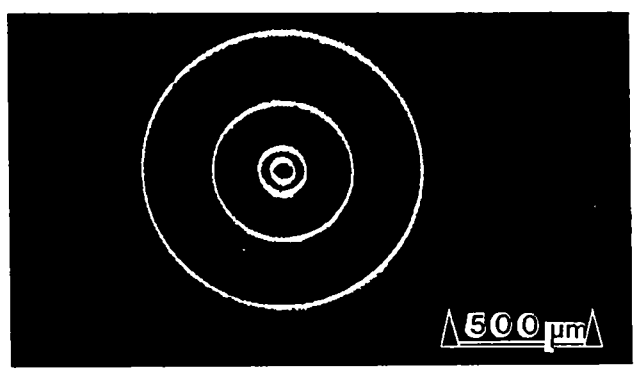

(b)

Fig. VI-10.
Photomicrographs of laser-machined circles (a) in 500-µm-thick silicon and (b) in 10-µm-thick platinum.

Clearly, if advanced targets are to be characterized to their required specifications, a much faster technology must be developed. One promising technique is acoustic microscopy at microwave frequencies where the predominant noise mechanism is thermal, which is bandwidth dependent. We have used a theoretical analysis to demonstrate that thickness can be measured to ±500 Å over spot diameters of 4 µm using our currently available microwave network analyzer. More expensive systems should be able to improve this measurement to ±100 Å.

The drawback to current microwave acoustic microscope technology, from the standpoint of target diagnostics, is the need for planar samples and the lack of real-time processing. Current acoustic microscopes mechanically scan a planar sample point by point, store the data obtained, and then reconstruct the entire image at the end of the X-Y scan sequence. Because the planar sample is coupled to the acoustic lens through a fluid, the scan rate is limited to the maximum turbulence that can be tolerated in the image. For a phase measurement in a complex geometry, such as a laser fusion target, the scan rate probably will be unacceptably low. One solution to this problem is to combine the acoustic diffraction with deflection in the same transducer, as has been done with the scanning electron microscope.

To see if such a scheme would work, we wrote a two-dimensional computer code that simulates the magneto-elastic optics in an axially biased rod geometry. Using the magnetoelastic code, we could obtain significant deflection with moderate fields. It thus appears possible that an electronically scanned acoustic microscope is possible, and a patent disclosure describing this technique has been submitted. Components for a proof-of-principle experiment have been ordered.

MIRAS Development (K. Moore, D. Stupin). MIRAS is an automated system for detection of defects in laser fusion targets. X-ray images of the targets are digitized and analyzed in a computer, using sophisticated algorithms to determine the concentricity, sphericity, and smoothness of targets. We have made significant progress in operating this system.

The x-ray images are manipulated by placing the glass plate containing them in a fixture that is moved 2 μm per step of stepper motors. The motor controller operates either by hand or by computer control. The stages use optical encoders, providing a digital readout of position and unambiguous feedback to the controlling computer. All hardware and software to control the stages was completed.

The x-ray photographic images are magnified by a conventional Zeiss microscope and scanned by a Fairchild Charge-Coupled Device (CCD) TV camera. The TV images are subsequently digitized by a serial digitizer, and the data are read and stored by the computer. The digitizer produces 8 bits of data, or 256 gray levels of information. The images can be scanned, digitized, and summed repetitively to increase the signal-to-noise ratio, for example, and any image processing can be observed visually on a scan converter and TV monitor. All hardware and software to operate the video equipment and store the images have been completed.

The digitized images of the targets are analyzed quantitatively by a large program described in a previous report.[6] The program has been modified and installed on the controlling computer. The controlling computer is a Data General Corporation Eclipse 230, with 64 K of memory, 20 megabytes of disk storage, and 9-track magnetic tape unit. The computer has been tested and is operating satisfactorily.

Only the data-filing system and the actual operator-computer interfacing software remain to be debugged. When this has been completed, the operator will move to each x-ray image manually, examine the image on a TV monitor, and accept or reject the target. After all targets have been examined, the computer will return to each acceptable target, digitize and analyze it, and store the results. Sensitivities of 1% in nonconcentricity and 10% in bumps and dimples (10 μm^2 or larger) should be attainable.

Quantitative Gas and Chemical Analysis Using Laser Raman Spectroscopy (J. E. Barefield II, V. Cottles). The laser Raman spectrograph described in a previous report[1] has been assembled and checked out with N_2 gas. Experiments are in progress to obtain the Raman spectra of T_2, D_2, and DT gas inside of GMBs and to confirm that quantitative analysis of these gases is possible from measurements of spectral line broadening.

DEVELOPMENT OF INORGANIC COATINGS

General. Many future targets will require metal shells. To enhance our ability to respond to new design requirements, we are developing a variety of methods for applying various metal coatings to several classes of substrates. The substrates of interest are GMBs and Solacels, and the coating techniques include electro- and electroless plating, CVD, PVD, and sputter deposition.

Electroplating Process Development (A. Mayer)

The current list of prospective metals for radiochemical target coatings includes molybdenum, nickel, zinc, aluminum, and indium. Nickel, zinc, and indium can be plated from aqueous solutions. We have successfully plated nickel and nickel-phosphorous alloy onto

microspheres, but we have not yet attempted to plate microspheres with either zinc or indium.

We initially considered copper as the radiochemical detector metal. The method developed for fabricating this target was to electroplate a stalk-mounted GMB from a copper bath doped with ^{67}Cu. The GMB was mounted on an Aramid fiber stalk and flashed with PVD copper. The assembly was then electroplated from a small-volume bright-acid copper electrolyte while being rotated. This technique provides relatively uniform electrodeposited copper (Fig. VI-11). This particular target was not made because copper turned out to be unsatisfactory and because stalk-mounting prior to plating was undesirable.

We are continuing to evaluate various modifications in the apparatus for electroplating discrete microparticles[7] to improve its performance and versatility. To ensure better particle recovery, the porous ceramic tube has been replacd by a threaded Pyrex plating column. The anodes have been positioned behind a retaining screen inside the plating cavity to allow close anode-to-cathode spacing. We are trying various cathode contact designs to determine which design causes the least surface damage while the parts make and break contact. We are investigating various methods to produce optimum solution turbulence in the plating cavity to disperse and randomly rotate the particles as they move between the two retaining screens. If adequate solution turbulence can be induced, the column-packing medium, which can damage the fragile microspheres, may be eliminated.

Fig. VI-11.
Photomicrograph of cross section of stalk-mounted GMB flash-coated with PVD copper and then electroplated.

Electroless Nickel Plating of GMBs (A. Mayer)

Wet sensitization and activation in $SnCl_2$ and $PdCl_2$ followed by chemical nickel plating produced some excellent, relatively thick nickel coatings on GMBs.[1] However, when we attempted to apply thin coatings (1 to 3 μm) by the same process, we only obtained very poor coatings with many surface imperfections and varied thickness (as much as ±15% over the surface of the spheres). The poor surface is probably due to incomplete activation and/or poor adhesion between the glass surface and the nickel deposit; the thickness variations may be caused by a nonhomogeneous activation of the glass surface, which would cause the initial catalytic deposition reaction to occur at uneven rates. The time period in which deposition is not uniform may last until the whole surface is covered with a monolayer of nickel. This may be an appreciable fraction of the total deposition time for thin coatings. We tried unsuccessfully to wet-activate and plate numerous batches of unselected GMBs and four batches of selected DT-filled GMBs. A reliable dry metallization technique is probably needed for successfully plating thin layers of GMBs.

We are actively engaged in developing a process for uniformly sputtering a few hundred angstroms of an active metal onto the GMBs, which we can then plate with 1 to 3 μm of nickel. We have made two plating runs with nickel-sputtered GMBs (sputtering thickness, 250 and 500 Å). Generally, the background surface is smoother than that of wet-metallized glass, although small, isolated bare spots are still found (Fig. VI-12). The bare areas may be caused by contamination on the glass surfaces, by incomplete coverage in sputtering, or by the electroless coating process. We are developing practical cleaning and coating techniques for both empty and DT-filled GMBs.

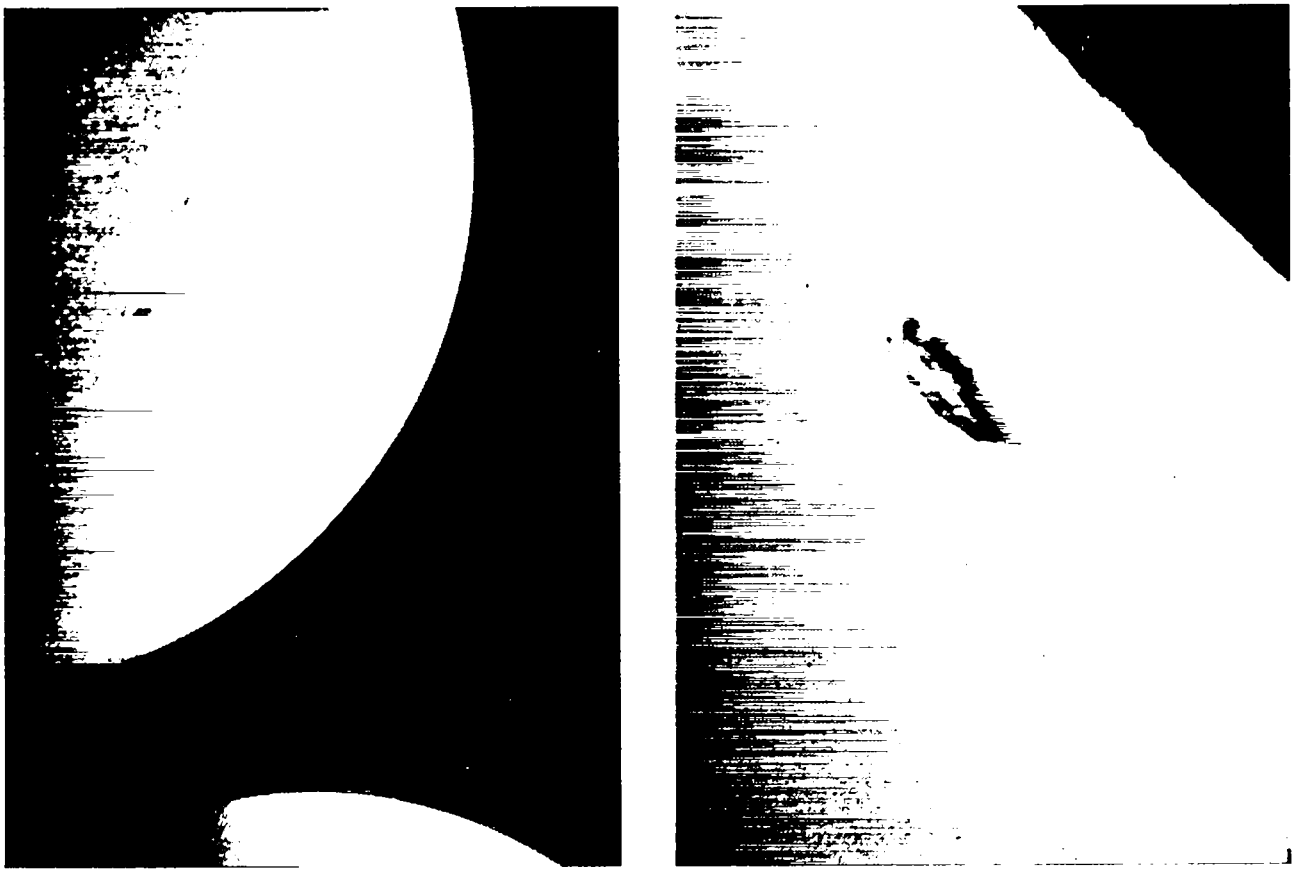

(a) (b)

Fig. VI-12.
Scanning electron micrograph (SEM) of a GMB sputtered with (a) 250 and (b) 500 Å of nickel. Bare spot probably is due to surface contamination.

Chemical Vapor Deposition (CVD) (W. McCreary, D. Carroll, J. Vogt)

General. We continued the development of CVD coatings for laser targets. Materials of interest were nickel from $Ni(CO)_4$, molybdenum dicarbide from $Mo(CO)_6$, and tungsten/rhenium from the fluorides. The coatings were formed on substrates of glass or metal in gas-fluidized beds. We have begun an extensive investigation into the behavior of fluidized-bed reactors.

CVD Nickel from $Ni(CO)_4$ (W. McCreary, D. Carroll). To deposit thin ($\leq$1 μm), relatively smooth CVD nickel on a few (~100) GMBs, we mix the GMBs with 1 to 3 cm^3 of carrier particles of different dimensions and then permit their separation by screening after coating. The process is adequate to deposit thin ($\leq$1 μm), relatively smooth nickel coatings, and ~75% of the GMBs can be recovered. However, some batches of large GMBs show multiple bare spots after coating, caused by carrier particles sticking to the GMBs and shielding small areas. The particles are coated in fluidized-bed reactors, using an inert gas for fluidization and for transporting the $Ni(CO)_4$ vapors into the heated bed. Typical coating conditions are

Bed Temperature (K)	Pressure (torr)	Carrier Flow (cm^3/min)	$Ni(CO)_4$ (g/min)
375-475	50-250	10-300	0.01

The GMBs are usually larger and more buoyant than the carrier particles and therefore ride high, that is, above the main body of the fluid bed. This fact complicates the coating process because $Ni(CO)_4$ pyrolysis and nickel

deposition occur mostly in the bed so that the GMBs are coated at a much lower rate than the carrier particles. In addition, excessive nucleation of the nickel atoms in the gas phase above the bed may contribute to nodule growth on the GMBs, especially on thicker coatings.

One small batch of GMBs was carefully cleaned by (1) washing in ethyl alcohol, (2) washing in 1-wt% Na_2CO_3 water solution at 363 K (90°C), (3) rinsing with H_2O, (4) washing in 0.5N HNO_3 + 0.1N NH_4F at 363 K, and (5) finally rinsing with H_2O and ethyl alcohol. These freshly cleaned GMBs were then coated along with 90- to 105-μm-diam glass beads and were free of uncoated spots. This indicates that small carrier particles did not stick to freshly cleaned GMBs. Additional tests should confirm that cleaning does solve the sticking problems.

Molybdenum di-Carbide Coatings from $Mo(CO)_6$ (W. McCreary, D. Carroll). We developed a procedure for depositing very smooth, nodule-free, thick (up to ~6 μm) Mo_2C Solacels. This method consisted of fluidizing the Solacels in a Pyrex apparatus under the following conditions.

Bed Temperature (K)	Pressure (torr)	H_2 Carrier (cm^3/min)	$Mo(CO)_6$ Temp (K)	P $Mo(CO)_6$ (torr)
575	200	200	323	~1.2

The H_2 carrier passed through the powdered $Mo(CO)_6$ and transported $Mo(CO)_6$ vapors into the reaction zone.

Attempts to adapt the Mo_2C process for coating a few selected GMBs in a carrier bed of small particles was partially successful. As with the nickel process, the major problem is fractionation of the particles, that is, the more buoyant GMBs ride high, above the most active coating zone, resulting in a lower coating rate and increased numbers of surface nodules. The results were somewhat improved by reducing the carrier gas flow to ~100 cm^3/min, which increased the mixing of particles in the fluid bed.

This work was continued with unselected GMBs (200-250 μm in diameter) mixed with 105- to 125-μm-diam Solacels, fluidized with lower flows of gas to improve particle mixing. Very smooth, nodule-free Mo_2C coatings were obtained. This procedure appears to be adequate for coating selected GMBs with Mo_2C.

CVD Tungsten 25 wt% Rhenium from WF_6/ReF_6 + H_2 (W. McCreary, D. Carroll). The chemical reduction of WF_6 to form tungsten coatings on metal spheroids in fluid beds is straightforward and produces smooth, strong, fine-grained metal under the following typical conditions.

Bed Temperature (K)	Pressure (torr)	H_2 (l/min)	WF_6 (cm^3/min)
700	~100	1-2	10-30

However, most hollow tungsten shells made in this process do not have sufficient strength to withstand the pressures desired.

Several molybdenum mandrels were coated with W/Re (tungsten-rhenium) to determine if W/Re shells are significantly stronger than pure tungsten shells. Coating conditions were similar to conditions listed above, except that a WF_6:ReF_6 ratio of ~3:1 was used. A rather spectacular laminar structure resulted (Fig. VI-13). Electron-microprobe analysis of the W/Re shell indicated a uniform increase in the W/Re ratio from the inside diameter to the outer diameter: as the coating progressed, it became richer in tungsten. The average composition was ~75 wt% W, 25 wt% Re.

Some of the W/Re shells were heat treated at 1475, 1875, and 2075 K and are being examined for any change in structure. Both treated and untreated shells will be tested with high-pressure D_2.

CVD Process Development (J. Vogt). To improve our fluidized-bed CVD coating process, we initiated a program to develop instrumentation for monitoring the real-time behavior in a fluidized-bed reactor. In such a reactor, under constant reactant-gas feed rates, the degree of bubbling in the fluidized bed will diminish as the density or size of the substrate increases with time, causing major changes in CVD coating conditions. These changes in fluidized-bed behavior are very pronounced for metal coatings on GMBs because a large density difference exists between the substrate and the coating.

We are developing instrumentation for monitoring the following CVD coating parameters: (1) the reactant-gas feed rate, (2) exhaust-gas temperature and gas composition, (3) reaction-zone temperature profile, (4) pressure fluctuations over the bed, and (5) variations in electrical properties of the fluidized bed from the pressure of rising bubbles.

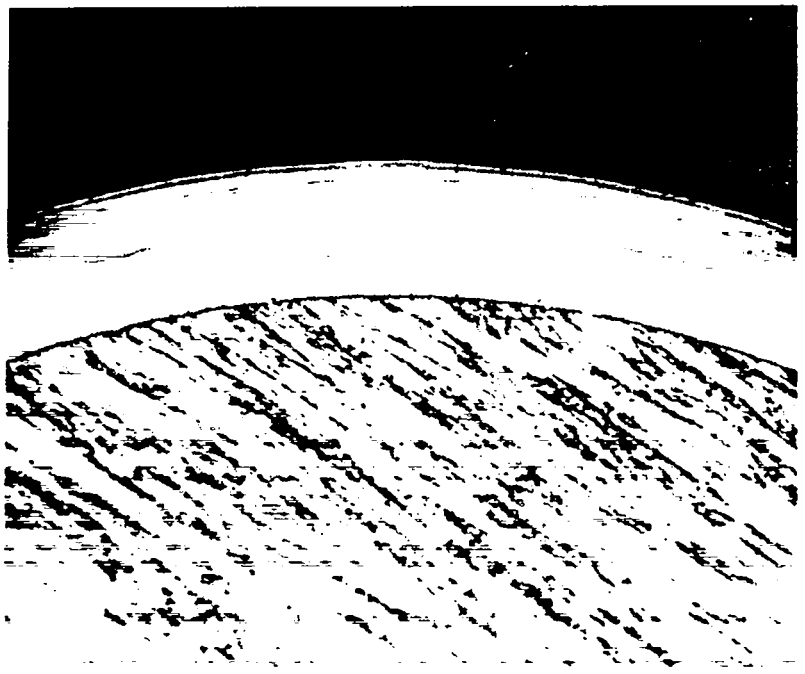

Fig. VI-13.
Photomicrograph of a section of a PVD coating (75 wt% W: 25 wt% Re) on a Ti/Zr/Mo mandrel. Rhenium content decreased as coating grew.

$W(CO)_6$ CVD Reduction by H_2. We are studying the CVD deposition of tungsten from $W(CO)_6$ on GMBs as an alternative to the WF_6 CVD process. In the earliest stage of WF_6 reduction by H_2, the GMBs are quite susceptible to a badly damaging HF attack. As an alternative we are proposing either to coat the GMBs by the $W(CO)_6$ process or to flash-coat them by the $W(CO)_6$ process for further coating by $WF_6 + H_2$ CVD deposition.

Only extremely thin, adherent, mirror-like coatings have been deposited; however, these thin coatings protect the surface of the GMBs from HF attack during $WF_6 + H_2$ CVD. The composition of the coating is not known because a satisfactory scheme for chemical analysis of the coating has not yet been found.

Physical Vapor Deposition (PVD) (W. Anderson)

Sputtered Coatings. Triode and ion-beam sputtering sources are now available in addition to the ring magnetron. We have almost completed a vacuum system for temporarily mounting our ion-beam source. This system will initially be used for an investigation of charging phenomena on levitated GMBs in a plasma environment. Delivery of an additional vacuum system, scheduled for late spring 1980, will allow mounting of both of the newer sources and initiating a parametric study of the factors affecting coating quality on spherical mandrels.

The ring magnetron, which has been used primarily for coating studies of levitated GMBs, is being equipped for a parametric study of coating quality on rotating hemispherical mandrels. This investigation will be performed with Battelle Northwest Laboratories as consultant.

Thermally Evaporated Coatings. We use thermal evaporation primarily for planar coatings and, to a lesser extent, for coating stalk-mounted GMBs and nonplanar substrates. To increase our efficiency, we are dedicating one evaporator to planar substrates only. We have fitted a second vacuum system with an electron-beam source and are equipping it as a vehicle for experimental investigations and as a coater for nonplanar substrates.

Photolithography. We have installed a small photolithographic facility and have established and characterized three standard photolithographic processes. Both positive and negative resist procedures have been characterized. Resolution appears adequate for current needs at 7.5-μm linewidth in the highest resolution process. Processes using relatively thick resist coatings have been emphasized because thick PVD coatings are needed for laser fusion diagnostic targets and military applications targets.

Levitation

Gas Levitation (J. Bunch). The molecular gas-flow levitation system developed by Liepins and Lowe[8] may allow the coating of GMBs with most metals by sputtering or other PVD or CVD methods without a support stalk that may cause perturbations during target implosion. The levitation coating process described earlier,[1] which used a dimpled collimated hole structure (CHS) with a magnetron rf sputtering system, was too slow to be practical for coatings thicker than ~1 μm and required undue attention by the operator to levitate the GMB initially and to control the gas flow precisely enough to keep it levitated. We have addressed the latter set of problems through refinements in levitation design, gas-flow control, GMB cleaning and preparation procedure, and development of an electronic "kicker" for breaking the initial attraction between GMB and CHS. We can levitate the GMB relatively easily now and are concentrating on improving deposition rates.

Bounce Levitation (J. Bunch). We have developed a method for bouncing GMBs in a loudspeaker cone driven at 100-200 Hz while they are sputtered with nickel by the rf magnetron. Bouncing in a cone is preferable to bouncing on a metal table for two reasons. First, the cone acts as a better acoustic impedance to GMBs than does a thick, massive metal table. Second, it is easy to drive the cone to larger amplitudes and at higher frequencies than the metal table, causing larger instantaneous accelerations of the support relative to the GMBs. We use this technique to produce thin (~250 to 500 Å) uniform metal coatings on GMBs as preliminary coatings for electroless nickel plating, to improve adhesion of gold or other coatings, and to facilitate initial levitation in the gas-flow system described above.

ORGANIC COATINGS DEVELOPMENT

General

Plastic coatings are routinely used as absorber/ablator layers on laser fusion targets. The important physical parameters for such coatings are uniformity of wall thickness and surface smoothness. The thickness of these coatings varies from about one to a few hundred micrometers. In addition, some target designs require the inclusion of high-Z elements in the coatings to shield the fuel from hot electrons. The density of these high-Z-loaded plastic layers should range from 1.3 to 2.3 g/cm^2.

Low-Pressure Plasma Process (LPP) (R. Liepins, J. Clements, J. Hammond, M. Campbell)

Thick Coatings. In previous work we demonstrated the ability to deposit multilayer coatings thicker than 100 μm.[1] Since then, we have tried to establish how physical and chemical properties of various monomers and background gases affect deposition rates. We found a strong correlation between electron impact ionization potential of the materials and the deposition rates: coating rates and thicknesses were inversely proportional to the ionization potentials of the monomer and/or the background gas. A new monomer, cyclooctatetraene, selected on the basis of these observations, produced a 40-μm-thick coating (limited only by the monomer supply) on our first try.

Other correlations of deposition rate with electron affinity, thermal decomposition temperature, activation energy for thermal decomposition, and activation energy for bond dissociation are being investigated.

Smooth Coatings. To achieve smooth surfaces (<30 nm p-v perturbations), we had controlled the smoothness of the deposition surface chemically by pulsing air into the chamber during the coating run.[7] We then found that the use of N_2O instead of air provides better control of the process and that deposition at 263 K (−10°C)

without air or N_2O produced very smooth coatings. This phenomenon is still unexplained.

Vapor-Phase Pyrolysis Process (VPP) (R. Liepins, J. Clements, J. Hammond, M. Campbell)

Smooth Transparent Coatings. In previous work we demonstrated the ability to deposit coatings with smooth surfaces (<100 nm p-v) by the copolymerization of 33 wt% 2-chloro-p-xylylene with p-xylylene.[9] With appropriate coating controls, we can now reduce the 2-chloro-p-xylylene concentration to as little as 10 wt% (2.5% actual chlorine content) and still obtain smooth transparent coatings more than 50 μm thick, with p-v perturbations less than 50 nm.

Coatings Loaded with High-Z Elements. VPP is also being used to develop the high-Z-element-loaded outer pusher shell for Polaris. We have deposited coatings up to 90 μm thick containing as much as 41 wt% chlorine or 44 wt% bromine. The monomers used were tetrachloro-di-xylylene and dibromo-di-p-xylylene, either by themselves or as copolymers with p-xylylene.

Coating of Bouncing GMBs. Attempts by others to VPP-coat bouncing GMBs have been largely unsuccessful.[10] Many methods of moving or levitating the GMBs were investigated, including coating nickel microballoons along with the GMBs, using a rotating twin-shell blender, tumbling in a glass vial attached to a rotating shaft, and bouncing by means of a mechanical vibrator. In all these attempts, the thickest coating obtained before agglomeration (GMBs sticking together) was only 0.1 μm.

We have built a deposition chamber with a platform attached to an electromechanical shaker. In initial runs we have achieved unagglomerated GMBs with coatings as thick as 1.6 μm. Modifications of the coating chamber should lead to even thicker coatings.

Development of Organometallic Coatings (R. Liepins, J. Clement, J. Hammond)

In previous work[9] we deposited organic coatings containing lead, tantalum, and iron on GMBs by the LPP process and produced coatings containing up to 30 wt% lead. This work has been extended to higher lead concentrations and to other metals. Some details are summarized in Table VI-I. Tetraethyl lead and dimethyl mercury were homopolymerized and copolymerized with p-xylene. The tetramethyl lead was copolymerized with toluene because it came as a solution in that solvent, whereas the trimethyl bismuth was copolymerized with p-xylene. We observed that the current density sustainable before the onset of arcing is inversely related to the metal content in the plasma atmosphere. For example, dimethyl mercury, which has the highest metal concentration (87%) in the molecule, sustained the lowest current density. Under arcing conditions, it is possible with dimethyl mercury to deposit an organic or organometallic coating filled with metallic mercury.

We obtained initial compositional data from films deposited on the electrodes. The low mercury values for the organomercury coating are attributed partly to analytical difficulties. (Mercury has a very strong tendency to form volatile organomercury compounds.) The higher-than-calculated bismuth concentration in the coating may be attributed to the higher vapor pressure of trimethyl bismuth (bp, 110°C) as compared to p-xylene (bp, 139°C).

We have increased the VPP coatings containing about 10 wt% iron[9] to coatings as thick as 221 μm and foresee no difficulties in depositing even thicker coatings.

Chemical Synthesis of Specialized Monomers (R. Liepins, D. Moreno)

4,16-Diobromo-di-p-xylylene. We prepared this material because it will yield a bromine-containing polymer that may be useful in making plastic shells containing a high-Z element. It was prepared from di-p-xylylene by dibromination in carbon tetrachloride in the presence of iron powder to obtain a 25% yield; however, the yield of all possible dibromo-derivatives was 91%. This is a complex synthesis because of the large number of di- and polybrominated derivatives possible, and the total number of isomers obtained has not been completely determined yet. We are using Nuclear Magnetic Resonance (NMR) spectroscopy to characterize this material.

4,16-Diiodo-di-p-xylylene. This iodine-containing monomer, intended for production of high-Z-element-loaded plastic shells, was prepared in a two-step reaction from 4,16-dibromo-di-p-xylylene. We first synthesized the corresponding dilithio derivative and then reacted this product with iodine to produce the desired monomer in a 60% yield.

TABLE VI-I

HIGH-Z METAL-LOADED PLASTIC COATINGS

Monomer Composition (wt%)	Appearance of Reflected Light	Coating Thickness (μm)	Metal Content (wt%)	
			Calculated	Found
$(C_2H_5)_4Pb$	Black	~3	64	44
$(CH_3)_4Pb$/Toluene (80.3/19.7)	Black	~3	62	56
$(CH_3)_3Bi$/p-Xylene (50/50)	Blue	5	41	44
$(CH_3)_2Hg$/p-Xylene (50/50)	Yellow	3.2	44	~3

5,5-Dimethyl-1-hexene. This monomer was prepared because our research indicated that it should yield a polymer with a bulk density below 0.80 g/cm^3, which is of interest in producing low-density foams. No simple synthesis exists for this compound.[11] We have devised a three-step synthesis, starting with the commercially available 5,5-dimethylhexanoic acid. At this time we have successfully prepared the alcohol product of the first step at a 90% yield.

ORGANIC FOAM DEVELOPMENT

Low-Density Microcellular Plastic Foam (A. T. Young)

Multiple shell targets, such as Polaris, require a hydrodynamic cushion layer between the metal shells to smooth transmitted shocks. A rigid low-density microcellular foam can be used for this purpose and also as the support structure. A foam for this shell layer should have a density less than 0.1 g/cm^3 (preferably less than 0.05 g/cm^3), a uniform cell size (~1-μm diam), and an open cell structure so that the voids can be filled with helium gas for cryogenic cooling of the DT fuel.

Earlier work involved the preparation of cellulose-acetate foams by a selective reverse-phase separation process.[12] Although cell sizes obtained were in the desirable range, densities of these foams were generally ~25% higher than theoretically expected (see Table VI-II). Attempts to duplicate these results at Monsanto Research Corporation[13] and more recently at Los Alamos have not been successful.

A contract study, conducted by Armak Research Laboratories in McCook, Illinois, has centered on a proprietary preferential phase separation process using a polymer (4-methyl-1-pentene) manufactured in Japan.[14] As seen in Table VI-II, foams obtained were 33% denser than theoretically predicted with uniform cell sizes of 8 to 10 μm (Fig. VI-14). The maximum theoretical void volume achieved by Armak to date is 94%.

After review of all methods for the manufacture of foamed polymeric materials, we decided that the most suitable process for our needs was induced reverse-phase separation of a polymer from a solution, followed by replacement of the solvent in the polymer microvoids by a suitable gas. The solvent selected for our initial study was water, and two processes to force the solvent phase to separate preferentially from the polymer phase have been studied.

The first process involved the desolvation of polymer in solution by crosslinking to produce the micro-reticulated structure commonly known as a gel. Droplets of solvent, in this case water, are trapped in microvoid areas in the gel matrix. Once a gel was obtained, the solution was rapidly frozen by immersion in liquid nitrogen, and the solvent was removed by freeze-drying. Aqueous gels of materials like polyacrylamidomethyl starch, gelatin, and a variety of formaldehyde resins yielded microcellular foams (Table VI-II). In almost all cases measured, foam densities were considerably higher than those calculated from the theoretical void volume.

The second process was more successful. Rather than crosslinking the polymer to form the gel matrix as we did in the first process, we forced the solvent to separate rapidly from the polymer by freezing an aqueous solution of the polymer in liquid nitrogen. The solvent was then removed by freeze-drying. This process yielded rigid microcellular foam structures with measured densities close to those we calculated for methyl cellulose, carboxy-methyl cellulose, and polyacrylamide. The foam

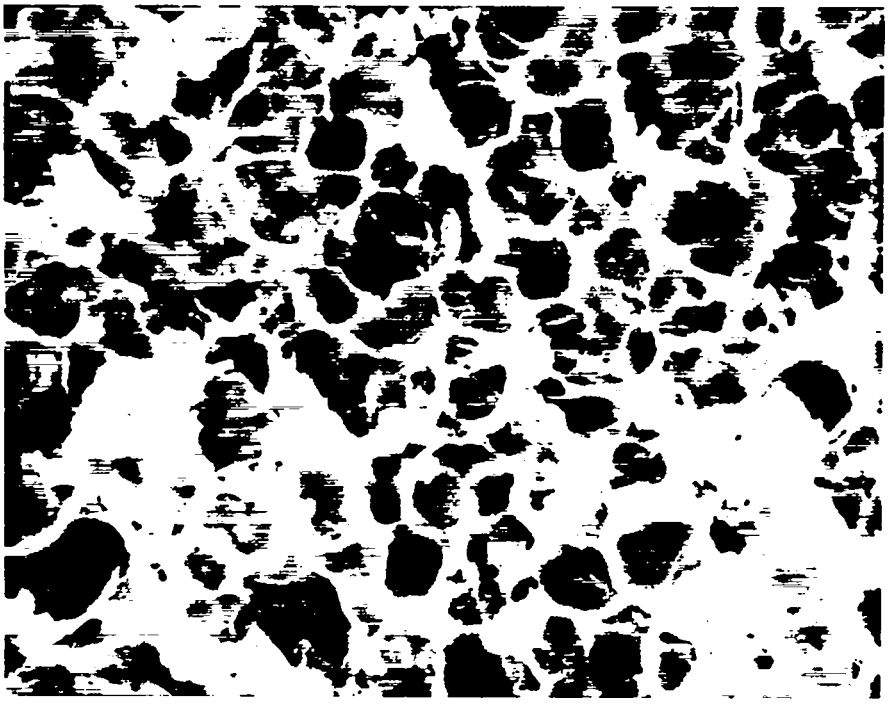

Fig. VI-14.
SEM of Armak-produced foam having a density of 0.11 g/cm^3 and a cell size of 8 to 10 μm.

TABLE VI-II

PHYSICAL CHARACTERISTICS OF MICROCELLULAR FOAMS

Foam Identification	Polymer	Polymer Density (g/cm^3)	Theoretical Void Volume (%)	Theoretical Density (g/cm^3)	Measured Density (g/cm^3)	Cell Size (μm)
Rinde-Stone	Cellulose acetate	1.3	95	0.065	0.08	1-2
Armak-91	Poly (r-Methyl-1-Pentene)	0.83	91	0.075	0.11	8-10
Armak-94	Poly (4-Methyl-1-Pentene)	0.83	94	0.050	0.10	Fused Flakes
ATY-15A	Polyvinyl formaldehyde gel	1.2	95	0.060	0.13	2
ATY-6	Polyacrylamido methyl starch gel	1.5	92	0.120	0.11	10
ATY-29	Carboxymethyl cellulose	1.6	99	0.016	0.016	Open Web 5-10
ATY-39A	Methyl cellulose	1.5	99	0.015	0.012	Open Web 10-20
ATY-45	Polyacrylamide	1.3	97.5	0.033	0.036	1-6
Limeil[15]	Dextran	1.0	95	0.050	0.05	1-2

structures at these high-void volumes are almost completely open, with the structure consisting only of ribs at the intersections of the faces of a regular dodecahedron, as shown in Fig. VI-15, which is a SEM of our polyacrylamide foam. This open cell structure should be very favorable as the cushion layer of a future laser fusion target because it would permit rapid, efficient cryogenic cooling of the DT-filled core.

Recently we learned that French researchers at the Centre D'Etudes De Limeil developed a low-density microcelluar foam by a similar process.* A 5-wt% solution of dextran (a bacterial polysaccharide by-product) in water is rapidly cooled in isopentane at 163 K (−110°C) and then freeze-dried to yield a microcellular foam whose density is reported to be the same as the theoretical density. This foam is being used in their target fabrication program.

*Dr. Alain Coudeville of the Centre D'Etudes De Limeil provided this information.

Gamma-Radiation Studies (R. Liepins, M. Campbell, D. Moreno, J. Clements)

Gamma-Ray Cross-Linking of Polymer Foams. In developing low-density microporous foam from water-extended polyester, we observed that the required small cell size could be generated in the emulsion but could not be maintained during curing. Regardless of the technique or material used, we always found some foam shrinkage in the final annealing and drying steps, apparently caused by microcell coalescence and growth.

Cross-linking the foam as it is initially formed by catalysis or by radiation should stabilize its cell size. In a radiation cross-linking study, we investigated three polymers irradiated by ^{60}Co γ-radiation: low-density polyethylene, high-density polyethylene, and an ethylene/propylene copolymer. The polymers were molded into 50- to 100-μm-thick films and were degased at 1.2×10^{-5} torr for at least 20 h before irradiation in

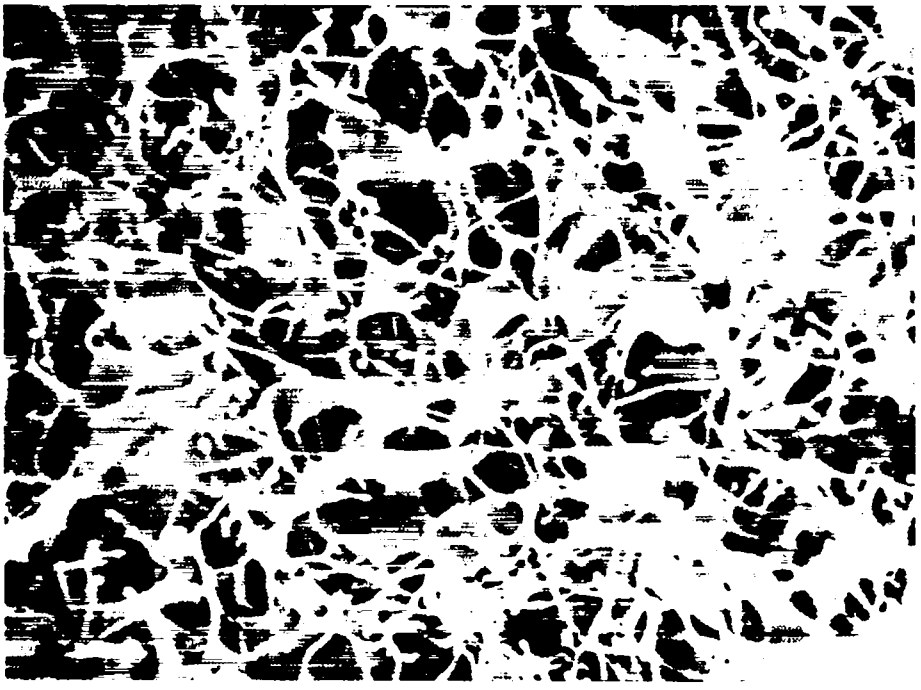

Fig. VI-15.
SEM of a Laboratory-produced polyacrylamide foam having a density of 0.036 g/cm^3 and a cell size of 1 to 6 μm.

evacuated (2.0×10^{-5} torr) glass ampules. The gamma-ray cross-linking efficiencies, determined by dissolution of the polymer in xylene, revealed that ^{60}Co irradiation should be very useful for cross-linking polyethylene foams, but probably not for the ethylene/propylene copolymer. Cross-linking by catalysis will be studied next.

Radiation-Initiated Polymerization. Radiation-initiated polymerization is another means of stabilizing as-formed foam cells. We have tried to polymerize two commercially available olefins: 4,5-dimethyl-1-hexene and 4,4-dimethyl-1-hexene. Initial attempts failed; however, the use of 10 wt% of methyl methacrylate comonomer with 4,4-dimethyl-1-hexene did result in the polymerization of the mixture. Future efforts will establish the effects of high-vacuum degasing, solvent additives, metal-oxide additives, and accelerators upon the polymerizability of these olefins.

LOW-DENSITY FIBER-BASED STRUCTURAL MATERIALS (J. V. Milewski)

Two major areas in advanced targets require low-density structural materials: a cushion of low-density plastic between the outer and inner pushers and a thin high-Z metal shell as an outer pusher.

Low-density plastic felts are being considered as back-up materials for plastic foams, and low-density thick metal felts of the same overall mass are being considered in place of thin metal shells to reduce hydrodynamic instability problems.

We are assuming that the felts will have to be made of submicron fibers so that the size of the solids and voids will be as small as possible and their distribution as uniform as possible. The preliminary evaluation of these low-density structural materials is being made on tenfold scaled-up models because submicron fibers of plastic and metal are more difficult and expensive to work with. On these larger models, we study the void content as a function of fiber length and binder content. We also study numerical and statistical values to characterize the void-to-solid distribution. A statistical package is being prepared for use in conjunction with image analysis.

We are using 4-μm-diam stainless steel fibers to make experimental 1- to 2-cm-diam metal-felt hemispheres. If the information developed at this scale is satisfactory, we plan to reduce the fibers to ~0.5-μm diam and use high-Z metals such as gold or tungsten to make 1- to 2-mm-diam hemispheres.

A similar scaledown is planned in producing low-density plastic felts. We are currently using 9-μm-diam polyester fiber to produce structures at 5% solid density.

Conceptual design of the automatic controller that will sequence the Helios cryogenic target-producing apparatus has been completed. Electrical layouts and panel designs are in process.

CRYOGENIC TARGET DEVELOPMENT

General

Laser fusion targets fueled with cryogenic liquid or solid DT offer the advantage of high initial fuel density without the disadvantage of diluent atoms being present as they are in room-temperature solids having a high hydrogen density [for example, lithium in Li-DT, carbon in $(CDT)_n$, or boron and nitrogen in NH_3BH_3]. In addition, calculations indicate that the yields from targets fueled with liquid or solid DT can be considerably higher than yields from targets of the same design fueled with high-pressure DT gas. Therefore, we actively pursued the development of cryogenic targets despite the significant experimental complications encountered in their fabrication and in their use in laser-target interaction experiments. We are testing the prototype cryogenic processing mechanism for loading and freezing these targets in the Helios target chamber.

Helios Cryogenic Target-Producing Prototype (J. R. Miller, J. T. Murphy, C. E. Cummings, J. B. Van Marter)

Tests on the experimental apparatus designed to produce cyrogenic targets in Helios continued. As described previously,[1] targets at room temperature will be loaded into the target chamber, processed by using the fast isothermal freezing (FIF) technique, and uncovered through rapid retraction of the cryogenic processing shroud just before laser irradiation.

Final design of the shroud retraction system has been completed. The entire assembly has been made coaxial (Fig. VI-16). A single latching magnet and linear shock absorber with two axial air bushings are used for improved performance. Drawings of this device have

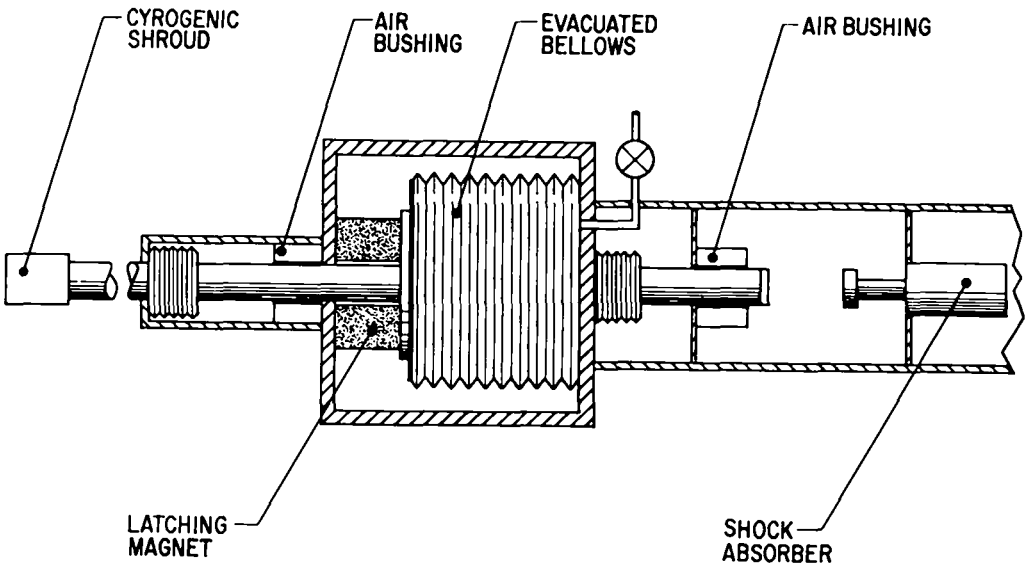

Fig. VI-16.
Redesigned cryogenic processing system for Helios.

been completed and are being checked before submission for fabrication.

PVT Measurements on Condensed T_2 (E. Grilly)

General. Future high-gain laser fusion targets may contain solid DT. Its behavior must be fully understood to design such targets. As part of this effort, we studied the PVT relationships of solid-to-liquid phase changes for T_2.

Experimental Results. The melting curve of tritium with varying orthotritium (o-T_2)/paratritium (p-T_2) ratios was measured up to 70 bar at 22.1 K. Extrapolation to normal tritium (75% o-T_2) gave melting pressures P_m that agreed with our earlier measurements. Because of ortho-para self-conversion, P_m increased with time. The rate of increase was consistent with a second-order reaction, similar to that in H_2 but three times faster. The difference in P_m between ortho and para forms is ~5 bar. Also, because the ortho and para molecules tend to fractionate between the liquid and solid phases, true equilibrium is not obtained in a reasonably short time, and P_m increases with time. At 37% o-T_2 and 21 K, the rate of increase in P_m was constant (about six times that observed earlier for 61% o-H_2 at 15 K).

Measurements of the volume change when T_2 melts and the thermal expansion and compressibility coefficients for liquid and solid T_2 are consistent with those for H_2 and D_2. Again, the background density changes from ortho-para conversion indicated a second-order reaction in contrast to outside evidence that the reaction is first order below 15 K. The increased rate in T_2 over that in H_2 near the melting curve can be explained simply by the greater nuclear magnetic moment in tritium and obviates the assumption that the rate is affected by electrons, ions, or atoms. Impurities such as H_2, HT, DT, and ^3He were removed by a technique that used an adsorption column of cold activated alumina, similar to one first developed at Los Alamos to prepare pure o-H_2 and p-D_2. The T_2 used in the present experiments usually contained only 0.1% H.

REFERENCES

1. Roger B. Perkins and the Inertial Fusion Program Staff, "Inertial Fusion Program, January 1—June 30, 1979," Frederick Skoberne, Comp., Los Alamos National Laboratory report LA-8114-PR (June 1981).

2. Roger R. Stone, "Measurement of Laser Fusion Capsules Using the Interferometer Method of Excess Fractions," Lawrence Livermore National Laboratory report UCRL-51788 (April 7, 1975).

3. R. J. Fries and E. H. Farnum, "Non-Destructive Fuel Assay of Laser Targets," Nucl. Instrum. Methods 126, 285 (1975).

4. W. B. Rensel, T. M. Henderson, and D. E. Solomon, "Novel Method for Measuring Total Pressure of Fuel Gas in Hollow, Glass Microshell Pellets," Rev. Sci. Instrum. 46, 787 (1975).

5. John R. Vig and John W. LeBus, "IEEE Transactions on Parts, Hybrids and Packaging," PHP-12, No. 4, 365 (December 1976).

6. R. L. Whitman, R. H. Day, R. P. Kruger, and D. M. Stupin, "Microradiographs of Laser Fusion Targets: 2-D Modeling and Analysis," Appl. Opt. 18, 1266 (1979).

7. "Inertial Fusion Program, January 1—June 30, 1978," Frederick Skoberne, Comp., Los Alamos Scientific Laboratory report LA-7587-PR (May 1980).

8. R. Liepins and A. Lowe, "Coating of Levitated Glass Microballoons," Polymer-Plastic Technology and Engineering 15, 51-60 (January 1980).

9. Roger B. Perkins and the Laser Fusion Program Staff, "Inertial Fusion Program, July 1—December 31, 1978," Frederick Skoberne, Comp., Los Alamos Scientific Laboratory report LA-7755-PR (November 1980).

10. J. W. Havenhill, "1973 Laser Target Activities," The Bendix Corporation Topical Report on Contract PD06984876 BDX-613-1087 (February 1975).

11. S. P. Melnikova and L. N. Vorobev, "Hydrogenization of tert-Butyldiacetylene in Stages," Zh. Org. Khim. 8, No. 2, 252 (1972).

12. J. A. Rinde and R. R. Stone, "Preparation and Fabrication of Low-Density Microcellular Foam Laser Targets," Lawrence Livermore National Laboratory report UCRL-51708 (January 1975).

13. C. E. McClug, J. L. Schwendeman, T. A. Orofino, S. M. Sun, and A. L. Wirstner, "Development of Small Cell Sized/Porous Structures," Monsanto Research Corporation report MRC-DA-848 under UCRL Contract LP8-4470D-1 (December 1978).

14. A. Castro, "Microporous Polyolefins, Second Progress Report," Armak Co., Research Laboratories-Polymer Section, Project 16,213 (August 1979).

VII. DIAGNOSTICS DEVELOPMENT
(D. Giovanielli)

The tiny volume and brief duration required by the laser fusion process create the need for new diagnostic techniques having spacial and temporal resolutions in the submicrometer and 1- to 100-ps regime, respectively. This need is being met with a vigorous diagnostics program in such areas as laser calorimetry, charged-particle and neutron detection, x-ray spectrometry, and subnanosecond streak-camera development.

INTRODUCTION

Diagnostics development, data acquisition, and data analysis provide the foundation for viable present and future experiments.

The quality of soft x-ray measurements has increased during this reporting period because of both improved XRDs and improved data analysis. We have developed an x-ray intensifier using microchannel plates (MCPs) that should significantly lower the threshold in present experiments using K_α imaging and open the way for much better experiments. We expect to apply x-ray imaging CCD arrays to our experimental problems.

Thomson parabola measurements of the charge-to-mass ratio of ions emitted from laser-produced plasmas have provided useful information on laser-matter interaction for years, but data analysis has been very tedious. We discuss a new photographic technique for pictorial presentation of the data. We are also implementing an automatic digital analysis.

Fiber optics is revolutionizing the communications industry. We describe the first direct use of fiber optics for laser-plasma diagnostics. We believe it can be used for the direct coupling of electron spectrometer scintillators to fast electronic recording devices.

We report numerical analyses of both x-ray data and x-ray image simulations and document the continuing evolution of our digital data-acquisition system.

X-RAY DIAGNOSTICS

X-Ray Diagnostics Development in Support of the Inertial Fusion Program (K. Mitchell)

Multiflex. We completed the design and construction of the major components of the fast multiple low-energy x-ray detection system (multiflex), which contains seven x-ray channels that are filtered for broadband response at discrete energies ranging from 50 eV to 1.5 keV. The detectors are fast XRDs, capable of yielding a temporal resolution of 100 ps. We are installing this system on the Helios target chamber. The signals will be recorded by high-frequency oscilloscopes in a new screen room close to the Helios target chamber.

We determined the efficiencies of micromachined aluminum photocathodes in the ranges of 1-10 Å and 50-500 Å. The long-term (4-month) stability of these surfaces was significantly better than that of standard machined aluminum samples previously tested.

Development of a High-Energy X-Ray Detection System. Using Helios, we conducted signal-to-background tests with four fluor-photomultiplier detectors filtered from 20 to 70 keV on 30 targets. These tests used GMBs, plastic-coated GMBs, and spherical gold targets. The background signals were strongest from gold targets; they were comparable to signals from the K-edge-filtered channels. However, on lower-Z targets, the background channel signals were 10 to 20 times as strong as signals from the filtered channels. The high background noise is a formidable problem that must be overcome in more advanced designs of high-energy x-ray systems.

X-Ray Image Intensifier (D. van Hulsteyn, S. Whitehill)

We constructed and tested a device for x-ray intensification. The device (Fig. VII-1) uses a MCP as a gain producer. Photons striking the front cause photoemission of electrons within the glass channels in the plate. The applied voltage potential causes a multiplication of the secondary electrons produced by the initial photoemission as they pass through the channels (Fig. VII-2).

This process resembles that occurring in a conventional photomultiplier tube and results in a voltage-dependent gain. Typically, the current gains in the MCP are $\sim 10^3$ and $\sim 10^4$ for supply voltages of 750 and 950

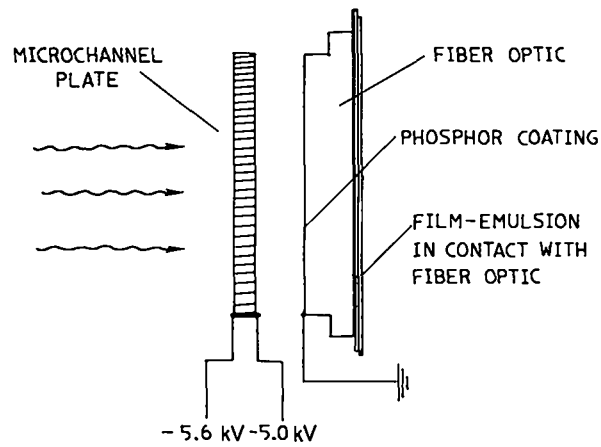

Fig. VII-1.
X-ray image intensifier showing principal components.

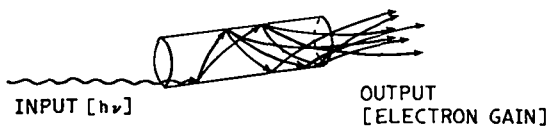

Fig. VII-2.
Photo-emission electrons caused by x rays accelerate under applied voltage and produce secondary electrons. Result is a voltage-damaged gain.

V, respectively. The electrons leaving the MCP are accelerated through a 6-kV electrostatic field over a distance of 2 mm to an aluminized phosphor surface. The phosphor converts the MCP emissions into blue light that is transmitted by fiber optics to a film emulsion.

Major features of this system are (1) lead glass tubes 25 μm in diam, which places a lower limit on spacial resolution; (2) absence of a photocathode, in the conventional sense, because x-ray conversion takes place in the plate itself; (3) proximity focusing, where typically 5 kV applied across 2 mm prevent significant electron spreading; and (4) an intensifier gain that is a product of conversion efficiency, MCP gain, and phosphor gain.

Our objective is to image x rays in the 1- to 10-keV range. As the incident photon energy is changed, the only quantity that varies in effective gain is the conversion efficiency. In future tests, we will use our Henke tube facility to determine the functional dependence of conversion efficiency on photon energy. In the interim, however, we used broadband emission from a copper anode source. We found film exposed when the Henke source was operated at 80 mA and 10 kV, with a 0.033-cm aperture placed 10 cm from the anode and 71 cm from the intensifier. With the MCP voltage at 600 V, a 5-s exposure produced an image of the anode.

An independent calibration of the source indicated that a piece of Kodak 2490 x-ray-sensitive film placed at the same location as the intensifier face would have required an exposure in excess of 1 h to produce the same optical density. Hence, the sensitivity was improved by a factor of 800. Alternatively, we estimate that a single x-ray photon incident on the MCP produces 2000 blue photons from the phosphor. We, therefore, demonstrated that significant image enhancement is possible from a dc source.

Using Gemini, we performed dynamic tests on the x-ray intensifier system to determine whether we could obtain strong K_α images from laser-irradiated targets. This was our first attempt to measure both the hot-electron spectrum and the preheat by the imaging technique. However, we encountered severe problems. First, in the Henke-tube tests, the intensifier was subject to electrical noise that increased as a function of applied voltage and of the time over which the voltage was applied. Initial efforts to gate the system were not very successful.

Second, the x rays produced by CO_2 laser irradiation of a target are created in a time of $\sim$1 ns, which creates a nonlinear saturation effect because the recovery time of the MCP is relatively long. Finally, because of high-energy x rays (>100 keV) in the chamber, we were concerned about the possibility of severe background noise on the film, but lead/plastic shielding appears to have eliminated this problem.

The image intensifier, as used in Gemini, produced an image with a 0.033-cm-diam aperture. In this case, the target was a 2-mm titanium square 0.0025 cm thick, with the single south beam focused at the center. The intensifier was located on the backside, 60° off target normal in the horizontal plane. The film-to-aperture and aperture-to-target distances were 182 and 23 cm, respectively, resulting in eightfold magnification. Finally, a 0.0025-cm-thick titanium filter was installed over the aperture.

The image showed a bright central spot, which appears to be a radiograph of the aperture, and a much dimmer background, which is an image of the faintly glowing titanium square. The bright spot was assumed to be primarily titanium K_α radiation because it was

detected on the backside of the target and passed through the 0.0025-cm titanium filter. The image was severely obscured by the MCP noise mentioned earlier.

The device, with modifications, can be used for K_α imaging. We are currently modifying it and expect to have it operational within a few months.

X-Ray Imaging Charge-Coupled Device (CCD) Area Array (P. D. Rockett)

A contract for the development of an x-ray sensitive, imaging CCD, placed with the Westinghouse Advanced Technology Laboratory in January 1979, produced a substantially new CCD with high x-ray sensitivity over a large spectral region (1.2 to 10.0 keV). This CCD is designed to supplement or replace film as a recording device in x-ray pinhole cameras and x-ray spectrographs. Its digital output will be read to a PDP 11/70 computer, where an analysis program will reconstruct the x ray on a video terminal in virtually real time.

The Westinghouse CCD has a depletion layer 200 μm thick with a 100 by 200 array of picture elements (pixels), each 20 μm square. The device is back-side illuminated through an extremely thin dead layer. The thin dead layer permits penetration of low-energy x rays (~1.2 keV), and high internal electric fields ensure minimal charge spillover to adjacent pixels. The large depletion depth results in high sensitivity at 10 keV, yielding a device with high quantum efficiency over a large spectral range. Imaging was recently completed with a copper K_α source, which showed a sensitivity higher than that of medical no-screen film.

Measurements have verified spacial resolution and background noise requirements. A resolution of <40 μm has been measured optically, and an extensive noise measurement as a function of temperature has been completed (Fig. VII-3). The noise at 200 K is so low that slow clocks and conventional Analog-to-Digital Converters (ADCs) can be used to read out the image data.

During 1980, Westinghouse will complete the spectral characterization of the CCD, design and build the off-chip electronics, and assemble them into a compact unit with the CCD. We also hope to demonstrate imaging of a laser plasma in its own x rays within narrow spectral regions.

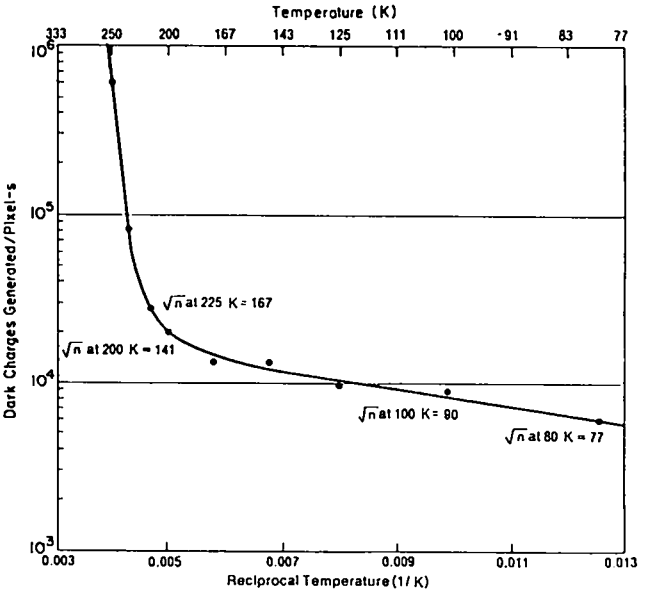

Fig. VII-3.
Dark charge generation as a function of temperature for 200-element line array. Pixel size, 60 by 20 μm.

A Novel Photographic Method to Record Images from Cellulose Nitrate Film (F. Begay; J. M. Grilly, H-DO)

In laser-matter interaction experiments, cellulose nitrate film* is widely used to record ions (protons and heavy ions) produced in laser-induced plasma.[1] In particular, we use the cellulose nitrate film as a particle counter in the Thomson parabola spectrograph[2] to detect protons and carbon ions produced in a CO_2-laser-induced polyethylene (CH_2) plasma.

The ions leave tiny tracks (track diameters, 10 μm or less) on the surface of the cellulose nitrate film, which are difficult to see with the unaided eye. A good photographically reproduced image of the data was desired to facilitate a preliminary qualitative analysis. Therefore, we developed a novel photographic method of using dark-field illumination to produce a high-contrast image of the tracks. (Dark-field illumination is widely used in optical microscopy.[3])

In dark-field illumination, the central portion of the light beam is blocked with a dark-field stop whose

*Kodak-Pathe cellulose nitrate film is available from Eastman Kodak Co., 343 State St., Rochester, NY 14650.

numerical aperture is equal to, or smaller than, that of the camera lens. In this method, the image is formed by light that has been scattered, reflected, and diffracted from the primary light beam by the object; that is, all direct light is excluded from reaching the cellulose nitrate film and the camera lens. Track detail thus shows up as a bright image against a dark background. The effective numerical apertures of the dark-field stop and of the camera lens are a measure of the light-collection efficiency of the photographic system.

The basic apparatus (Fig. VII-4) for this method of photography includes a light source, a dark-field stop, a film holder, and a camera. The distances between the different components and the size of the dark-field stop (Fig. VII-4) were adjusted to optimum light collection efficiency at the camera.

Ion data from the same polyethylene (CH_2) plasma experiment obtained with two different photographic methods are shown in Fig. VII-5. The data are a series of parbolic traces where each parabola determines a charge-to-mass ratio, Z/M, and its associated ion velocity distribution.[3] A conventional image recorded on contact film is shown in Fig. VII-5(a), whereas a dark-field image is shown in Fig. VII-5(b). Note that the dark-field illumination produces higher contrast than standard photography, and thus more detail.

Dark-field photography has proven to be a valuable tool in the examination and analysis of ion data recorded on cellulose nitrate film in laser-induced plasma experiments.

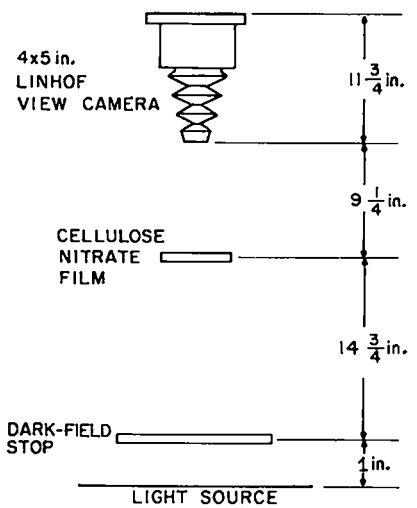

Fig. VII-4.
Apparatus for dark-field photography.

Fig. VII-5.
Image of ion tracks obtained by (a) conventional contact photography and (b) dark-field illumination.

FIBER-OPTICS TECHNOLOGY

Fiber-Optic Diagnostic Instrument for Electron Measurement (T. H. Tan, A. Williams)

We developed our first diagnostic instrumentation using optical fibers rather than metallic coaxial cables for signal transmission. As a modest beginning, we built an electron detector assembly capable of measuring electron energies from a few kilovolts to 1 MeV and measuring electron emission time profiles to a few hundred picoseconds. As shown in Fig. VII-6, the assembly consists of a magnetic spectrometer, collimators, scintillators, optical fibers, and photodetectors. Oscilloscopes with gigahertz bandwidths are used to record the detector output signals and to provide temporal information on the electron-generation history. To economize on the number of oscilloscopes used, the signals from different detector channels are delayed so that they arrive at one oscilloscope at different times. This is accomplished simply by varying the fiber length of each channel. The

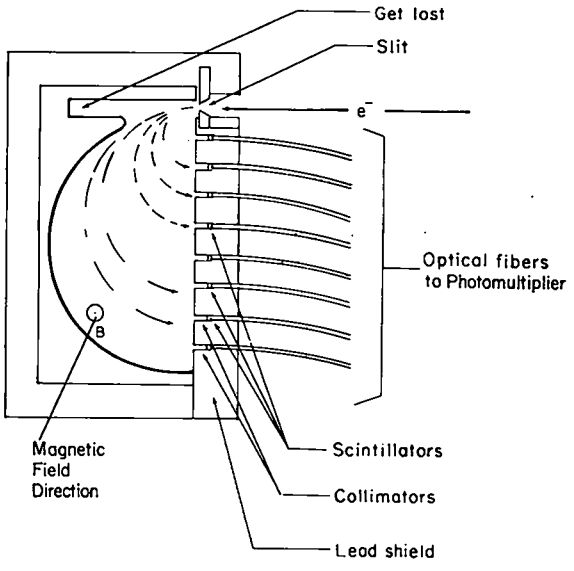

Fig. VII-6.
Magnetic spectrometer for measuring electron energy and emission time profile.

gain and the speed of the detectors can be adjusted by using scintillators having different quenched fractions and different types of photomultipliers and multichannel plates. Several channels can be allocated for background measurements. Thus, even if a nonnegligible amount of background noise exists, it can be properly subtracted.

This device will soon be tested at Gemini. Successful measurements will open new vistas for rapid development of other fiber-optic diagnostic instruments that would affect Antares.

Spectral Reduction (W. Priedhorsky)

The present XRD array for Helios spans the 0.03-2.0-keV range (nearly two decades) with at most five detectors. These data have been fitted by iterative reduction programs[4] in which an array S_i, defining the spectrum at i points, is fitted to the measured signal array M_j, known at j points. The problem is to invert the detector equation,

$$\varepsilon S = M \ , \qquad \text{(VII-1)}$$

where ε_{ji} is a matrix defining the detector response functions. In our case, the number of spectral points i required to define the spectrum smoothly over two decades in photon energy is much larger than j. The inversion problem is badly underdetermined and thus unstable. If we choose i small enough that $i < j$, the shape of the spectrum S is strongly affected by the choice of bins i.

We have, instead, chosen to reduce the data by fitting them to an assumed spectral form and finding the best parameter fit for that form, corresponding to the minimum variance χ^2. This form of analysis is often used in x-ray astronomy.[5] In such a parameter-fit analysis, one is limited to a spectral form that may not represent the actual spectrum. Even if the fundamental spectrum has an analytical form, such as a Planckian or bremsstrahlung, it may be distorted by temporal or spacial integration and spectral lines. However, the acceptability of a given spectral form may be tested routinely on the best $\chi^2 = \chi^2_{min}$ for that form. If χ^2_{min} is acceptable, the spectral form is adequate to fit the data, and it is as acceptable as any nonanalytical fit. If χ^2_{min} is acceptable, the range of acceptable parameters for the fit are those for which $\chi^2 < \chi^2_{min} + \chi^2_p$, where χ^2_p is the allowed range of χ^2 as defined below.

To reduce broadband spectral data, one must know the detector calibrations. In pulsed detection, detector response is the signal per unit incident energy (C/J) as a function of photon energy. For an XRD, the response is simply the product of the window transmission and the cathode response (C/J). Cathode response has been measured by R. H. Day et al.[6] and is repeatable to ±10% for newly machined aluminum cathodes. We use this nominal aluminum cathode response for all cathodes. Window transmission is determined either by weighting a known window area and using the absorption data of Veigele,[7] or by measuring x-ray transmission at selected points and interpolating, with the same absorption data, to obtain the full transmission function.

Detector signals are measured on fast oscilloscopes. The signal in a pulse is obtained by integrating the area under a trace photograph.

All data are reduced on a PDP-11/70 computer. The reduction program, VARYSP3, is a semiautomated interactive program that allows the user to test various spectral forms and parameters on a given data set. A single set of parameters or a parameter scan may be selected by the user. The spectral forms available are bremsstrahlung, blackbody, bremsstrahlung plus blackbody, and two-component bremsstrahlung.

For each test fit of the data, the user enters one or a series of spectra of the form

$$F(E) = Cf \qquad \text{(VII-2)}$$

or

$$F(E) = Af + Bg \ , \qquad \text{(VII-3)}$$

where A, B, and C are normalization constants, and f and g are analytical spectral forms (J/keV-sr). For example, a blackbody spectrum has the form

$$f = f(kT) = \frac{E^3}{e^{E/kT}-1} \ . \qquad \text{(VII-4)}$$

The detector matrix, $S_i(E)$, is used to calculate

$$calcf_i = \int S_i(E)\, f(E)\, dE \qquad \text{(VII-5)}$$

and

$$calcg_i = \int S_i(E)\, g(E)\, dE \ , \qquad \text{(VII-6)}$$

where S_i is the sensitivity of detector i at energy E.

Because the spectra F(E) are linear functions of the analytical forms f and g, the best-fit normalization factors can be calculated analytically. For example, in a one-component fit,

$$C = \frac{\sum_i x_i.calcf_i/\sigma_i^2}{\sum_i calcf_i^2/\sigma_i^2} \ , \qquad \text{(VII-7)}$$

where x_i and σ_i are the signal and probable error associated with detector i.

The best fit for a given set of nonlinear parameters (kT) or (kT_1, kT_2) is obtained by substituting the optimum C or A, B into

$$c_i = C.calcf_i \qquad \text{(VII-8)}$$

or

$$c_i = A.calcf_i + B.calcg_i \ , \qquad \text{(VII-9)}$$

where c_i is the best fit calculated signal for channel i. We then calculate

$$\chi^2 = \sum_i \frac{(x_i - c_i)^2}{\sigma_i^2} \ . \qquad \text{(VII-10)}$$

For a blackbody spectrum, the total emitted energy is given by

$$L_{blackbody} = 4\lambda \frac{\pi^4}{15}.C.[kT_{(keV)}]^4 \ . \qquad \text{(VII-11)}$$

The normalization constant C is proportional only to the blackbody area and to the emission time Δt. For a spherical emitter of radius r,

$$C = 1.58 \times 10^7\, (r_{cm})^2\, \Delta t_{ns}\ (J/sr\text{-}keV) \ . \qquad \text{(VII-12)}$$

The user scans (kT) or (kT_1, kT_2) to find the parameter set yielding the minimum $\chi^2 = \chi^2_{min}$ for the spectral form. The acceptability of the form is then tested by standard χ^2 criteria. For example, a blackbody fit to five detector signals has two free parameters (kT, C) and, thus, three degrees of freedom. In this case, χ^2_{min} must be less than 3.4 to be acceptable at a 1-σ level of confidence.

The χ^2 criteria for the acceptable range of spectral parameters, given a spectral form, are derived in Ref. 1. For a given spectral form, all sets of parameters that satisfy $\chi^2 < \chi^2_{min} + \chi^2_p$ are acceptable; χ^2_p is obtained[1] for a given confidence level and number of free parameters. If, in the example above, $\chi^2_{min} = 3.0$ is the best fit (kT_0, C_0), any parameter set (kT, C) that satisfies $\chi^2_{min} < 5.3 = 3.0 + 2.3$ is acceptable at the 1-σ level of confidence.

Because the normalization factors C or A, B can be optimized analytically, VARYSP3 calculates $\chi^2(kT)|_C$ or $\chi^2(kT_1, kT_2)|_{A,B}$, where $|_C$ indicates that χ^2 is optimized over all C. The confidence limits on kT or kT_1, kT_2 are thus immediately available from the program output. Confidence limits on C can be calculated analytically by the following formula:

$$\chi^2(kT, C) = \chi^2(kT)|_C + \frac{C}{(C_o - 1)^2} \left[\sum_i \left(\frac{x_i}{\sigma_i}\right)^2 - \chi^2(kT)|_C \right] \ . \qquad \text{(VII-13)}$$

COMPUTER TECHNOLOGY

Mathematical Modeling and Code Modification (M. M. Mueller)

Improved Iterative Integral Technique for Reconstructing Spherical Source Emission Profiles. The iterative integral technique developed previously[8] was

improved in several significant ways, based in part on experience in fitting actual data. The calculation of the radiance distribution from spherical sources was revised. (The iterative method works better with histogrammic, as opposed to analytical, representation of the source emission model.) Convergence was improved by modifying the constraints. The final histogram was replaced by a fitted smooth curve, which can be digitized at an arbitrary number of points. This smooth emission curve produced an image irradiance distribution that has a maximum deviation of a few percent (except in the extreme tail) from that produced by the final histogram. Thus, although the fitting procedure itself is best carried out with a fairly coarse source histogram (10-15 cells, typically), the final result is about the same as if a particular (fitted) smooth curve had been used.

A Photographic-Image Simulation Algorithm. For direct visual comparisons with photographic x-ray images of imploded targets, we need to simulate those images by using a particular source model, along with the actual imaging geometry used in the experiment. Therefore, we developed an algorithm for both slits and circular apertures that produces a simulated image by plotting dots in a randomized manner consistent with the irradiance distribution in the image.

The results often bear striking resemblance to actual pinhole photographs if the asymmetries present in the latter are averaged out. An example is given in Fig. VII-7, which simulates the pinhole image for a GMB target containing unseeded fuel. The emission model has a hollow core with a diameter 0.16 times the diameter of the unimploded glass shell, and the pinhole diameter is 0.08 times the diameter of the unimploded shell. Note some dimness at the center (caused by the hollow core) despite the relatively large pinhole. This would not be the case with a slit image, even with perfect resolution.

A Faster Convolution Algorithm. Because the iterative integral (model-adjusting) method could become a routine diagnostic of compressed cores in laser fusion experiments, computational efficiency is important. Iterative fitting with the aid of the PDP-11/70 computer system would be particularly advantageous but would require a tenfold reduction in computation time. We decided that this reduction is important enough to warrant the development of a new computational approach to two-dimensional convolutions.

The algorithm developed previously is purely numerical. It has served our needs well and has the advantage

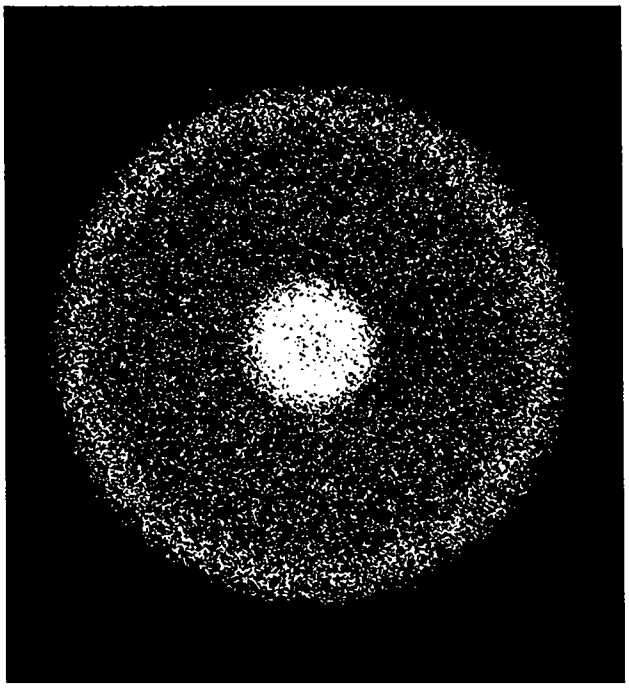

Fig. VII-7.
Simulated pinhole image of an imploded GMB target containing unseeded fuel of a low atomic number. The emission model has a hollow core with an inner diameter 0.16 that of the unimploded glass shell; the pinhole diameter is 0.08 that of the unimploded shell.

of broad generality. However, the bulk of our requirements could better be met by a much faster algorithm restricted to a circular aperture, viewing a generally nonuniform disk of radiance.

Such an algorithm is feasible if one uses a quasi-analytical approach; that is, analytical expressions are coupled with routine numerical integration. Although this approach is straightforward, it is rendered tedious by complicated boundary conditions. A new convolution code was constructed around this quasi-analytical approach and is working well for sources of arbitrary spherical symmetry. We constructed it for generalization in polar coordinates to handle sources giving a nonradial radiance distribution.

The payoff is in faster execution time: depending on circumstances, the new code is 4 to over 30 times faster than the old one. It is typically 10 times faster for the pinholes and the targets we normally employ. Thus, for nearly all our pinhole images, it should be possible to carry out the iterative fitting on the local PDP-11/70 system.

This new approach was also applied to the problem of slit imaging, which is considerably simpler; however, in

this case, computation speed was increased only two- or threefold. This is not very signficant, especially if one considers the rather fast execution times of the old code. Nevertheless, our work produced an important spinoff: an exact, closed analytical expression for the irradiance distribution in the image formed by a slit viewing an optically thin, homogeneous sphere of emission. This result should prove most helpful in least squares fitting of spectral-line spacial profiles from seeded compressed fuel.

Fitting of Spectroscopic X-Ray Data from Argon-Seeded Compressed Targets. Using a modification of the convolution code developed to simulate slit images, we successfully fitted the spacial profile data for two argon lines from two different shots by assuming the source was a homogeneous sphere of emission. The particular lines were selected for minimal self-absorption, and the success of the homogeneous-sphere model indicates that absorption is indeed negligible for these lines. Existing slight systematic deviations can be interpreted as being caused by somewhat augmented emission from the center of the compressed core. This demonstration of negligible self-absorption for some lines is important because it indicates that significant x-ray information can be retrieved from the central region of compressed high-density targets.

Our diagnostics data center provides the following services in support of laser target experiments.

(1) The center maintains computing capability for analysis of experimental data. Timesharing is managed on the PDP-11/70 computer by the IAS operating system. There are now 10 active timesharing terminals. Consulting and programming staff offer a wide range of skills. We have installed an extensive library of mathematical functions and a handler for high-quality plotting on an electrostatic printer/plotter.

(2) We are building a data base on disks and on magnetic tape for row data and for access by analysis programs. Disk files are transferred to tape when the disk is old enough to be used infrequently or when it is filled. A second 174-Mbyte disk for the PDP-11 computer (on order) will make it possible for most of the data base to remain on the disk. Two types of raw data are managed, one from CAMAC modules and one from film. The film data are processed according to their character by one of several digitizing devices.

(3) The center interfaces experiments to the computer for direct input to the data base. When possible, we digitize signals from detectors on laser experiments immediately by CAMAC modules. Soon after the shot, the computer acquires all data by interrogating the modules. Signals that must be recorded with a <20-ns time resolution are recorded on fast oscilloscopes. Attenuators for these fast channels are packaged in Laboratory-designed CAMAC modules with the attenuation readable by CAMAC. All CAMAC data are sent directly to the data base as soon as they are acquired.

(4) Several digitizers are used to process films that record data in analog form, and each has a means of sending its output to the data base using the PDP-11 computer. One digitizer, designed and built at Los Alamos, reads Polaroid prints from oscilloscope cameras and is interfaced through CAMAC. A graphics digitizing tablet, interfaced through a computer terminal, reads large prints or projected images. Films from spectrometers and pinhole cameras are read by a one-dimensional microdensitometer or sent to a service group at the Laboratory for reading. We have recently acquired a scanning microdensitometer and will be able to read most of our own film, transferring data onto magnetic tape. Nonphotographic films from the Thomson parabola detector are analysed by the Bausch & Lomb Inc. Omnicon, a particle counting instrument. Control and data paths to and from the Omnicon are being developed through CAMAC. Another instrument, now being designed by a contractor, will use an imaging CCD as a film reader with some densitometry capability and will use local microprocessor control.

(5) A data librarian maintains the film files and notebooks of analog data media. We plan to replace notebooks with computer record-keeping whenever possible. The librarian's duties include operation of digitizing equipment.

(6) The center acquires unclassified laser and target information for use by analysis programs. Laser diagnostics are received from the operating group and entered by hand into a computer program. We plan to develop data links between laser control computers and our PDP-11/70 diagnostics computer so that this information can be transferred automatically.

(7) The center develops microprocessor-based systems for data acquisition and instrument calibration for use on-line with the lasers and in laboratories where experiments are prepared. We now have adequate facilities and personnel to develop other control and data-acquisition systems as needed. As laser experiments become more complex, distributed control and processing will play an ever greater part in the management of these experiments.

RADIOCHEMICAL DIAGNOSTICS DEVELOPMENT AT HELIOS (M. A. Yates, A. H. Williams, J. T. Ganley)

Given a source of neutrons inside a spherical shell of detector atoms, the number of activated product atoms, N_o, is

$$N_o = \frac{N F_\ell F_A \sigma_{RN}}{\sigma_{ABS}} ,$$

where

N = number of source neutrons,
F_ℓ = fraction of neutrons that escape,
F_A = fraction of neutrons absorbed in the shell,
σ_{RN} = detector reaction cross section, and
σ_{ABS} = total absorption cross section.

Assuming that the shell is thin compared to the source and that the source is thin to 14-MeV neutrons,

$$F_\ell \approx 1 \text{ and } F_A \approx 1 - e^{-\tau} \approx \tau .$$

In this expression, τ is the mean free path equal to the (number of atoms/unit volume) $\times$ σ_{ABS} $\times$ shell thickness.

The expression for N_o may then be rewritten

$$N_o = \frac{N_\rho \times 6.023 \times 10^{23}}{W} \Delta R \, \sigma_{RN} ,$$

where

ρ = density of the shell (g/cm^3),
w = molecular weight of the shell, and
ΔR = shell thickness.

This leads to the expression of interest,

$$N_\rho \, \Delta R = \frac{W N_o}{\sigma \times 6.023 \times 10^{23}} ,$$

where ΔR is the thickness of the pusher material at burn time.

By making the following assumptions, one may relate the $\rho\Delta R$ of the pusher to the ρR of the fuel.

(1) The mass of fuel and mass of pusher (M_F and M_P) are conserved.
(2) No appreciable fuel-pusher mixing takes place.
(3) Densities can be represented as an average value, $\rho(R) = \bar{\rho}$.
(4) Only 14-MeV neutrons are produced.
(5) The time for neutron production is short compared to that for any change in $\rho_P \Delta R$.

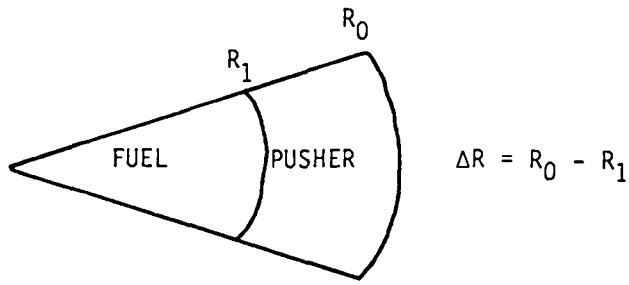

If we let ρ_P be the density of the pusher shell and ρ_F be the fuel density, we may represent the masses of the fuel and pusher as

$$M_P = \int_{R_1}^{R_o} \rho_P(R) \, 4\pi R^2 \, dR = \pi_P \frac{4}{3} \cdot \pi(R_0^3 - R_1^3)$$

$$= \rho_P \frac{4}{3} \pi[(R_1 + \Delta R)^3 - R_1^3]$$

$$= \rho_p \, 4\pi \, R_1^2 \, \Delta R \left(1 + \frac{\Delta R}{R_1} + \frac{1}{3} \frac{\Delta R^2}{R_1^2} \right) ,$$

and

$$M_F = \int_o^{R_1} \rho_F (R) \, 4\pi \, R^2 \, dR = \rho_F \frac{4}{3} \pi \, R_1^3 .$$

Then,

$$\frac{M_P}{M_F} = \frac{(\rho\Delta R)_P}{(\rho R)_F} 3 \left(1 + \frac{\Delta R}{R_1} + \frac{1}{3} \frac{\Delta R^2}{R_2^1} \right) .$$

For thin pusher shells,

$$M_P = 4\pi R_I^2 \, \Delta R \, \rho_P$$

and

$$\frac{M_P}{M_F} = 3 \frac{(\rho \Delta R)_P}{(\rho \dot{R})_F} \rightarrow (\rho R)_F = K \, (\rho \Delta R)_P \, .$$

If $(\rho \Delta R)_p/(\rho R)_F$ is constant,

$$(\rho_F)_{burn} = (\rho_F)_o \left[\frac{(\rho_P \, \Delta R)_{burn}}{(\rho_P \, \Delta R)_o} \right]^{3/2} .$$

Thus, measuring $\rho \Delta R$ of the pusher at burn, one may get an indirect measurement of the fuel density at burn.

In principle, to make the measurement of $\rho \Delta R$, one determines the number of pusher atoms activated. In practice, this involves catching a known fraction of debris from the imploding material. Given the amount of material available and the geometrical restriction of the target chamber, this determination is not trivial.

The collector design is shown in Figs. VII-8 and VII-9. The surface that is not normal to the flight path of the debris allows collection efficiencies of up to 15%. The lower foil vaporizes but apparently increases the collection efficiency by driving debris into the collector. Damage to the titanium foils is shown in Figs. VII-10 and VII-11. We have observed that these foils are activated by high-energy protons from the target-plasma corona and have discontinued their use.

Following the shot, the foils are retrieved and placed in a Ge(Li) well counter (Fig. VII-12). The detection efficiency of this system is 40%.

The efficiency of the catcher system is determined by activating a GMB in a reactor to form ^{24}Na in the glass, counting it in the well, shooting it in Helios, and counting the ^{24}Na retrieved in the titanium foils.

For the Sirius-B targets (Fig. VII-13) used to date, the only reasonable reaction is the $^{28}Si(n,p)^{28}Al$ with a half-life of 2.31 min. The counting system we now use is located too far from Helios for us to look conveniently for such a short half-life. We are, therefore, planning to use this technique on the next generation of targets. The Rigel-A target is similar to the Sirius-B but has a medium-Z pusher material between the glass mandrel and the plastic ablator (Fig. VII-14) that provides both greater protection from radioactive and electron preheat and better hydrodynamic pusher action during compression. A variety of reactions are possible (Table VII-I).

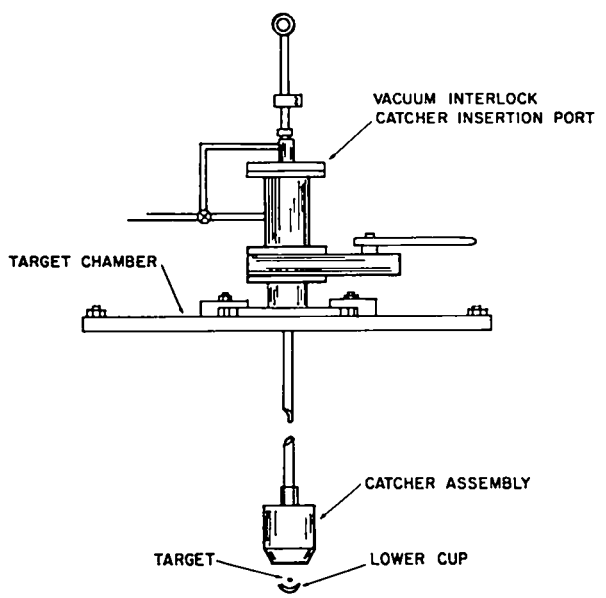

Fig. VII-8.
Device for collecting debris for radiochemical analysis of laser-target interactions.

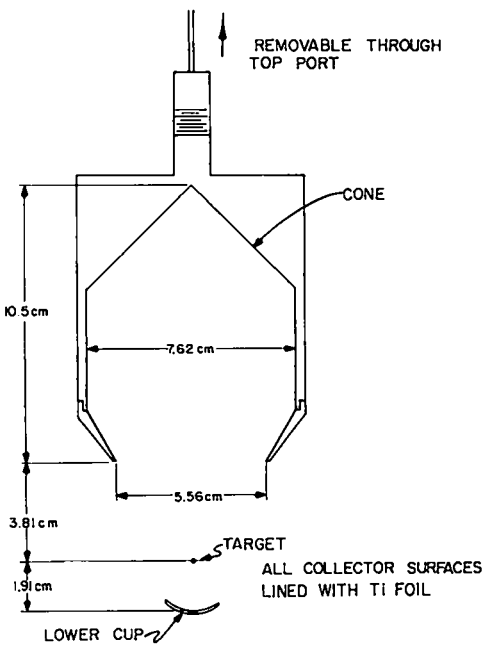

Fig. VII-9.
Catcher assembly for radiochemistry sample collector.

TABLE VII-I
γ-ENERGY

Reaction	Half-Life (min)	γ-Energy, keV (%)	Cross Section (mb)	Density (g/cm^3)	NρΔR (g/cm^2)
$^{97}Mo(n,p)^{97}Nb$	72.1	658	50	10.2	$7 \times 5 \times 10^7$
9.6		(98.5)			
$^{60}Ni(n,p)^{60m}Co$	10.5	658		8.9	7×10^6
26.1		(99.8)			(if $\sigma = 100$ mb)
$^{64}Zn(n,2n)^{63}Zn$	38.1	670	160	7.1	1×10^8
38.1		(8.4)			
$^{27}Al(n,p)^{27}Mg$	9.46	844	80	2.7	5.5×10^6
100		(73)			
$^{113}In(n,2n)^{112m}In$	20.6	155		7.3	1.6×10^6
4.3		(100)			(if $\sigma = 700$ mb)
$^{63}Cu(n,2n)^{62}Cu$	9.74	511 (β^+)	480	9.0	1.3×10^6
69.2		(93.9)			

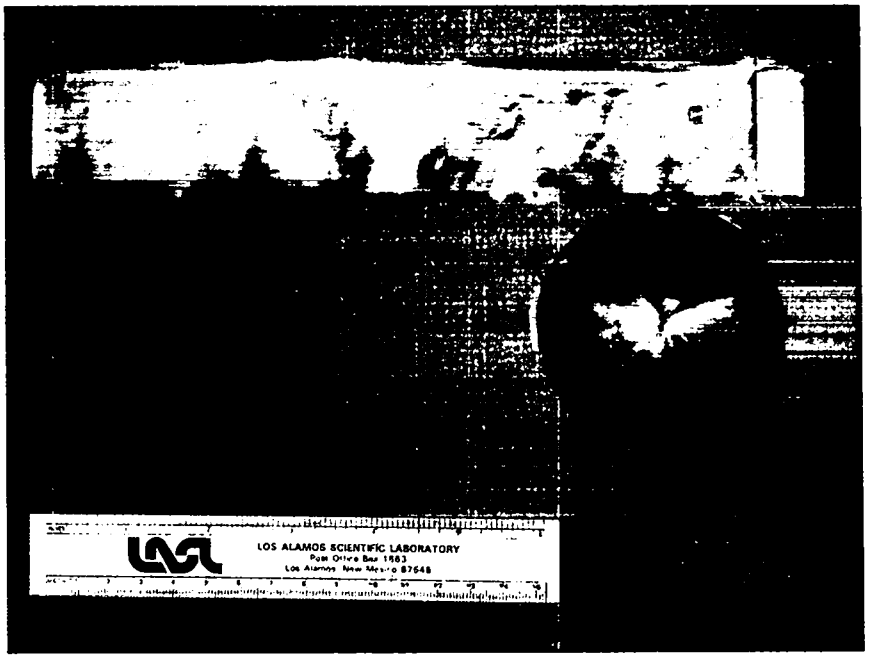

Fig. VII-10.
Titanium foils damaged by laser-target implosion.

The next step will be to put a dopant, such as bromine, in the fuel itself to obtain a direct measure of fuel density. When we begin to use multishell targets, radiochemistry will provide a means for detecting possible mixing of layers by measuring products from the different shells. All these advances will require higher neutron yields than are now available.

Fig. VII-11.
Titanium foils damaged by laser-target implosion.

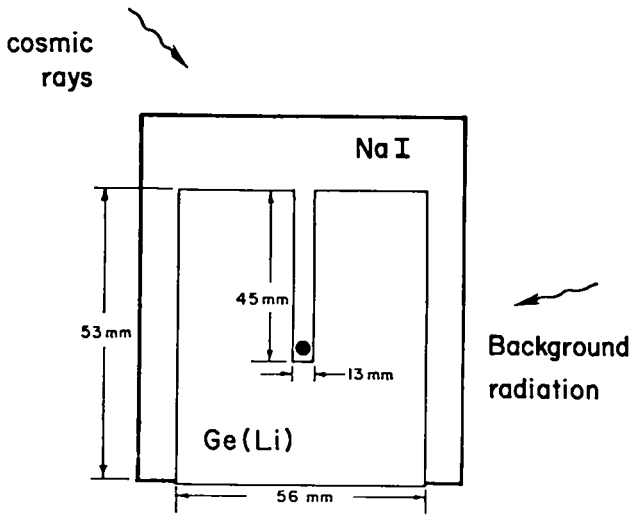

Fig. VII-12.
Well counter used to determine the efficiency of the catcher system.

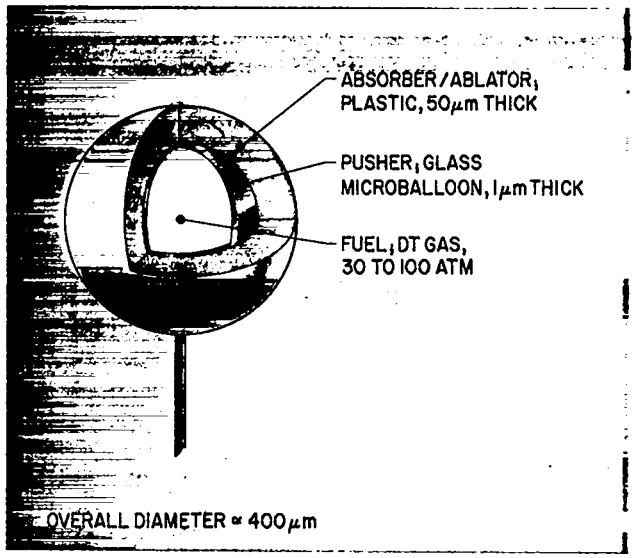

Fig. VII-13.
The Sirius-B target gives the reaction $^{28}Si(n,p)^{28}Al$ with a short half-life of 2.31 min.

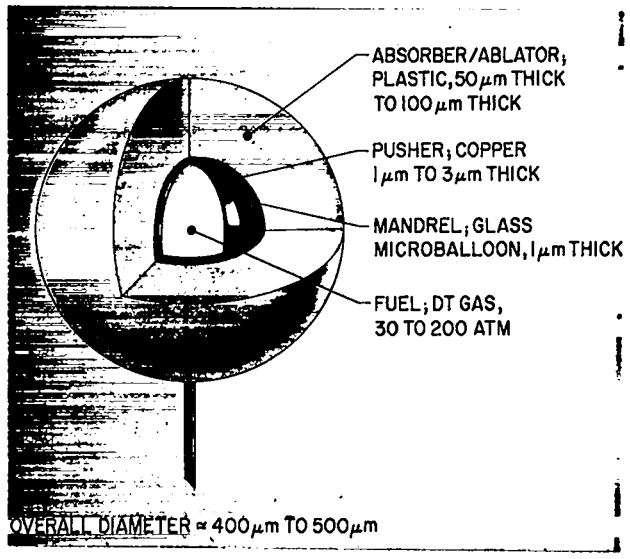

Fig. VII-14.
The Rigel-A target is similar to the Sirius-B target. It has a medium-Z pusher material between the glass mandrel and plastic ablator that provides protection from radioactive and electron preheat and gives better hydrodynamic pusher action during compression.

X-RAY INTERFEROMETRY AND THOMSON SCATTERING AS HIGH-DENSITY DIAGNOSTICS (P. Rockett)

Introduction

Laser-driven compression of low-Z-coated GMBs has pushed core electron densities into the range of 10^{23} to 10^{24} cm^{-3}. These high-density regions vary in diameter from 30 to 50 μm in argon-DT-filled Helios targets. Such high densities can be rigorously examined by x-ray emission or x-ray probe beams. Longer wavelength probes, such as optical probes might reach electron densities of 10^{22} cm^{-2} but with severe refraction. Pulsed x-ray interferometry could provide a detailed view of the spacial electron-density distribution, whereas holographic x-ray interferograms could provide more than absolute density values. The derived distributions would constitute a diagnostic for R-T stability.

An additional diagnostic in this high-density regime could be Thomson scattering. However, the low-level scattered signal and the lack of adequate spacial information make pursuit of this diagnostic inadvisable. A summary discussion will outline the plasma characteristics relevant to Thomson scattering; it will show that, if data were obtained, interpretation would be difficult in our plasma because the number of particles in a Debye sphere is approximately one.

Thomson Scattering of X Rays

Measurable Parameters. The temporally brief microballoon compression would have to be probed with an even shorter burst of x rays. Only laser-generated sources would have sufficient energy and time resolution to probe a laser fusion target. Regrettably, control of line emission intensity and measurement of absolute fluxes are not well in hand. We are currently considering a measurement of ion density n_i from Thomson scattering because it requires an absolute measurement of incident and scattered flux. Electron density n_e and ion temperature T_i are measured by spectral position and width of the scattered probe beam, repectively. Figure VII-15 shows data from the experiment of Ramsden and Davies[9] and of Forrest and Peacock,[10] who used probes in plasmas with $n_e = 10^{19}$ to 10^{20} cm^{-3}. The spectral position of the plasma peaks indentifies the plasma frequency and thus n_e. If all unscattered probe radiation

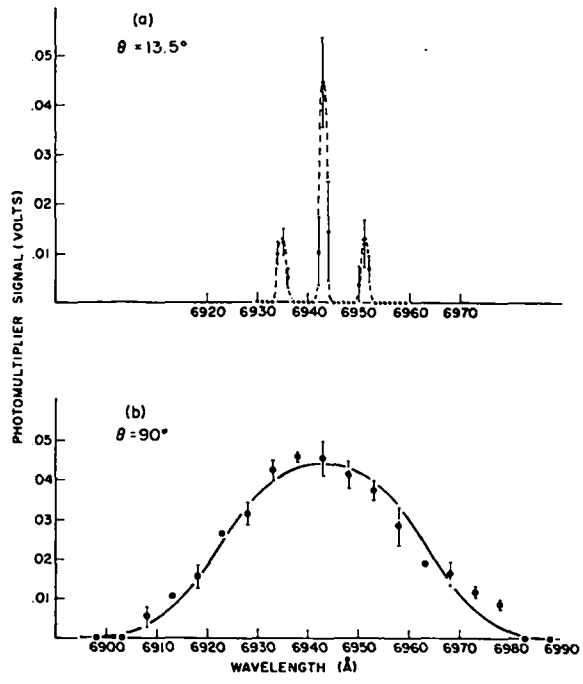

S. A. RAMSDEN AND W. DAVIES, PHYS. REV. LETT. 16, 303 (1966).

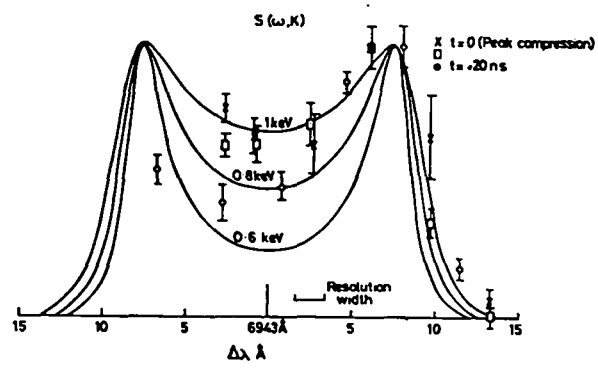

M. J. FORREST AND N. J. PEACOCK, PLASMA PHYSICS 16, 489 (1974).

Fig. VII-15.
Examples of Thomson scattering spectra in plasma physics experiments.[9,10]

is blocked from the spectrograph, the width of the ion line provides a measure of T_i.

To measure ion temperature (a very relevant parameter), we must have $\alpha \gg 1$, where $\alpha = (K \lambda_D)^{-1} \ll 1$ (K is the change in the scattered wavevector and λ_D is the Debye length). If we choose a probe wavelength $\lambda_o =$ 2.63 Å (He-like T_i, $1s^2 - 1s2p$), which will pass with little

absorption through the core, $\alpha \gg 1$ implies $K\,\lambda_D \ll 1$, which restricts the scattering angle ϕ to much less than 3.0°. Using a spacially resolving Bragg spectrograph, it would not be possible to shield completely against direct light at λ_o. This would obscure any spacial detail in the spectra because the probe source would be located behind the compressed plasma and would also make a spectral measurement exceedingly difficult.

Extracting T_e from this scattering measurement may still be possible. If $\alpha \ll 1$, the single particle limit is obtained and T_e should be readily measurable. One can show that

$$K = \frac{4\pi}{\lambda_o} \sin \frac{\phi}{2} . \qquad \text{(VII-14)}$$

For the argon-DT plasma mentioned earlier, Eq. (VII-14) and the constraint on α demand that $\phi \gg 3.0°$. Ninety-degree scattering yields $\alpha = 0.038$ and would permit adequate shielding against direct λ_o radiation entering the spectrograph. Apparently T_e could be measured by Thomson scattering far easier than n_e, n_i, or T_i. Typical values of plasma parameters involved in Thomson scattering measurements are:

$$Ne \approx 5 \times 10^{23}\ cm^{-3}$$

$$Te \approx 500\ eV$$

$$\lambda_D = \left(\frac{kTe}{8\pi ne^2}\right)^{1/2} \approx 9 \times 10^{-9} cm$$

$$Ne\lambda_D^3 = 0.8 .$$

Signal Level. The scattered signal level will be so low that noise could be a serious problem. The total Thomson scattering cross section is 6.63×10^{-25} cm^2. A beam of x-ray photons of intensity I_o will lose only 1.7×10^{-3} I_o by passing through 50 μm of plasma with $n_e = 5 \times 10^{23}$ cm^{-2}. In the case of 90° scattering, $d\sigma/d\Omega = 3.96 \times 10^{-26}$ cm^2 sr^{-1}. A spectrograph could have a collecting solid angle of 10^{-5} sr and, thus, would see $I_o\,\{1 - \exp[-(3.9 \times 10^{-31}\ cm^2) \times (5 \times 10^{23}\ cm^{-3})(5 \times 10^{-3}\ cm)]\} = I_o \times 10^{-9}$. This must be compared to the target plasma radiation contained within some energy interval dE about the probe energy E_o.

A worst case was chosen to estimate this background or noise level by measuring the radiation from a gold-coated microballoon irradiated with 3 kJ of CO_2 laser light at 10.6 μm. The high Z creates short mean-free paths near the critical layer and produces blackbody radiation at low energies and in a strong bremsstrahlung tail above ~2 keV. The measured dE/hυ on one shot was 10^{11} J/keV at E = 4.7 keV into d = 10^{-5} sr. An attempt to measure T_e in the single-particle limit requires that the background signal in a bandwidth of T_e (~E_o) be much less than the scattered signal. If T_e = 500 eV, then the noise signal is $E = (10^{-11}\text{J/keV})(0.5\ \text{keV}) = 5 \times 10^{-12}$ J. Therefore, the scattered probe energy E_s must obey $E_s = E_o \times 10^{-9} \gg 5 \times 10^{-12}$ J or $E_o \gg 5$ mJ. However, E_o is only the energy entering the plasma core. The total probe energy will go into 2π sr, with most of the energy leaving normal to the disk. If the probe-to-target distance were 1 cm and a 50-μm-diam core were assumed, then 8×10^3 more probe energy must be generated than sees the target. Thus, E_o (total) ≫ 40 J. If one assumes a 0.1 emission efficiency of x-ray line energy from laser light, one needs to strike the small titanium disk with ≫ 40 kJ. Clearly, the background noise level is too high considering the small percentage of Thomson scattered radiation.

X-Ray Interferometry

Introduction and Historical Perspective. A probe diagnostic for the compressed core of a laser fusion plasma will require a wavelength far shorter than that set by the plasma frequency. For $n_e = 10^{24}$ cm^{-3}, the critical wavelength is 334 Å. The probe must also have a long mean-free path to minimize absorption through the corona and the core. Experiments have shown that we must exceed 3 keV to transport radiation efficiently out of the core. Other experiments have confirmed adequate helium-like line emission in titanium by striking a titanium disk with a laser.* The relevant transition is $1s^2$-1s2p at $\lambda_o = 2.63$ Å (E = 4.71 keV), and all further calculations will assume use of this realistic probe. An x-ray interferometer must show sufficient phase shift to be measurable by conventional means. The fringe shift p(x) of a finite-fringe interferogram can be related to n_e and the path length 2x as

$$p(x) = \frac{2}{\lambda_o} \int_0^x (4.48 \times 10^{-14}) n_e \lambda_o^2 \, dx , \qquad \text{(VII-15)}$$

which for a slab plasma can be expressed as

$$p(x) = (4.48 \times 10^{14})\, 2x\, n_e\, \lambda_o ,$$

*D. Atwood of Lawrence Livermore National Laboratory provided this information (September 1979).

where all parameters are in cgs units. For a core plasma with $2x = 50$ μm, $n_e = 5 \times 10^{23}$ cm^{-3}, and $\lambda_o = 2.63 \times 10^{-8}$ cm, one finds $p = 3$ fringe shifts or a phase change of 6π. This is readily measurable and suggests that holographic x-ray microscopy could be a valuable diagnostic.

Variations. There are many approaches to interferometry in the x-ray regime, just as there are in the optical regime. Bragg reflectors and Laue splitters have been used to generate the classical reference and object beams. Bonse and Graeff[11] describe such three-and-four-element interferometers, which are fragile devices with little room for positional error of the elements. A high-power laser environment would be quite damaging to interferometers, which are machined primarily from a single crystal. The signal loss, after two to three Laue reflections, is also not tolerable when we are using laser-produced probe sources.

In 1974 Aoki and Kikuta[12] reported a somewhat successful attempt to use aluminum K_α radiation for holographic x-ray microscopy. Even though their probe source diameter was ~6 μm, their spacial coherence was fairly poor as evidenced by a measured fringe visibility, $\gamma = 0.018$. Niemann, Rudolf, and Schmahl[13] applied the wave nature of x rays more successfully using zone plates with high zone numbers.

One interferometer design that would provide maximum signal usage and that could possibly be protected from laser damage is the Lloyd's mirror interferometer. Kellstrohm[14] generated interference patterns with a Lloyd's mirror using Al K_α, Mo L_{α}, Cu $L_{\alpha\beta}$, and C K_α radiation. His goal was not only to improve x-ray interferometer design, but also to measure the wavelengths of these materials' characteristic radiation accurately (within 1 to 2%). He also worked successfully with the Fresnel double-mirror geometry. Because of its more complicated geometry and more exposed structure, this geometry will not be considered here. The following discussion will deal exclusively with a Lloyd's mirror design, showing that temporal coherence, fringe spacing, mirror angles, and signal strength can all be maintained within acceptable limits. However, spacial coherence of the laser plasma x-ray source may not be adequate to obtain a fringe visibility, $\gamma > 0.5$ at $\lambda_o = 2.63$ Å. This will probably be the undoing of laser-initiated pulsed x-ray interferometry. Nevertheless, the design should be considered in light of the wealth of information available. If this diagnostic technique proves impractical at 4.71 keV, it could possibly be applied to other problems at 500 eV or less.

Detailed Interferometer Design. The Lloyd's mirror interferometer (Fig. VII-16) has a point source that radiates the probe beam at λ_o into 4π sr and a spherical wave that arises from a second virtual source. Part of the original spherical wave, which is not reflected from the mirror, interferes with the wave originating from the virtual source and equally spaced fringes are formed at the screen. Such a small solid angle is used that the two waves are virtually plane. Hence, one has a reference wave (the reflected wave) and an object wave (the direct wave) into which a phase-shifting object may be placed. One should immediately note the similarity to Young's double-slit experiment and should expect the fringe spacing to be

$$\frac{1}{\upsilon} = \Delta x = \frac{a\lambda_o}{d}\,, \qquad \text{(VII-16)}$$

where

Δx = fringe spacing,

υ = fringe spacial frequency at the film,

a = source-to-film distance, and

d = spacing between the source and the virtual source.

(From this relation, Kellstrom[14] measured the wavelengths of radiation that previously had only been known to ±15%.) The grazing angle θ and the height $d/2$

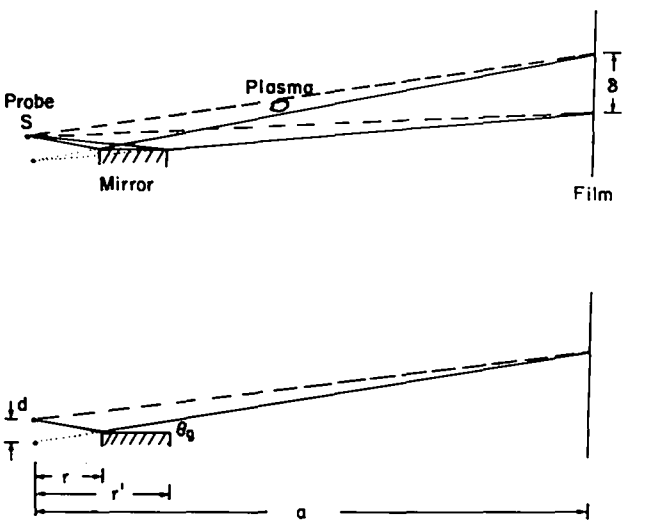

Fig. VII-16.
Lloyd's mirror interferometer.

are typically very small; for example, $\theta_g \ll 1.0°$ and $d \ll 0.1$ cm.

Several criteria severely restrict the choices of d, θ_g, r, and s, where r is the distance from the source to the first edge of the mirror, and s is the source diameter. An immediate question is whether sufficient temporal coherence can be obtained. Fortunately, the path-length differences in the Lloyd geometry are very small as long as θ_g is small. The coherence length L_c must be greater than 0.1 μm; the probe bandwidth must be less than 12.4 eV for $E_o = 4.71$ keV, or equivalently $\Delta\lambda_o < 7.0$ mÅ for $\lambda_o = 2.63$ Å. If one calculates the *maximum* θ_g required to maintain the path-length difference, one obtains the relation

$$\theta_g \leq \frac{L_c}{d} + \frac{d}{2a} . \qquad \text{(VII-17)}$$

Typically, the first term dominates; for example, if d = 25 μm and $L_c = 0.1$ μm, then $\theta_g < 4$ mrd = 0.23°. Fixing d and θ_g determines r, the position of the mirror, because $r \sim d/2\theta_g$. One could, of course, choose as small a θ_g as would be physically possible.

Another restriction when working at such short wavelengths is the modulating transfer function (MTF) of the recording film. One could choose a slow film with a high MTF up to 3000 1/mm or a slow film with MTF up to 200 1/mm. This design will function with a film that can record to $\upsilon = 10^4$ cm^{-1}. From Eq. (VII-16), this film constraint results in

$$d < a\,\lambda_o \upsilon . \qquad \text{(VII-18)}$$

Film coverage by the interfering beams must be adequate to allow complete coverage of the target plasma core back from the film. The overlapping length δ can be expressed as

$$\delta = \frac{adl}{2rr'} , \qquad \text{(VII-19)}$$

where l = mirror length and r′ = r + l. We will present a complete design later and will show that δ can easily be made greater than 500 μm, permitting coverage of the 50-μm core at distances from the probe that are much less than a.

Finally, we must ascertain the level of spacial coherence. Without adequate spacial coherence, fringe visibility γ will fall so far below 0.5 that the data will be unreadable. Kellstrom[14] used a heuristic argument to minimize the angular extent of the slit seen from the mirror compared to the angular extent of the fringes. His analysis required that the source diameter s obey

$$s \ll \left[\upsilon\left(\frac{a}{r'} - 1\right)\right]^{-1} . \qquad \text{(VII-20)}$$

Collier et al.[15] were more rigorous in their calculations of visibility. They computed the degree of coherence, which is defined as the modulus of the correlation between the object and reference fields at the recording screen, divided by the autocorrelation of each field. Using the van Cittert-Zernike theorem, and assuming a uniform source, one can plot the degree of coherence vs $s\delta/2s\lambda_o$. The stringent limit thus set upon s is

$$s \leq \frac{0.5\ a\lambda_o}{\delta} . \qquad \text{(VII-21)}$$

The results of a complete design appear below. They were obtained by choosing a = 80 cm and then calculating Eq. (VII-17), (VII-18), (VII-19), (VII-20), and (VII-21). The design criteria are as follows:

(1) Film resolution $\frac{1}{\upsilon} = \frac{a\lambda_o}{d}$, $d \leq a\lambda_o\upsilon_{max}$

(2) Temporal coherence $\theta_g \leq \frac{L_c}{d} + \frac{d}{2a}$

(3) $r = d/2\theta g$

(4) Spacial coherence $s \leq \frac{0.5\ a\lambda_o}{8}$

(5) $\delta = \frac{ad\ell}{2r(r+\ell)}$.

We also assumed that $\upsilon_{max} = 10^3$ cm^{-1}. The calculated dimensions are

$d = 2.0 \times 10^{-3}$ cm,
$\theta_g = 0.001$ rad,
$r = 1$ cm,
$r' = 6$ cm,
$s \ll 0.8$ μm,
$s < 0.2$ μm, and
$\delta = 6.7 \times 10^{-2}$ cm.

Spot source diameters of 4 to 5 μm are readily obtainable; however, diameters less than 1 μm are not possible on this or other interferometers in this

wavelength region. Note that s scales with λ_o. One more design may be instructive. Assume a = 80 cm, but that $\upsilon_{max} = 10^4$ cm^{-1}. The Lloyd's mirror dimensions now are

$d = 2.1 \times 10^{-2}$ cm,
$\theta_g = 4.75 \times 10^{-4}$ rad,
r = 22.1 cm,
r′ = 27.1 cm,
$s \ll 5.0$ μm,
$s < 1.5$ μm, and
$\delta = 70$ μm.

The source diameter has increased, but now δ is too small to be usable. No matter how one tries, the limits on s are too severe. In spite of the favorable values for all but one of the required design dimensions, the lack of spacial coherence in short-wavelength, laser-produced x-ray sources will probably prevent adequate fringe visibility. This additional signal-to-noise increase would not be tolerable in a laser fusion diagnostic.

Conclusions

Before such complex diagnostics as Thomson scattering of x rays or x-ray interferometry are attempted, the experimenter should know (1) whether any useful data could arise from his attempts and (2) whether there are any constraints that physically prevent application of the diagnostic. In considering Thomson scattering, we determined that only T_e could be extracted from the scattered signal from the compressed core. However, we also showed that the signal-to-noise ratio was far too low because of the small fraction of probe beam scattered. Condition (1) was satisfied, but condition (2) was not.

X-ray interferometry was also considered as a laser fusion diagnostic and a probe wavelength of 2.63 Å was chosen, based on empirical observations of compressed-core opacity. Several design options were discarded, but the Lloyd's mirror geometry appeared promising. The value of $n_e(r)$ was readily measurable because distances, angles, spacial frequency, and temporal coherence were obtainable. However, the short probe wavelength demanded an unreasonably small probe-source diameter to meet the spacial coherence requirements. Thus, condition (2) was violated. Neither Thomson scattering or x-ray interferometry may be currently applied to analyzing the plasma state in the compressed core of laser fusion targets.

REFERENCES

1. C. Joshi, M. C. Richardson, and G. D. Enright, Appl. Phys. Lett. 34 (10), 625 (1979). This information is also discussed by D. C. Slater, Appl. Phys. Lett. 31 (3), 196 (1977) and N. M. Ceglio and L. W. Coleman, Phys. Rev. Lett. 39 (1), 20 (1977).

2. "Laser Fusion Program at LASL, January 1—June 30, 1977," E. Stark and F. Skoberne, Comps., Los Alamos Scientific Laboratory report LA-6982-PR (April 1978).

3. J. H. Richardson, *Optical Microscopy for the Materials Sciences*, (Marcel Dekker, Inc., New York, 1971). This information is also discussed by *Applied Optics and Optical Engineering*, Vol. IV, Part I, R. Kinslake, Ed. (Academic Press, New York, 1967).

4. H. Kornblum, Lawrence Livermore National Laboratory Annual Report, 344 (1976).

5. Lampton, Margon, and Bowyer, Ap. J. 208, 177 (1976).

6. R. H. Day, P. Lee, E. B. Salomon, and D. J. Nagel, Los Alamos Scientific Laboratory report LA-UR-79-1360 (1979).

7. W. J. Viegle, "Photo Cross Sections from 0.1 keV to 1 MeV for Elements Z = 1 to Z = 94," Atomic Data Tables 5, 51 (1973).

8. Roger B. Perkins and the Inertial Fusion Program Staff, "Inertial Fusion Program, January 1—June 30, 1979," Frederick Skoberne, Comp., Los Alamos National Laboratory report LA-8114-PR (June 1981).

9. S. A. Ramsden and W. E. R. Davies, Phys. Rev. Lett. 16, 303 (1966).

10. M. J. Forrest and N. J. Peacock, Plasma Physics 16, 489 (1974).

11. V. Bonse and W. Graeff, "X-Ray and Neutron Interferometry," in *X-Ray Optics*, H. J. Queisser,

Ed., Topics on Applied Physics 22 (Springer-Verlag, Berlin, 1977).

12. S. Aoki and S. Kikuta, Japan. J. Appl. Phys. 13, 1385 (1974).

13. B. Niemann, D. Rudolph, and G. Schmahl, Appl. Opt. 15, 1883 (1976).

14. G. Kellstrom, Nov. Act. Reg. Soc. Sci. Upsaliensis 8, 1-66 (1932).

15. R. Collier, C. Burckhardt, and L. Lin, *Optical Holography* (Academic Press, New York, 1971).

VIII. HEAVY-ION FUSION DRIVER DEVELOPMENT
(G. A. Sawyer)

Heavy-ion accelerators are being considered as alternative drivers for ICF. A study at the Los Alamos National Laboratory has resulted in a favorable outlook for the development of heavy-ion fusion. Laboratory efforts in ion-beam transport theory and in low-velocity ion-accelerator development are described.

INTRODUCTION

Heavy ions provide a new approach to ICF. High-current beams of heavy ions (for example, xenon or uranium), provided by nuclear particle accelerators at energies of 5-10 GeV, are used instead of laser beams to heat a fusion target. The targets are similar to those used for laser fusion.

At Los Alamos the Heavy Ion Fusion (HIF) Task Group has completed its assessment, examining in detail accelerator technology, heavy-ion beam transport, target-interaction physics, commercial power generation, and military applications. Although they recognized formidable technical problems, the Task Group endorsed a vigorous national research program and defined areas for Laboratory involvement.

Heavy ions appear to be more efficient and less expensive than lasers as high-energy drivers for ICF. The efficiency of nuclear particle accelerators for turning electric power into heavy-ion kinetic energy can be as high as 20-30%. In addition, the coupling of ion-beam energy to the target is expected to be straightforward and efficient.

However, many problems concerning HIF remain to be solved because the accelerators, although based on well-established technology, must operate at beam currents much higher than ever achieved previously. Using uranium as the beam particle, typical design parameters for HIF are 10-GeV, 30-kA peak beam current, 300-TW beam power, 3-MJ beam energy, and 5-mm focal-spot size.

Two approaches to heavy-ion acceleration are being explored, principally by Argonne National Laboratory (ANL) and Lawrence Berkeley Laboratory (LBL). ANL is investigating aspects of the rf-linac approach, and LBL is concentrating on the linear-induction approach. Test-bed experiments in the $24- to 50-million range have been proposed by both laboratories and will be built as funding permits. Brookhaven National Laboratory (BNL) has also been active in the rf-linac approach, and Los Alamos is developing the radio-frequency quadrupole (rfq) concept for application as a low-energy injector. Target design studies are being conducted at both LLNL and Los Alamos.

The Laboratory technical support activities concentrate on critical issues in areas in which we possess skills and expertise, including accelerator development, beam transport, target physics, and systems studies. This section covers accelerator development and beam transport; the target physics and system studies efforts, as they relate to HIF, are covered in other sections.

BEAM TRANSPORT (L. E. Thode)

Our theoretical studies in beam transport have addressed the problem of propagating and focusing an ion beam through the various background environments that may be encountered in a reactor chamber, that is, plasma, neutral gas, or vacuum. In particular, these studies have been conducted by the TRW systems group in support of a Light Ion Fusion Experiment (LIFE), designed to demonstrate a new light-ion ICF driver.

Our progress included (1) formulation of a linear and nonlinear theory of the collisional, homogeneous, two-stream instability of a cold ion beam interacting with a cold plasma; (2) derivation of a dispersion relation for the two-stream and filamentation instabilities in a periodic array of beamlets characteristic of LIFE and other accelerators; (3) completion of a series of particle-in-cell simulations for ion-beam injection into a background plasma; (4) simulation of an actively neutralized ion beam injected into a vacuum and identification of problems associated with the kinetic energy of neutralizing electrons; (5) completion of a report on statistical thermodynamics of temperature anisotropy-driven Weibel instabilities; and (6) development of an electrostatic version of the two-dimensional, electromagnetic particle simulation code. The importance of this work and our future plans are summarized as follows.

The linear and nonlinear theory of the cold collisional two-stream instability caused by an ion-beam electron interaction is an extension of previous work on the theory of the electron beam-driven two-stream instability.[1] The collisionless limit of this theory agrees with results from particle simulations discussed below. Preliminary calculations indicate that the correct spacial instability growth rates from the more complete theory are significantly higher than those predicted by more limited models. We plan to study instability growth rates and nonlinear field levels achieved in typical propagation distances as a function of collision frequency.

Filamentation instability is another beam-plasma instability that can occur in the currently envisioned propagation scheme. In contrast to the two-stream instability, it is an electromagnetic instability and propagates in the plane perpendicular to the beam. Because beam boundaries lie in this direction, boundary effects can modify the theory of the filamentation instability. Therefore, we have generalized the linear filamentation instability theory to include the equilibrium case of an infinite periodic array of interacting beamlets. The case reduces to previously known dispersion relations in the limit of a homogeneous beam and a single beam. Parameter studies are not complete but indicate that growth rates are always reduced below their homogeneous values.

The issues of current and charge neutralization of an unneutralized ion beam injected into a dense plasma and the ion-beam background plasma two-stream instability have been investigated in a series of two-dimensional electromagnetic particle simulations. Beam-charge neutralization was always complete within a few plasma periods, ω_{pe}^{-1}, after injection. Current neutralization was inhibited both by the nonlinear state of the two-stream instability and by the depletion of neutralizing electrons near the injection boundary. This lack of current neutralization resulted in beam self-fields and major orbit modifications of the beam ions. The two-stream instability, which was strongly driven in these simulations, remained one-dimensional throughout its nonlinear evolution; therefore, it was easier to explain with known theories. Further discussions of these simulations, including phase plots of the beam, were reported at the 1979 HIF workshop.[2]

Especially for light ions, beam propagation in a vacuum requires active charge and current neutralization of the ion beam. In the LIFE concept, this is achieved by the coinjection of electrons. Because the electrons and ions are initially separated in space, large space-charge fields develop and cause a large electron kinetic energy. We discovered this behavior in a particle simulation of the injection of such a neutralized beam into a vacuum. Ion-beam dynamics may be modified by the presence of such energetic electrons either by sharing the energy with the ions or by incomplete neutralization. Further work will concentrate on developing an envelope equation describing an ion beam neutralized with such "hot" electrons.

We have investigated the statistical thermodynamics of temperature anisotropy-driven Weibel instabilities, which are of interest because they are likely to develop in radially and axially focused charged particle beams.

The development of an electrostatic version of the particle simulation code CCUBE* represents an advance for ion-beam studies because its more time-efficient operation makes feasible the simulation of ion beams in more realistic parameter regimes and configurations. Like its predecessor, the new code allows for simulations in any two-dimensional orthogonal coordinate system with a variety of particle and field-boundary conditions and injection capabilities.

ION-BEAM PROPAGATION SIMULATIONS (Don S. Lemons)

Numerical particle-in-cell simulations of ion-beam propagation have been performed with our two-dimensional electromagnetic code, CCUBE. A few results for each of two different simulations are presented. They illustrate plasma effects relevant to (1) ion propagation in a relatively dense plasma background, and (2) ion vacuum propagation with comoving electrons.

Propagation in Plasma Background

For inertial confinement application, we considered ion propagation through a background gas sufficiently dense to produce a plasma needed for charge and current neutralization of the beam, but tenuous enough to avoid serious degradation of beam quality. In this mode,

*CCUBE is a family of electromagnetic and electrostatic one- and two-dimensional particle-in-cell simulation codes developed by Brendan Godfrey, Mission Research, Albuquerque, New Mexico.

ballistic ion-beam propagation and focusing are a possibility, provided that the beam ion-background electron two-stream instability remains harmless. In the first simulation, we investigated this issue, along with the effects of incomplete current neutralization.

The simulation was performed in r, z cylindrical spacial coordinates, which were divided, respectively, into 50 and 150 grid points. Spacial dimensions of the simulation grid and the unperturbed ion-beam envelope are shown in Fig. VIII-1(a).

The ion beam is injected at t = 0, from the left-hand side of the simulation grid. Beam ion speed is given by $\beta = 0.548$, beam ion-to-electron mass ratio by $m_b/m_e = 50$, and beam-to-background plasma density by $n_b/n_e = 10^{-1}$. These and other dimensionless simulation parameters are listed in the figure caption where V_{th} denotes thermal speed, and the subscripts b, i, and e denote beam ion, background ion, and background electron parameters, respectively.

The beam rises to full strength and propagates across the simulation in 200 plasma periods, ω_{pe}^{-1}. During this time, the beam first becomes charge and current neutralized (0-10 ω_{pe}^{-1}), begins to lose current neutralization, and consequently, to pinch magnetically ($\sim$100 ω_{pe}^{-1}). It then starts to develop axial modulations in beam density and velocity, a result of the nonlinear development of the ion-electron two-stream instability (100-150 ω_{pe}^{-1}).

Figures VIII-1(a) and (b) are, respectively, r – z and v_z – z phase plots of the beam ions after the beam has propagated across the simulation grid, the two-stream instability has saturated, and magnetic pinching has become active. Spacial dimensions are in units of c/ω_{pe}; time is in units of ω_{pe}^{-1}; and velocity is in terms of $\beta_z\gamma$, where $\beta_z = V_z/c$ and $\gamma = (1 - \beta_z^2)^{-1/2}$.

For the initial beam and background plasma parameters, the ion electron two-stream growth rate (ω_I) and group velocity (V_{gr}) are given by $\omega_I = 0.0695\ \omega_{pe}$ and $V_{gr} = 0.643\ \beta C$. These parameters correspond to a tenfold growth in wave amplitude at the point $10\ V_{gr}/\omega_I$ or $50.6\ c/\omega_{pe}$. According to Figs. VIII-1(a) and VIII-1(b), this distance is associated with large one-dimensional beam density and velocity modulations. At about this point, wave saturation by trapping of the beam ions occurs. After saturation, the background plasma is observed to heat at a rate consistent with a 17% transfer of beam energy to plasma energy. This transfer is in line with the prediction of a single-wave two-stream heating model,[3]

$$2\left(\frac{n_b}{2n_p}\,\frac{m_e}{m_i}\right)^{1/3},$$

which, given the present simulation parameters, is 20%. We observed no instability-produced deflection of beam particles in the radial direction.

Magnetic pinching of the beam occurs in part because the neutralizing background-electron stream depletes the electron population in the region of beam injection and because electrons initially outside the beam cannot

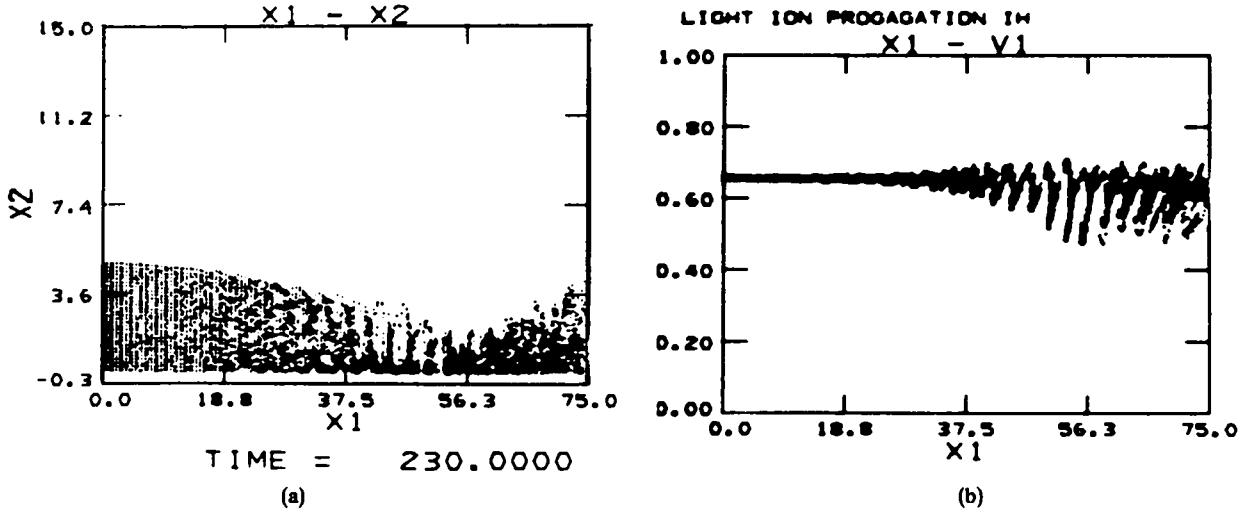

Fig. VIII-1.
Ion-beam particle plots: (a) X1-X2 (r-z) space and (b) XI-VI (V_z-z) space. Simulation parameters are $\beta = 0.548$, $m_b/m_e = 50$, $m_i/m_e = 100$, $n_b/n_e = 10^{-1}$, $V_{thb}/c = 10^{-3}$, $V_{thi}/c = 10^{-4}$, and $V_{the}/c = 10^{-2}$.

efficiently neutralize the beam current. This boundary effect was not anticipated but nonetheless results in a gross distortion of the beam. In general, the resulting beam envelope is consistent with the ion-beam envelope equations derived by Wright.[4]

Vacuum Propagation with Comoving Electrons

Vacuum or near-vacuum ion-beam propagation is also an attractive mode because it avoids uncertainties and instabilities involved in beam plasma production. In this case, active current and charge neutralization are necessary for ballistic propagation. This may be achieved earlier by beam electron pickup or by the injection of comoving electrons as proposed in TRW's light-ion driver.[5] The ion electron charge separation at injection, a feature of the latter scheme, provides considerable electrostatic energy that initially is transmitted to the electrons. How and whether this energy is transferred to the ions in amounts that can inhibit ballistic focusing is a subject of continuing investigation.

It is, however, easy to estimate the electrostatic energy involved for a typical parameter. If we assume an infinite sheet of ions and an infinite sheet of electrons both with thickness δ and density n separated by a distance Δ, the electrostatic energy per electron (W) that is due to the charge separation is then given by $W = 2\pi e^2 n\,(\Delta + 2/3\Delta)$. If $n = 10^{10}/cm^3$, $\delta = 5$ mm, and $\Delta = 3$ mm, then $W = 2.86$ keV; a significant amount of transverse energy is equally partitioned with the ions.

Electron motion within self-fields is illustrated by the numerical simulation of the simultaneous injection into a vacuum of three pairs of cylindrical, concentric, hollow-ion, and electron beamlets. The simulation was performed in r, z coordinates on a grid of 80 by 100 grid points. Figures VIII-2(a) and VIII-2(b) are, respectively, ion and electron r, z phase plots, 24.5 ω_{pe}^{-1} after injection. Beamlet charge densities were initialized to provide for zero net charge within each beamlet pair.

The ion time scale, ω_{pi}^{-1}, is too long in this simulation to observe ion motion. In contrast, the electrons are propelled into large excursions from the ions both axially and radially by electrostatic forces. The heads of the electron beamlets remain intact because beam charge densities are initially zero and rise exponentially to their full value in $\sim 20\ \omega_{pe}^{-1}$.

ACCELERATOR TECHNOLOGY (W. L. Talbert)

Accelerator development activities for heavy-ion fusion concentrated mainly on low-velocity accelerator studies and on the broader assessment of heavy-ion fusion issues.[6,7]

We studied an rfq accelerating structure for low-velocity ions and developed methods to synthesize the beam dynamics design of such a system. To achieve desired performance characteristics, we have optimized parameters for the rfq structure for specific designs; for example, high transmission efficiency at specified current, radial emittance growth, and accelerator length. A

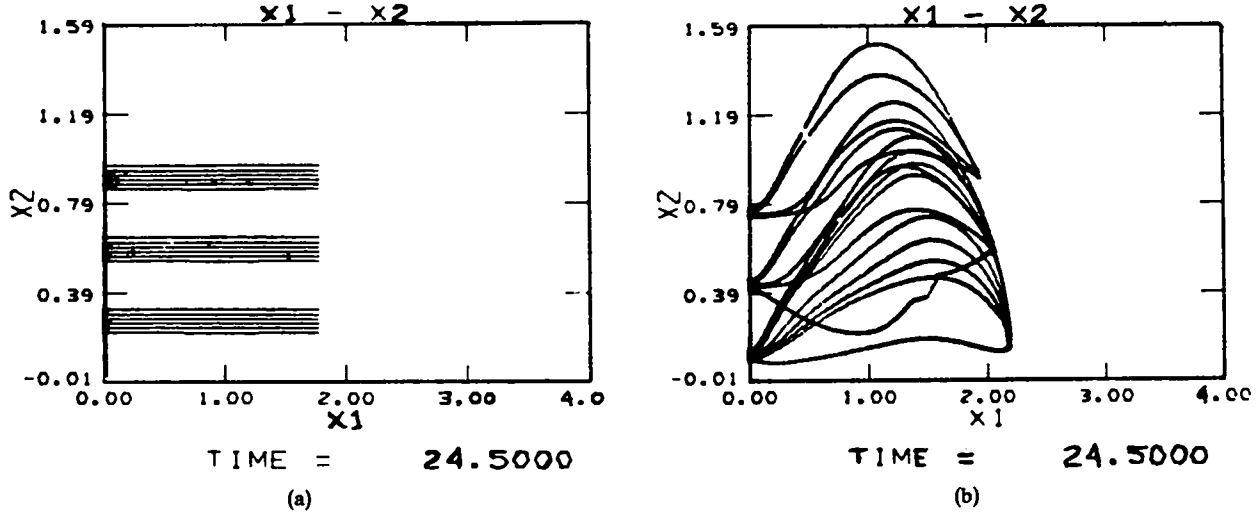

Fig. VIII-2.
Phase plots: (a) ion beam and (b) comoving electron particle plots in X1-X2 (r-z) space. Simulation parameters are $\beta = 0.0728$ and $m_b/m_e = 3670.5$. Particles are completely cold. Distances and times are in units of c/ω_{pe} and ω_{pe}^{-1}, respectively.

specific proof-of-principle design was developed, together with an rfq design appropriate for U^{+11} ions to be injected into the UNILAC heavy-ion accelerator at Darmstadt, West Germany.

Potential problems in the design of heavy-ion drivers for inertial fusion were examined, and low-velocity accelerating structures operating at low frequencies (~10 MHz) were identified as needing significant development. We prepared an rfq structure design for Xe^{+1} ions that would operate at low frequency. This design incorporated current limits, imposed by space-charge forces, that were shown to occur at other than the input to the structure, in contrast to other low-velocity structures. The rfq design thus offers an advantage over other approaches in accepting an intense ion-beam load at lower injection energy.

We evaluated a design that features the geometrical advantages of the rfq structure in arrays funneled into subsequent, higher frequency stages of an rf linac heavy-ion driver. In this scheme, the use of an arrayed, electrostatically focused Wideröe stage is suggested, and staging (or transition) energies for funneling were chosen to push current limits as high as possible, consistent with minimizing the overall linac length. Work on rfq beam dynamics and low-beta linac structures is presented in Appendixes A and B.

Application of Radio-Frequency Quadrupole in Linear Accelerators for Heavy-Ion Fusion (T. P. Wangler, R. H. Stokes)

Introduction. The low-velocity accelerator is an important element in heavy-ion drivers for ICF. It is widely recognized that beam intensity limitations and radial emittance growth usually occur at low velocities in linear accelerator systems. The characteristics of the rfq make it an attractive alternative approach to other designs that have been proposed. One proposal[8-10] suggests the use of a high-voltage dc injector to accelerate a heavy-ion beam, for example, Xe^{+1}, to ~1.5 MeV. The injector is followed by an rf buncher and several independently phased cavities with magnetic quadrupoles between the cavities. At ~2.3 MeV, the xenon beam is injected into a sequence of three Wideröe linacs and accelerated to an energy of ~20 MeV. This arrangement provides for acceleration of ~20 to 25 mA of xenon under current-saturated conditions. Swenson argues[11] that the high voltage of the dc injector is needed to obtain a high current limit and a higher starting frequency (23.5 MHz) as compared with other possible schemes that use a lower voltage injector. We suggest an alternative approach that would use the rfq to accept the injector beam, bunch it, and accelerate it to a few MeV. A major advantage of the rfq is that an injection at a much lower voltage (≤250 kV) can be used without lowering the space-charge limit. In addition, the rfq has the potential for adiabatic bunching, which can result in capture efficiencies exceeding 90% and minimal brightness reduction, and lends itself to array-like configurations that can be used to increase the total beam intensity.[12] The bunches from the different beam channels in the array can easily be interlaced longitudinally, which is desirable when funneling before a frequency transition.

The rfq can operate at lower beta than conventional drift-tube linacs because the focusing is obtained from the rf electric fields; therefore, there is no requirement to include magnetic quadrupoles within the small cells. This opportunity to use a linear accelerator at low beta values permits adiabatic bunching of the dc beam, resulting in high capture and transmission efficiencies (>90%). In principle, adiabatic bunching is not restricted to low energies, but its application at higher energies can require too much time. Good transmission efficiency implies small beam loss. Reducing the amount of lost beam and keeping the energy of lost particles low may be important to minimize potential problems associated with localized heating of components by an intense beam.

Radio-Frequency Quadrupole. Our rfq design approach has been reported elsewhere. (See Appendix A and Ref. 13.) In the most general case, it consists of combining four sections called the radial matching section, the shaper, the gentle buncher, and the accelerator section. The adiabatic bunching is done in the shaper and gentle buncher sections. The synchronous phase angle is ramped from −90° to its final value at the end of the gentle buncher, so that the beam reaches its minimum phase extent at this point. For this and other reasons, the space-charge limit typically does not occur for the dc beam at the input, but instead occurs at the end of the gentle buncher.[14] If the focusing force is restricted by the maximum obtainable electric field, the current limit for a given aperture size scales approximately as

$$I \propto \frac{q}{A} E_s^2 \beta\lambda^2 , \qquad \text{(VIII-1)}$$

where q and A are, respectively, the charge state and mass number of the ion, E_s is the maximum surface electric field, β is the ratio of ion velocity to the velocity of light at the end of the gentle buncher, and λ is the rf wavelength. One can also show that for a fixed energy gain ratio within the section, the length of the gentle buncher section scales as

$$L \propto \frac{A}{q} \frac{\beta^3 \lambda}{E_s} . \qquad \text{(VIII-2)}$$

The length formulas for the shaper and accelerator sections are similar to Eq. (VIII-2) and show that the current limit increases in proportion to β but that the length increases in proportion to β^3. Thus, the advantage of high energy, which raises the current limit, is soon offset by a rapidly increased structure length.

Radio-Frequency Quadrupole Linacs for Heavy Ions. Two examples of rfq linac designs for singly charged xenon have been prepared. The first demonstrates acceleration under a current-saturated condition, which is always accompanied by high beam losses and an output emittance characterized by the geometric acceptance of the channel. In this case, the output emittance is kept small by using a small bore. The second example illustrates acceleration under more lightly loaded conditions where a smaller fraction of the input current is lost.

Both examples contain the four sections mentioned earlier. We chose 0.25 and 2.5 MeV as the gentle buncher's initial and final energies, respectively. These choices represent a compromise between good performance for high beam currents and overall length. In accordance with our standard design approach,[13] we chose 0.242 MeV as the initial energy at the beginning of the shaper section. A final energy of 5 MeV is arbitrary and could be increased without adding greatly to the length. A maximum surface field was assumed to be E_s = 15 MV/m, which we regard as a conservative operating point.

The computer program that we use to study the rfq beam dynamics is called PARMTEQ[12] (a modified version of PARMILA). For the input, we used a zero-energy-spread dc beam, whose initial transverse phase-space distribution was generated by uniformly filling the volume of a four-dimensional hyperellipsoid. The normalized input emittances in both x,x′ and y,y′ phase space, which contains 100% of the beam, were taken to be 0.01π cm·mr. This results in 90% of the input beam being within 0.007π cm·mr and an rms input emittance of 0.0017π cm·mr.

Table VIII-I summarizes the parameters for the two cases. The frequency is 12.5 MHz, and the synchronous phase begins at −90° and ends at −32° in both cases. The initial and final vane-modulation parameters m_i and m_f are listed (see Appendix A and Ref. 13); V is the intervane voltage and r_o is the average radius parameter, which is equal to the initial radial aperture. The length L for both cases includes a radial matching section at the input. An important difference between Linacs 1 and 2 is a difference in aperture, as indicated by r_o. Also, although Linac 2 has a higher voltage than Linac 1, it is longer because of its smaller vane-modulation parameter m.

Table VIII-II shows the results for Linac 1 at four input beam currents. The entries include average input current I_i, average output current I_o, and transmission efficiency T. The normalized output transverse emittance at the 90% contour is ε_{90}, and the rms normalized output emittance is ε_{rms}. Linac 1 is operated essentially at its saturated current limit of slightly more than 20 mA for input current values higher than 30 mA. The aperture limits the final normalized emittance to a relatively small value. The transmission at I_i = 30 mA of 74.7% is still higher than that of most conventional single-gap buncher configurations.

TABLE VIII-I

RADIO-FREQUENCY QUADRUPOLE PARAMETERS

Parameter	Linac 1	Linac 2
q	1	1
Ion	^{132}Xe	^{132}Xe
f(MHz)	12.5	12.5
W_i(MeV)	0.242	0.242
W_f(MeV)	5.0	5.0
ϕ_i(deg)	−90	−90
ϕ_f(deg)	−32	−32
m_i	1.00	1.00
m_f	2.00	1.48
V(MV)	0.134	0.200
r_o(cm)	1.22	1.81
L(m)	23.3	27.1

TABLE VIII-II

LINAC 1 RESULTS

I_i (mA)	I_o (mA)	T (%)	ε_{90} [(cm·mr)/π]	ε_{rms} [(cm·mr)/π]
20	1818	93.9	0.015	0.0032
30	22.4	74.7	0.018	0.0038
40	22.4	56.1	0.021	0.0045
50	21.1	42.2	0.021	0.0045

TABLE VIII-III

LINAC 2 RESULTS

I_i (mA)	I_o (mA)	T (%)	ε_{90} [(cm·mr)/π]	ε_{rms} [(cm·mr)/π]
20	19.9	99.7	0.027	0.0056
30	29.1	96.9	0.031	0.0068
40	33.8	84.4	0.037	0.0077
50	33.9	67.8	0.041	0.0085

Table VIII-III shows some Linac 2 results for four input beam currents. The aperture of Linac 2 is larger than that of Linac 1 and, consequently, its acceptance is greater. In contrast to Linac 1, almost no restriction is caused by the aperture at $I_i = 30$ mA. This causes a higher transmission (96.9%) and a larger output emittance ($\varepsilon_{90} = 0.031\pi$ cm·mr) than for Linac 1. As the input current increases, we observe the expected decrease in transmission. For input currents of 40 and 50 mA, the output current approaches its saturated limit at a value higher than 30 mA.

From the Linac 1 results, we see that, as might be expected, a high-current beam can be obtained with a small output emittance at the cost of reduced transmission. However, Linac 2 probably best illustrates the advantages of the rfq. For input currents less than 30 mA, it captures and transmits nearly all of the injected beam and thereby minimizes any problems associated with beam losses. The output transverse emittance ε_{90} at 5 MeV obtained from the simulation code for $I_i \leq 30$ mA is consistent with the estimate assumed in design studies using the beam from the independently phased cavity system of the alternative buncher.[13] For Linac 2 at $I_i = 30$ mA, we calculate a two-dimensional output brightness of $B = 6.1$ A/cm^2·mr^2, where we have defined the brightness as $B = 2I/\pi^2\varepsilon_{90}^2$. In addition, we have calculated that the longitudinal output emittance at the 90% contour is 0.85π MeV-deg.

Radio-Frequency Linac Approach to Heavy-Ion Fusion (D. A. Swenson)

When operated at sufficiently high currents of singly charged heavy ions in the range of 1-10 GeV and at frequencies in the range of 100-400 MHz, the rf linac is an efficient accelerator, that is, most of the power is transferred to the beam. Under these conditions, the total rf power required to accelerate a given particle to a given particle energy is essentially independent of the charge state; thus, if the singly charged heavy ion, with its low charge-to-mass ratio, is the preferred particle for reasons associated with other parts of the facility, it is quite acceptable from the rf linac point of view. Furthermore, the relatively high current reduces the required linac pulselength, causing the optimum acceleration gradient to be higher and the optimum accelerator length to be shorter than would be the case for lower currents of similar ions.

On the other hand, filling such machines is a major problem, requiring multiple low-frequency linacs at the lowest energy with relatively low currents, followed by fewer linacs at higher energies with higher frequencies and currents, culminating in a single linac at the highest frequency and current for the major portion of the facility.

We define "funneling" as the interlaced filling of one linac of frequency Nf from N linacs of frequency f. For a number of reasons, the most interesting value of N is 2. For N = 2, funneling implies a doubling of the frequency whenever the space-charge limits of the structure permit and a combination of the beams from two linacs at the old frequency into each linac at the new frequency. In principle, it is possible to accomplish the funneling with no increase in the transverse phase space and a simple addition of the longitudinal phases from the two linacs using an rf deflector.

Funneling is an important concept. It implies the filling of every bucket at each new frequency, thereby using the full space-charge capabilities of each portion of the linac. It maximizes the frequency and, consequently, minimizes the size and power consumption of each

portion of the structure. Empty buckets represent a valuable resource that must not be wasted. They represent prime space in which an additional beam can be accelerated with no additional hardware, space, or pulselength, and with only the additional power required for the additional beam. The additional beam current reduces the linac pulselength and the severe requirements on the final bunching system, which involve multiple accumulator rings and linear induction bunchers.

The concept of funneling was invented at the 1977 HIF Workshop.[15] Since then, neither the ANL nor BNL designs have fully exploited this concept: the designs have only one-eighth to one-twelfth of the buckets filled and particle currents that are factors of 10 to 100 below what they could be. This causes the pulses in these designs to be longer, the optimum gradients to be lower, and the linacs to be longer than in designs that fully exploit funneling.

Strict funneling implies a constant ratio between the beam current and the frequency of each portion of the linac. The relative difficulty of funneling depends on the ratio of the physical separation of the beams to their particle wavelength ($\beta\lambda$). The larger this ratio, the more difficult the funneling. At the lowest betas, it is attractive to consider arrays of linac channels within a common linac structure where the beam-to-beam spacings can be quite small.

The rfq promises to be the best low-beta linac structure, offering high capture of very-low-energy beams and acceleration with a minimal emittance growth; it is the best transition we know of between a dc injector and an rf linac. (See Appendix B.) Furthermore, the rfq lends itself to array-like configurations (Fig. VIII-3), which can be driven by external resonant circuits in the same manner as Wideröe linacs. By staggering the geometrical modulations that produce the accelerating voltages, we can make the beams interlace as required by funneling, without introducing varying lengths into the funneling transport lines.

For the second linac structure in the system, we are considering an rfq linac, an electrostatically focused π, 3π Wideröe linac, and a magnetically focused π, 3π Wideröe linac. At a few MeV, the electrostatically focused π, 3π Wideröe linac seems to be the best choice, because the rfq efficiency is dropping, although the required magnet strengths are still impractical.

If the original array of rfq linacs involves more than two interlaced beam channels, the second structure must also accommodate an array of more than one interlaced channel. Multiple-holed drift tubes in a Wideröe or Alvarez configuration *do not* satisfy the interlaced requirements of funneling. Figure VIII-4 suggests the basic features of a double-barreled, electrostatically focused, π, 3π Wideröe linac that does satisfy this requirement and would seem to have some attractive rf and mechanical properties. This idea could be extended to a larger number of beams at the cost of further complication.

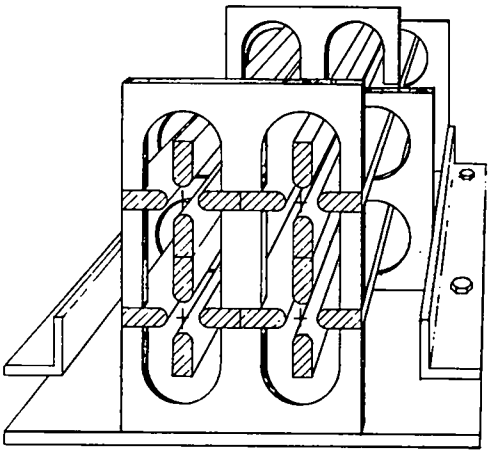

Fig. VIII-3.
Array of four rfq channels.

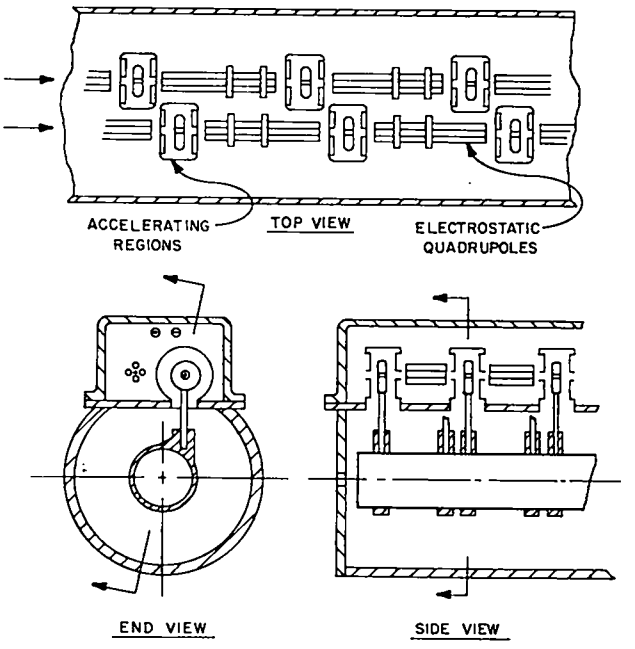

Fig. VIII-4.
Double-barreled, electrostatically focused, π, 3π Wideröe linac.

A multiple-channel, magnetically focused π, 3π Wideröe linac could be based on the same idea, where the magnetic quadrupoles could have an outer diameter equal to the channel separation (not an undue constraint). In this case, it would seem preferable to limit the vacuum to the rf accelerating regions and the interior of a beam tube passing through the magnetic quadrupoles. This would leave the magnetic quadrupoles completely exposed on top of the structure to facilitate alignment and servicing.

We realize that brightness requirements have a strong effect on how close we can operate to the space-charge limit. However, the important properties of funneling and the impact on structure selection (outlined above) are equally valid for lower currents. We are proceeding with more detailed design of a facility configuration using these ideas. In the following paragraphs, we outline a preliminary idealized configuration that illustrates the potential advantages of full funneling.

We believe that the space-charge limit for Xe^{+1} in a magnetically focused rf linac is about 1 A at 1 GeV and 100 MHz, based on a uniformly filled, three-dimensional ellipsoidal model and a smooth approximation of the transverse focusing forces.[13] This limit increases with energy and decreases with frequency in such a way that at 3 GeV and 400 MHz the limit is also about 1 A. Thus, for the major portion of a 10-GeV heavy-ion fusion facility based on the rf-linac approach, currents of ~1 A can be accommodated at frequencies as high as 400 MHz. To aim for 800 mA at 400 MHz in the major portion of the facility, it is necessary to start out with 32 linac channels, each carrying 25 mA at 12.5 MHz, followed by five stages of funneling.

A sequence of linac structures that if combined through funneling, would produce an 800-mA beam of Xe^{+1} at 10 GeV is given in Table VIII-IV. After the initial rfq section, each structure is near its space-charge limit at the low-energy end and is significantly below its space-charge limit at the high-energy end. Detailed studies of the beam dynamics in these structures have not been performed, nor have studies been made of the problems associated with funneling.

The transition energies in Table VIII-IV are based on a ratio of the space-charge force to the focusing force of 0.5, which corresponds to an allowed change in frequency (tune depression) of ~30%.[13] Within the rfq, this limit is evaluated at the end of a bunching subsection. For all other cases, these limits apply at the input or transition energy to each new structure. If we decide to operate further from the space-charge limit, because of emittance growth or current loss, we can delay the transitions to somewhat higher energies where the limiting currents are higher.

TABLE VIII-IV

SEQUENCE OF LINAC STRUCTURES

Structure	1	2	3	4	5	6
Type	rfq[a]	EFW[b]	MFW[c]	MFA[d]	MFA[d]	MFA[d]
Number	32	16	8	4	2	1
Current, mA	25	50	100	200	400	800
Frequency, MHz	12.5	25	50	100	200	400
Energy entering, MeV	0.2	6	28	190	750	3000
Beta entering	0.02	0.010	0.021	0.056	0.110	0.217
Beta*Lambda, m	0.043	0.118	0.128	0.166	0.165	0.163
Energy out, MeV	6	28	190	750	3000	10^5
Length, m	21	26	125	373	1125	1750
Total length, m						3420

[a]rfq = radio-frequency quadrupole linac.

[b]EFW = electrostatically focused Wideröe linac.

[c]MFW = magnetically focused Wideröe linac.

[d]MFA = magnetically focused Alvarez linac.

The total length of the linac is only 3.4 km, which is short compared to previous designs. This is the result of the relatively high acceleration gradients in the latter portions of the facility; namely, 1.5 MeV/m at 100 MHz, 2.0 MeV/m at 200 MHz, and 4.0 MeV/m at 400 MHz. These gradients at these frequencies are known to be technically feasible, and they can be shown to be economically attractive because of the high frequencies and high peak beam currents that result from funneling.

We propose to configure the 32 channels of the first structure as 8 independent arrays of 4 channels each (Fig. VIII-3); the 16 channels of the second structure as 8 independent double-barreled structures (Fig. VIII-4); and the 8 channels of the third structure as 8 conventional 50-MHz Wideröe structures. Those configurations with the highest multiplicities would take the form of eight identical assemblies, each accommodating a total current of 100 mA. Such configuration allows the possibility of developing, prototyping, and testing one-eighth of the total configuration in a staged development of the total facility.

REFERENCES

1. L. E. Thode, "Effect of Electron-Ion Collisions on the Nonlinear State of the Relativistic Two-Stream Instability," Phys. Fluids **20**, 2121 (1977).

2. W. B. Herrmannsfeldt, Ed., Proc. HIF Workshop, Berkeley, Calif., October 29-November 9, 1979, Lawrence Berkeley Laboratory report LBL-10301 (September 1980).

3. L. E. Thode and R. W. Sudan, "Two-Stream Instability Heating of Plasmas by Relativistic Electron Beams," Phys. Rev. Lett. **30**, 732 (1973).

4. T. P. Wright, "Analytic Ion Self-Pinch Formulae," Phys. Fluids **22**, 1831 (1979).

5. TRW Proposal No. 33876.000, "L.I.F.E., Light Ion Fusion Experiment," September 1978.

6. R. Jameson and P. Lapastolle, "Summary of Low-β Linac Working Group," Proc. HIF Workshop, Berkeley, Calif., October 29-November 9, 1979, Lawrence Berkeley Laboratory report LBL-10301 (September 1980), p. 6.

7. R. Jameson, "Emittance Growth in RF Linacs," Proc. HIF Workshop, Berkeley, Calif., October 29-November 9, 1979, Lawrence Berkeley Laboratory report LBL-10301 (September 1980), p. 4.

8. R. L. Martin, "Overview of the Argonne National Laboratory Program," Proc. HIF Workshop, Argonne National Laboratory, Chicago, Ill., September 19-26, 1978, Argonne National Laboratory report ANL-79-41 (1978), p. 1.

9. J. M. Watson, "ANL Experimental Program," Proc. HIF Workshop, Argonne National Laboratory, Chicago, Ill., September 19-26, 1978, Argonne National Laboratory report ANL-79-41 (1978), p. 17.

10. J. M. Watson, J. M. Bogaty, R. J. Burke, R. L. Martin, M. G. Mazarakis, K. K. Menefee, E. F. Parker, and R. L. Stockley, "A High Intensity 1.5 Megavolt Heavy Ion Preaccelerator for Ion Beam Fusion," IEEE Trans. Nucl. Sci. **NS-26**, No. 3, 3098 (June 1979).

11. D. A. Swenson, "RF Linac Approach to Heavy Ion Fusion," Proc. HIF Workshop, Berkeley, Calif., October 29-November 9, 1979, Lawrence Berkeley Laboratory report LBL-10301 (September 1980), p. 239.

12. R. H. Stokes, K. R. Crandall, J. E. Stovall, and D. A. Swenson, "RF Quadrupole Beam Dynamics," IEEE Trans. Nucl. Sci. **NS-26**, No. 3, 3469 (June 1979).

13. Thomas P. Wangler, "Space-Charge Limits in Linear Accelerators," Los Alamos Scientific Laboratory report LA-8388 (December 1980).

14. A. Moretti, J. M. Watson, R. L. Stockley, J. S. Moenich, R. J. Lari, T. K. Khoe, J. A. Bywater, R. J. Burke, and S. Jorna, "The Design of a 12.5 MHz Wideröe Linac for Ion Beam Fusion," Proc. 1979 Linear Accel. Conf., Montauk, New York, September 10-14, 1979, p. 152.

15. Lyle W. Smith, Ed., Proc. HIF Workshop, Berkeley, Calif., October 17-21, 1977, Brookhaven National Laboratory report BNL 50769 (February 1978), p. 17.

APPENDIX A

1979 LINAC ACCELERATOR CONFERENCE

RF QUADRUPOLE BEAM DYNAMICS DESIGN STUDIES*

K. R. Crandall, R. H. Stokes, and T. P. Wangler
Los Alamos Scientific Laboratory
Los Alamos, New Mexico 87545

Summary

The radio-frequency quadrupole (RFQ) linear accelerator structure is expected to permit considerable flexibility in achieving linac design objectives at low velocities. Calculational studies show that the RFQ can accept a high-current, low-velocity, dc beam, bunch it with high efficiency, and accelerate it to a velocity suitable for injection into a drift-tube linac. Although it is relatively easy to generate a satisfactory design for an RFQ linac for low beam currents, the space-charge effects produced by high currents dominate the design criteria. Methods have been developed to generate solutions that make suitable compromises between the effects of emittance growth, transmission efficiency, and overall structure length. Results are given for a test RFQ linac operating at 425 MHz.

Introduction

Soon after the linear accelerator was invented, searches began for methods to circumvent the incompatibility between longitudinal and radial stability. The use of drift-tube foils or grids, externally applied fields, and alternating phase focusing has met with success in specific areas of application. However, each of these solutions has serious disadvantages particularly in the acceleration of low-velocity ions. Since 1956, there have been suggestions[1-4] that linear accelerator electric fields could be used for radial focusing as well as for acceleration. These proposals were based on noncylindrically symmetric electrode shapes that would generate transverse quadrupole fields. This rf self-focusing is an important new idea especially at low velocities because the electric force is velocity independent.

In 1970, Kapchinskii and Teplyakov[5,6] (K-T) proposed a particularly attractive form of these new ideas. The previous proposals to generate quadrupole fields used specially shaped gaps between drift tubes or waveguides to generate localized focusing forces. However, the scheme proposed by K-T was a more basic and flexible idea in which the quadrupole focusing field was spatially continuous along the z-axis. We call this structure the RFQ. Figure 1 shows a schematic view of a four-vane resonator that is the form of the RFQ being developed at the Los Alamos Scientific Laboratory (LASL).

The RFQ may have important applications in the low-velocity part of many types of ion accelerators. It can provide several necessary functions in a continuous manner to produce a final beam suitable for injection into a conventional accelerator. Briefly these functions are the following: (1) acceptance of a dc beam (50-keV protons, for example) and radially matching it into the following sections of the RFQ; (2) bunching this beam adiabatically with high capture efficiency (>90%); and (3) accelerating the beam to an energy (1-MeV protons, for example) that is convenient for injection into the next acceleration stage. In this paper we will consider the next stage to be a drift-tube linac. Through proper design it is possible to control the particle distribution in the phase-stable bucket so that nonadiabatic acceleration effects are minimized. Also, the final synchronous phase can be brought to a value (say -30°) that is suitable for capture by a drift-tube linac. Because the radial focusing forces are electric and retain their full strength at low velocity, and also because the forces are spatially continuous, the above functions can be accomplished at low velocities with minimal effects from space charge. Also, as suggested by K-T, space-charge effects can be further minimized through proper control of the bunching process. This idea is an important contribution that is compatible with possible choices of RFQ design parameters.

There are several possible applications of the RFQ now under consideration at LASL. These include: (1) a high-intensity deuteron accelerator for the Hanford Fusion Materials Irradia-

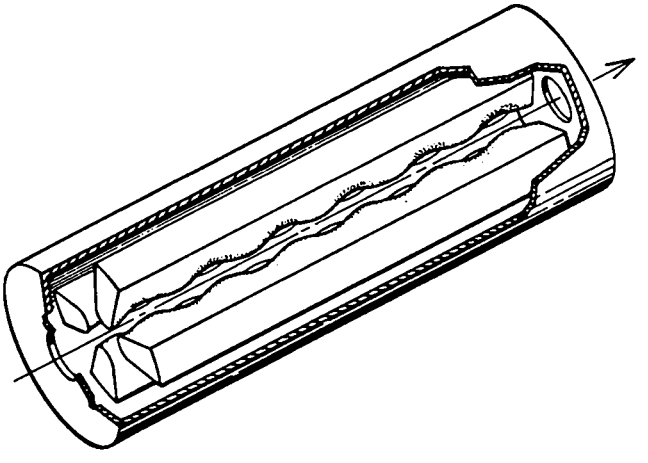

Fig. 1. Four-vane resonator.

*Work performed under the auspices of the U. S. Department of Energy.

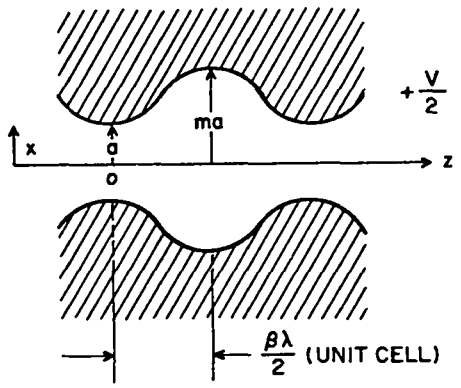

Fig. 2. RFQ pole-tip geometry.

tion Test (FMIT) Facility, (2) the Pion Generator for Medical Irradiation (PIGMI), a high-intensity proton accelerator for use in pion and neutron radiotherapy, (3) a heavy-ion accelerator for inertial fusion, and (4) a high-energy accelerator for ions such as neon. Methods we have found useful in choosing beam-dynamics parameters for RFQ systems are presented. As a specific example, we give the results of these methods applied to a proton linac designed to test the RFQ principle.

RFQ Electric Fields and Pole-Tip Geometry

In the RFQ the electric field distribution is generated by four poles arranged symmetrically around a central z-axis. The poles are excited with rf power so that at a given time, adjacent pole tips have equal voltages of opposite signs. If the pole tips have constant radius as z is varied, then only a transverse field (mainly quadrupole) is present. In the x-z plane for example, this quadrupole field is focusing for one-half of the rf period and defocusing the other half. The structure has the properties of an alternating-gradient focusing system with a strength independent of particle velocity. To generate a longitudinal accelerating field the pole tips are periodically varied in radius. The variation is such that, at a value of z where the pole tips in the x-z plane have minimum radius, the pole tips in the y-z plane have maximum radius. This is shown in Fig. 1. Figure 2 shows a cut through the x-z plane, and shows the mirror symmetry of the opposite poles. In Fig. 2 the radius parameter a, the radius modulation parameter m, and the cell length are defined. The longitudinal field is generated between the x pole tip that has minimum radius at z = 0, and the y pole tip that has minimum radius at z = βλ/2. The unit cell is βλ/2 in length and corresponds to one acceleration gap. Adjacent unit cells have oppositely direct E_z fields, so that in practice only every other cell contains a particle bunch.

In the coordinate system of Fig. 2 the lowest-order potential function given by K-T is written in cylindrical coordinates (r, ψ, z) as follows:

$$U = \frac{V}{2}\left[X\left(\frac{r}{a}\right)^2 \cos 2\psi + AI_o(kr)\cos kz\right] \cdot \sin(\omega t + \phi) \quad , \tag{1}$$

where V is the potential difference between adjacent pole tips, and $k = 2\pi/\beta\lambda$.

From this we obtain the following electric field components:

$$E_r = -\frac{XV}{a^2} r \cos 2\psi - \frac{kAV}{2} I_1(kr)\cos kz \quad , \tag{2}$$

$$E_\psi = \frac{XV}{a^2} r \sin 2\psi \quad , \tag{3}$$

$$E_z = \frac{kAV}{2} I_o(kr)\sin kz \quad , \tag{4}$$

each multiplied by sin (ωt + φ). Our method of calculating RFQ beam dynamics is based on these fields and is described in Ref. 7. The quantities A and X are given by:

$$A = \frac{m^2 - 1}{m^2 I_o(ka) + I_o(mka)} \tag{5}$$

$$X = 1 - AI_o(ka) \quad . \tag{6}$$

The quantity VA is the potential difference that exists on the axis between the beginning and the end of the unit cell. This means that the space-average longitudinal field is given by $E_o = 2AV/\beta\lambda$. The energy gain of a particle with charge q and synchronous velocity βc traversing a unit cell is approximately:

$$\Delta W = qE_o \ell T \cos\phi_s \quad , \tag{7}$$

where $\ell = \beta\lambda/2$, and $T = \pi/4$ is the value of the transit-time factor for a longitudinal field with space variation sin kz. Our notation is similar to K-T except that our A equals their θ divided by $T = \pi/4$.

A radial stability diagram for the RFQ is given in Fig. 3. The abscissa is given by:

$$\Delta = \frac{\pi^2 qVA \sin\phi}{2Mc^2\beta^2} \quad . \tag{8}$$

This is proportional to the usual "rf defocus" force that gives radial defocusing when a linac

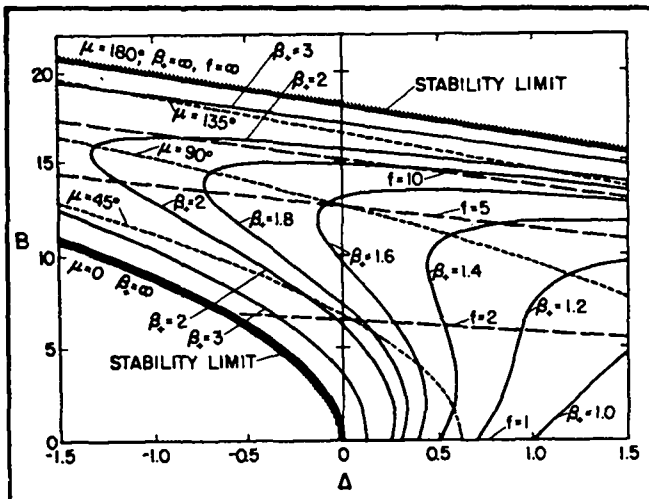

Fig. 3. RFQ radial stability diagram.

is operated with a negative phase angle in the range -90 to 0 degrees. The ordinate in Fig. 3 is:

$$B = \frac{q\lambda^2}{Mc^2} \cdot \frac{XV}{a^2} \quad . \tag{9}$$

This is proportional to the radial focusing force, and depends on the magnitude of the electric quadrupole strength XV/a^2. The electric quadrupole strength does not explicitly depend on z. This means that for given values of a, m, and β, the focusing strength is constant through a unit cell. It also means that one can maintain the same focusing strength in every unit cell by varying the parameters such that XV/a^2 is held fixed. Except for the short, initial, radial matching section, the linac discussed in the section "Design of the 425-MHz RFQ Test" has been designed to have a constant radial-focusing strength. Later we show that this has a geometrical consequence that may be beneficial in the design of RFQ resonators.

The pole-tip shape required to produce the above electric fields is given by:

$$x^2 - y^2 = r^2 \cos 2\psi = \frac{a^2}{X} \left[1 - AI_o(kr) \cos kz\right] . \tag{10}$$

To obtain the shape of one pole tip in the x-z plane we let $\psi = 0$. This gives:

$$\frac{x^2}{a^2} = \frac{1 - AI_o(kx) \cos kz}{1 - AI_o(ka)} \quad . \tag{11}$$

We then solve this equation numerically to find values of x as a function of z. Call these values of x, which are solutions, $\alpha(z)$. To describe the geometry in the transverse plane we have derived an equation for the transverse radius of curvature of the pole tip. This curvature is:

$$R(z) = \alpha(z) \frac{P + Q}{P - Q} \quad , \tag{12}$$

where

$$P = I_o(ka) + I_o(mka)$$

and

$$Q = \frac{ka^2}{2\alpha} (m^2 - 1) I_1(k\alpha) \cos kz \quad .$$

In our pole-tip geometrical design we have made the radius of the pole tips equal to $\alpha(z)$. The pole-tip shape in the transverse plane was approximated by requiring the pole tips to have the radius of curvature R(z). The pole tips are constructed by repeated cuts in the transverse plane by a tape-controlled milling machine. This procedure is discussed more fully in Ref. 8.

At $z = \beta\lambda/4$, half way through the unit cell, the RFQ has quadrupolar symmetry. At this point both the x and y pole tips have a radius equal to $r_o = aX^{-1/2}$. Also, at this point the radius of curvature $R = r_o$. The quantity r_o can be regarded as a characteristic average radius of the RFQ pole tips. As we have discussed, if V is constant, keeping the focusing strength at a fixed value requires X/a^2 to be constant, and also this is equivalent to keeping r_o fixed. In general, a fixed value of r_o can be expected to minimize variations in the vane-to-vane capacitance, and should facilitate the design of an RFQ resonator in which the pole-tip voltage distribution is required to be flat over its entire length.

RFQ Design Procedures

If the ion species and the initial and final energies are given, and if the frequency and intervane potential are specified, the RFQ design is determined when the three independent functions a(z), m(z), and $\phi_s(z)$ are given, where z is the axial distance along the accelerator. Although it may be more convenient to explicitly use other related functions such A, X, or B, the designer must determine three independent functions that produce the desired objectives in terms of adequate radial focusing, capture efficiency, radial emittance growth overall length, or other stated criteria. Simple linear forms for the above functions can achieve these objectives for low beam currents as long as the rate of change of the variables is slow enough to approximate an adiabatic condition. However, as the magnitude of the space-charge force increases, more complex forms for these functions appear to become necessary to minimize both particle loss and radial emittance growth.

One possible solution to this problem has been proposed by K-T. In this method Ω_o, the longitudinal, small oscillation, angular frequency at zero current, and Z_b, the spatial length of the separatrix, are held constant. If the functional form of B is specified, then the three independent functions a, m and ϕ_s are determined. Expressions for Ω_o and Z_b are:

$$\Omega_o^2 = \frac{qV\lambda\omega^2|\sin\ \phi_s|}{4Mc^2\beta^2} \tag{13}$$

$$Z_b = \frac{\beta\lambda\Phi}{2\pi} \ , \tag{14}$$

where Φ is the angular length of the separatrix, which is related to the synchronous phase ϕ_s by:

$$\tan\ \phi_s = \frac{\sin\Phi - \Phi}{1 - \cos\Phi} \tag{15}$$

In the region of small longitudinal oscillations and for adiabatic changes, constant Ω_o implies a beam envelope of constant length. For a longitudinally matched beam this also implies an invariant longitudinal charge density distribution and fixed beam length. This result holds for zero current and is also true in the presence of space-charge forces, if one assumes the beam bunch to be uniformly distributed in a three-dimensional ellipsoid of constant dimensions. Constant Z_b together with constant Ω_o can furthermore be shown to make the charge-density distribution approximately constant for large, longitudinal oscillations at zero current. As can be seen from Eqs. (14) and (15), the invariance of Z_b determines ϕ_s (β). Then equation (13) determines A(β).

This method of attempting to keep the charge density distribution approximately constant, while accelerating and bunching in phase, will be expected to reduce those space-charge effects, such as radial emittance growth, that appear to be correlated with longitudinal compression of the beam bunch. However, after the resulting velocity profile $\beta(z)$ is determined, the function A(z) takes on small values, especially for large synchronous phases, and increases very slowly except near the end. This can result in an excessively long structure, particularly as the input synchronous phase approaches $\phi_s = -90^o$. To reduce the length, the initial value of ϕ_s must depart appreciably from -90^o, but this reduces the initial value of Φ, and results in reduced capture efficiency.

We have explored a generalization of the above method, where we replace the two constants Ω_o and Z_b by the new invariants ε and α, given as;

$$\varepsilon = \frac{-2\pi\dot{\Omega}_o}{\Omega_o^2} \tag{16}$$

and

$$\alpha = \Omega_o Z_b^2 \ . \tag{17}$$

When $\varepsilon = 0$ this reduces to the K-T method. For positive ε the small oscillation frequency Ω_o decreases at a constant percentage rate, and the separatrix length Z_b gradually increases. We expect this approach to yield a charge distribution that can slowly compress or expand in size depending upon the value of ε. In addition, for fixed final values of A and ϕ_s, the overall length decreases as ε increases. Generally we have found acceptable solutions with ε in the range $0 \leq \varepsilon \leq 0.2$.

We find that the use of either the K-T approach or the generalized approach is effective in reducing radial emittance growth, while the beam is being bunched. We refer to this section of the RFQ as the Gentle Bunching Section. We also find that to obtain high capture efficiency, it is necessary to introduce a section before the Gentle Buncher in which the input variables are specified as a function of z rather than β, so that the input synchronous phase can start at $\phi_s = -90^o$ and the initial value of A can be A = 0. In order to reduce the overall length following the Gentle Buncher, we add a section that maintains a high value of A at the final synchronous phase. The remaining problem of radially matching the beam into the time-varying acceptance of the RFQ requires an initial section for matching. We are thus led to four stages in the overall design as shown schematically in Fig. 4. We will now describe the first stage, the Radial Matching Section.

The matched ellipse parameters in the RFQ depend on the rf phase and are relatively independent of position along the linac. Therefore the orientation of the acceptance ellipse depends on time. For proper matching into the RFQ, one must provide a transition from a beam having time-independent characteristics to one that has the proper variations with time. This means that at the input, a time-independent set of ellipse parameters is required. These parameters will depend on the beam current. Our solution is to taper the vanes at the input of the RFQ so that the focusing strength changes from almost zero to its full value over a distance of several (5-10) focusing periods. This procedure allows the time-independent beam to adapt itself to the time structure of the focusing system. Quadrupole symmetry is maintained throughout this section (no vane modulation).

This procedure is illustrated in Fig. 5, a display generated by the program TRACE,[9] which has been modified to include rf quadrupoles,

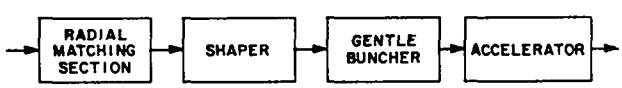

Fig. 4. Functional block diagram.

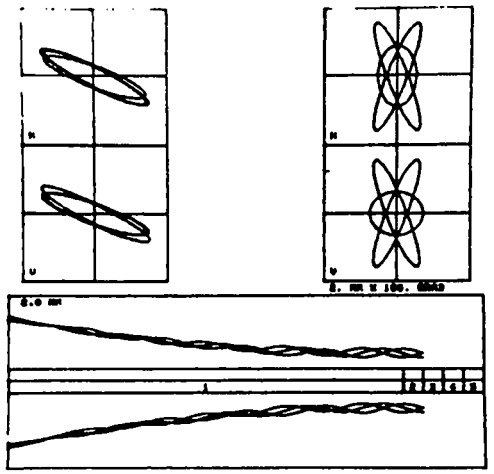

Fig. 5. Radial Matching Section.

either of constant or tapered strengths. The matched ellipse parameters are first found for various phases in the constant-strength section. Three such matched ellipses, corresponding to phases 90° apart, are shown in the upper right side of the figure for both the x-x' and y-y' planes. This graphically demonstrates how different the matched ellipses can be as a function of phase, and also shows the relatively small area of overlap that is common to all of these ellipses. The phase-space plots at the upper left are the result of following these same three ellipses backward through a tapered section of the RFQ, 5-periods long (10 cells). One can see that these ellipses are very similar and have a high degree of overlap. The bottom graph in the figure shows the horizontal and vertical profiles that result from following these three ellipses through the tapered rf quadrupole. Space-charge effects were included in this calculation, which assumed a beam current of 30 mA.

An unexpected benefit of the Radial Matching Section is that the increase in aperture at the input results in weak fringe fields and negligible fringe effects for both longitudinal and radial motions. The longitudinal field generated within the matching section is also negligible because of the fact that the change in B occurs over many rf cycles.

The second stage, which we call the Shaper Section, can begin at $\phi_s = -90°$. The accelerating field is increased steadily from zero, while ϕ_s is maintained at a large value, so as to obtain a high capture efficiency. Under the influence of the rising axial field, an input dc beam with small energy spread will rotate through many cycles of longitudinal oscillation. The filament in phase space wraps around itself to approximate a matched beam in longitudinal phase space. Some compression of the beam within the phase stable area is desirable to anticipate subsequent non adiabatic behavior, which could lead to particle loss. At high beam currents, such compression should be limited, however, because of the large radial emittance growth that can result when the beam is tightly bunched. Even so, dramatic effects of space-charge repulsion will be especially apparent at the first phase foci for an input dc beam with small energy spread.

For the third stage, the Gentle Buncher, we employ the generalized method, where we satisfy equations (16) and (17) and hold B constant. The Gentle Buncher Section completes the bunching begun in the Shaper Section and accelerates the quasi-matched beam from the Shaper, until the final synchronous phase is reached. The bunch length and the charge density undergo no large change in the process.

When the final synchronous phase is reached, the Acceleration Section begins. In this section ϕ_s, m, and a are held at constant final values to apply a relatively large fraction of the intervane voltage on axis, and to bring the beam to its final energy within a short distance.

An important step in the design procedure is a choice of operating intervane potential, which normally should be as large as possible, consistent with the sparking limit. The results from program SUPERFISH[10] show that for the RFQ vanes constructed at LASL, the highest surface fields, E_s, occur in the middle of each cell at the point of pure quadrupole symmetry. The maximum field does not occur at the pole tip, but occurs at the point where the vanes have minimum separation. The field at the pole tip is V/r_o and the peak field $E_s = \kappa V/r_o$ where for our geometry $\kappa = 1.36$. Once the choice of maximum allowable surface field is made, the ratio V/r_o is determined.

After a choice of B is made, which provides a good compromise between radial stability and adequate aperture size, the quantities V and r_o can be obtained from the relations:

$$r_o = \frac{q\lambda^2 E_s}{Mc^2 B\kappa} \tag{18}$$

$$V = \frac{q\lambda^2 E_s^2}{Mc^2 B\,\kappa^2} \tag{19}$$

We see that higher surface field E_s and smaller B will increase both r_o and V. The average axial field then becomes:

$$E_o = \frac{2q\lambda A E_s^2}{Mc^2 B\beta\kappa^2} \quad . \tag{20}$$

We choose an initial m value of m = 1. A final value of m = 2 produces a good compromise between acceleration efficiency, A, and focusing efficiency, X, at the end. If X is too small, the constraint that B is constant may make the final radius parameter too small.

Error Tolerances

After a linac has been designed, one must try to determine how sensitive the design is to all probable sources of error. The quantity and quality of the output beam can be degraded by a variety of things, such as a mismatch and a misteering of the input beam, and alignment errors and excitation errors in the linac. Tolerances can be specified for some of these errors only by running a large number of numerical simulations. For other types of errors, it is possible to make more general statements, and it is these types that we will be concerned with in this section.

The results can be specified in terms of the magnitudes of the multipoles of the focusing field relative to the quadrupole strength at the bore radius. The radial component of the nth multipole at radius, r, and angle, ψ, is defined to be:

$$E_{r,n} = A_n \left(\frac{r}{r_o}\right)^{n-1} \cos\ (n\psi - \delta_n) \quad , \tag{21}$$

where A_n is the amplitude and δ_n is the phase of the nth multipole, and r_o is the bore radius.

The values given below, as well as those given for image charge effects, (see Appendix) were obtained using a computer program that calculates the charge density induced on equipotential surfaces.[11] The unperturbed calculations were made with the vanes approximated by four circular cylinders symmetrically placed about the z-axis. The cylinder walls were a distance r_o from the z-axis and the diameter of each cylinder was $2r_o$.

Alignment Errors

The vanes are displaced slightly from their proper positions. Symmetric displacements of opposite poles, inward or outward, will have no significant effect other than changing the quadrupole strength slightly, which is equivalent to changing the operating voltage. Nonsymmetric displacements will introduce odd-order multipoles. An example of a nonsymmetric displacement is a horizontal displacement of the vertical vanes. A small displacement, d, has been calculated to produce multipoles of order 1, 3, and 5 having fractions of the quadrupole term of 0.16 d/r_o, 0.64 d/r_o, and 0.024 d/r_o, respectively. The dominant term appears to be the sextupole (n = 3), and by placing an acceptable limit on it one can specify a tolerance on d/r_o. If it is desirable to keep the sextupole term below 1%, then the tolerance on d/r_o is approximately 1.5%.

Excitation Errors

The ideal excitation is for the potential on each of the four vanes to oscillate between $\pm V/2$ at all points along the linac. Variations in the potential in the longitudinal direction will probably be gradual and small. Information about the longitudinal field can be obtained from beadpull measurements.

Errors in the transverse fields can be represented most generally by assuming that each vane is oscillating at a different potential. The potential on the ith vane would oscillate between $\pm(V + \Delta V_i)/2$, and the excitation level could be adjusted so that the average potential is correct, which would make

$$\sum_{i=1}^{4} \Delta V_i = 0 \quad . \tag{22}$$

The voltage errors, ΔV_i, can be divided into symmetric and antisymmetric parts. The symmetric components correspond to errors on opposite poles having the same magnitude and the same sign; the antisymmetric components correspond to errors on opposite poles having the same magnitude and opposite signs. The symmetric components have no effect on the multipole spectrum, but the antisymmetric components will generate odd-order multipoles. Let v_x and v_y be the fractional antisymmetric components in the horizontal and vertical vanes, respectively. That is, the potential on the opposing horizontal vanes would oscillate with the magnitudes $(1 \pm v_x)V/2$. The magnitudes of the odd multipoles are found to be proportional to $v = (v_x^2 + v_y^2)^{1/2}$, and the ratio of the first four to the quadrupole strengths are given below:

$$A_1/A_2 = 0.397\ v \quad ; \tag{23}$$

$$A_3/A_2 = 0.308\ v \quad ; \tag{24}$$

$$A_5/A_2 = 0.029\ v \quad ; \tag{25}$$

$$A_7/A_2 = 0.041\ v \quad . \tag{26}$$

That is, a 10% antisymmetric component (v = 0.1) would cause a 4% dipole field and a 3% sextupole field. If it is necessary to keep the sextupole

field below 1%, then one must keep $v < 0.032$. The dipole field would simply cause a displacement of the electrical axis of the quadrupole by the same percentage.

Design of the 425-MHz RFQ Test

One of the applications of the RFQ under consideration at LASL is for the high-intensity 35-MeV deuteron accelerator being designed for the Hanford Fusion Materials Irradiation Test (FMIT) Facility to be installed at the Hanford Engineering Development Laboratory (HEDL) at Richland Washington. An important step in evaluation of the RFQ for this linac is a full power test, which uses an existing proton injector and an existing source of rf power. As an example of the design method discussed above, we present the RFQ design for this test, which we will call the 425-MHz Test Design. Table I shows a list of parameters. Because of limitations imposed by the existing hardware, the frequency was chosen at f = 425 MHz and the length was constrained to be equal to L = 110.8 cm.

The surface gradient, E_s, was chosen to have the conservative value 27 MV/m. After the Radial Matching Section, a constant value B = 5.85 provides a compromise between radial stability and tolerance requirements arising from the small aperture. The resulting characteristic average radius is r_o = 0.2 cm and the resulting intervane voltage is V = 44 kV. The objective of the test is to capture a dc beam of energy W_i = 0.1 MeV, bunch and accelerate it to some energy greater than about 0.5 MeV, and to study the performance as a function of input current. The exact value of the final synchronous phase is not important, as long as good bunching can be demonstrated. Two computer programs have been written to help generate parameters for the beam-dynamics program PARMTEQ (see Appendix). The first program generates the Gentle Buncher parameters as a function of axial distance z, given initial and final energies for this section and given the ϵ parameter. The second program takes the initial Gentle Buncher parameters as final values for the Shaper Section, generates Shaper parameters as a function of z, then traces particles through the Shaper in longitudinal phase space, thus giving an estimate of expected capture efficiency. In addition, both programs calculate several quantities as a function of z, such as the ratio of space charge to focusing force (see Appendix), and longitudinal and radial oscillation frequencies. These results are useful as a guide to predict and interpret subsequent PARMTEQ results.

The chosen design is one with a Gentle Buncher parameter ϵ = 0, which corresponds to the K-T approach. Several designs made with ϵ = 0.2 gave comparable results. Figure 6 shows the resulting profiles from PARMTEQ for several variables. The four basic sections of the structure are indicated. The final energy after 110.8 cm and 165 cells is W_f = 0.640 MeV. The radial matching is done in the first ten cells or 5.2 cm, where B is linearly varied from an initial value of B = 0.20 to a final value B = 5.85, and is kept constant throughout the rest of the structure. The slow increase of m during the first half of the structure appears to be necessary in order to reduce radial space-charge effects as was discussed previously. As m increases and the acceleration efficiency A (not shown) also increases, the focusing efficiency, X, decreases. The constant value of B then implies a decrease in the radius parameter a. The transverse acceptance is determined by the final aperture and has a normalized value $A_n = 0.09\pi$ cm-mr at the nominal current of I = 15 mA. This can be compared with an expected input beam from the ion source having a normalized emittance of $E_n = 0.05\pi$ cm-mr. The input particle distribution used in the PARMTEQ calculation gave 100% of the beam within this phase-space area, and 90% within a normalized area of 0.034π cm-mr.

In Table II we list the PARMTEQ results for the beam transmission efficiency, the output beam current, and the radial emittance growth. The emittance growth is the normalized emittance of the transmitted beam divided by the normalized emittance of the input beam. Both emittances are obtained from ellipses which

TABLE I

425-MHz TEST DESIGN PARAMETERS

Ion	H^+
Frequency	425 MHz
Input Energy	0.100 MeV
Output Energy	0.640 MeV
Intervane Voltage	44 kV
Minimum Radius Parameter	0.126 cm
Overall Vane Length	110.8 cm
Number of Cells	165
Nominal Current	15 mA

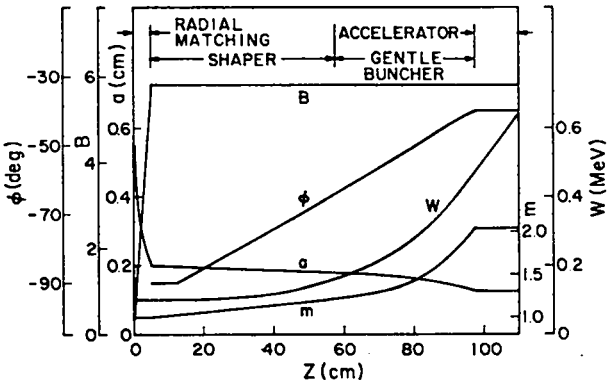

Fig. 6. Parameters for the 425-MHz test design.

TABLE II

RESULTS FROM 425-MHA TEST DESIGN

Input Current (mA)	Transmission Efficiency (%)	Output Current (mA)	Radial Emittance Growth (90% Contour)
0	96.7	0	1.04
15	96.1	14.4	1.13
30	86.4	25.9	1.23
45	73.6	33.1	1.19
60	68.6	41.2	1.22
100	54.4	54.4	1.07

contain 90% of their respective beams. As the input current increases, a larger number of particles is lost radially to the bore, which decreases in size from the input to the output. This selective radial loss explains the decreasing emittance growth for the higher currents.

Figure 7 shows the phase, energy, and radial profiles and the transverse phase space in both planes for I=0 and for the nominal beam current of I=15 mA. The dotted lines on the x profile plot indicate the aperture size. Figure 8 shows the longitudinal phase space at several cells along the RFQ for both I=0 and I=15 mA, starting with an initial dc beam with zero energy spread. Space-charge effects, which become apparent near the first phase focus, persist throughout the remaining I=15 mA plots.

It is of interest to compare the results of our 425-MHz Test Design with those that are obtained by a more simple approach, where, after the initial matching section, ϕ_s is linearly increased from -90^o to -40^o and the modulation parameter m is linearly ramped from m = 1 to 2 over the total distance of 110.8 cm. We refer to this design as the Linear Ramp Design, and it is characterized by the lack of a Gentle Buncher Section. The Linear Ramp Design gives a larger final energy of W_f = 0.719 MeV in 150 cells, which exceeds that of the 425-MHz Test Design because of a larger average axial field. Results showing the beam transmission efficiency, output current and radial emittance growth for the Linear Ramp Design are presented in Table III.

TABLE III

RESULTS FROM LINEAR RAMP DESIGN

Input Current (mA)	Transmission Efficiency (%)	Output Current (mA)	Radial Emittance Growth (90% Contour)
0	96.9	0	1.12
15	79.2	11.9	1.48
45	41.4	18.6	1.16

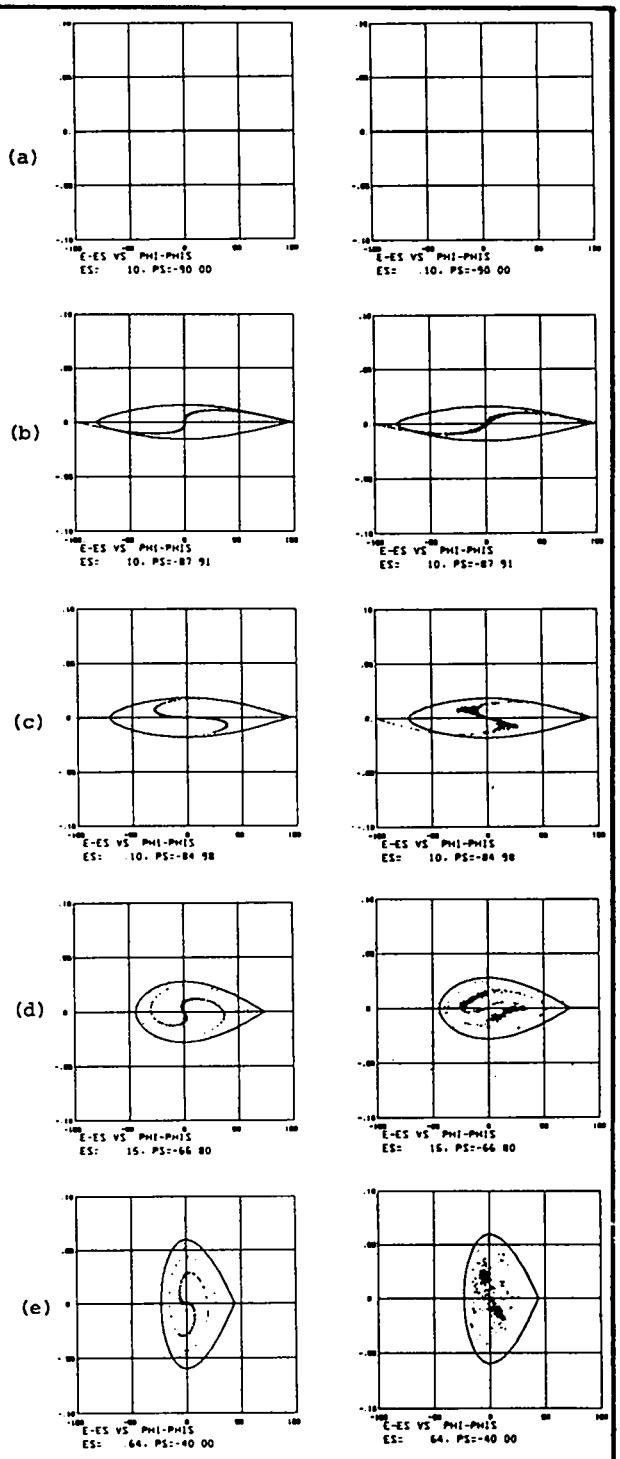

Fig. 8. Longitudinal phase space at center of cell for 425-MHz test design: (a) cell 1 (beginning), (b) cell 32 (near first phase focus), (c) cell 42 (after first phase focus), (d) cell 100 (start of Gentle Buncher), (e) cell 165 (end).

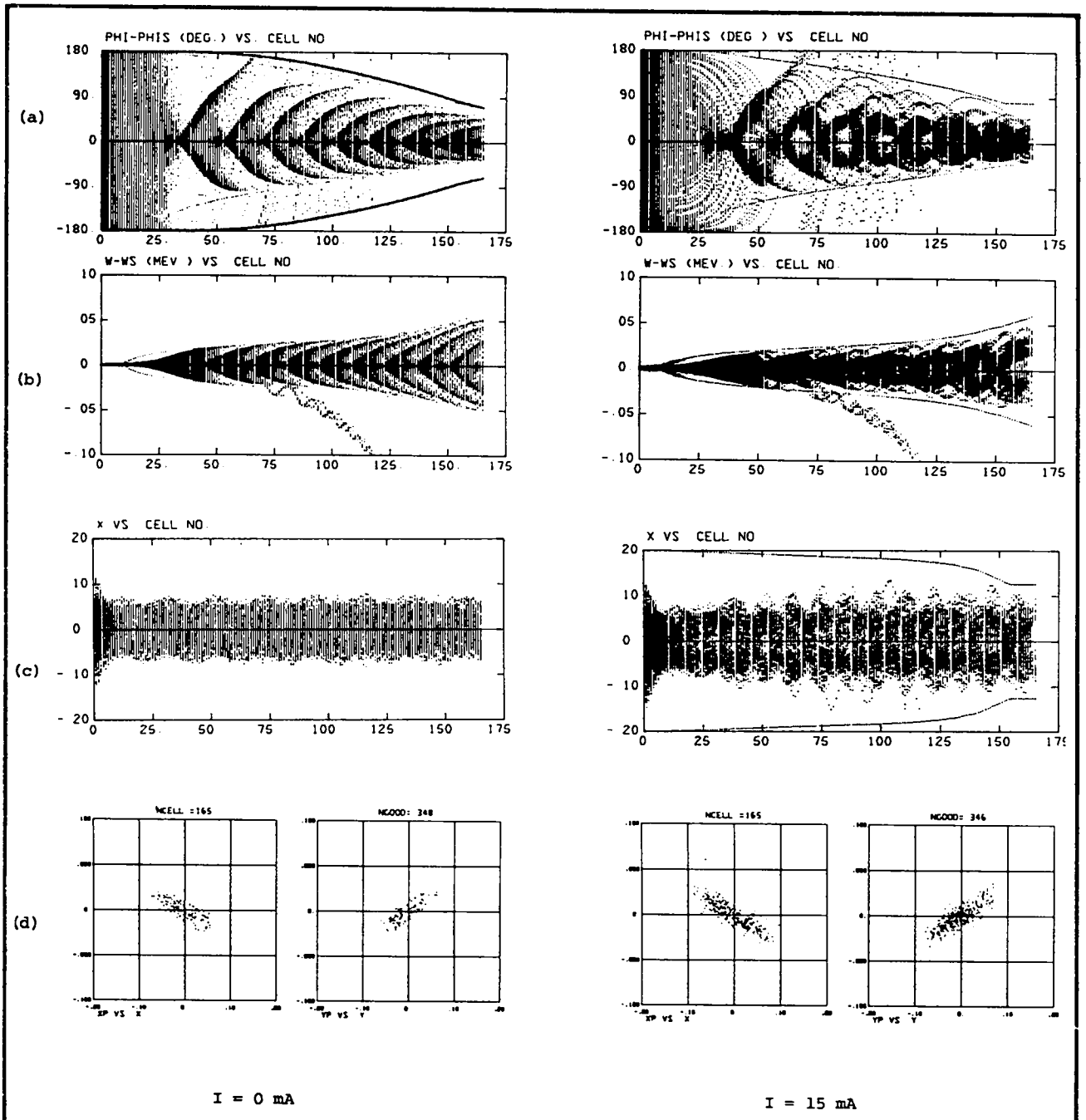

Figure 7

Results from the 425-MHz Test Design:

(a) phase profile,
(b) energy profile,
(c) x profile,
(d) final radial phase space.

If we compare the results in Table III with those presented in Table II, we see that the simple linear-ramp approach gives good transmission efficiency when space charge can be neglected. But, as expected, the 425-MHz Test Design is clearly superior in terms of transmission efficency at the nonzero beam currents shown. The radial emittance-growth numbers are significantly perturbed by particle loss at the larger beam currents in both designs.

Acknowledgments

We thank E. A. Knapp, R. A. Jameson, and D. A. Swenson for advice and encouragement. We acknowledge valuable discussions with R. L. Gluckstern, LASL consultant, concerning the Shaper design, and we thank G. W. Rodenz for assistance with the computer calculations.

Appendix

Image Charge Effects

We have tried to estimate the magnitude of the effects on the beam caused by the image charges induced on the vanes by the beam itself. The simplifying assumptions made in this analysis overestimate the image-charge effects.

In the high-energy end of the linac, where the beam is bunched and the vanes have a relatively large modulation, it appears that the image charges actually produce an alternating focusing and defocusing effect for both the longitudinal and radial motions. As present we have no quantitative estimate of the image forces at the high-energy end but we have calculated the effects at the low-energy end, where the main effect is radially defocusing.

The image charges produced by a continuous beam with a circular cross section, centered on axis, will cause multipole fields of order 4, 8, . . ., proportional to the beam current. For a beam with radius r_b, the ratio of the magnitudes of the image force to the space-charge force at the edge of the beam was calculated to be:

$$\frac{\text{image force}}{\text{space-charge force}} = 0.422\left(\frac{r_b}{r_o}\right)^4 + 0.118\left(\frac{r_b}{r_o}\right)^8 + \ldots, \quad \text{(A-1)}$$

where r_o is the bore radius. If $r_b = 0.5\ r_o$, then this ratio is less than 3%.

A displacement of the beam center from the axis produces image charges that cause other multipole components, the main ones being the n = 1, 3, and 5 terms. The magnitudes of the n = 4, 8, . . . multipoles are relatively unchanged by small displacements of the beam. The strength of the dipole field is approximately 0.78 E r_c/r_o, where r_c is the displacement of the beam center from the axis, and E is the space-charge field produced by the beam at a distance r_o from its center. The magnitudes of the n = 3 and n = 5 multipole fields are each approximately half of the magnitude of the dipole field.

Based on these results, we make the following conclusion: As long as the beam is well centered (say $r_c < 0.2\ r_o$) and the beam does not fill a large fraction of the aperture (say $r_b < 0.6\ r_o$), then the image forces are at least an order of magnitude lower than the space-charge forces and can be neglected without seriously affecting the results. If these conditions are violated, then the image forces might become comparable to the space-charge forces and could cause an increase in the beam loss and in the emittance growth.

Outline of PARMTEQ

The computer program that we use to study the beam dynamics of the RFQ linac is called PARMTEQ, (Phase and Radial Motion in Transverse Electric Quadrupoles). It is a modified version of PARMILA, and performs four basic functions. It generates an RFQ linac, generates a variety of input particle distributions, performs beam dynamics calculations, and generates a variety of outputs.

The information required for generating an RFQ linac consists of the following: the vane voltage; the linac frequency; the mass of the particles; the initial and final energies; and a table of values specifying the radial focusing strength B, the vane modulation parameter m, and the synchronous phase, all at specified distances along the structure. The linac is generated cell by cell, in an iterative procedure.

The beam-dynamics calculations are performed as follows: Each cell is divided into a number of segments (typically four, with a maximum of eight). Initial values of the dynamical quantities x, x', y, y', ϕ, and W are transformed to final values through each segment. The phase and energy coordinates are the first to be transformed. In the radial transformations, the quadrupole and the rf-defocusing terms are treated separately. The quadrupole transformation is that of a standard quadrupole having a length equal to the segment length, and a strength that depends on the rf phase as the particle passes through the segment. Consequently, each particle will experience a different quadrupole force depending on its own phase. The rf defocusing term is treated as an impulse or thin lens, whose strength depends on the rf phase as well as on the location of the particle in the cell.

At the middle of each cell, the particles are given an impulse to simulate the space-charge forces. This is the most difficult transformation to make satisfactorily. In order to calculate properly the space-charge forces, one needs to know the positions of all the particles at a given instant in time. Instead,

one knows the particle coordinates as they arrive at a particular location along the linac. There is a big difference between these two situations when there is a large phase spread in the beam, as there is in the low energy portion of the RFQ. Consequently, before calculating the space-charge forces it is important to estimate the particle positions at a given instant in time, which we have chosen to be the time when the rf field is zero. At this particular time, the cross section of the beam should be very nearly circular. A series of transformation matrices is generated, considering only the quadrupole term, that transforms the radial coordinates from their values at all other phases within $\pm 180^{\circ}$ in 5° increments. For each particle we find the transformation matrix that most nearly agrees with the phase of the particle, and we apply the inverse of the transformation. This gives us the estimate of the particle's radial coordinate at the desired phase. The longitudinal position is estimated from the particle's velocity and phase. After doing this for all of the particles, the space-charge forces are calculated and the impulses are applied by changing x', y', and W for each particle. The radial coordinates are then similarly transformed back to their modified values at their original phases, and this completes the space-charge transformation for one cell.

After the space-charge transformation, the coordinates are transformed through the remainder of the segments in the cell. A variety of output subroutines can be called at the end of any cell, or at the middle of any cell, either before or after the space-charge impulse is applied.

Some RFQ Scaling Methods

Some RFQ applications may require a method of scaling an existing design to some new frequency. At fixed β a change in frequency will cause a change in the operating point on the radial stability chart, which changes the transverse beam dynamics. An exactly equivalent structure may not be obtainable when the frequency is changed. We find that a useful guide for generating solutions at new frequencies is to impose a direct geometric scaling of dimensions in proportion to wavelength. Thus at each cell we have the radius parameter a proportional to λ, and m is unchanged. The frequency dependence of a and E_s tends to make B, Δ, and V decrease as frequency increases and makes E_o increase somewhat with increasing frequency.

For high-current applications of the RFQ it is useful to have some means of evaluating the expected importance of space charge effects. We find it useful to compute the ratio μ of the space charge force to the average or smoothed restoring force. We assume a model where the beam bunch is represented by a uniform distribution of charge within a three dimensional ellipsoid. For longitudinal motion we obtain:

$$\mu_\ell = \frac{90\, I(\text{amps})\lambda^3\beta^2 f(b/r_b)}{\pi^2 V(\text{volts}) b r_b^{\,2} A |\sin \phi_s|} \qquad \text{(A-2)}$$

where $r_b^{\,2} = r_x r_y$ and b is the half length of the bunch. The function $f(b/r_b)$ has the approximate value $f(b/r_b) = r_b/3b$ in the range $0.8 < b/r_b < 5$.

For radial motion we use

$$\mu_r = \frac{45 q I(\text{amps})\lambda[1 - f(b/r_b)]}{Mc^2(\text{eV})\beta^2 r_b^{\,2} b k_r^{\,2}} \qquad \text{(A-3)}$$

$$\text{where } k_r^{\,2} = \frac{1}{8\pi^2\beta^2\lambda^2}\left[B^2 + 8\pi^2\Delta\right] .$$

Generally we try to keep μ_ℓ and μ_r less than about 0.5 in order to control beam losses due to a reduced stable phase space area. Since μ_ℓ and μ_r affect the frequencies of longitudinal and radial motion, the additional condition must be met, that resonance must be avoided.

We can also obtain limiting current expressions, if we assume the limits occur when $\mu_\ell = 1$ and $\mu_r = 1$. We assume that the bunch half-length is related to the synchronous phase by:

$$b = \frac{\beta\lambda|\phi_s|}{2\pi} \qquad \text{(A-4)}$$

The approximate form for $f(b/r_b)$ is assumed and we replace $\sin \phi_s$ by ϕ_s. For the longitudinal limit we obtain:

$$I_\ell = \frac{AV|\phi_s|^3 r_b}{120\lambda} \qquad \text{(A-5)}$$

where r_b is the beam radius. The radial limit is:

$$I_r = \frac{\beta|\phi_s| r_b^{\,2} Mc^2\left[B^2 + 8\pi^2\Delta\right]}{720\pi^3\lambda^2 q[1 - f]} . \qquad \text{(A-6)}$$

The longitudinal limit decreases rapidly as the beam is bunched in phase. The radial limit increases with β, but also decreases while the beam is bunched in phase.

At the front end of the RFQ, where the beam is in transition between a DC and a bunched

beam, these formulas will not apply. The lack of separation of bunches will be expected to reduce the longitudinal space charge repulsion, but the conditions arising at each phase focus can create localized unstable regions, where space charge forces may exceed the focusing forces.

References

1. V. V. Vladimirskii, Prib. Tekh. Eksp. No. 3, 35 (1956).
2. G. M. Anisimov and V. A. Teplyakov, Prib. Tekh. Eksp. No. 1, 21 (1963).
3. V. A. Teplyakov, Prib. Tekh. Eksp. No. 6, 24 (1964).
4. F. Fer, P. Lapostolle, C. Beith, and A. Cabrespine, Proc. Int. Conf. on Linear Accelerators, Dubna (Aug. 1963), ed. A. A. Kolomesky, A. B. Kusnetsov, and A. N. Lebedev.
5. I. M. Kapchinskii and V. A. Teplyakov, Prib. Tekh. Eksp. No. 2, 19 (1970).
6. I. M. Kapchinskii and V. A. Teplyakov, Prib. Tekh. Eksp. No. 4, 17 (1970).
7. R. H. Stokes, K. R. Crandall, J. E. Stovall, and D. A. Swenson, IEEE Trans. on Nucl. Sci. NS-26, 3469 (1979).
8. J. M. Potter, S. W. Williams, F. J. Humphry, and G. W. Rodenz, IEEE Trans. on Nucl. Sci. NS-26, 3745 (1979).
9. K. R. Crandall, "TRACE"; An Interactive Beam-Transport Program," LA-5332, (October 1973).
10. K. Halbach, R. F. Holsinger, W. E. Jule and D. A. Swenson, "Properties of the Cylindrical RF Cavity Evaluation Code SUPERFISH," Proc. of 1976 Proton Linac Conf., Atomic Energy of Canada Ltd. Report No. AECL-5677, 122 (1976).
11. K. R. Crandall, "Computation of Charge Distribution on or Near Equipotential Surfaces," LA-3512, (December 1966).

APPENDIX B

1979 LINEAR ACCELERATOR CONFERENCE

LOW-BETA LINAC STRUCTURES*

D. A. Swenson
Los Alamos Scientific Laboratory
Los Alamos, New Mexico 87545

Summary

The magnetically focused, post-coupled, drift-tube linac is our standard linac structure. It offers efficient acceleration and adequate focusing over a remarkably large range of betas from $\beta = 0.04$ to $\beta = 0.50$. The term "low-beta linac structure" has come to mean those linac structures that outperform our standard Alvarez structure in the region of beta below 0.04, and the term "high-beta linac structure" has come to mean those linac structures that outperform our standard Alvarez structure in the region of beta above 0.50. A companion to this paper will be presented later in the week on the subject of high-beta linac structures.[1]

Low-beta linac structures are the bane of our existence as linac specialists. It is here that we work the hardest to achieve the least in the way of acceleration and focusing. Our structures in this region are characterized by inadequate focusing, limited apertures, and poor transit-time factors. It is here that our beams are the most poorly bunched, have the largest angular divergence, are the most susceptible to space-charge effects, and are thought to be the most vulnerable to "emittance growth" driving terms. Everything that is bad in linacs is worse at the low-beta end. Nevertheless, every linac has one, and if we are to remain active in this profession--if there are to be more conferences in this series--we must continue to develop and improve these structures.

The principal linac structures that we consider for this duty, in addition to the standard Alvarez linac, are: (1) the $2\beta\lambda$ Alvarez linac structure; (2) the π,π Wideroe linac structure; (3) the $\pi,3\pi$ Wideroe linac structure; (4) the Interdigital H-Mode structure; (5) the Parallel-Plate Transmission Line structure; (6) a variety of heavily loaded, low-frequency cavity structures with independent phasing and intercavity focusing; (7) the Alternating Phase Focused (APF) linac structure; and (8) the Radio-Frequency Quadrupole (RFQ) linac structure. The relative geometry of a number of these structures is shown in Fig. 1 from the particle's point of view.

The most serious problem at low beta is to keep the beam small compared to $\beta\lambda$. As always, we need focusing elements to control the size of the beam. The vast majority of our efforts have been expended on magnetically focused structures in spite of the fact that magnetic focusing is particularly ineffective at low beta because of the velocity term in the force equation. Electric focusing, on the other hand, has no such velocity term in the force equation and should be a prime candidate for the focusing role in low-beta linac structures.

I emphasize--"it should be a prime candidate," but it is not. We have, for a variety of practical reasons, chosen not to develop the electrostatically focused linac structure in spite of its potential advantage at low beta. Perhaps in the renewed quest for low-beta linac structures for the heavy-ion fusion program, a fresh look will be taken at the practical problems of electrostatic focusing,[2] and some solutions will be found.

Two types of rf electric focusing are being studied at LASL. One is the APF linac structure[3] that we have developed for the low-beta chore in PIGMI (Pion Generator for Medical Irradiations)[4] under the support of the National Cancer Institute, and the other is the RFQ linac structure[5] that we are developing for the low-beta chore in the Fusion Materials Irradiation Test (FMIT) facility[6] under the support of the Department of Energy. We have an operating model of the APF structure, and are well on our way to having a working model of the RFQ structure.

APF Linac Structure

The APF linac structure[7] is being developed for the acceleration and focusing role in the low-beta portion of PIGMI. In this structure, the transverse, as well as the longitudinal, focusing forces are produced by the rf

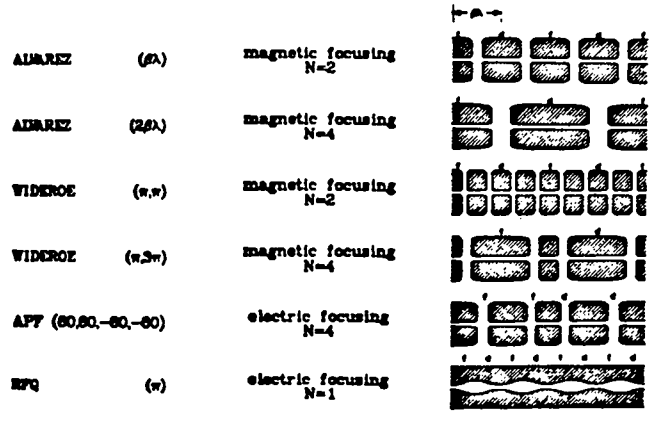

Fig. 1. Low-beta linac structures from the particles point of view.

*Work performed under the auspices of the U. S. Department of Energy and the National Cancer Institute.

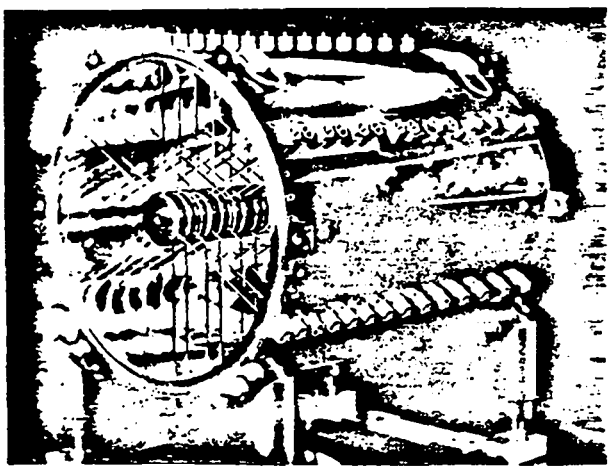

Fig. 2. The PIGMI prototype.

electric fields. By arranging the drift-tube lengths, and hence gap positions, in an appropriate way, in a more or less conventional standing-wave drift-tube linac, the particles can be made to experience acceleration and a succession of focusing and defocusing forces that result in satisfactory containment of the beam in the six-dimensional phase space without dependence on additional focusing fields.

The APF portion of the PIGMI prototype[8] is shown Fig. 2. It is 63 cm long, 46 cm in diameter, and contains 28 drift tubes, none of which contain quadrupole lenses. The drift-tube bodies vary in length from a minimum of 0.690 cm to a maximum of 3.003 cm, and are 8 cm in diameter. The bore-hole radius increases from 0.402 cm in the first drift tube to 0.487 cm in the 28th drift tube. It is designed to operate at 450 MHz and to accelerate a proton beam from 250 keV to 1.011 MeV.

Preliminary tests of the performance of the APF linac structure were made in the following way. The APF section, which has no provisions for rf excitation, was bolted to another short linac section that does have such provisions. A special drift tube, containing an energy-discrimination foil (600 keV) followed by a Faraday cup, was installed between the structures to adjust the resonant frequency of the combination and to provide a minimal beam-diagnostics capability. The combined structure requires a total rf power of about 700 kW to reach the design excitation.

The combined structure was driven to a peak power of about 850 kW, corresponding to an average axial electric field approximately 10 per cent higher than the design value of 6 MV/m. The maximum surface fields were in the vicinity of 28 MV/m.

The 250-keV proton beam from the PIGMI injector[9] was used for the preliminary beam tests. The net current signals from a Faraday cup at the entrance to the linac, the energy-discrimination foil in the special drift tube,

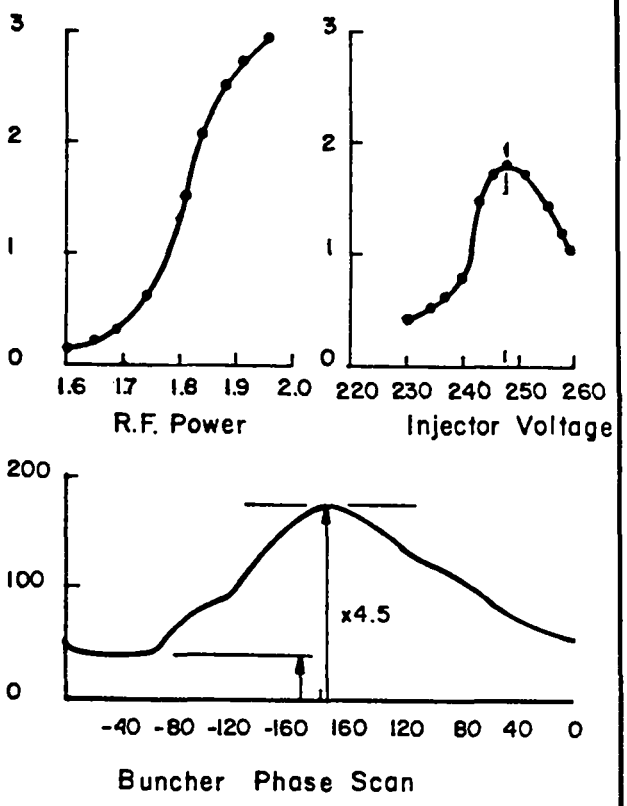

Fig. 3. The APF performance data.

and the Faraday cup in the special drift tube were monitored as a function of rf power, injector voltage, solenoid current, steering current, buncher excitation, buncher phase, and ion source parameters. Some of these data are presented in Fig. 3.

Protons entering the special drift tube with an energy less than 600 keV are absorbed in the foil and contribute to the signal from that element. Protons entering the special drift tube with an energy greater than 600 keV pass through the absorber and contribute to the signal from the Faraday cup within the drift tube. Stray electrons from the foil and Faraday cup are returned to their original element by a 1-kG magnetic field produced by a pair of permanent magnets. The signal from the Faraday cup is taken as a measure of the accelerated beam current.

The dependence of accelerated current, I_b, on rf power is shown in Fig. 3. The threshold for acceleration (1.75 in the arbitrary units given here) corresponds to an rf power of 750 kW, and the peak acceptance corresponds to an rf power of 850 kW. These data are in fair agreement with our expectations.

At the optimum excitation, the percentage capture of a well-collimated beam is 15.7% or $\pm$28 degrees of phase. This is in good agreement with the expected performance.

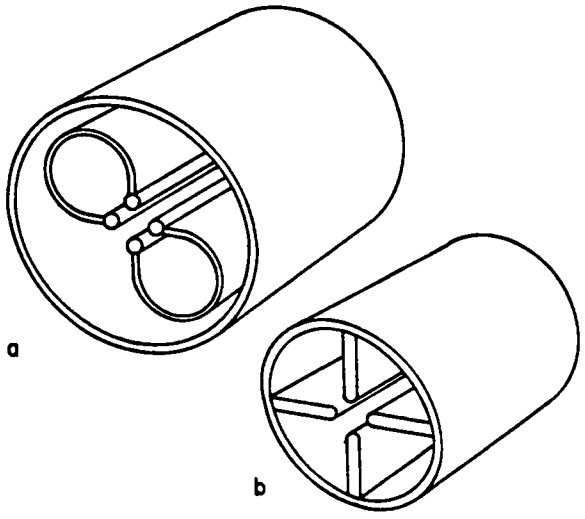

Fig. 4. Two basic configurations of the RFQ.

The dependence of accelerated beam on injector voltage is shown in Fig. 3, revealing a rather sharp peak at 248 kV. The width of the peak is in good agreement with the design calculations. The apparent deviation of the peak position from the design value of 250 kV may be real or may be due to an error in the calibration of the voltage measurement.

The dependence of accelerated beam on buncher phase is shown in Fig. 3 for the buncher excitation that produces the maximum accelerated beam at the optimum phase. The general features of this phase scan look correct, but the detailed shape has not been analyzed.

The maximum current accelerated to date is 3 mA. There are a number of hardware problems and it is hoped that this limit can be raised in the near future.

RFQ Linac Structure

A variety of schemes for producing a quadrupole focusing component in the rf accelerating fields of linac structures have been described in the literature of the last decade. Some of the most recent and promising work is that of I. M. Kapchinskii and V. A. Teplyakov[10] and of N. V. Lazarev[11] based on a four-wire configuration excited so as to produce an electric quadrupole field in the plane perpendicular to the wires.

In the case of uniform wires with no longitudinal variations, the electric fields are strictly transverse, and have no accelerating component. As such, the structure is primarily a focusing structure and not an accelerating structure. Kapchinskii and Teplyakov have introduced an accelerating component by modulating the wire geometry in a periodic way. In this form it represents a very exciting

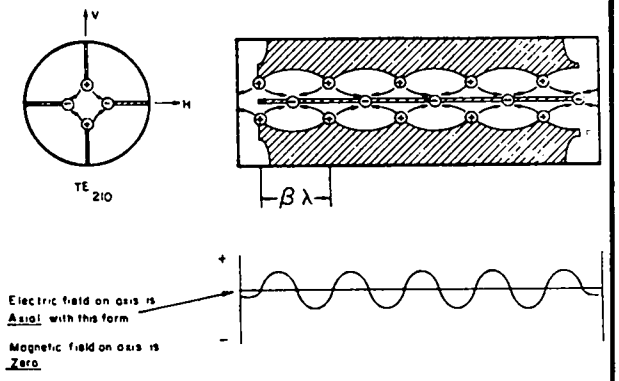

Fig. 5. Four-vane linac structure.

accelerating and focusing structure for low-velocity protons, deuterons, and heavy ions.

There are a variety of ways to connect the four wires into an rf circuit. The Russians have chosen to use the "split-cylinder" geometry shown in Fig. 4a. Our interest is based primarily on the "four-vane" geometry shown in Fig. 4b. Our preference for the four-vane configurations is based on its four-pole symmetry, and its apparent mechanical simplicity. Nevertheless, in our preliminary investigations, we studied both configurations.

Figure 5 shows the four-vane configuration with a "ball and scallop" modulation on the vane geometry. The structure is excited so that the top and bottom vane tips are of one polarity while the side vane tips are of the other polarity. The quadrupole electric field is readily apparent in the end view. These same vectors, when viewed from the side, have a longitudinal component that is due to the interlaced nature of the horizontal and vertical vane modulations. From the symmetry, it can be established that the electric fields on the axis are strictly axial, and that there are no transverse electric fields or magnetic fields on the axis. The axial electric field alternates in direction as shown in the figure.

The structure shown in Fig. 5 should be capable of both accelerating and focusing a beam of charged particles. Because the focusing forces are electric, the focal properties are velocity-independent, and the structure should be superb for low-beta applications.

In actual practice, the vanes would not be built with the "ball and scallop" geometry, but rather with a smooth scalloped geometry as shown in Fig. 6, where the modulation factor "m" is seen to be the ratio of the maximum radial dimension to the minimum radial dimension over the scallop. The longitudinally components of the electric field are zero at the two points of symmetry in the scalloped geometry, and nonzero elsewhere. The transverse components of the elctric field are spatially uniform, and independent of the longitudinal position within the scalloped geometry.

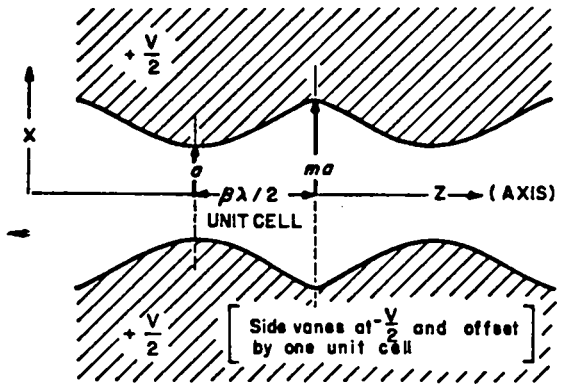

Fig. 6. The RFQ pole-tip geometry.

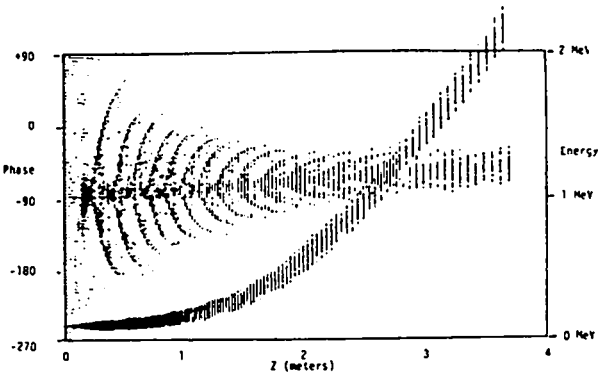

Fig. 8. Phase and energy profiles through the structure.

The structure is simple, consisting of a vane-loaded cylinder excited with rf power. In fact, the structure is so simple that, for the first time, one might consider configuring the linac for adiabatic capture of a continuous beam at low energy. This could be done by introducing the scallops gradually so that the structure acts primarily as a buncher at the beginning, transforming gradually to an accelerator at the end. A computer-generated picture of such a vane tip is shown in Fig. 7.

Simulation of the longitudinal beam dynamics without space charge in such structures demonstrates that capture efficiencies approaching 100% are feasible in reasonable lengths.[12] Figure 8 shows the phase and energy profiles of a beam in one such structure that bunches a 100-keV deuteron beam and accelerates 100% of it to 2 MeV in a total length of about 3.6 meters. Figure 9 shows the longitudinal phase space at 12 points throughout the structure. Subsequent calculations including the transverse motion and space-charge effects suggest capture efficiencies in excess of 90% and emittance growths of less than 50% for a 100-mA deuteron beam injected at 100 keV.[13]

The rf cavity mode employed in these structures is a TE_{210}-like mode.[14] This mode is a "cutoff" mode, and cannot be excited in a finite-length closed cylinder. With special terminations, however, it is possible to excite the mode in all but the immediate vicinity of the end walls. The vanes must not touch the end wall of the termination, as this would short out the wanted mode. The vanes may be cut away near the cylinder wall to provide a crossover for the magnetic flux, and extended toward the terminating plane near the axis to provide additional capacitive loading between the vanes and to the terminating plane. These features tend to support the wanted TE_{21} modes and destroy the unwanted TE_{11} modes.

A coaxial manifold has been developed that provides a symmetrical, multislot driving arrangement for the RFQ cavity.[15] A coaxial cavity surrounding the RFQ cavity is excited in a coaxial TEM mode. The magnetic fields in the TEM mode are orthogonal to the magnetic fields in the RFQ mode. These fields can be coupled by diagonal slots, where the slot angle is

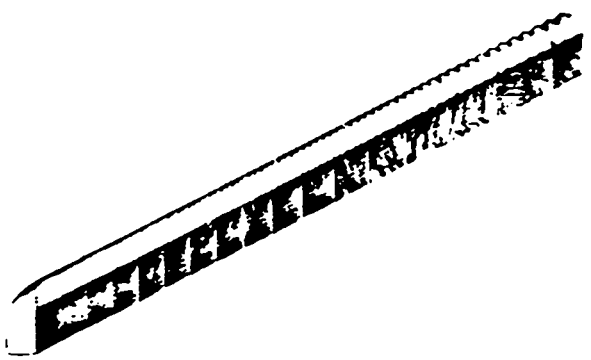

Fig. 7. An RFQ vane tip.

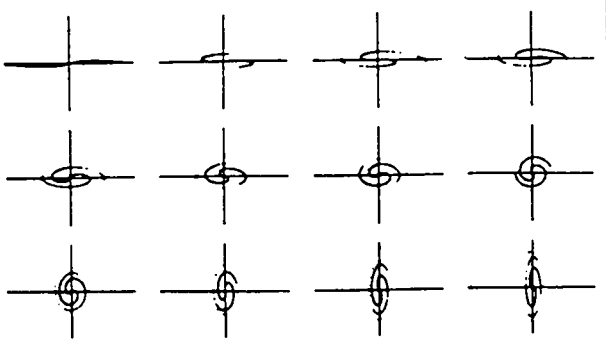

Fig. 9. Longitudinal phase space at every 10th scallop.

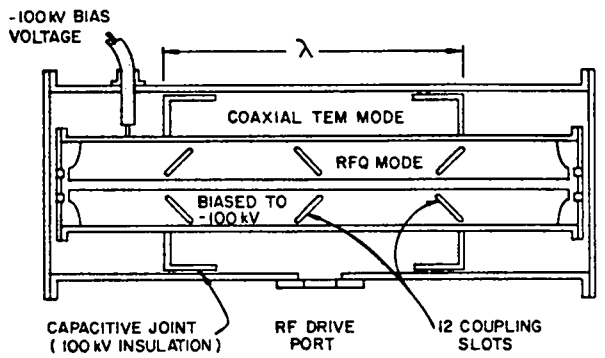

Fig. 10. Biased, manifold-driven RFQ linac structure.

determined by the magnitude and direction of the magnetic fields in the vicinity of the slot.

The first operational model of the RFQ linac structure to be tested at LASL is shown in Fig. 10. Fabrication is well underway. The structure will accelerate 100-keV protons to an energy of 640 keV in a length of 1.2 meters. It will be manifold driven through a total of 12 symmetrically located coupling slots. For the first test, the structure will be electrically grounded, rather than biased as shown in the figure. For subsequent tests, the structure can be biased to -100 kV, making it possible for the ion source and its control and instrumentation to be at ground potential.

Comparison of Linac Focusing Properties

It is natural to extend the magnetically focused linac structures downward in energy (and beta) to the limits of the technology. In so doing, it is necessary to pack as much magnetic focusing in the limited confines of the drift tubes as possible. We have pushed the standard 200-MHz Alvarez linac to a beta of 0.04 by this technique. To go lower in beta with these structures, it is necessary to increase the space available for focusing, or increase the field intensities that can be packed into the available space.

One way to get more room for focusing is to lower the frequency, making everything larger. At the lower frequencies, the larger size of the Alvarez structure is a distinct disadvantage, and the smaller size of the Wideroe structure is a distinct advantage.

Another way to get more room for focusing is to eliminate some of the accelerating gaps in exchange for longer, larger drift tubes. In the Alvarez structure we refer to this as the $2\beta\lambda$ configuration, and in the Wideroe structure we refer to this as the $\pi,3\pi$ configuration.

Recent developments in permanent magnet technology by K. Halbach[16] of Lawrence Berkeley Laboratory, R. Holsinger[17] of New England Nuclear, and J. Farrell of LASL, and independently by N. V. Lazarev and V. S. Skachkov[18] of the Institute of Theoretical Experimental Physics, Moscow, offer significant increases in the magnetic-field gradients that can be packed into small volumes. Furthermore, these quadrupoles require no power supplies, require no cooling, exhibit no ripple, and offer no control. These "superquads" should find their way into low-beta linac structures.

All of these linac structures employ a periodic alternating-gradient focusing system of either the magnetostatic, electrostatic, or rf electric type. In the static versions, the alternations occur in space, whereas in the rf version, the alternation occurs in time with a spatial uniformity in the instantaneous fields.

In either case, the general differential equation operating on the particle is

$$\ddot{x} + [(g + h\cos(\omega t)x] = 0 \qquad (1)$$

where g accounts for constant linear forces and $h\cos(\omega t)$ accounts for the alternating gradient force. By changing to the independent variable n, where $n = \omega t/2\pi = ft$, the equation can be written as a function of two parameters, namely $A = g/f^2$ and $B = h/f^2$:

$$\frac{d^2x}{dn^2} + [A + B(\cos 2\pi n)]x = 0 \quad . \qquad (2)$$

The quantity n advances by unity during each period of the focusing structure. The x, dx/dn phase space is identical to the $x,\dot{x}/f$ phase space of Smith and Gluckstern.[19]

This is Mathieu's equation,[20] the general properties of which are well known. It is stable for some combinations of A and B, and unstable for others. It is standard practice to map the A-B space, designating the stable and unstable regions, and giving some properties of the stable motion in the stable regions.

Figure 11 represents the stability chart for the first and most useful stability region of this equation. The properties of the stable motion are described in terms of the μ, α, β, and γ quantitites of Courant and Snyder,[21] where μ is the phase advance of the solution per period, and β is related to the size of the beam of a given emittance at a given moment. The quantity β_+ corresponds to the beta for the maximum beam size, and occurs at the moment of maximum focusing. The quantity β_- corresponds to the beta for the minimum beam size, and occurs at the moment of maximum defocusing. At these two moments, $\alpha = 0$ and $\gamma = -1/\beta$. The flutter factor, f, is defined equal to β_+/β_-. Contours of μ, β_+, and f are included on the stability chart.

For A = 0, the equation has a range of stability from B = 0 to B = 17.92, where $B = (dF/dx)/m(f/N)^2$, dF/dx is the electromagnetic force gradient, m is the particle mass, f is the frequency of the rf, and N is the length of focal period divided by $\beta\lambda$. For magnetic focusing, $dF/dx = q\beta c(dBy/dx)$, and for electric focusing $dF/dx = q(dEx/dx)$, where q is the particle charge and βc is the particle

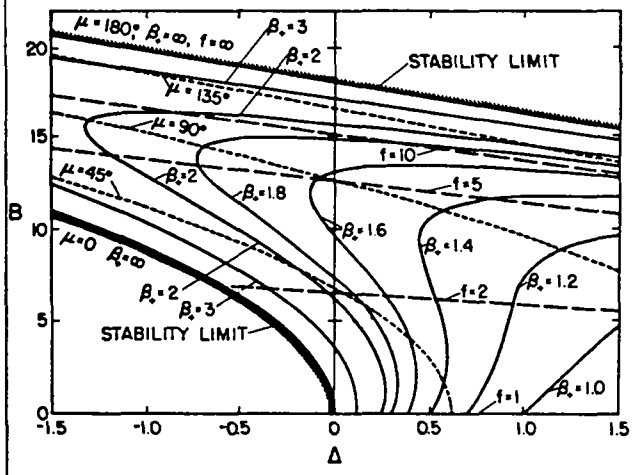

Fig. 11. The RFQ stability chart.

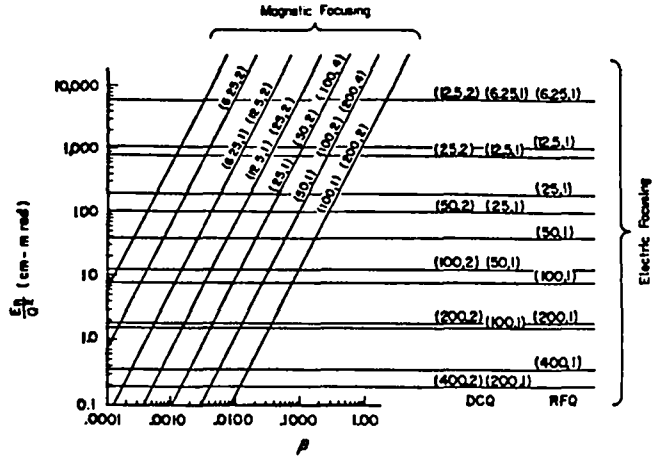

Fig. 12. Admittance of low-beta linac structures.

velocity. The maximum acceptance for A = 0 occurs at B = 11.39 where β_+ has its minimum value of 1.554.

The area in the x, dx/dn phase space that is admitted by a structure with a radial aperture of "a" is $\pi a^2/\beta_+$. Because $n = z/(N\beta\lambda)$, the admittance of the structure in the x,x' phase space is $\pi a^2/(\beta_+ N\beta\lambda)$, and the normalized admittance (area in xx' over π times $\beta\gamma$) is $a^2\gamma f/(\beta_+ Nc)$.

A convenient comparison of the relative focal properties of different linac structures can be made if one imposes a couple of reasonable constraints, namely that (1) the structures be compared at the same operating point in the stability chart (A,B); (2) the bore radius, a, be increased until the pole-tip fields reach some prescribed limit (B_s in the magnetic case, and E_s in the electric case); and (3) the average of the focusing fields over a half period is approximately consistent with the average of the sine wave over a half period. Under these constraints, the normalized admittance of the magnetically focused structure is

$$E_n = \frac{c^3}{\beta_+ B^2}\left(\frac{ecB_s}{m_o c^2}\right)^2 \frac{\beta^2 Q^2}{\gamma}\left(\frac{N}{f}\right)^3 , \qquad (3)$$

and the normalized admittance of the electrically focused structure is

$$E_n = \frac{c^3}{\beta_+ B^2}\left(\frac{eE_s}{m_o c^2}\right)^2 \frac{Q^2}{\gamma}\left(\frac{N}{f}\right)^3 , \qquad (4)$$

where Q is the charge-to-mass ratio of the particle as compared to a proton.

Figure 12 facilitates this comparison for the operating point A = 0 and B = 11.39, where $\beta_+ = 1.554$, and for a pole-tip magnetic field limit of 1 tesla, and a pole-tip electric field limit of 10 MV/m for the static case, and 1.5 times the Kilpatrick limit[22] for the rf case. The numbers in brackets on the lines are the frequency in MHz and the N value of the focusing period. For example, the (200,2) slanted line corresponds to our standard 200 MHz, magnetically focused, drift-tube linac structure in the + - + - configuration.

The lines representing the magnetically focused structures have a slope of 2 on this log-log plot as a result of the β^2 dependence of the admittance. The admittance of the electrically focused structures is independent of β, and hence represented by the horizontal lines. The admittance of the RFQ structure is higher than the admittance of the corresponding electrostatically focused structure (DCQ), because of the higher surface field limits at rf frequencies.

Given the normalized emittance, E_n, of the ion beam, the charge-to-mass ratio, Q, and the N value of the first magnetically focused structure, the following quantities are immediately obvious from Fig. 12: (1) the maximum frequency of the RFQ that will accept the beam, (2) the beta value at which the admittance of this RFQ intercepts the admittance of the magnetically focused structure with the same frequency and given N value. The aperture, a, of the RFQ can readily be determined from the equations given above, from which the minimum suitable beta for the RFQ can be determined ($\beta_{min} \sim 2a/\lambda$).

A Uranium +11 RFQ Example

Let us consider an RFQ/Wideroe marriage for U^{+11}. This choice allows convenient comparison with the first Wideroe tank (π,3π) of the UNILAC,[23] which spans a range of beta from 0.005 to 0.0216 in a length of 5.58 meters.

TABLE I

URANIUM +11 RFQ LINAC STRUCTURE

Frequency	25 MHz
Cavity length	4 m
Number of cells	88
Radial aperture	1.3 - 0.9 cm
Injection voltage	100 kV
Beta initial	0.00315
W/q initial	0.1 MeV
Beta final	0.01580
W/q final	2.5 MeV
Normalized admittance	0.28 cm mrad
Capture efficiency	92%

Tom Wangler of our group did a preliminary design of such a machine. The admittance of a 25-MHz RFQ is approximately equal to the admittance of a 25-MHz (π,3π) Wideroe linac at $\beta = 0.005$ corresponding to the UNILAC injection voltage of 250 kV for U^{+11}. However, this initial beta does not realize the maximum benefits from the RFQ, which for the best bunching action, prefers a lower starting value.

The design presented in Table I is based on an initial beta of 0.00315 corresponding to an injection voltage of 100 kV for U^{+11}. This RFQ intercepts the (π,π) Wideroe linac acceptance at a beta of 0.0158, corresponding to an energy of 2.5 MeV per unit charge.

General Role of RFQ

The general properties of the RFQ and some speculation on its role in the general scheme of things are:

1. It is the strongest focusing device we know for low beta.
2. Consequently, the beam sizes are shockingly small.
3. Furthermore, the aperture for a given normalized emittance is independent of β, and hence constant throughout an accelerating structure.
4. The minimum β would seem to be limited only by the relationship of $\beta\lambda$ to the beam aperture. Perhaps, for some applications, $\beta\lambda$ could be as small as twice the radial aperture.
5. The maximum β is also limited by the relationship of $\beta\lambda$ to the beam aperture. As this ratio gets too large, the acceleration efficiency drops. It appears to be a prime candidate up to the point where the Wideroes can take over.
6. It offers some of the same size advantages that the Wideroe offers in comparison to the Alvarez structure. In the four-vane configuration, it is considerably smaller than an Alvarez structure of the same frequency but somewhat larger than a Wideroe.
7. The rf efficiency is a strong function of frequency and aperture, and in general is comparable or superior to the other low-beta structures.
8. It is mechanically sound and simple, particularly in the four-vane configuration.
9. It is the best buncher we have ever seen, offering capture efficiencies in excess of 90%.
10. It offers the lowest injection voltages of any known structure.
11. It offers higher frequencies than other very-low-beta structures.
12. In the realm of emittance growth, it seems to be no worse than, and perhaps even better than, other known structures.

In addition to this impressive list of properties, the biased version of the RFQ offers (1) a grounded ion source with its associated equipment and control; (2) a grounded rf manifold and drive port; (3) no exposed high voltage; and (4) no beam loading on the high-voltage power supply.

Acknowledgments

We are all indebted to I. M. Kapchinskii of ITEP and V. A. Teplyakov of IHEP and their associates in the USSR for their invention of the RFQ linac structure, and their pioneering work in the design, analysis, fabrication and operation of the first prototypes.

The author credits J. J. Manca of Varian, Pierre Grand of BNL, and R. A. Jameson of LASL for triggering our current interest in the RFQ in this country. The RFQ developments reported here are the work of a strong team pulled together at LASL for this purpose consisting of R. Stokes (theoretical program coordinator), K. Crandall (beam dynamics), T. Wangler, S. Schriber (CRNL), S. Inagaki (KEK), J. Potter (rf structures), F. Humphry, A. Thomas, S. Williams (HEDL), G. Rodenz, and C. Fuller (engineering).

The APF linac structure whose initial operation is reported here was designed, fabricated, and put into operation by J. Stovall (principal responsibility for the PIGMI laboratory), L. Hansborough (chief mechanical engineer), E. Bush, V. Hart, R. Hamm (ion source), R. Sturgess, T. Boyd, P. Tallerico, D. Keffeler, J. Johnson, R. DePaula, S. Klosterbuer (control and diagnostics), and V. Martinez.

References

1. S. O. Schriber, "High-Beta Linac Structures," to be published in the Proceedings of the 1979 Linear Accelerator Conference, Montauk, NY (Sept. 1979).
2. A. W. Maschke, "MEQALAC: A New Approach to Low Beta Acceleration," Particle Accelerators and High Voltage Machines-TID 4500, Brookhaven National Laboratory report BNL-51029 (June 1979).
3. D. A. Swenson and J. E. Stovall, "Low-Energy Linac Structure for PIGMI," IEEE Trans. on Nucl. Sci. NS-24, 1127 (June 1977).

4. E. A. Knapp and D. A. Swenson, "The PIGMI Program at LASL," Proc. of the 1976 Proton Linear Acc. Conf., Chalk River, Ontario, Canada, Sept. 14-17, 1976, Atomic Energy of Canada Limited report AECL-5677 (November 1976).
5. J. M. Potter, S. W. Williams, F. J. Humphry, and G. W. Rodenz, "Radio-Frequency Quadrupole Accelerating Structure Research at Los Alamos," IEEE Trans. on Nucl. Sci. NS-26, 3745 (June 1979).
6. R. A. Jameson, "High-Intensity Deuteron Linear Accelerator (FMIT)," IEEE Trans. Nucl. Sci. NS-26, 2986 (June 1979).
7. D. A. Swenson, "Alternating Phase Focused Linacs," Particle Accelerators 7, 61-67 (1976).
8. L. Hansborough, E. Bush, and V. Hart, "Mechanical Description of PIGMI," IEEE Trans. Nucl. Sci. NS-26, 1464 (February 1979).
9. R. W. Hamm, R. R. Stevens, Jr., D. W. Mueller, J. N. Leavitt, and H. M. Lederer, "A Compact 250-kV Injector System for PIGMI," IEEE Trans. Nuclear Sci. NS-26, 1493 (February 1979).
10. M. Kapchinskii and V. A. Teplyakov, "Linear Ion Accelerator with Spatially Homogeneous Strong Focusing," Nuclear Experimental Techniques, 1970 Consultants Bureau, Plenum Publishing Corporation, report UDC 621.384.64 (1970).
11. I. M. Kapchinskii and N. V. Lazarev, "The Linear Accelerator Structures with Space-Uniform Quadrupole Focusing," IEEE Trans. Nucl. Sci. NS-26, 3462 (June 1979).
12. R. H. Stokes, K. R. Crandall, J. E. Stovall, and D. A. Swenson, "RF Quadrupole Beam Dynamics," IEEE Trans. Nucl. Sci. NS-26, 3469 (June 1979).
13. K. R. Crandall, R. H. Stokes, and T. P. Wangler, "RF Quadrupole Beam Dynamics Design Studies," to be published in the Proceedings of the 1979 Linear Accelerator Conference, Montauk, NY (Sept. 1979).
14. J. M. Potter, S. W. Williams, F. J. Humphry, and G. W. Rodenz, "Radio-Frequency Quadrupole Accelerating Structure Research at Los Alamos," IEEE Trans. Nucl. Sci. NS-26, 3745 (June 1979).
15. J. M. Potter, "An RF Power Manifold for the Radio-Frequency Quadrupole Linear Accelerator," to be published in the Proceedings of the 1979 Linear Accelerator Conference, Montauk, NY (Sept. 1979).
16. K. Halbach, "Strong Rare Earth Cobalt Quadrupoles," IEEE Trans. Nucl. Sci. NS-26, 3882 (June 1979).
17. R. Holsinger, "The Drift Tube and Beam Line Permanent Magnets for the NEN Proton Linac," to be published in the Proceedings of the 1979 Linear Accelerator Conference, Montauk, NY (Sept. 1979).
18. N. V. Lazarev, "Permanent Magnet Quadrupoles without Marked Poles," to be published in the Proceedings of the 1979 Linear Accelerator Conference, Montauk, NY (Sept. 1979).
19. L. Smith and R. L. Gluckstern, "Focusing in Linear Ion Accelerators," Rev. Sci. Inst. 26, 220 (February 1955).
20. L. Jackson Laslett, Focusing of Charged Particles, "Strong Focusing in Circular Particle Accelerators, (Academic Press, New York, 1967), Vol. II, p. 355. 2.
21. E. D. Courant and H. S. Snyder, "Theory of the Alternating-Gradient Synchrotron, Ann. Phys. 3, 1-48 (January 1958).
22. S. W. Williams, G. W. Rodenz, F. J. Humphry, and J. M. Potter, "Voltage Breakdown Testing for the Radio-Frequency Quadrupole Accelerator, to be published in the Proceedings of the 1979 Linac Accelerator Conference, Montauk, NY, (Sept. 1979).
23. Klaus Kaspar, "The Prestripper Accelerator of the UNILAC," Proc. of the 1976 Proton Linear Acc. Conf., Chalk River, Ontario, Canada, Sept. 14-17, 1976, Atomic Energy of Canada Limited report AECL-5677 (November 1976).

IX. SYSTEMS AND APPLICATIONS STUDIES OF INERTIAL FUSION

(T. G. Frank and I. O. Bohachevsky)

Our feasibility and systems studies analyze the technical and economic aspects of various commercial and military applications of inertial fusion. Commercial applications include electric power generation, fissile-fuel production from fusion-fission hybrid reactors, and production of synthetic fuels such as hydrogen. We are also assessing advanced technology development for commercial use of inertial fusion. Our general objectives are the theoretical understanding and preliminary engineering assessment of laser fusion reactors and other energy production subsystems; the computer modeling of integrated plant systems for economic and technology comparison studies; and the identification of critical technology areas requiring long-term development efforts.

INTRODUCTION

In general, past efforts in systems and applications studies were devoted to investigations of the technical and economic feasibility of ICF reactors and total energy conversion systems; therefore, progress has been most significant in this area. Our studies developed models and methods to analyze technical problems in ICF reactor design, arrived at integrated plant layouts, derived scaling laws (that is, sensitivities to parameter changes), and established cost estimates.

Modeling of ICF reactor cavity interpulse clearing processes led to a new operating principle for the wetted-wall reactor cavity that alleviates previous restrictions on the allowable pulse repetition frequency. A preliminary analysis established the concept feasibility of the modified wetted wall.

The LIFE-B plasma simulation code has been completed successfully and is being used to determine magnetically protected reactor cavity configurations to use with magnetohydrodynamic (MHD) ion decelerators. The first-wall material losses in these cavities are being calculated with the previously developed models, and the results indicate that radii as small as 2 to 3 m may be sufficient to ensure satisfactory operation.

To facilitate parametric studies of neutronic effects, we have adopted a method based on the use of the adjoint of the neutron transport operator; this approach greatly reduces the computational effort required for responses to neutron spectra of different ICF fuel pellet designs.

In a study of fissile-fuel production in fusion-fission hybrid reactors, we have examined high and low blanket power-density options in combination with the wetted-wall and magnetically protected wall reactor-vessel concepts and concluded that the preferred combination is a low-power blanket in a magnetically protected vessel.

Finally, we have begun studying ICF reactors driven with heavy-ion beams and have identified the modified wetted-wall reactor cavity as a promising design for this driver option.

REACTOR STUDIES

Modified Wetted-Wall Reactor Cavity Concept (J. H. Pendergrass, I. O. Bohachevsky, T. G. Frank)

The wetted-wall reactor cavity concept in which liquid lithium is forced through a porous wall to form a thin protective film on its interior surface has two potential disadvantages. First, we are not sure we can fabricate and maintain a shell with the necessary porosity or monitor this aspect of its operation successfully. Second, the pellet firing frequency is limited by the time required to remove the lithium vapor produced by a microexplosion through an exhaust nozzle.

Our studies of problems associated with the restoration of interpulse cavity conditions necessary for injection of successive fusion pellets and laser beams revealed the possibility of exploiting two different physical mechanisms for this task. The first, exhaust through a DeLaval nozzle, we had considered before; the second is removal of lithium vapor by condensation on a relatively cool liquid film adherent to the cavity wall. Idealized analyses and comparisons of these two mechanisms are presented below.

The following is a simplified description of the operation of the wetted-wall reactor with exhaust of vaporized lithium through a nozzle. Following a pellet microexplosion, x-ray and pellet-debris energy vaporizes and heats part of the liquid lithium in the protective film to a high temperature. Within a short time, the vapor relaxes into a uniform, quasi-equilibrium ideal gas state. For our analysis of vapor exhaust from the cavity, we assume the lithium film remaining on the cavity wall becomes and remains sufficiently hot that condensation of lithium vapor on the wall can be neglected and that the vapor in the cavity expands adiabatically and reversibly in choked flow through a nozzle with a constant value of the ratio of specific heats.

The time ε_n required for exhaust of lithium vapor from the reactor cavity to a density ρ^* required for efficient transmission of CO_2 laser pulses (estimated to be 10^{15} atom/cm^3) is given by

$$\tau_n = \frac{V}{A}\frac{2}{(\gamma-1)}\left(\frac{\gamma+1}{2}\right)^{1/(\gamma-1)}\left(\frac{\gamma+1}{2\gamma}\right)^{1/2}$$

$$\left(\frac{M}{RT_o}\right)^{1/2}\left[\left(\frac{\rho_o}{\rho^*}\right)^{(\gamma-1)/2}\right]-1$$

$$=\frac{V}{A}F_1(\gamma)\left(\frac{M}{RT_o}\right)^{1/2}\left[\left(\frac{\rho_o}{\rho^*}\right)^{(\gamma-1)/2}-1\right], \qquad \text{(IX-1)}$$

where V is the cavity volume, A is the nozzle throat area, M is the gas molecular weight, T_o and ρ_o are the quasi-equilibrium postexplosion vapor temperature and density, respectively, R is the gas constant, and γ is the ratio of specific heats. The postexplosion vapor temperature and density can be related to the pellet x-ray and debris energy yield, Y_{X+D}, and to the fraction f of this energy that is absorbed in evaporating and heating lithium according to

$$\rho_o = \frac{M}{\Delta H_v V} - fY_{X+D} \qquad \text{(IX-2)}$$

and

$$T_o = T_v + \frac{1-f}{f}\frac{\Delta H_v}{C}, \qquad \text{(IX-3)}$$

respectively, where ΔH_v is the molar heat of vaporization, T_v is the vaporization temperature, and C is the molar heat capacity. Substitution into Eq. (IX-1) gives

$$\tau_n = \frac{V}{A}F_1(\gamma)\left\{\frac{M}{R\left[T_v=\frac{(1-f)}{f}\frac{\Delta H_v}{C}\right]}\right\}^{1/2}$$

$$\left[\left(\frac{MfY_{X+D}}{\Delta H_v V\rho^*}\right)^{(\gamma-1)/2}-1\right]. \qquad \text{(IX-4)}$$

If the cavity is spherical, then V/A is conveniently represented as

$$V/A = (r/3)/(A/S), \qquad \text{(IX-5)}$$

where S is the cavity surface area and r is the cavity radius. The sensitivities of τ_n to variations in Y_{X+D}, f, r, and A/S for a spherical cavity are illustrated in Fig. IX-1.

An alternative to removal of lithium vapor through a DeLaval nozzle is condensation on a relatively cool liquid film adherent to the cavity wall. An idealization of this process, similar to that for exhaust through a nozzle, with nozzle flow replaced by kinetic theory of condensation leads to the following expression for the interpulse clearing time τ_c:

$$\tau_c = \frac{V}{S}\frac{2(2\pi)^{1/2}}{(\gamma-1)}\left(\frac{M}{RT_o}\right)^{1/2}\left[\left(\frac{\rho_o}{\rho^*}\right)^{(\gamma-1)/2}-1\right]$$

$$=\frac{V}{S}F_2(\gamma)\left(\frac{M}{RT_o}\right)^{1/2}\left[\left(\frac{\rho_o}{\rho^*}\right)^{(\gamma-1)/2}-1\right]. \qquad \text{(IX-6)}$$

This result differs from that given by Eq. (IX-1) in that V/A is replaced by V/S and the function $F_1(\gamma)$ by $F_2(\gamma)$. The functions $F_1(\gamma)$ and $F_2(\gamma)$ differ by less than a factor of 2 for γ values of interest. Therefore, the time required to restore the cavity to the conditions necessary for a subsequent pulse transmission using the condensation mechanism τ_c is about A/S times shorter than that required for exhausting through a nozzle τ_n, that is, $\tau_c/\tau_n \approx$ A/S. For practical commercial reactor vessel designs, the ratio A/S will not be larger than a few hundredths; consequently, the exploitation of the condensation mechanism for interpulse cavity clearing will increase the allowable reactor repetition frequency by a factor between 10 and 100 over that achievable with exhaust through a nozzle. In this case, the nozzle is replaced by a simple drain pipe.

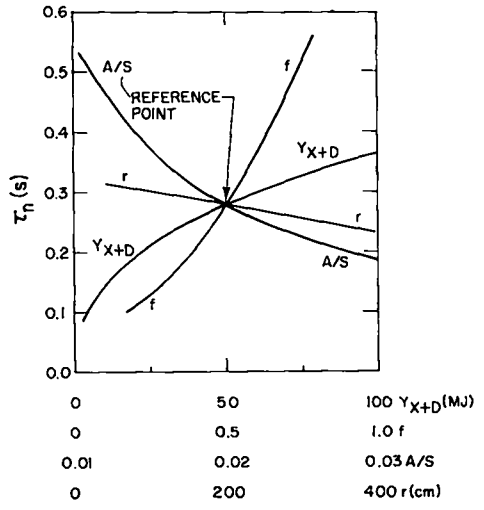

Fig. IX-1.
Parametric dependence of nozzle exhaust time τ_n for Los Alamos wetted-wall reactor concept.

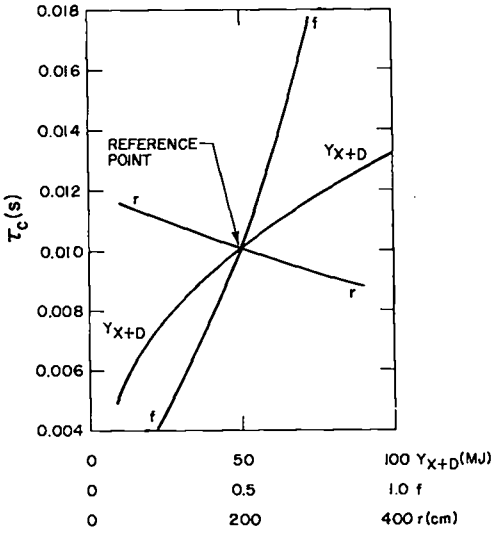

Fig. IX-2.
Parametric dependence of condensation clearing time τ_c for Los Alamos modified wetted-wall reactor concept.

Figure IX-2 presents the results of a sensitivity study of cavity clearing by condensation. Comparisons between these results and those presented in Fig. IX-1 confirm the anticipated reduction in the time required for cavity clearing using condensation instead of exhaust through a nozzle. The assumptions on which these analyses are based are valid only approximately; nevertheless, the conclusions are sufficiently optimistic to warrant examination of a scheme for first-wall protection to ensure that the interpulse lithium vapor removal is dominated by condensation.

In wetted-wall concepts, two requirements must be met to ensure restoration of cavity conditions by condensation of lithium vapor. The first is maintenance of the reactor-cavity-wall and protective-lithium-layer temperature so that the density corresponding to the vapor pressure is sufficiently low to permit transmission of laser pulses without significant degradation ($\lesssim$800 K). The second requirement is a mass flow rate of lithium sufficiently high to transport all the energy deposited in the film by pellet microexplosions. Removal of 500 MJ/s (that is, 10 microexplosions/s with 50 MJ of x-ray and debris energy released by each) deposited in the lithium layer with an arbitrarily prescribed 100-K temperature rise requires an easily achievable flow rate of $\sim$2.4 m^3/s. The required film flow can be produced with circular slit nozzles that inject lithium tangentially to the wall near the uppermost point of the cavity (Fig. IX-3). The nozzles can be located behind a porous cone protected by a thin film of lithium seeping through the pores. An

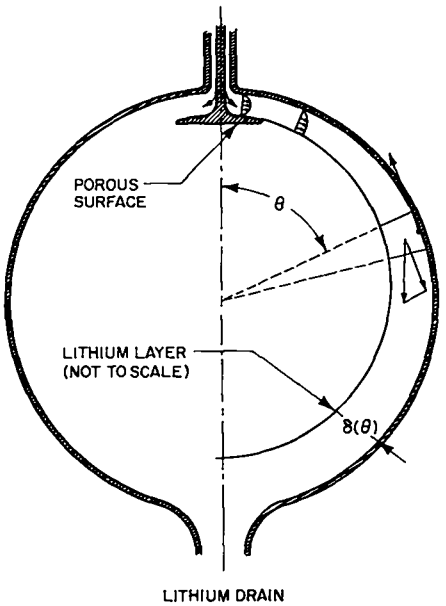

Fig. IX-3.
Model for the Los Alamos modified wetted-wall reactor cavity concept flow calculations.

injection velocity sufficient to provide the necessary film flow and overcome wall friction loss far exceeds the value needed to hold the film against the wall by centrifugal force.

To permit detailed analysis of the film flow, we extended previous analyses to include treatment of variable (Reynolds-number-dependent) friction factors

and different surface roughnesses. In the refined analysis, we assume fully developed turbulence, constant physical properties, steady one-dimensional flow, friction factor/Reynolds-number relationships derived from pipe flow experiments, and neglect of shear stress at the free surface. Typical results of a parameter study of flow velocity and lithium layer thickness as functions of angular distance from the top of a spherical cavity are presented in Figs. IX-4 and IX-5, respectively.

The discussion of the feasibility of reactor cavity clearing by condensation would be incomplete without mention of the problem of providing openings in the cavity wall for injection of the laser beams. We are examining several concepts that could solve this problem, but the details have not been worked out.

A new operating principle has been conceived for the wetted-wall reactor cavity that exploits condensation for interpulse clearing of the cavity. This concept alleviates previous restrictions on allowable pulse repetition frequency and permits consideration of separable cavity and blanket coolant streams. Thus, the cavity might be operated at lower temperature than the blanket, with consequent low cavity vapor pressure and high-temperature use of energy deposited in the blanket coolant. Moreover, different fluids could be used in the reactor cavity and blanket; for example, the cavity might be cooled by a low-vapor-pressure liquid metal eutectic, and the blanket by pressurized helium, eliminating the use of liquid lithium altogether.

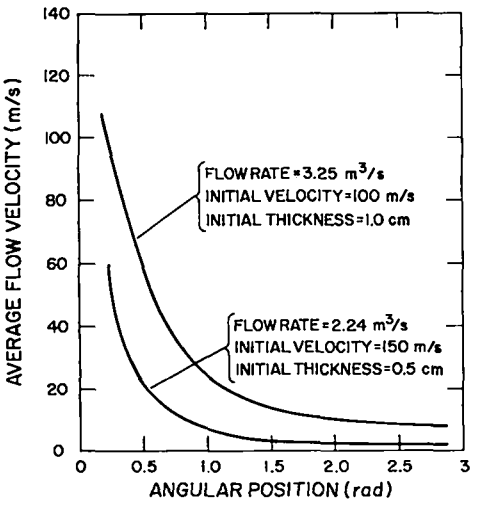

Fig. IX-4.
Representative average flow velocities of lithium layer in the Laboratory's modified wetted-wall reactor concept as functions of injection velocity, flow rate, and angular distance (from top of reactor).

Heavy-Ion Beam Fusion Reactor Conceptual Designs (T. G. Frank, J. Pendergrass)

The use of heavy-ion beams to drive inertial fusion pellets has been studied intensively for the past several years and is now established as a promising alternative to laser-beam-driven fusion for the production of commercial power. Requirements for ion and beam pulse energies, accelerator performance, and reactor operating conditions have been tentatively established so that meaningful systems analyses can be performed.[1] Our initial results are summarized below.

The requirements on heavy-ion beam pulses are compromises among target requirements, accelerator operating conditions, and beam transport and focusing requirements; they include (1) particle energy equivalent to a 5- to 10-GeV uranium atom, (2) beam energy per pulse in the range 1-10 MJ, (3) pulse width of 10 ns, and (4) a focused spot radius of 2.5 mm.

These beam properties lead to a number of restrictions on reactor design and operation. Although several approaches to beam transport and focusing inside the reactor cavity are being studied, the least uncertainty is associated with ballistic propagation of singly ionized atoms. For particle kinetic energies now being considered, an upper limit on reactor cavity density of 10^{12} to 10^{13} atom/cm^3, where two-stream instability is not too serious, is expected to be the dominant consideration.

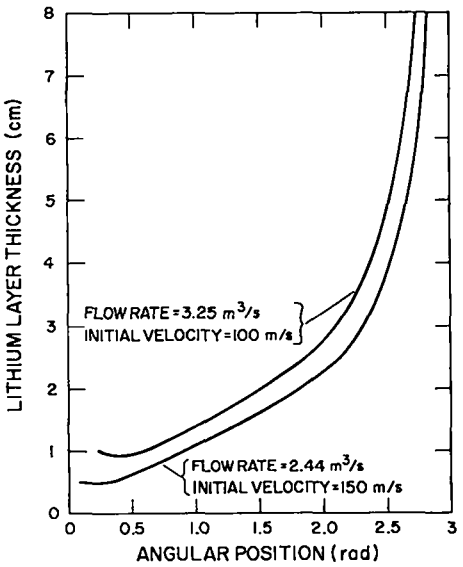

Fig. IX-5.
Representative lithium layer thickness in the Laboratory's modified wetted-wall reactor concept as functions of injection velocity, flow rate, and angular distance (from top of reactor).

For beam bunches of sufficiently high quality, propagation and focusing at densities below 10^{13} atom/cm^3 for distances from the focusing magnets of up to 5 m is straightforward; however, space-charge effects may require that the number of beams be large. Target designs for heavy-ion fusion are not firmly established, but we expect that some degree of energy deposition symmetry will be required, implying symmetric propagation of multiple beams.

The choice of a heavy-ion fusion reactor concept will also be influenced by accelerator operating characteristics. Because there is an economic incentive to operate the reactors at the highest practical pulse-repetition rate, one important characteristic is the potential for high pulse-repetition rate without significant penalty in capital investment.

The discussion above and considerations relating to efficiency of energy conversion lead to the following required and/or desired reactor characteristics for heavy-ion fusion.

- The gas density in the reactor cavity at the time of pellet injection and beam propagation should be less than 10^{13} atom/cm^3.
- The reactor concept should admit a symmetric arrangment of a large number of beams.
- The reactor concept should permit operation at a high pulse-repetition rate.
- The blanket should be capable of high-temperature operation.
- No unreasonable economic penalties should be associated with reactor construction, operation, or maintenance.

The first two items are, or may be, requirements, whereas the last three items are merely desirable and may not be achievable simultaneously.

The essential requirement for any inertial-fusion reactor concept is the provision of some means for protecting the reactor cavity wall from damaging pellet-microexplosion emissions. Heavy-ion pellet microexplosions are expected to have the same general characteristics as laser fusion pellets; thus, the same generic classes of reactor concepts that have been developed for laser fusion may also be applicable to heavy-ion fusion. Reactor concepts, classified according to cavity wall protection scheme, include:

- solid dry-wall cavities protected by sacrificial liners with or without magnetic fields to divert ionized-pellet debris,
- fluid-wall cavities in which exposed surfaces are protected by a layer of lithium, and
- gas-filled cavities in which x-ray and pellet-debris energies are attentuated and/or absorbed before reaching the cavity wall.

Gas-filled cavities may be dismissed immediately from further consideration because the gas densities required for significant attentuation of x-ray and pellet-debris energies in 10-m-diam or smaller cavities exceed those permitted for heavy-ion-beam transmission and focusing. Cavities protected by sacrificial liners appear to be marginal for cavity diameters of 10 m or less because of excessively rapid wall erosion for economically practical pellet yields (that is, higher than 100 MJ). However, high-repetition-rate systems using relatively low pellet yields do warrant additional study. One conceptual design, which has the potential of satisfying all the required and desirable characteristics enumerated above, is the modified wetted-wall concept using condensation for the interpulse cavity clearing described above. However, the lithium temperature corresponding to a vapor pressure with a density of 10^{13} atom/cm^3 is ~620 K, which although possibly acceptable, is an unattractively low maximum cavity operating temperature. A liquid metal with a lower vapor pressure than lithium at the same temperature would be advantageous for this purpose. In addition, an alternative liquid metal should have a low melting point, be relatively inexpensive, should not be excessively corrosive, and should not present excessive chemical or induced radioactivity hazards. A survey of the elements reveals few pure elements with all these desirable characteristics.

A promising liquid metal eutectic for use in heavy-ion beam-driven reactor cavities is lead/bismuth (~56 at/% bismuth) with a melting point of ~400 K (compared to 453 K for pure lithium). The gain in cavity operating temperature corresponding to a vapor pressure density of 10^{13} atom/cm^3 is 250 K. The cost of lead/bismuth is less than that of lithium, and the eutectic presents no extraordinary chemical hazard. Although not expected to be a serious problem, lead/bismuth mixtures may be more corrosive than lithium. To obtain the same heat-carrying capacity as lithium, ~1.37 times the volume of lead/bismuth eutectic must be circulated (28.6 times the mass). However, pumping-power requirements are not expected to be unacceptably large for the proposed application.

More study will be required to determine quantitative tradeoffs for heavy-ion beam-driven systems before optimized reactor concepts can be defined; however, there are several concepts that appear to be applicable.

Modeling of Plasma in Magnetically Protected Reactor Cavity (I. O. Bohachevsky, D. O. Dickman, J. C. Goldstein)

The development of a new plasma model for ICF reactor studies was motivated by our current best estimates of parameter ranges for reactor cavities. The model, the estimates, and some preliminary results have been discussed previously.[2,3] Here, we discuss one aspect of the calculations that is unique to the problem examined and present solutions relevant to ICF reactor design and analysis. Most of these results have been published.[4-6]

Exploratory calculations and supporting analyses of debris ion expansion through a background fluid showed that the relaxation time for the transfer of momentum and energy from the ions to the fluid is much shorter than the characteristic fluid-dynamic time, because in the early stages of expansion the mass ratio of the ions to the entrained fluid is much larger than unity. Therefore, the complete set of the governing difference equations is stiff; the degree of stiffness is illustrated by the fact that while the characteristic interaction time is $\sim 10^{-12}$ s, the typical characteristic fluid-dynamic time is only $\sim 10^{-6}$ s. To resolve the associated computational difficulties, we found an approximate but asymptotically correct characterization of the ion-fluid interaction in each computational cell and incorporated the corresponding expressions for the velocity and internal energy into the code.

Our solutions indicate that the background fluid has little effect on the ion trajectories before the pressure waves reflect from the cavity walls. However, the ions impart such a high velocity to the background fluid that despite large energy deposition, the temperature and density in the region interior to the expanding ions decrease to very low values. Thus, the action of individual ions is analogous to a jet ejector and the effect is quite strong: it reduces the density inside the expanding ion region to a value less than one-thousandth of the initial ambient density (Fig. IX-6). Figure IX-6 illustrates the pressure wave generated by the interaction of pellet products and background fluid, and the low-temperature region that develops inside the expanding ion region because temperature is proportional to pressure.

The distribution of the axial velocity corresponding to a slightly earlier time (Fig. IX-7) indicates that the background fluid acquires nearly uniform axial velocity, well suited to driving MHD generators.[3,7-9] Consequently, we continued investigations of cavity shapes suitable for use with these ion-decelerating devices in place of energy sinks. Such a shape is shown in Fig. IX-8: it is a straight cylinder with sharply converging ends leading into MHD channels; to ensure adequate wall protection, the magnetic field is made to increase along the axis away from the cavity midplane. The shape of the expanding debris and of the magnetic contour lines in

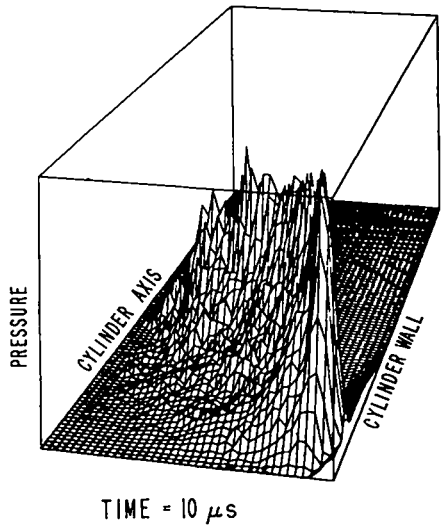

Fig. IX-6.
Pressure wave and low-temperature region inside expanding ion region in magnetically protected wall cavity at 10 μs after pellet microexplosion for 150-mJ pellet thermonuclear yield.

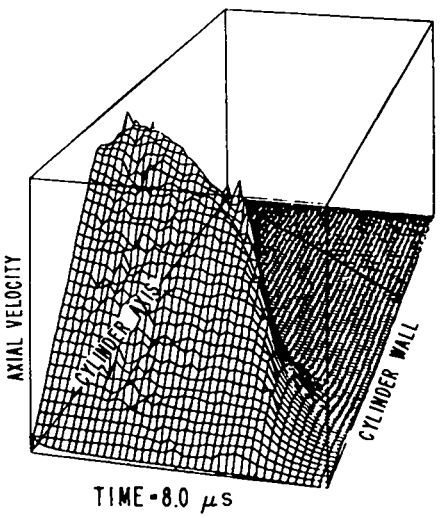

Fig. IX-7.
Axial velocity distribution in the background fluid in magnetically protected wall cavity at 8.0 μs after pellet microexplosion.

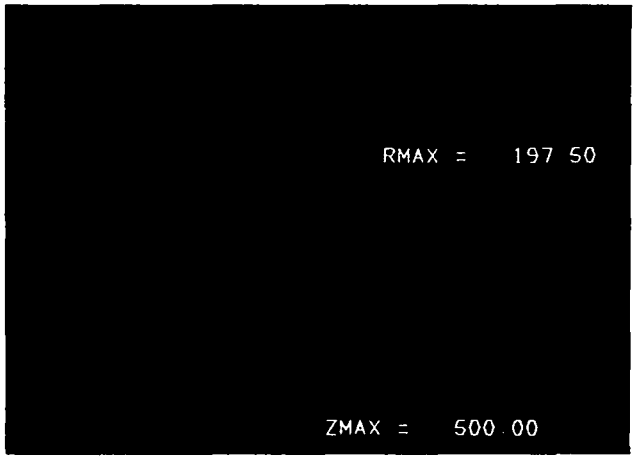

Fig. IX-8.
Debris expansion in magnetically protected wall cavity with MHD channel at 72 μs after pellet microexplosion.

such a cavity is shown in Fig. IX-9(a) and the intensity of the field in Fig. IX-9(b). The formation of the magnetic funnel that protects the solid wall and directs the debris ions into the inlets to MHD channels is significant.

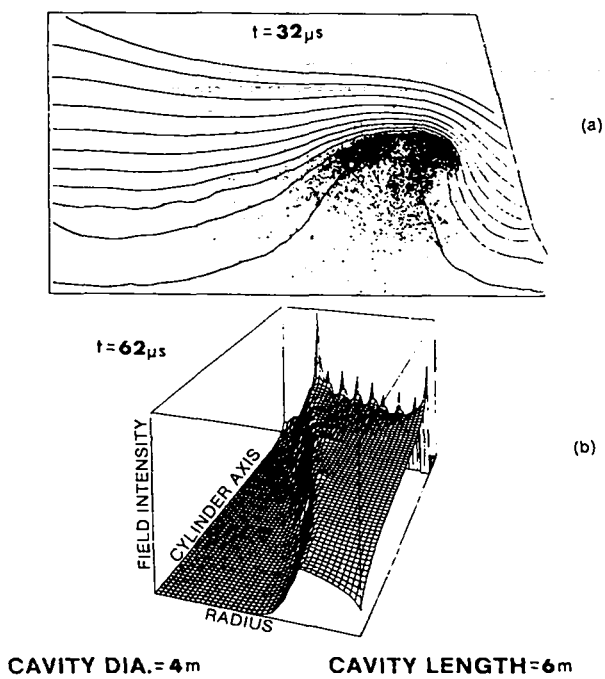

Fig. IX-9.
Expanding debris and magnetic contour lines in magnetically protected wall cavity. (a) Debris expansion in a 6-kG field. (b) Magnetic field intensity.

The Adjoint Method in ICF Reactor Neutronics (W. A. Reupke, I. O. Bohachevsky)

The adjoint of the neutron transport operator has been exploited to facilitate neutronic calculations for ICF reactor studies. Here we outline the approach and illustrate the technique with specific calculations.

We represent the neutron transport equation in symbolic form,

$$L\psi = S \ , \tag{IX-7}$$

where L is the transport operator, ψ is the neutron flux, and S is the source.

In general, we are seldom interested in the detailed behavior of the solution but only in responses to ψ, which can be characterized with a single number, for example, as the tritium breeding ratio or the blanket heat production. These responses are represented as functionals of ψ given by

$$f = (\psi, R) \ , \tag{IX-8}$$

where R is the appropriate response function and the parentheses indicate the inner product, that is, the integral of the product over the appropriate region.

From the theory of differential operators, we know that L has an adjoint L^* so that

$$(L\psi, \psi^*) = (\psi, L^*\psi^*) \tag{IX-9}$$

for any function ψ^*; let ψ^* be the solution of the adjoint equation with the source given by the response function R, that is,

$$L^*\psi^* = R \ . \tag{IX-10}$$

Then, using Eqs. (IX-7) and (IX-10) in Eq. (IX-9), we obtain the equality

$$(S, \psi^*) = (\psi, R) \ ,$$

which, because of Eq. (IX-8), implies that

$$f = (S, \psi^*) \ . \tag{IX-11}$$

Thus the desired response f can be calculated for any given neutron source S from the solution ψ^* of the adjoint Eq. (IX-10).

The advantage of Eq. (IX-11) over Eq. (IX-8) is in the fact that it enables us to determine responses to any number of sources with only one solution ψ^* of the adjoint Eq. (IX-10). Therefore, once the adjoint solution ψ^* has been calculated, the effects of a varying pellet spectrum S can be investigated parametrically with very little effort; the additional computations only require evaluations of definite integrals [Eq. (IX-11)].

We illustrate this advantage with two examples. Figure IX-10 shows the neutron spectrum corresponding to a pellet composed of 1 mg pure, equimolar DT that was compressed uniformly to a radius at which $\rho R = 1$ g/cm^2. The spectrum was calculated with our discrete-ordinates code ONETRAN-DA in S_8P_3 approximation and required a few seconds of CDC 7600 computer time. The calculation used 30 group cross sections processed from the nuclear data file ENDF/B-IV with our processing code system NJOY. The spectrum is normalized to one D-T source neutron and contains three regions: a 14.1-MeV fusion peak, a region of first- and second-collided flux, and a 1/E tail. Because of the presence of (n,2n) reactions, the area under the histogram is slightly larger than unity. Spectra for pellets of $\rho R = 2$ and 4 g/cm^2 were similarly calculated. Each spectrum represents a source term S that is to be folded with the adjoint function ψ^*.

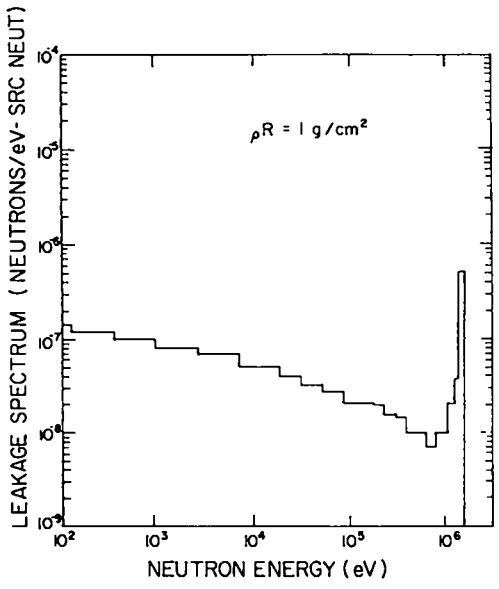

Fig. IX-10.
Pellet-neutron energy leakage spectrum. One mg equimolar DT.

We first illustrate the rapid calculation of the tritium breeding ratio for pellets of varying ρR; in this case, the adjoint source is the response function for tritium production with the cross sections for natural lithium. The energy-dependent cross sections are multiplied by the lithium atom density in a typical commercial reactor blanket. Solutions of the adjoint to the transport equation give the adjoint function for tritium production (Fig. IX-11). The extreme right-hand side of the plot shows the value of the tritium breeding ratio expected for a pure 14.1-MeV source, ~1.35; this value agrees with the direct determination using Eq. (IX-7) with a 14.1-MeV source. However, as indicated above, the adjoint function contains implicitly the tritium breeding ratio for all possible pellets. In particular, the tritium breeding ratio for pellets of $\rho R = 1$, 2, and 4 g/cm^2 was determined by folding the adjoint function (Fig. IX-11) with pellet spectra, such as those shown in Fig. IX-10, in a simple desk calculator operation. The result is presented in Fig. IX-12. For very high values of ρR, the trititum breeding ratio decreases to near unity. Direct calculations of the tritium breeding ratio from Eqs. (IX-7) and (IX-8) would have required several solutions of the transport equation, Eq. (IX-7), to generate the same figure.

The adjoint function also can be used in tailoring pellet spectra to produce a given blanket response or to mitigate an undesirable response. For example, helium production in the first wall of the vessel can be minimized by use of high ρR pellets. Here the energy-dependent helium production in niobium, for example, is multiplied by the niobium atom density to obtain the response

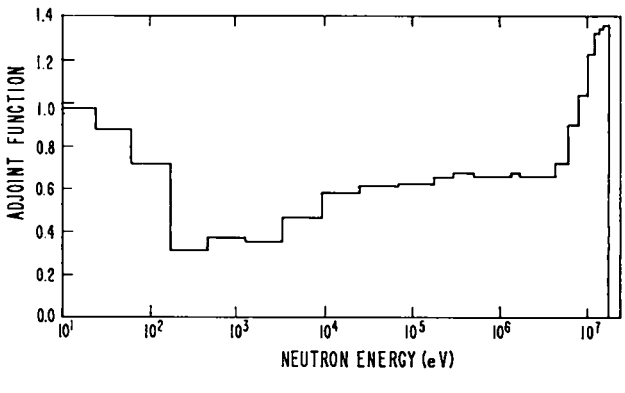

Fig. IX-11.
Adjoint function for tritium breeding ratio in wetted-wall-reactor niobium blanket.

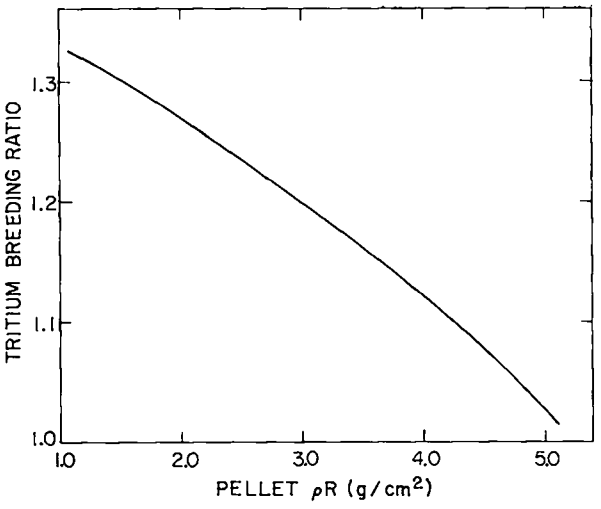

Fig. IX-12.
Tritium breeding ratio vs pellet ρR.

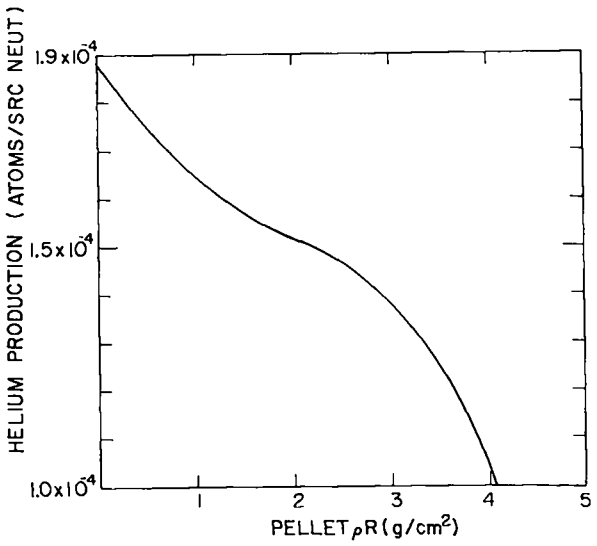

Fig. IX-14.
First-wall helium production vs pellet ρR.

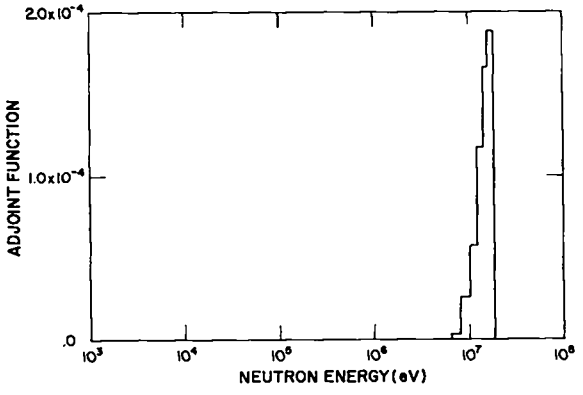

Fig. IX-13.
Adjoint function for first-wall helium production in wetted-wall-reactor niobium blanket.

function, that is, the source for the adjoint equation. The adjoint function (Fig. IX-13) shows a sharp threshold; pellet spectra degraded below this threshold should give sharply reduced helium production. The first-wall helium production as a function of pellet ρR (Fig. IX-14) confirms the behavior predicted by the adjoint function. A fourfold increase in ρR (from 1 to 4) reduces the helium production by not much more than 60.

The examples presented above demonstrate the use of the adjoint function to reduce computational effort in investigations of the pellet-spectra effects on blanket response and to aid in tailoring pellet spectra to achieve a desired blanket response.

HYBRID REACTOR CONCEPTS (W. A. Reupke; H. S. Cullingford, WX-4; T. G. Frank)

Introduction

For some time it has been recognized that fusion energy release from the deuterium-tritium fuel cycle could be multiplied effectively if combined with fission technologies. In this combination, fusion neutrons are used to produce fission and to breed fissile material. Fissionable material in such a hybrid system could be burned in two ways: (1) directly, by fusion neutron irradiation of the fissionable material, that is, uranium or thorium, in a high-power-density concept or (2) indirectly, by converting uranium or thorium into fissile materials, that is, ^{239}Pu or ^{233}U, using a low-power-density concept, and subsequently burning the fissile material in satellite thermal fission reactors. Here we summarize the analysis of two high-power-density and two low-power-density hybrid concepts. The high-power-density concept also converts fertile material (thorium) into ^{233}U and is therefore a blend of both concepts.

Basic Concepts

We restrict our studies of hybrids to concepts that are self-sufficient in electricity and tritium production. Our objectives are maximum thermal-energy and fissile-fuel

production for the high-power-density concepts and maximum fissile product per unit of blanket heat for the low-power-density concepts. Electrically self-sufficient hybrids may operate with relaxed pellet gain requirements compared to those of commercial pure fusion reactors. In our studies, we assume a fusion pellet gain of 100 for all concepts to increase the likelihood that fissile fuel will be produced at an economically attractive rate. In the four reactor concepts studied, liquid lithium was used as a coolant and tritium breeding medium. First-wall production schemes were based on either the wetted-wall concept or the magnetically protected graphite-liner concept. We examined several promising structural materials for various properties and selected three: austenitic stainless steel, ferritic steel, and zirconium. We considered a modular approach to the spherical wetted-wall concept to achieve simplicity, reliability, ease of maintenance, and increased reactor availability. A double-wall design was adopted to achieve tritium containment and fuel isolation in an off-normal condition. In the nonmodular, cylindrical magnetic-wall geometry, a guard vessel encloses the reactor for protection against inadvertent coolant spillage. Two refueling approaches were taken: in the modular concept a hot cell was used for fuel handling, whereas, in the nonmodular concept, refueling was performed with fuel-transfer machines.

Wetted-Wall Concepts

General. The cavity wall in this concept is protected against damage from x rays and pellet debris by a thin film of lithium. The lithium film is replenished either by radial inflow through pores in the cavity wall or by injection tangentially to the wall in the modified wetted-wall design. The porous wall admits microexplosion rates of only ~1/s (1 Hz), whereas the modified wetted-wall design admits rates up to 10 times higher. However, the study of hybrids outlined here was completed before the characteristics of the modified wetted-wall reactor vessel were established; therefore, the conclusions summarized below are valid only for the porous-wall design.

Wetted-Wall High-Power-Density Concept. This concept has been described previously;[7,8] the design consists of a plutonium-enriched ^{238}U-driven region and a driven ThC-^{233}U conversion region. Most of the 3000-MW thermal power developed in this reactor is contributed by the oxide region. Beginning-of-life characteristics of this concept are summarized in Table IX-I.

Wetted-Wall Low-Power-Density Concept. This design consists of a modular blanket containing an inner region of pure lithium for tritium breeding followed by another region of thorium metal for ^{233}U breeding. The concept also has been described previously.[3,9-11] Beginning-of-cycle operating characteristics are shown in Table IX-II. Figure IX-15 shows the reactor cell layout.

Magnetic-Wall Concepts

General. We have pursued in somewhat greater depth studies of high-power-density and low-power-density hybrids using the magnetic-wall protection scheme.

TABLE IX-I

OPERATING CHARACTERISTICS OF HIGH-POWER WETTED-WALL REACTOR

Pulse rate, Hz	1
Pellet yield, MJ	100
Pellet gain	100
Laser efficiency, %	6
Cavity radius, m	2.0
Multiplier region	
Atom (percentage plutonium in heavy metal)	9
Max centerline fuel temp, K	2700
Max thermal stress in clad, 10^{-8} N/m^2	0.69
k-effective with coolant	0.78
k-effective without coolant	0.83
Lithium inlet temp, K	600
Lithium outlet temp, K	800
Conversion region	
Material	ThC
^{233}U conversion ratio	1.18
Annual ^{233}U output, kg	526
Blanket neutron energy multiplication	38
Thermal power output, MW	3040
Electric power output, MW	963
Tritium breeding ratio	1.19
Support ratio[a]	0.4

[a]Defined as the ratio of the total fissile reactor's thermal power to the hybrid thermal power.

TABLE IX-II

OPERATING CHARACTERISTICS OF WETTED-WALL LOW-POWER REACTOR CONCEPT

Pulse rate, Hz	1
Pellet yield, MJ	100
Pellet gain	100
Laser efficiency, %	6
Cavity radius, m	2.0
Conversion material	Th
Maximum fuel centerline temp, K	843
Lithium inlet temp, K	723
Lithium outlet temp, K	843
Coolant velocity, m/s	0.04
^{233}U conversion ratio	0.63
Annual ^{233}U output, kg	280
Blanket neutron energy multiplication	1.5
Thermal power output, MW	140
Tritium breeding ratio	1.1
Support ratio	4.6

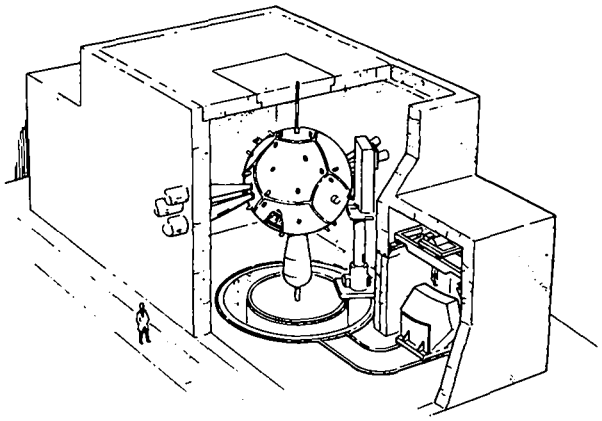

Fig. IX-15.
ICF fissile-fuel factory. Wetted-wall concept.

Here, ionized debris originating in the pellet microexplosion is magnetically funneled to MHD decelerators at the ends of a cylindrical cavity so that only x rays and neutral particles impinge on a sacrificial graphite liner.

High-Power-Density Magnetic Wall. Our design has the following general characteristics.

- The high-power-density blanket is power limited to ~1 Hz even though the magnetically protected reactor cavity allows higher repetition rates.
- ThC is replaced with thorium metal because of the relatively modest power level in the ^{233}U breeding region.
- A graphite reflector is added to the ^{233}U breeding region to trap neutrons more effectively.
- The cylinder end-regions contain only lithium; the ^{233}U breeding coverage, limited to the central cylinder, is only two-thirds of 4π.

The decision not to provide ^{233}U breeding material in the end-regions of the cylinder resulted from a balance of mechanical, thermohydraulic, and neutronics considerations. A somewhat greater equilibrium concentration of plutonium resulted in a more reactive blanket than that for the driven spherical design, as seen from the k-effective values in Table IX-III. Because only two-thirds of 4π is covered, the neutron multiplication and the net power production are about the same for wetted-wall and magnetic-wall high-power-density concepts, in spite of the greater reactivity of the magnetic-wall blanket.

We estimated the ^{233}U build-up rate in the center of the fissile breeding region by assuming a simple constant-flux model. Figure IX-16 (lower curve) shows the build-up rate as a function of time. Detailed system studies, including reprocessing costs at various concentrations of ^{233}U and ^{232}U, are required to determine the optimum end-of-cycle time. However, if it is assumed that a minimum concentration of ~3% is desired, end-of-cycle occurs at about 4 yr. This end-of-cycle time is considerably less than the first-wall changeout time. The pulse repetition rate at end-of-cycle is lowered to retain constant power.

Figures IX-17 and IX-18 show the configuration of the high-power magnetic-wall reactor. At each end of the vessel is the MHD channel to decelerate the hot plasma funneled into the channel by the solenoid-generated magnetic field. Lithium coolant is introduced into a manifold at the top of the reactor, flows through a downcomer, an inlet plenum, and is distributed into the rod bundles. The coolant emerges at the top of the rod bundles and flows into a return manifold. A guard vessel completely surrounds the coolant system to prevent loss of coolant in the event of a leak. The solenoid magnet is insulated by a radiation-resistant material, such as fiber glass or alumina, to allow its location within the concrete

TABLE IX-III

OPERATING CHARACTERISTICS OF MAGNETIC-WALL REACTORS

	High-Power Reactor	Low-Power Reactor
Pulse rate, Hz BOC/EOC	1.2/0.92	10.0/8.9
Pellet yield, MJ	100	100
Pellet gain	100	100
Laser efficiency, %	6	6
Cavity radius, m		
Cylinder	2.0	2.0
End cap	3.0	3.0
Multiplier region		
Atom (percentage plutonium in heavy metal)	10.5	---
Clad temp limit, K	1223	---
k-effective with coolant, BOC/EOC[a]	0.84/0.88	---
k-effective without coolant, BOC/EOC[a]	0.90/0.96	---
Lithium inlet temp, K	723	---
Lithium outlet temp, K	873	---
Lithium flow rate, kg/s	5000 (5050/4950)	---
Conversion region		
Material	Th	Th
Clad temp limit, K	1223	1223
Lithium inlet temp, K	723	723
Lithium outlet temp, K	873	873
Lithium flow rate, kg/s	285 (230/340)	3030
^{233}U conversion ratio BOC/EOC	1.7/2.6	0.74/0.91
Annual ^{233}U output, kg, BOC/EOC	1020/1196	3280/3590
Blanket neutron energy multiplication, BOC/EOC	30/40	1.9/2.1
Thermal power output, MW, BOC/EOC	3000/3000	1720/1720
Net electric power output, MW, BOC/EOC	910/915	366/385
Tritium breeding ratio, BOC/EOC	0.86/1.27	0.99/1.08
Support ratio, BOC/EOC	0.48/0.56	4.4/4.90
Cycle time, yr	4.2	1.7
^{233}U concentration, %	2.8	2.5

[a]Values for an infinitely long cylinder.

shield. The shield reduces the blanket neutron shine-through in the reactor cell to a level comparable to that produced by streaming through laser beam ducts.

Magnetic-Wall Low-Power Concept. The blanket chosen for the magnetic-wall low-power reactor is a variant of the wetted-wall low-power blanket. Unlike the magnetic-wall high-power blanket, which is power-limited to 1 Hz, the magnetic-wall low-power blanket operates at the 10-Hz repetition rate made possible with the magnetic-wall protection scheme. As a result, the lower ^{233}U conversion rate per source neutron for the low-power design is offset by more frequent pulses to produce more of ^{233}U annually than any other system described here. Also, we have configured the cylinder end-regions in a manner similar to the central region to

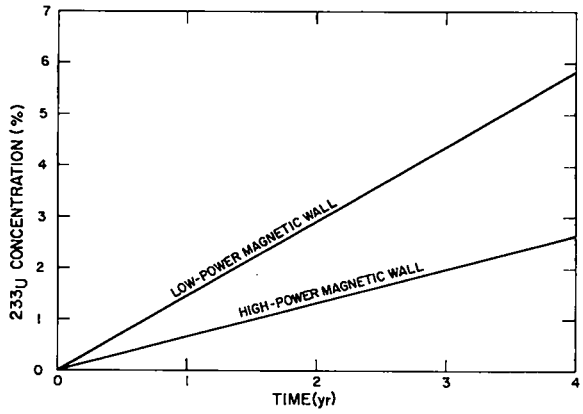

Fig. IX-16.
Uranium-233 build-up in low-power and high-power magnetic-wall reactors.

achieve 4π coverage. At the higher repetition rate, first-wall lifetime for neutron damage is about 2 yr. At that time, the ^{233}U concentration is ~3%. Figure IX-16 (upper curve) shows the ^{233}U build-up as a function of time, and Table IX-III lists the operating characteristics for a 2-yr cycle time.

Discussion and Conclusions

After comparing the four concepts, we can eliminate provisionally the low-power wetted-wall concept on grounds that the rate of fissile-fuel build-up is not economically advantageous. As we have seen, the 10-Hz low-power magnetic-wall concept provides a 2-yr cycle time for ~3% ^{233}U concentration. Therefore, the cycle time for the 1-Hz wetted-wall low-power concept is ~20 yr. The long cycle time could be reduced somewhat while retaining the low-power feature by using a beryllium neutron multiplier (at some penalty in resource economics) and by raising the repetition rate as much as possible, consistent with the restoration of cavity conditions after each microexplosion.

The kinetics of the high-power form of the wetted-wall hybrid will resemble the power-limited, magnetic-wall high-power case, namely 4 yr for ~3% ^{233}U concentration. Although a detailed system analysis is required to establish the point conclusively, it appears probable that even a 4-yr cycle is longer than can be justified economically. Such a reactor might be justified primarily

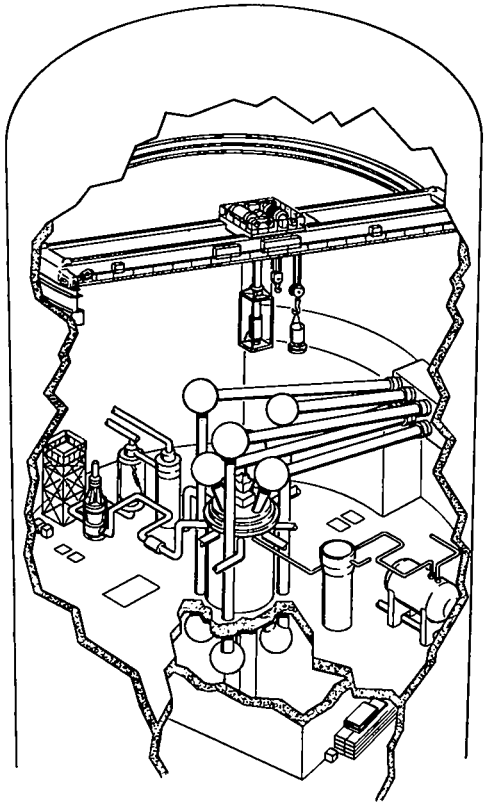

Fig. IX-17.
Plant layout. High-power-density magnetic-wall cavity fusion-fission hybrid.

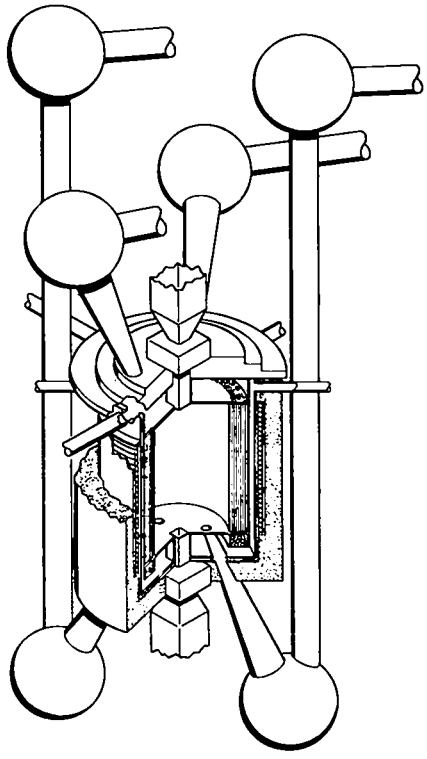

Fig. IX-18.
High-power-density magnetic-wall cavity fusion-fission hybrid.

as an electricity producer and only incidentally as a fuel factory.

Because the repetition rate is limited by power-handling considerations, the high-power form of the hybrid does not exploit the magnetic-wall principle to its greatest advantage. The fuel-cycle times are probably marginal, and the reactor must be justified in terms of electrical output.

We are thus left with the low-power magnetic-wall concept as preferred among the designs studied. Because it is not power-limited, it is the only concept we examined that fully exploits the benefits of high-repetition-rate operation such as, for example, the 2-yr fuel-cycle time. As is evident from the support ratio, which exceeds 4 and approaches 40 for high-conversion-ratio satellites, the magnetic-wall low-power concept excels as a fissile-fuel factory. Electrical output, as expected, is below conventional plant size.

We have identified two concepts, high-power and low-power blankets using magnetic-wall protection, that can serve effectively as power generators or as fissile-fuel factories. The optimum mix of the two requires a detailed cost analysis that is sensitive to assumptions concerning the nature of the system of satellite reactors involved and the exact time frame in which the hybrids are introduced.

TARGET NEUTRON MULTIPLICATION (W. A. Reupke)

Introduction

We are summarizing the results of an investigation into the feasibility of multiplying the neutron output of a laser fusion target by using a fission plate. We wanted to generate as high a neutron fluence as possible over as large an area as possible and thus simulate pulsed radiation effects that are unattainable with a low-yield target. For purposes of the present investigation, we assume a fusion pellet of 100 kJ thermonuclear output, subject to certain geometric constraints on the shape of the fission plate.

Geometry Description

The volume available for the fission plate is the space of a 55° half-angle cone with a vertex some 87 cm downstream of the pellet (Fig. IX-19). A free, spherical volume, ~7.5 cm in radius, is present around the pellet,

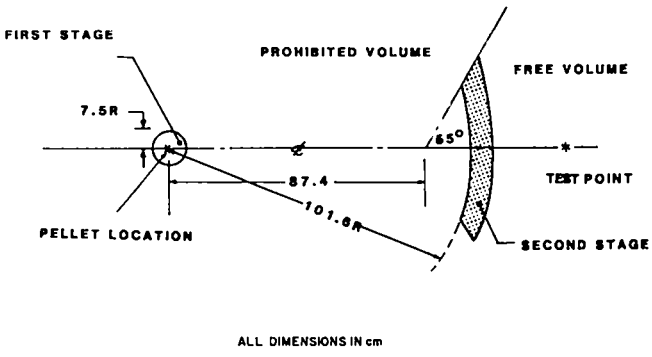

Fig. IX-19.
Two-stage neutron multiplier geometry.

pierced by six focused laser beams and a target support structure.

Calculational Methods

Preliminary calculations were performed with the one-dimensional discrete-ordinates code ONETRAN-DA in a 30 neutron-group/12 gamma-ray-group structure derived from the evaluated nuclear data file ENDF/B-IV. Multidimensional time-dependent calculations were performed with the coupled neutron-photon code MCNP. Multidimensional criticality calculations were performed with the criticality code MCNPK. The continuous-energy cross sections used in the MCNP calculations were also derived from ENDF/B-IV. In all cases, the neutron source consisted of a multigroup source centered at 14.1 MeV.

Procedure and Results

General. One-dimensional calculations were performed in spherical geometry for concentric layers of ^{238}U (inside) and ^{235}U (outside). A configuration consisting of 8 cm ^{238}U and 3.5 cm ^{235}U provided optimal fluence multiplication consistent with a reasonable k-effective value. Two-dimensional calculations were then performed for the conical segment shown in Fig. IX-19, and the ^{235}U thickness was increased to 5.0 cm. Fluence multiplication at a point 50 cm downstream of the plate was 4.1 at a k-effective value of 0.9. To improve the performance of the multiplier, we divided the multiplier into two stages: a spherical fissile shell with an outer radius of 7.5 cm centered about the pellet, and (2) a downstream multiplier plate as described above. The first

stage would be temperature-limited, and the second stage would be k-effective limited.

Two approaches to the first stage were considered: (1) a single shell composed of a fissile material, that is, OyC, Oy, or Pu, driven to ~0.9 of the melt temperature, and (2) a set of nested shells graded outwards from the center according to the melting point, for example, OyC, Oy, and/or Pu. In all calculations, the voids created by the focused beams and target support were omitted.

Single Shell. The critical radii at which samples of the fissile material will melt are shown in Table IX-IV. We determined the maximum thickness of fissile material permissible without exceeding the volume limit and without exceeding 0.9 of the melt temperature. The results, together with the fluence multiplication 50 cm downstream of the multiplier second stage, are shown also in Table IX-IV. The maximum performance, $\phi/\phi_0 = 6.1$, obtained with plutonium is an improvement over the second-stage-only value of 4.1.

Nested Shells. Because OyC has the highest melting point of the three materials, followed by Oy and Pu, it seems reasonable to nest the materials in order of melting point to obtain maximum use of the available volume. After several trials, the two-shell configurations shown in Table IX-V were found. Here each material rises to 0.9 of the melt temperature on its inside surface when driven by a 100-kJ fusion pellet. The fluence multiplication increase is, however, marginal. Further trials gave a more substantial improvement with the three-shell arrangement of Table IX-VI. The multiplication is roughly doubled, but the k-effective value of the system is not appreciably increased.

It must be emphasized that such nested shells, when driven to near melting, may nevertheless later melt by heat conduction between shells unless adequate insulation is present between shells or unless the radiative heat transfer to the surroundings is sufficiently large. Moreover, thermal shock may fracture the shells. In this investigation, heat-transfer and thermal-shock calculations were not performed. Differential energy deposition across inside and outside surfaces of the shells, which must be known for heat-transfer and thermal-shock calculations, has been determined for the three-shell arrangement (Fig. IX-20). The volume perturbations caused by the focused beams and target support will probably lower the performance of the first stage.

TABLE IX-IV

CRITICAL RADIUS, INSIDE RADIUS (IR), OUTSIDE RADIUS (OR), AND FLUENCE MULTIPLICATION FOR ONE-MATERIAL SHELLS

Material	Critical Radius (cm)[a]	IR (cm)	OR (cm)	ϕ/ϕ_0 at 50 cm from Plate[b]
OyC	1.0	1.3	7.5	4.6
Oy	1.4	3.0	7.5	5.4
Pu	2.0	5.0	7.5	6.1

[a]Radius at which a small sample will melt.

[b]Plate consisting of 8.0 cm ^{238}U and 5.0 cm ^{235}U.

TABLE IX-V

INSIDE RADIUS (IR), OUTSIDE RADIUS (OR), AND FLUENCE MULTIPLICATION FOR TWO-MATERIAL SHELLS

Material	IR (cm)	OR (cm)	ϕ/ϕ_0 at 50 cm from Plate
OyC	1.4	3.9	6.9
Oy	3.9	7.5	
Oy	3.2	6.7	7.1
Pu	6.7	7.5	

TABLE IX-VI

INSIDE RADIUS (IR), OUTSIDE RADIUS (OR), AND FLUENCE MULTIPLICATION FOR THREE-MATERIAL SHELLS

Material	OR (cm)	IR (cm)	ϕ/ϕ_0 at 50 cm from Plate
OyC	4.0	1.3	
Oy	7.0	4.0	10.0
Pu	7.5	7.0	

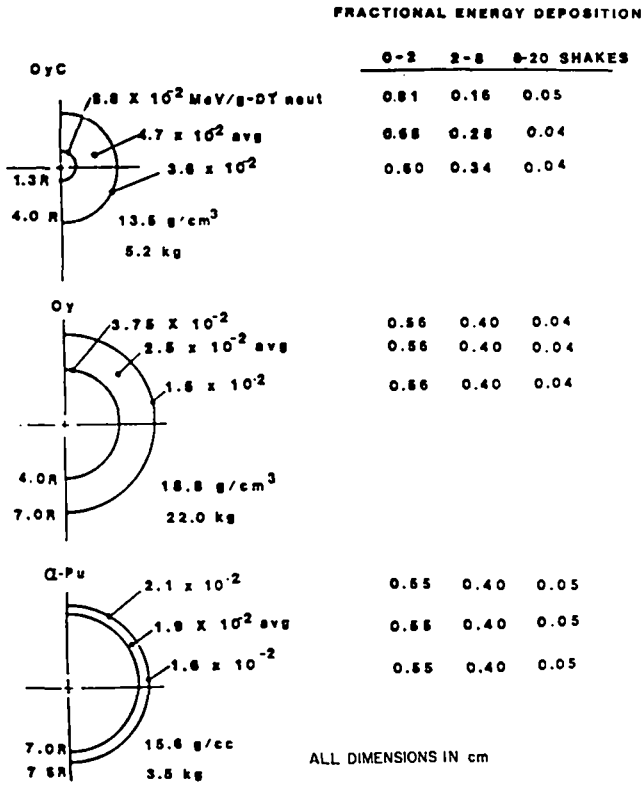

Fig. IX-20.
Energy deposition at selected points in the nested shells of the first stage.

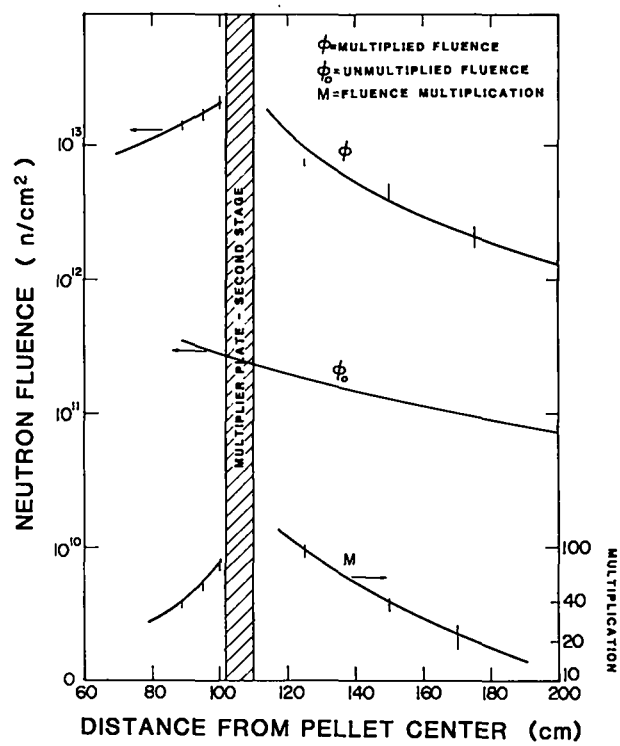

Fig. IX-21.
Neutron fluence as a function of distance from pellet center (100-kJ pellet).

Tuning of Second Stage. Because the neutron energy spectrum emitted by the first stage is degraded relative to the 14.1-MeV source that drove the second stage alone, a configuration of 8.0 cm ^{238}U and 5.0 cm ^{235}U is no longer optimal. A calculation shows that over half of the neutrons emitted by the first stage lie below the threshold for fission in ^{238}U. Accordingly, the second stage was returned by omitting the ^{238}U entirely. We found that the three-shell arrangement with a second-stage multiplier consisting of 8.0 cm ^{235}U gave a fluence multiplication 50 cm downstream of the second stage of 37 ± 5 at a k-effective value of 0.8. The available area at this station is over 2 m^2, but the fluence will not be uniform. The multiplied fluence at 50 cm downstream of the second stage is $\sim 4.5 \times 10^{12}$ for a 100-kJ pellet.

The fluence as a function of position for the three-shell/^{235}U plate is shown in Fig. IX-21. The close-in fluence for a 100-kJ pellet is as high as 10^{13} n/cm^2, and the available area is as large as 1 m^2. The time-dependence of the fluence at downstream locations shows that the neutron pulse width is ~40 ns. Use of a reflector around the second stage would lengthen the pulse somewhat.

Conclusions

By using a two-stage multiplier design with a 100-kJ pellet yield, and provided thermal analysis of the first stage is satisfactory, we can realize the following performance parameters:

- centerline fluence, 10^{13} n/cm^2 per shot;
- total available area, 1 m^2; and
- k-effective value, 0.8.

REFERENCES

1. W. B. Hermannsfeldt, Ed., Proc. HIF Workshop, Berkeley, Calif., October 29-November 9, 1979, Lawrence Berkeley Laboratory report LBL-10301 (Semptember 1980).

2. I. O. Bohachevsky, D. O. Dickman, and J. C. Goldstein, "A New Plasma Model for the ICF Magnetic Wall Reactor Cavity Concept," ANS Trans. 30, 20-21 (November 1978). This material was also published in "Inertial Fusion Program, January 1—June 30, 1978," Frederick Skoberne, Comp., Los Alamos Scientific Laboratory report LA-7587-PR (May 1980).

3. J. C. Goldstein, I. O. Bohachevsky, and D. O. Dickman, "Plasma Evolution in a Gas Buffered ICF Reactor Vessel," APS Bull. 24, 8, 1071, paper 7 x 4 (October 1979). This material was also published in Roger B. Perkins and the Inertial Fusion Program Staff, "Inertial Fusion Program, January 1—June 30, 1979," Los Alamos National Laboratory report LA-8114-PR (June 1981).

4. I. O. Bohachevsky, D. O. Dickman, J. J. Devaney, J. C. Goldstein, A. R. Larson, and J. H. Pendergrass, "Modeling of Phenomena in Magnetically Protected ICF Reactor Cavities," ANS Trans. 33, 47 (November 1979).

5. I. O. Bohachevsky, D. O. Dickman, and J. C. Goldstein, "Plasma Modeling for the Magnetically Protected Reactor Cavity," Technical Digest, 2nd Topical Meeting on ICF, CLEOS 1980 Conference, San Diego, Calif., February 26-28, 1980.

6. I. O. Bohachevsky, J. C. Goldstein, and D. O. Dickman, "A Plasma Model for ICF Reactor Studies," Proc. Conf. on Plasma Physics, Nagoya, Japan, April 7-11, 1980, (Fusion Research Association of Japan, 1980), Vol. 1, p. 384.

7. "Laser-Fusion Program at LASL, July 1—December 31, 1975," F. Skoberne, Comp., Los Alamos Scientific Laboratory report LA-6245-PR (July 1976).

8. T. G. Frank, "A Thorium-Uranium Cycle ICF Hybrid Concept," Proc. 3rd Topical Meeting Technology of Controlled Nuclear Fusion, Santa Fe, N. Mex., May 9-11, 1978 (National Technical Information Service, U. S. Department of Commerce), CONF-78058, Vol. 2, p. 1254.

9. Roger B. Perkins and the Laser Fusion Program Staff, "Inertial Fusion Program, July 1—December 31, 1978," Frederick Skoberne, Comp., Los Alamos Scientific Laboratory report LA-7755-PR (November 1980).

10. W. A. Reupke, H. S. Cullingford, T. G. Frank, and L. A. Booth, "Fissile Fuel Production of Laser-Driven Fusion," US/USSR Symposium on Fusion-Fission (Hybrid) Reactors, Princeton Plasma Physics Laboratory, Princeton, New Jersey, January 22-26, 1979.

11. W. A. Reupke, H. S. Cullingford, T. G. Frank, and L. A. Booth, "Wetted-Wall ICF Fissile Fuel Factory Studies," Trans. Amer. Nucl. Soc. 32, 29 (1979).

X. RESOURCES, FACILITIES, AND OPERATIONAL SAFETY

The construction of HEGLF (Antares) continued. Operational safety policies and procedures continued to be applied successfully to minimize the hazards of operating high-power lasers.

MANPOWER DISTRIBUTION

The distribution of employees assigned to the various categories of the DOE-supported Inertial Fusion Research Program is shown in Table X-I.

FACILITIES

High-Energy Gas Laser Facility (HEGLF)

Construction Package I, including the laser building, the mechanical building, the office building, and a warehouse is 96.3% complete, with a scheduled completion date of June 1980.

Construction Package II, including the target building, the power-transmission system, and miscellaneous construction is 93.8% complete, with a scheduled completion date of June 1980.

TABLE X-I

APPROXIMATE STAFFING LEVEL
OF LASER PROGRAM
December 31, 1979

Tasks	Direct Employees
CO_2 laser development	60
CO_2 laser experiments	115
Target design	28
Target fabrication	49
Diagnostics development	40
Heavy ion source development	4
Systems and applications studies	8
Advanced technology	2
Weapons application	9
TOTAL	315

In the interest of continuity, we have presented details of HEGLF Design and Construction in Section II.

Target Fabrication Facility

Design criteria have been completed and Black & Veatch, Kansas City, has been selected as the architect/engineer for this project. The Congress has appropriated $1 million of FY 1980 funding for facility design; it is expected that this work will begin in April 1980. Authorization for construction is being requested as a FY 1981 line item with a total estimated cost of $15.3 million. The proposed facility has 45 000 sq ft of laboratory space and 13 000 sq ft of office space and will support fabrication for the Laboratory's Inertial Fusion Program, as well as Sandia National Laboratory's Pulsed Power Program.

OPERATIONAL SAFETY

General

The excellent lost-time injury rate continued during this period with no serious accidents reported.

Laser Safety Publication

An article titled "A Practical Approach to Laser Safety," authored by the L-Division Safety Officer, was prepared for publication in the Electro Optics Systems Design Magazine.

Laser Fusion Facility Final Safety Analysis Report (FSAR)

The FSAR was submitted to DOE for certification of the three-building complex.

An inspection team from the Albuquerque Operations Office visited the facility to confirm the details of the FSAR. Formal certification of the facility is anticipated soon.

XI. PATENTS, PUBLICATIONS, AND PRESENTATIONS

PATENTS

Serial numbers, filing dates, patent numbers, and issue dates may not be known for several months after they are assigned. Therefore, for any given period, cases may be missing from these listings if patent activity occurred later in the reporting period.

The following applications were filed in the U. S. Patent Office.

S. N. 067859 — "Method and Apparatus for Producing Cryogenic Inertially Driven Fusion Targets," John R. Miller, filed August 20, 1979.

S. N. 071603 — "Device and Method for Electron Beam Heating of a High Density Plasma," Lester E. Thode, filed August 31, 1979.

S. N. 083484 — "Light Modulated Electron Beam Driven Radiofrequency Emitter," Mahlon T. Wilson, Paul J. Tallerico, and Thomas D. Hayward, filed October 10, 1979.

S. N. 092155 — "RF Feedback Free Electron Laser," Charles A. Brau, Donald A. Swenson, and Thomas J. Boyd, Jr., filed November 2, 1979.

S. N. 095681 — "Sputter Coating of Microspherical Substrates by Levitation," Arthur T. Lowe and Charles D. Hosford, filed November 19, 1979.

PUBLICATIONS

This list of publications is prepared from a stored computer data base.

Target Fabrication

J. R. Miller, S. Butler, and J. K. Feuerherd, "Microparticle Dispenser," Rev. Sci. Instrum. 49, 268-9 (1978).

A. Mayer and D. S. Catlett, "Plating Laser Fusion and Electron Beam Fusion Targets," TIC.

E. H. Farnum, R. J. Fries, and J. E. Barefield, "Materials Problems with Inertial Confinement Fusion Targets," TINC Journal of Nuclear Materials, TIC (1979), 10 pp., micronegative.

J. R. Miller and W. J. Press, "Cryogenic Laser Fusion Target Materials," TINC J. Nucl. Materials, TIC (1979), 19 pp., micronegative.

Theory

B. Bezzerides, D. W. Forslund, and E. L. Lindman, "Existence of Rarefraction Shocks in a Laser-Plasma Corona," Phys. Fluids 21, 2179-85 (1978); Phys. Rev. Lett. 42, 239-43 (1979).

D. B. Henderson and A. G. Petschek, "Effect of Deviaions from the Maxwell Distribution on Neutron Production in Laser Targets," Los Alamos Scientific Laboratory report LA-7532-MS (1978).

A. T. Peaslee, "Proceedings of the Impact Fusion Workshop," Los Alamos Scientific Laboratory report LA-8000-C (1979).

Experiments and Diagnostics

R. F. Benjamin, P. D. Goldstone, and J. P. Carpenter, "Direct Measurement of the Accuracy of Carbon Dioxide Laser Alignment on Target," Appl. Opt. 17, 3809-11 (1978).

L. R. Veeser, J. C. Solem, and A. J. Lieber, "Impedance-Match Experiments Using Laser-Driven Shock Waves," Appl. Phys. Lett. 35, 761 (1979).

Ronald E. Brown, F. D. Correll, R. F. Haglund, Jr., R. A. Hardekopf, Nelson Jarmie, G. G. Ohlsen, and P. A. Schmelzbach, "Direct-Reaction and Isopin Symmetries in d + d Reactions," Phys. Rev. C 20, 892 (1979).

E. R. Flynn, Ronald E. Brown, R. F. Haglund, R. A. Hardekopf, P. A. Schmelzbach, J. W. Sunier, and V. von Dertzen, "Analyzing Power in the Mass-Six Supermultiplet System," Nucl. Phys. A319, 61 (1979).

R. P. Godwin, "Absorption in Laser-Produced Plasma Experiments: A Personal View," Appl. Opt. **18**, No. 21, 3555 (1979).

Systems Studies

I. O. Bohachevsky and J. F. Hafer, "Sputtering Erosion in Inertial Confinement Fusion Reactors," Nucl. Technol. **41**, 299-311 (1978).

I. O. Bohachevsky, J. F. Hafer, J. J. Devaney, and J. H. Pendergrass, "Inertial Confinement Fusion Reactor Cavity Phenomena," TIC (1978), 12 pp., micronegative.

I. O. Bohachevsky, L. A. Booth, T. G. Frank, and J. H. Pendergrass, "Loads and Stresses in ICP Reactors," TIC (1979), 16 pp., micronegative.

V. K. Viswanathan and P. D. Bolen, "Use of the Smartt Interferometer as an Alignment Tool for Infrared Laser Systems," Adaptive Optical Components, II Seminar Proc., Washington, D.C., (1979), pp. 107-13; Soc. of Photo-Optical Instrumentation Engineers (1979), 621.26/A2210-/1979; TIC (1979), 8 pp., micronegative.

Laser Development

E. T. Salesky and D. Korff, "Calculation of HCl Linewidths Using a New Impact Parameter Theory," Phys. Lett. 72A (August 1979).

R. B. Gibson, "Fast High-Voltage High-Current Switch: Thyratron-Spark Gap Hybrid," Rev. Sci. Instrum. **50**, 1489 (November 1979).

R. B. Gibson, K. Boyer, and A. Javan, "Mixed Isotope Multiatmosphere CO_2 Laser," J. Quant. Elec. QE-15, 1224 (November 1979).

E. J. McLellan and J. F. Figueira, "Ultrafast Pockels Cells for the Infrared," Rev. Sci. Instrum. **50**, 1213 (1979).

J. A. Hanlon, M. D. Bausman, M. Caine, M. Calcote, R. L. Carlson, J. J. Hayden, I. Liberman, J. Murphy, R. Parnell, R. Partridge, J. Reay, G. Salazar, and F. H. Tucker, "Helios Carbon Dioxide Fusion Laser Alignment System," Adaptive Optical Components, II Seminar Proc., Washington, D.C., (1979), pp. 61-6; SPIE (1979).

R. D. Stine, Jr., G. F. Ross, and C. Silvernail, "Antares Laser Power Amplifier," TIC (1979), 8 pp., micronegative.

R. R. Williamson, "60-Inch Annular Pitch Polisher for LASL's Laser-Fusion Effort," TIC (1978), 6 pp., micronegative.

E. J. McLellan and S. Stotlar, "Sub-One-Hundred-PS Pyroelectric Detector Research and Evaluation Program at LASL," TIC (1978), 13 pp., micronegative.

R. K. Ahrenkiel, D. J. Dunlavy, J. F. Figueira, C. R. Phipps, Jr., S. Thomas, and A. J. Sievers, "New 10.6-Micrometer Saturable Absorber-Potassium Chloride Doped with DREO(4)," TIC, n.d., 8 pp., micronegative.

I. J. Bigio, G. J. Feldman, R. A. Fisher, and E. E. Bergmann, "High Efficiency Phase-Conjugate Reflection in Germanium and in Inverted Carbon Dioxide," TIC (1978), 8 pp., micronegative.

R. E. Partridge, Jr., "Automated Alignment of a 10-Kilojoule Laser," Laser Focus, 66-9 (March 1979).

D. Blevins and J. L. Munroe, "Plated Copper Substrates for the LASL Antares Carbon Dioxide Laser System," TIC (1979), 7 pp., micronegative.

R. A. Dougal, C. R. Jones, M. Gundersen, and L. Y. Nelson, "Longitudinal-Mode Control of a Carbon Dioxide TE Laser by Means of Intracavity Absorbers," Appl. Opt. **18**, 1311-3 (1979).

B. E. Newnam and D. H. Gill, "Ultraviolet Damage Resistance of Laser Coatings," TINC, TIC (1978), 19 pp., micronegative.

V. K. Viswanathan, J. E. Sollid, W. S. Hall, I. Liberman, and G. Lawrence, "Interferogram Reduction and Interpretation as Applied to the Optical Analysis of a

Laser Fusion System," TIC (1978), 16 pp., and *Optical Interferograms-Reduction and Interpretation*, A. H. Guenther and D. H. Liebenberg, Eds. (American Society for Testing and Materials, 1978), pp. 98-106.

H. Volkin, "A Direct Solar Pumped Laser," Los Alamos Scientific Laboratory report LA-7982-MS (1979).

A. E. Greene and C. A. Brau, "Theoretical Studies of UV-Preionized Transverse Discharge Krypton Fluoride and Argon Fluoride Laser," J. Quant. Elec. **QE-14**, 951-7 (1978).

C. A. Fenstermacher, "High-Energy, Short-Pulse, Carbon-Dioxide Lasers," TIC (1979), 26 pp., micronegative.

Robert A. Fisher and B. J. Feldman, "On-Resonant Phase-Conjugate Reflection and Amplification at 10.6 μm in Inverted CO_2," Opt. Lett. 4, No. 5 (May 1979).

I. J. Bigio, B. J. Feldman, R. A. Fisher, and E. E. Bergmann, "High-Efficiency Wavefront Reversal in Germanium and in Inverted CO_2," Kvantovaya Elektron (Moscow) 6, 2318-2325 (November 1979), translated in Sov. J. Quant. Electron. 9, 11 (November 1979).

J. E. Sollid, C. R. Phipps, Jr., S. J. Thomas, and E. J. McLellan, "Lensless Method of Measuring Gaussian Laser Beam Divergence," Appl. Opt. **16**, 3527-9 (1978).

C. R. Phipps, Jr., J. F. Figueira, S. J. Czuchlewski, and S. J. Thomas, "Efficient Plasma Isolator for High-Power 10-μm Lasers," Annual Meeting of the Plasma Physics Division, Bull. Am. Phys. Soc. 24, 1078 (1979).

Irving J. Bigio, "Electron-Attaching Gases in Laser Discharges: Altered Discharge Parameters and Negative-Ion Production," French Journal de Physique C7, No. 7-40, 365 (July 1979).

PRESENTATIONS

Target Fabrication

E. H. Farnum and Jurgen K. Feuerherd, "Micro-Machining Laser Fusion Targets with a Pulsed Dye Laser," Plasa Physics Division, Boston, Massachusetts, November 12-16, 1979.

Experiments and Diagnostics

The following presentations were made at the APS Annual Meeting of the Plasma Physics Division, Boston, Massachusetts, November 12-16, 1979.

K. B. Mitchell, "X-Ray Diagnostics for High Density Laser-Produced Plasmas."

M. M. Mueller, "Reconstruction of Spherical Source Emission Profiles from X-Ray Pinhole Photographs by Means of an Iterative Integral Technique."

F. Begay, "Ion Acceleration Processes in CO_2 Laser-Induced Carbon Plasmas."

R. F. Benjamin, "Optical Measurements of Return Current in CO_2 Laser Plasmas."

D. M. Stupin, R. H. Day, M. A. Winkler, C. K. Crawford, and T. S. Tyrie, "Low-Energy, Intense, Monoenergetic X-Ray Source for Laser Fusion."

M. A. Yates, "Development of a Radiochemical Diagnostic for the Helios System."

A. W. Ehler, "Effect of Target Purity on Laser Produced Plasma Expansion."

D. B. van Hulsteyn, "Compression Measurements of High Density Laser-Imploded Targets."

A. H. Williams, "Ultra-Fast Neutron Detectors for Laser Fusion Diagnostics."

A. W. Ehler, "Impurity Effects on the Isothermal Expansion of a Laser Produced Plasma."

A. Hauer, "Diagnosis of High Density Laser Compression with Argon Spectroscopy."

R. F. Benjamin, "Optical Measurements of Energy Transport in Laser-Plasma."

V. M. Cottles, "The Absorption Apparatus for the Gemini Laser System."

M. M. Mueller, "Reconstruction of Spherical Source Emission Profiles from X-Ray Pinhole Photographs by Means of an Iterative Integral Technique."

P. D. Rockett and J. S. McGurn, "Temporally Resolved X-Ray Measurements of CO_2 Laser Irradiated, Seeded Glass Microballoons."

In addition, the following presentations were made at various institutions.

L. R. Veeser, A. J. Lieber, and J. C. Solem, "Planar Streak Camera Laser-Driven Shock Studies," Int. Conf. on Lasers 1979 (Society for Optical and Quantum Electronics), Orlando, Florida, December 17, 1979.

K. B. Mitchell, "X-Ray Measurements of Density from Ablative Targets Irradiated with 10 Micrometer Lasers," Gordon Conference, Tilton, New Hamsphire, August 12-16, 1979.

T. H. Tan, "Ion and Neutron Measurements and High Density Experiments," Gordon Conference, Tilton, New Hampshire, August 12-16, 1979.

M. A. Yates, "Progress in Laser Experiments at Los Alamos," Brookhaven National Laboratory, Upton, New York, November 10, 1979; the University of South Carolina, Columbia, South Carolina, November 11, 1979.

R. J. Fries, R. A. Kopp, G. H. McCall, and Tai-Ho Tan, "The Twenty-Times-Liquid-Density Experiment," IEEE Minicourse, Montreal, Quebec, June 4-8, 1979.

G. H. McCall, "Medium Density Laser Driven Implosion Experiments," 13th Eur. Conf. on Laser Interact. with Matter, Leipzig, Germany, 1979.

R. F. Benjamin and J. H. Riffle, "Optical Measurements of Energy Transport in Laser-Fusion," Annual Meeting of the Optical Society of America, Rochester, New York, October 8-12, 1979.

Laser Development

The following presentations were made at the Los Alamos Scientific Conference on Optics '79, Los Alamos, New Mexico, May 23-25, 1979.

J. F. Figueira, R. K. Ahrenkiel, and D. Dunlavy, "Nonlinear Optical Properties of the Perrhenate Ion in KCl," SPIE Vol. 190, pp. 293-296.

I. Liberman, "Application of Phase Conjugation to Carbon-Dioxide Fusion Lasers," SPIE Vol. 190, pp. 426-29.

V. K. Viswanathan, J. V. Parker, T. A. Nussmeier, C. J. Swigert, W. King, A. S. Lau, and K. Price, "Use of Adaptive Optics Element for Wavefront Error Correction in the Gemini CO_2 Laser Fusion System," SPIE Vol. 190, pp. 251-257.

S. V. Gunn, T. A. Heinz, W. D. Henderson, N. A. Massie, and V. K. Viswanathan, "Novel Deformable Mirror Design for Possible Wavefront Correction in CO_2 Laser Fusion Systems," SPIE Vol. 190, p. 258.

B. J. Feldman, R. A. Fisher, E. E. Bergman, I. J. Bigio, R. G. Tercovich, and F. Sena, "Intracavity Techniques for High Reflectivity Phase Conjugation at 10.6 μm in Germanium and Inverted CO_2," SPIE Vol. 190, p. 412.

R. L. Carlson, D. E. Casperson, J. Hanlon, J. S. Ladish, R. Quicksilver, and C. Smith, "Beam Simultaneity in Multi-Terawatt CO_2 Laser Fusion Systems," SPIE Vol. 190, pp. 172-177.

R. F. Haglund, Jr., D. E. Casperson, S. J. Czuchlewski, C. J. Elliott, J. C. Goldstein, J. S. Ladish, and A. V. Nowak, "Optimization of a Multicomponent Gaseous Saturable Absorber for the Helios CO_2 Laser System," SPIE Vol. 190, pp. 178-185.

V. K. Viswanathan and P. D. Bolen, "Infrared Smartt Interferometer as an Alignment Tool for CO_2 Laser Fusion Systems," SPIE Vol. 190, pp. 243-250.

V. K. Viswanathan, J. J. Hayden, and I. Liberman, "Optical Performance of the Gemini CO_2 Laser Fusion System," SPIE Vol. 190, pp. 165-171.

V. K. Viswanathan, "Optical Design and Analysis of CO_2 Laser Fusion Systems Using Interferometry and Fast Fourier Transform Techniques," SPIE Vol. 190, pp. 158-164.

The following presentations were made at the Annual Meeting of the Optical Society of America, Rochester, New York, October 8-12, 1979.

S. C. Stotlar, E. J. McLellan, A. J. Gibbs, and J. A. Webb, "Short-Pulsed Carbon Dioxide Laser Damage Studies on Pyroelectric Materials."

V. K. Viswanathan, R. B. Hammond, I. Liberman, B. D. Seery, A. Gibbs, and P. D. Bolen, "Infrared Smartt Interferometer."

J. L. Munroe, "Interferometric Evaluation of Diamond-Turned Mirrors for Carbon-Dioxide Laser Fusion."

The following presentations were made at the International Conference on Lasers '79, Orlando, Florida, December 17-21, 1979.

B. J. Feldman, R. A. Fisher, and W. W. Rigrod, "Studies of Infrared Phase Conjugation in Germanium."

D. E. Watkins and S. J. Thomas, "Degenerate Four-Wave Mixing in P-Type Ge at CO_2 Wavelengths."

C. R. Phipps, S. J. Thomas, and D. E. Watkins, "Effect of Nonlinear Refraction on Beam Brightness in Laser Applications."

E. J. McLellan, S. C. Stotlar, J. A. Webb, and A. Gibbs, "Generation and Detection of Ultrafast CO_2 Laser Pulses."

D. E. Watkins and W. W. Rigrod, "Degenerate Four-Wave Mixing in Inhomogeneously Broadened Absorbing Media."

E. J. McLellan, "Short Pulse Generation and Detection for CO_2 Lasers."

In addition, the following presentations were made at various institutions.

G. T. Schappert, "Fusion with CO_2 Lasers," Colloquium, University of New Mexico (November 1979).

G. T. Schappert, "The LASL Gemini and Helios Laser System in Operation," Electro-Optics '79, Proc. of the Technical Program, Anaheim, California (October 1979), pp. 457-464.

R. P. Leavitt and E. T. Salesky, "Pressure Broadening and Shifting of Rotation and Rotation-Vibration Spectral Lines of HCl by Nobel Gases," 4th International Conference on Infrared and Millimeter Waves, Miami, Florida (December 1979).

R. A. Fisher and B. J. Feldman, "Phase Conjugation in Inverted Media," 1979 Gordon Conference on Lasers and Nonlinear Optics, Wolfeboro, New Hamsphire (July 3, 1979).

Irving J. Bigio, "Beam Diagnostics in the Helios Laser Fusion Facility," Max-Planck Institute, Laser Research Project, Garching bei Munchen, West Germany (July 1979).

Irving J. Bigio, "Kinetics of Discharges in Electron-Attaching Gases," C.G.E. Laboratoires de Marcoussis, Marcoussis, France (July 1979).

Irving J. Bigio, "Status of the Helios Laser Fusion Facility," Ecole Polytechnique, Palaiseau, France (July 1979).

J. S. Ladish, "Helios, A 20 TW CO_2 Laser Fusion Facility," Laser '79 Conf., Munich, IPC Science and Technology Press (1979).

S. C. Stotlar, E. J. McLellan, A. J. Gibbs, J. A. Webb, "Sub-One-Hundred-ps Pyroelectric Detectors for 10.6 μm," Quantum Electronics Conference, England (October 1979).

C. R. Phipps, Jr., J. F. Figueira, S. J. Czuchlewksi, and S. J. Thomas, "Efficient Plasma Isolator for High-Power 10-μm Lasers," APS Annual Meeting of the Plasma Physics Division, Boston, Massachusetts (November 12-16, 1979).

C. M. Gillespie, R. P. Godwin, and J. S. Ladish, "Helios and the LASL ICF Experimental Program," Am. Nucl. Soc., San Francisco, California (November 11-16, 1979).

☆ U.S. GOVERNMENT PRINTING OFFICE: 1981—376-088/2

Printed in the United States of America
Available from
National Technical Information Service
US Department of Commerce
5285 Port Royal Road
Springfield, VA 22161

Microfiche $3.50 (A01)

Page Range	Domestic Price	NTIS Price Code	Page Range	Domestic Price	NTIS Price Code	Page Range	Domestic Price	NTIS Price Code	Page Range	Domestic Price	NTIS Price Code
001-025	$ 5.00	A02	151-175	$11.00	A08	301-325	$17.00	A14	451-475	$23.00	A20
026-050	6.00	A03	176-200	12.00	A09	326-350	18.00	A15	476-500	24.00	A21
051-075	7.00	A04	201-225	13.00	A10	351-375	19.00	A16	501-525	25.00	A22
076-100	8.00	A05	226-250	14.00	A11	376-400	20.00	A17	526-550	26.00	A23
101-125	9.00	A06	251-275	15.00	A12	401-425	21.00	A18	551-575	27.00	A24
126-150	10.00	A07	276-300	16.00	A13	426-450	22.00	A19	576-600	28.00	A25
									601-up	†	A99

†Add $1.00 for each additional 25-page increment or portion thereof from 601 pages up.